TECHNISCHE UNIVERSITÄT MÜNCHEN
Max-Planck-Institut für Physik
Werner-Heisenberg-Institut

Physik-Department
Lehrstuhl für Experimentelle Astroteilchenphysik (E15)

Exploring Light Dark Matter With CRESST-II Low-Threshold Detectors

Florian Reindl

Vollständiger Abdruck der von der Fakultät für Physik der Technischen Universität München zur Erlangung des akademischen Grades eines

Doktors der Naturwissenschaften (Dr. rer. nat.)

genehmigten Dissertation.

Vorsitzender:		Prof. Dr. Alejandro Ibarra
Prüfer der Dissertation:	1.	Prof. Dr. Stefan Schönert
	2.	Priv.-Doz. Dr. Hubert Kroha
	3.	Prof. Dr. Gilles Gerbier (nur schriftliche Beurteilung)

Die Dissertation wurde am 29.02.2016 bei der Technischen Universität München eingereicht und durch die Fakultät für Physik am 23.05.2016 angenommen.

Contents

Abstract

Already more than 80 years ago F. Zwicky found first evidence for the existence of dark matter. Today, we precisely know that dark matter is roughly five times more abundant than ordinary, baryonic matter. The underlying nature of dark matter, however, remains an unsolved mystery.

The first chapter of this work presents seminal astronomic evidence for dark matter and the resulting constraints which a potential dark matter particle has to fulfill. This thesis was written in the framework of the CRESST-II experiment, one of the leading direct dark matter search experiments world-wide. The goal of direct dark matter detection is to measure interactions of dark matter particles with ordinary matter. Chapter 2 points out the main challenges of direct searches: small anticipated event rate and little energy being transferred ($\mathcal{O}$(keV)) in the interaction. Currently, different technologies are applied by numerous experiments around the globe to face these challenges - a brief review concludes chapter 2.

Chapters 3 and 4 describe the set-up of the CRESST-II experiment and results of the previous measurement campaign (phase 1), which ended in 2011 after two years of measurement. Core element of a CRESST-II detector is a calcium tungstate crystal ($CaWO_4$), equipped with a highly-sensitive thermometer. Every particle interaction in the crystal heats it up. The temperature rise is measured by the thermometer allowing a precise determination of the energy deposited in the crystal (phonon signal). Simultaneously, the crystal emits scintillation light, measured by a separate light detector. The amount of light produced, however, depends on the type of particle and, thus, allows to discriminate backgrounds from a potential signal.

In phase 1, a likelihood analysis was carried out finding more events than expected from the known backgrounds. Moreover, the excess could be explained by a potential dark matter signal, with reasonable features for the dark matter particle concerning its mass and the interaction cross section. Since this interpretation was in tension with previous CRESST-II results, as well as with results from other direct dark matter searches, one main goal of phase 2 was to clarify the origin of this excess. Measures undertaken to reach this goal are presented at the end of chapter 4.

Phase 2 denotes the measurement campaign carried out between July 2013 and August 2015. The main aspect of this thesis is the development of a *low-threshold* analysis allowing to make use of all data down to the trigger threshold of a detector. Thereby, the analysis focuses on data acquired with the detector modules TUM40 and Lise. TUM40 is chosen, because of its superior overall performance in terms of energy resolution, trigger threshold and background level. Lise exhibits a threshold of 307 eV, which is the lowest value obtained for all detector modules operated in phase 2 and simultaneously among the lowest thresholds for nuclear recoils of all direct dark matter searches. The first step of any

analysis is the processing and cleaning of the raw data, as outlined in the chapters 5 and 6, with a special emphasis on new developments arising from the analysis of small pulses (small energy depositions).

As already mentioned the amount of scintillation light produced depends on the type of the interacting particle, quantified by the so-called quenching factors. Recent measurements showed that these quenching factors are not constant, but depend on the deposited energy. The implementation of this energy dependence is another novelty of this thesis, as discussed in chapter 7.

In contrast to phase 1, no hint for a dark matter signal is seen in the data of phase 2. Therefore, this thesis presents upper limits on the cross section for dark matter interacting with ordinary matter. In general, the simplest method to calculate such an upper limit is to relate the number of events expected from dark matter to the number of events observed (measured) in the detector. However, for the given application this method provides too conservative limits in the light of a non-negligible number of background events. Thus, two different statistical methods are applied to derive exclusion limits from the data.

The first method, named after its developer S. Yellin, is discussed in chapter 8. The basic idea thereby is to not only base the exclusion limits on the number of events, but to also take into account the energy spectrum, or more precisely the differences in the energy spectra of signal and background. Since the anticipated dark matter energy spectrum rises exponentially towards low energies, while the background spectrum stays rather flat, the Yellin method yields powerful exclusion limits. It should be emphasized that no assumption on the background energy spectrum are imposed, which renders the results immune against potential uncertainties in the modeling of the background. For this reason, the Yellin method was used to derive the main results of this low-threshold analysis as presented in chapter 9. For dark matter particles lighter than 1.7 GeV/c^2 CRESST-II exhibits world-leading sensitivity, corresponding to the most stringent exclusion limit. Moreover, dark matter particle masses down to 0.5 GeV/c^2 could be probed - a novelty in the field of direct dark matter detection.

Chapter 10 presents the (profile) likelihood method as a second statistical method for the data analysis. The likelihood method goes beyond the Yellin approach in two aspects. Firstly, the measured events are not only evaluated concerning the deposited energy, but also the scintillation light signal of each event is considered. Secondly, it allows to include knowledge about the two-dimensional background distribution. Since the dominant backgrounds in TUM40 and Lise are precisely known, as it is shown in this thesis, the likelihood framework gains in sensitivity compared to the Yellin method, in particular for very light dark matter particles.

The success of this low-threshold analysis motivated the CRESST collaboration to dedicatedly optimize its detectors regarding low trigger thresholds. The enhanced sensitivity will allow to further explore the regime of low-mass dark matter particles.

Zusammenfassung

Bereits vor mehr als 80 Jahren fand F. Zwicky erste Indizien füer die Existenz der Dunklen Materie, heute wissen wir sehr genau dass es im Universum etwa fünf mal so viel Dunkle Materie, als gewöhnliche, baryonische Materie gibt. Woraus die Dunkle Materie aber besteht ist bisher im Verborgenen geblieben.

Das erste Kapitel präsentiert bahnbrechende astronomische Nachweise Dunkler Materie und daraus resultierenden Eigenschaften, welche potentielle Teilchen der Dunklen Materie erfüllen müssen. Die vorliegende Arbeit ist im Rahmen des CRESST-II Experiments entstanden, eines der weltweit führenden Experimente zum direkten Nachweis der Dunklen Materie. Ziel des direkten Nachweises ist es Wechselwirkungen von Teilchen der Dunklen Materie mit gewöhnlicher Materie zu messen. Das Kapitel 2 legt die wesentlichen Herausforderungen der direkten Suche nach Dunkler Materie dar: die geringe Anzahl an zu erwartenden Ereignissen, sowie der geringe Energieübertrag ($\mathcal{O}$(keV)) in der Wechselwirkung. Weltweit werden derzeit verschiedene Technologien eingesetzt um diesen Herausforderungen gerecht zu werden - eine Übersicht rundet Kapitel 2 ab.

Die Kapitel 3 und 4 beschreiben den Aufbau des CRESST-II Experimentes und die Ergebnisse der vorangegangenen Messkampagne (Phase 1), welche im Jahre 2011 nach zweijähriger Messzeit beendet wurde. Kernstück eines CRESST-II-Detektors ist ein Kristall aus Kalziumwolframat ($CaWO_4$), bestückt mit einem hochsensiblen Thermometer. Jegliche Wechselwirkung eines Teilchens in diesem Kristall führt zu Erwärmung desselbigen, wobei der durch das Thermometer gemessene Temperaturanstieg (auch das Phononsignal genannt) eine präzise Messung der im Kristall deponierten Energie erlaubt. Gleichzeitig emittiert der Kristall Szintillationslicht, welches durch einen separaten Lichtdetektor nachgewiesen wird. Wieviel Licht jedoch produziert wird hängt von der Art des Teilchens ab, was erlaubt Untergründe von einem potentiellen Signal zu trennen.

In Phase 1 fand eine Likelihood-Analyse mehr Ereignisse als von den bekannten Untergründen erwartet wurde. Darüber hinaus konnte man diese Ereignisse durch die Existenz Dunklen Materie Teilchen, mit plausiblen Eigenschaften hinsichtlich der Masse und des Wechselwirkungsquerschnittes, erklären. Da diese Interpretation jedoch im Widerspruch, sowohl zu vorangegangen Ergebnissen des CRESST-II Experimentes, als auch zu Ergebnissen anderer direkter Suchen, stand, war die Klärung des Ursprungs dieses Überschusses eines der wesentlichen Ziele von Phase 2. Zum Ende von Kapitel 4 werden die Maßnahmen diskutiert, welche unternommen wurden um dieses Ziel zu erreichen.

Phase 2 bezeichnet die Messkampagne, welche von Juli 2013 bis August 2015 andauerte. Das Hauptaugenmerk dieser Arbeit liegt auf der Entwicklung einer Analyse welche es ermöglicht alle Daten bis zur Triggerschwelle eines Detektors auszuwerten. Dabei konzentriert sich die Analyse auf Daten die mit den Dektormodulen TUM40 und Lise aufgezeichnet wurden. TUM40 wurde ausgewählt aufgrund der überlegenen Gesamtleistung,

insbesondere hinsichtlich der Energieauflösung, der Triggerschwelle und des Untergrundniveaus. Lise hat mit 307 eV die niedrigste Schwelle aller Detektoren von Phase 2. Diese Schwelle ist gleichzeitig unter den niedrigsten Werten (für Kernrückstöße) aller Experimente zur direkten Suche nach Dunkler Materie. Der erste Schritt einer jeden Analyse ist die Aufbereitung und Reinigung der Rohdaten, welche in den Kapiteln 5 und 6 beschrieben werden, wobei besonderes Augenmerk auf die Neuentwicklungen gelegt wird, welche sich durch die Anforderungen der Analyse sehr kleinen Pulse (sehr kleiner Energiedepositionen) ergeben.

Wie bereist erwähnt hängt die Menge an produziertem Szintillationslicht von der Art des Teilchens ab, quantifiziert durch die sogenannten Quenchingfaktoren. Jüngste Messungen zeigen, dass diese Faktoren nicht konstant sind, sondern von der deponierten Energie abhängen. Die Implementierung dieser Energieabhängigkeit ist eine weitere Neuerung der vorliegenden Arbeit, welche in Kapitel 7 beschrieben wird.

Im Gegensatz zu Phase 1 sind keine Indizien für ein Signal Dunkler Materie in den Daten von Phase 2 erkenntlich. Deshalb präsentiert diese Arbeit obere Ausschlussgrenzen hinsichtlich des Wechselwirkungsquerschnittes von Dunkler Materie mit normaler Materie. Die im Allgemeinen denkbar einfachste Methode ein solches Ausschlusslimit zu berechnen ist die Anzahl der für Wechselwirkungen von Dunkler Materie zu erwartenden Ereignisse in Relation zu setzen mit der Anzahl an beobachteten, gemessenen Ereignissen. Im vorliegenden Fall würde diese Vorgehensweise allerdings zu viel zu konservativen Limits führen, da auch eine nicht unbedeutende Anzahl an Untergrundereignissen in den Daten vorhanden ist. Deshalb werden zwei verschiedene statistische Methoden zur Berechnung aussagekräftiger Limits angewandt.

Die erste Methode, benannt nach ihrem Entwickler S. Yellin, wird in Kapitel 8 beschrieben. Die Grundidee hierbei ist nicht nur die Anzahl der Ereignisse, sondern auch deren Energiespektrum heranzuziehen, bzw. genauer die Unterschiede in den Energiespektren von Signal und Untergrund. Da das erwartete Energiespektrum von Dunkler Materie zu kleinen Energien exponentiell ansteigt, aber das Spektrum der Untergrundereignisse tendenziell eher flach bleibt liefert die Yellin-Methode starke Ausschlusslimits. Hierbei sollte deutlich gemacht werden, dass für die Yellin Methode keinerlei Annahmen über das Energiespektrum der Untergrundsereignisse gemacht werden, was die Resultate immun gegenüber potentielle Unsicherheiten einer Untergrundsmodellierung macht. Aus diesem Grund wurde die Yellin-Methode auch angewandt um die wesentlichen Resultate, dargestellt in Kapitel 9, dieser *low-threshold* Analyse zu berechnen. Für Teilchen der Dunklen Materie leichter als 1.7 GeV/c^2 weist CRESST-II die weltweit höchste Sensitivität auf, was gleichbedeutend mit dem stringentesten Ausschlusslimit ist. Darüber hinaus konnte erstmals der Massebereich bis 0.5 GeV/c^2 untersucht werden - ein Novum für die direkte Suche nach Dunkler Materie.

Kapitel 10 stellt mit einer (profile) Likelihood-Methode eine zweite statistische Methode zur Auswertung der Daten vor. Die Likelhihood-Methode geht in zweierlei Hinsicht über die Yellin-Methode hinaus. Zum einen bewertet sie die Daten nicht nur anhand der deponierten Energie, sondern zieht auch das Szintillationslichtsignal eines jeden Ereignisses heran. Zum anderen kann Wissen über die zweidimensionale Verteilung des Untergrundes berücksichtigt werden. Da die dominanten Untergründe in Lise und TUM40 gut verstan-

den sind, wie im Verlauf dieser Arbeit dargelegt wird, ermöglicht die Likelihood Methode eine abermals gesteigerte Sensitvität, insbesondere für sehr leichte Teilchen der Dunklen Materie.

Der Erfolg dieser *low-threshold* Analyse war Motivation für die CRESST Kollaboration ihre Detektoren dediziert auf niedrige Triggerschellen zu optimieren um mit der so gewonnenen Sensitivität weiter in den Bereich niedriger Massen für das Teilchen der Dunklen Materie vorzustoßen.

1. Dark Matter

The expression *dark matter* dates back to the beginning of the past century, introduced as generic term describing non-visible and gravitationally interacting matter. First studies aiming to determine the local matter density in the vicinity of the sun were performed by E. Öpik (1915,[1]), J.H. Kapteyn (1922,[2]), J.C. Jeans (1922,[3]) and J.H. Oort (1927,1932,[4, 5]), however yielding inconclusive and incompatible results (review e.g. given in [6]). In 1933 first compelling evidence for the existence of dark matter was provided by F. Zwicky, who found that additional non-luminous matter is needed to explain the velocities of galaxies in the COMA cluster [7].

The dark matter paradigm became widely accepted in the physics community since the measurement of rotation curves of stars in galaxies pushed forward by V. Rubin and W.K. Ford in the 1970s (starting with the study of the Andromeda nebula in [8]).

Today, there is hardly any doubt remaining that dark matter exists. Furthermore, its contribution to the total energy density of the Universe is precisely known, in particular from measurements of the cosmic microwave background. Latest values are put forward by the Planck satellite mission [9], accounting 26.8 % of the energy content of the Universe to dark matter. This is more than five times more than the 4.9 % attributed to ordinary, baryonic matter. The rest of 68.3 % and, thus, the lion's share of the energy density in the Universe consists of the so-called dark energy.

This chapter will briefly review major astronomic observations yielding evidence on the existence of dark matter. Although the amount of dark matter is precisely known, its underlying nature remains an unsolved mystery of present-date physics. The most-favored models for a particle nature, including their constraints, will be the second topic of this chapter, laying ground for the discussion on the detection of dark matter, in particular with the CRESST direct dark matter search experiment.

1.1. Cosmological Framework

In the past centuries the picture of the Universe underwent several paradigm changes, which is in particular true for the 20th century. Today, we think of the Universe as starting from an extremely dense hot phase about 14 billion years ago, expanding ever since. This model of the Universe is denoted *Big Bang theory*.

A central element of cosmology is the so-called *cosmological principle* which states that the Universe is isotropic and homogeneous on very large scales.

Another important consideration is that for sufficiently high distances only gravitation is of importance, assuming an overall electrically neutral Universe.

In 1929 E. Hubble made a seminal observation measuring the redshift of spectral lines of galaxies at various distances [10]. The redshift arises from the relativistic Doppler effect, thus spectral lines of receding galaxies will be shifted to longer wavelengths. Vice versa, spectral lines of objects approaching the observer will exhibit shorter wavelengths. E. Hubble found that all galaxies move away from the Milky Way with a few exceptions for very close-by ones. The relation between the distance to a galaxy d and its velocity v (derived from the redshift) is linear and known today as Hubbles' law

$$v = H_0 d \tag{1.1}$$

with the H_0 being the Hubble constant (at present time). Thus, velocities increase with increasing distance, which is, at first glance, incompatible with the cosmological principle, predicting random velocities globally averaging to zero. However, already two years before the measurements of E. Hubble, F. Lemaître postulated an expanding Universe [11] providing the correct explanation by introducing a scale factor $a(t)$ at the time t, which allows to rewrite Hubbles' law:

$$v = \underbrace{\frac{\dot{a}(t)}{a(t)}}_{H(t)} d \tag{1.2}$$

In the formula above $H(t)$ may then be understood as the expansion rate of the Universe. Lemaître's postulation is based on a solution of the Einstein field equation describing the Universe in the framework of General Relativity:

$$G_{\mu\nu} + \Lambda g_{\mu\nu} = \frac{8\pi G}{c^4} T_{\mu\nu} \tag{1.3}$$

Basically, the equation above relates the curvature of space-time described by the so-called Einstein-tensor $G_{\mu\nu}$ [1] with the stress-energy-tensor $T_{\mu\nu}$. The latter is a measure of flux and density of energy. Since special relativity postulates equivalency between mass and energy ($E = mc^2$), $T_{\mu\nu}$ accounts for all matter, radiation and force fields in space-time. Local momentum and (non-gravitational) energy conservation implies that the divergence of the stress-energy-tensor is zero: $\nabla_\nu T_{\mu\nu} = 0$.

The cosmological constant Λ was originally added to force a steady Universe. If chosen with the right value it introduces an expansion exactly compensating the gravitational contraction. However, with the discovery of the expansion of the Universe, Λ was thought to be zero for several decades. Today, observations point to a non-zero positive cosmological constant. Its origin, however remains an unsolved mystery (referred to the problem of the cosmological constant, among many other discussed in [12]).

The Friedmann–Lemaître–Robertson–Walker (FLRW) metric is an exact solution of the Einstein Field equation and describes a perfectly homogeneous and isotropic distribution of matter and radiation (often referred to as frictionless fluid). At first glance, the structures present in the Universe (e.g. galaxies, cluster of galaxies) contradict the assumption

[1] Often die Einstein-tensor is also written as the difference of the so-called Ricci-tensor $\mathcal{R}_{\mu\nu}$ with the curvature scalar R multiplied with the metric tensor $g_{\mu\nu}$: $G_{\mu\nu} = \mathcal{R}_{\mu\nu} - \frac{R}{2} g_{\mu\nu}$.

of a perfect homogeneity. However, the cosmic microwave background (CMB, discussed in subsection 1.2.1) proves that at a time of 380.000 years after the Big Bang fluctuations were smaller than $1/10^5$, hence justifying the above assumption. The FLRW metric can be written as:

$$ds^2 = c^2dt^2 - a^2(t)\left[\frac{dr^2}{1-kr^2} + r^2(d\theta^2 + \sin^2\theta d\phi)\right] \tag{1.4}$$

with the scale factor $a(t)$ (at time t) and the curvature k ($k = 0, \pm 1$). The solution of the Einstein field equation with the FLRW metric then takes the following form:

$$(H(t) =) \quad \frac{\dot{a}(t)}{a(t)} = \frac{8\pi G\rho}{3} - \frac{kc^2}{a^2(t)} + \frac{c^2\Lambda}{3} \tag{1.5}$$

The above equation bears the famous name *Friedmann equation*, although the original version of this formula was defined without the term containing the cosmological constant Λ. A more compact representation is obtained by firstly defining the critical density ρ_c

$$\rho_c = \frac{3H_0^2}{8\pi G} \tag{1.6}$$

and secondly expressing the densities (as they are today) as fraction of the critical density:

$$\Omega_x = \frac{\rho_x}{\rho_c} \tag{1.7}$$

The quantities Ω_x are called density parameters. The most important contributions to the total density Ω arise from radiation Ω_R, matter Ω_m and the cosmological constant Ω_V which is, as already mentioned, typically called dark energy. Thus, the total density is given by:

$$\Omega = \Omega_R + \Omega_m + \Omega_V \tag{1.8}$$

which allows to write the Friedmann equation 1.5 in the following way:

$$\frac{kc^2}{H_0^2 a_0^2} = \Omega - 1 \tag{1.9}$$

with a_0 and H_0 being todays value of the scale factor and the Hubble constant, respectively. From this equation it can immediately be seen that the curvature k of the space-time of the Universe depends on the density Ω. For $k = -1$ the Universe is said to be hyperbolic (open), a value of $k = +1$ corresponds to a spherical and, thus, closed Universe. For $\Omega = 1$ the total density matching exactly the critical density, the Universe is said to be flat ($k = 0$). Depending on the composition of the densities different consequences on the evolution of the Universe arise. Today, we know that the Universe is flat, does expand (E. Hubble) and that the expansion rate increases [13, 14]. An accelerated expansion can be explained by a substantial contribution of so-called dark energy, however its underlying nature remains a mystery at present date.

The matter density Ω_m splits up further in main components of dark matter (Ω_χ), baryonic matter (Ω_{baryon}) and neutrinos (Ω_ν):

$$\Omega_m = \Omega_\chi + \Omega_{\text{baryon}} + \Omega_\nu + \dots \tag{1.10}$$

From various observations, which will be discussed in the following section, the different components can be disentangled. As will be outlined, observations show that dark matter is roughly five times more abundant than ordinary, baryonic matter and that neutrinos only play a negligible role for the energy density.

1.2. Evidence

Today, evidence for the existence of dark matter is found on various astronomical scales. Some of the most striking observations are briefly explained in this section.

1.2.1. Cosmic Microwave Background

In the early Universe production and disintegration of hydrogen were in equilibrium:

$$p + e^- \leftrightarrow H + \gamma \tag{1.11}$$

The disintegration ($\leftarrow$) is only possible for photons (γ) exceeding the hydrogen binding energy of 13.6 eV. However, with the expanding and, thus, cooling of the Universe the mean photon energy decreases. 380.000 years after the Big Bang equality is reached between the number of photons with an energy $E_\gamma \geq 13.6$ eV and the number of baryons.[2] From that time on the disintegration ($\leftarrow$) rate is strongly suppressed and the lack of free electrons and protons leads to a decoupling of radiation and baryonic matter. In other words, photons travel basically unharmed through the Universe ever since - the Universe is said to become transparent. The photons produced in the last recombinations ($\rightarrow$) are seen today, redshifted to microwave wavelengths and, thus, denoted *cosmic microwave background* (CMB). In summary, the CMB gives insight on the Universe shorty (in cosmological timescales) after the Big Bang.

The CMB exhibits an almost perfect black body spectrum with a temperature of T= (2.7260 $\pm$ 0.0013) K [15]. A. Penzias and R. Wilson discovered the CMB in 1964 [16, 17]. Another break-through was the COBE satellite mission detecting small anisotropies ($\mathcal{O}(1/10^5)$) in the CMB temperature. Until today, the CMB has been studied with high precision, in particular by the COBE-successors WMAP and Planck.

The anisotropies seen in the CMB basically measure the distribution of baryonic matter at the time of the decoupling. Photons emitted (from baryonic matter) inside dense regions loose energy upon leaving the gravitational potential and, thus, experience a redshift. The amount of redshift corresponds to the depth of the respective potential. Vice versa, photons coming from diluted regions are blueshifted with respect to the average CMB photon. This effect is commonly known as the Sachs-Wolfe-effect [18]. In summary, the anisotropies

[2] Due to the much higher abundance of photons compared to baryons in the early Universe, the Universe has to cool significantly below the hydrogen binding energy to achieve an equal number of baryons and photons with $E_\gamma \geq 13.6$ eV. The temperature of the Universe at $t = 380.000$ y is about 0.3 eV.

seen in the CMB prove that the baryonic matter at the time of the decoupling was not perfectly homogeneous. This fact, however, cannot be understood without the presence of dark matter in the early Universe, for the following consideration.

As already mentioned, baryonic matter and radiation were in equilibrium at the time of the decoupling. Since random fluctuations in the baryonic matter density would immediately be washed out, the CMB should be a perfect black-body spectrum today. The fact that there are anisotropies points to additional non-baryonic matter component not (significantly) affected by radiation. This dark matter then may form structures, which in turn affect the baryonic matter (via gravitation), thus explaining the anisotropies seen in the CMB today.

As already mentioned in the introduction of this chapter, precision measurements of the CMB (values taken from latest published Planck release [9]) allow to determine the energy density of baryonic matter to be 4.9 %, while dark matter is roughly five times more abundant (26.8 %). From CMB data many other cosmological parameters can be derived, such as the dark energy density (68.3 %), the flatness of the Universe (percent-level precision) and the age of the Universe ($13.8 \cdot 10^9$ years).

1.2.2. Big Bang Nucleosynthesis

The Big Bang nucleosynthesis describes the production of light elements in the early Universe up to ^{7}Li, beginning with the production of deuterium:

$$p + n \rightarrow d + \gamma \tag{1.12}$$

Then, through additional reactions with protons light elements are created.

Following a similar argument as in the discussion of the CMB photons, the deuterium content in the Universe can only build up, if the disintegration ($\leftarrow$) becomes inefficient due to the expansion of the Universe leading to a lack of photons exceeding the deuterium binding energy of 2.2 MeV. The exact time of the so-called freeze-out ($\mathcal{O}$(minutes) after the Big Bang) depends on the baryon to photon ratio. However, as free neutrons are unstable and decay, the total amount of light elements in the Universe constrains the baryon density with a current value of $\Omega_{\text{baryon}} = 0.04$ [19].

1.2.3. Bullet Cluster

The CMB (and in combination also Big Bang Nucleosynthesis) provides evidence for the existence of dark matter on cosmological scales. However, as already mentioned, historically the first widely accepted observation hinting dark matter was the application of the virial theorem to the velocities of galaxies in the COMA-cluster by F. Zwicky [7].

Another rather recent observation was the collision of two galaxy clusters [20], often referred to as *Bullet Cluster* because of the different sizes of the two clusters. Figure 1.1 shows an overlay of three measurements of the Bullet Cluster: an optical image in the background depicting the visible spectrum, the X-ray spectrum in red and the mass distribution in blue (as measured with gravitational lensing).

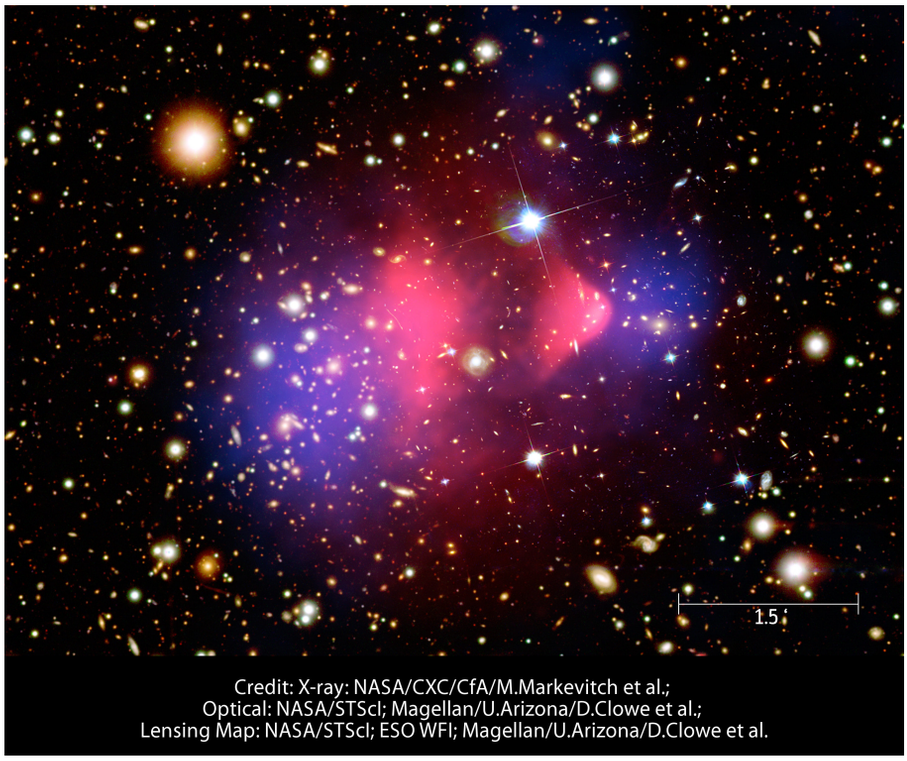

Figure 1.1.: Overlay of the optical image (background), the X-ray image (red) and the mass distribution (blue) from the cluster 1E 0657-558, which is better known as Bullet Cluster. The image corresponds to the time after the collision (taken from [21]). For explanation see text.

It is known that the baryonic matter in a cluster of galaxies is made up of stars and of gas in between, with the gas accounting for its major part. The collision of two clusters spatially separates the two components, because the stars of the two clusters will travel basically unharmed on their respective trajectories, whereas the gas interacts and slows down. Via the X-ray measurement (red in figure 1.1) the gas can be localized and shows a significant spacial mismatch to the mass distribution (blue). The latter is found at the position of the stars rather then at the position of the gas. This is explained by the clusters containing a substantial amount of non-baryonic dark matter with no or only little self-interaction (apart from gravitation of course) and, thus, also hardly slowing down due to friction. The observation of the Bullet Cluster is often considered to finally rule out the so-called MOND (MOdified Newton Dynamics) theories, which aim to provide an alternative explanation for the various observations interpreted as evidence for dark matter by proposing a deviation from the law of gravity at large scales (at small accelerations) [22].

1.2.4. Rotation Curves

On the scale of individual galaxies convincing evidence for the existence of dark matter can be acquired, with the measurements of so-called rotation curves (the first ones dating back

to the 1970s). A rotation-curve relates the orbital velocities of stars to the distance from the center of the galaxy. For a star (with mass m) on a circular orbit with a distance r to the center of the galaxy the velocity v can be calculated with classical mechanics, assuming equal absolute values for the centripetal force and the attracting gravitational force of the mass inside the orbit $M(r)$:

$$|\vec{F}_z| = \frac{mv^2}{r} = G\frac{mM(r)}{r^2} = |\vec{F}_g| \tag{1.13}$$

Solving the above equation for the velocity v yields:

$$v = \sqrt{G\frac{M(r)}{r}} \qquad \left(\text{with } M(r) = 4\pi \int_0^r \rho(r')r'^2 dr'\right) \tag{1.14}$$

Thus, for stars with orbits in the outer part of the galaxy, where $M(r)$ is equal to the total mass of the galaxy the velocities should decrease with $v \propto 1/\sqrt{r}$. However, for the spiral galaxy M33 shown in figure 1.2 the measured velocities (data points in yellow and blue) continue to slightly rise, even for radii far outside the luminous disc. This observation has been made for numerous galaxies, in particular for spiral galaxies which typically feature a bulge at the center which makes up for most of the luminous matter of a spiral galaxy (see also figure 2.2).

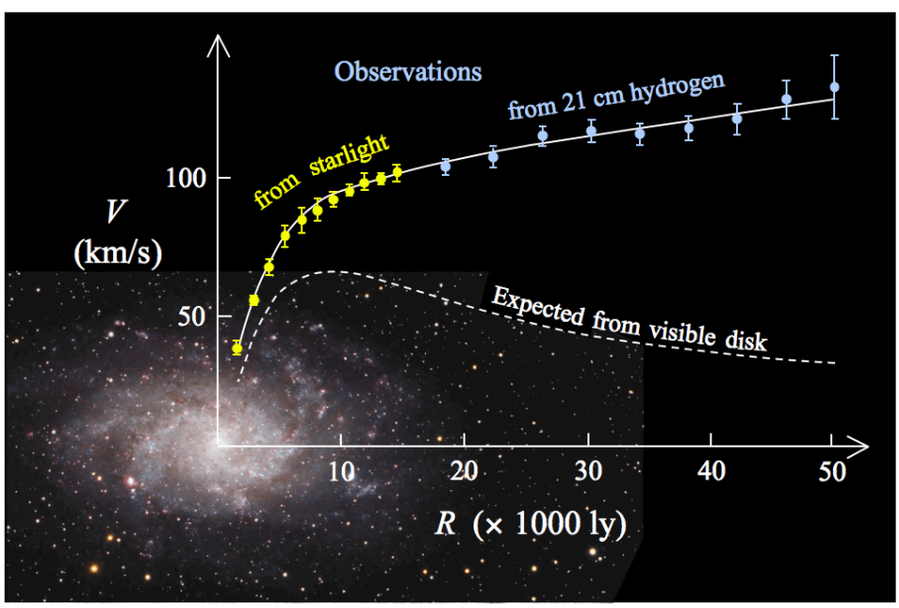

Figure 1.2.: Measured rotation curve of the spiral galaxy M33 (yellow and blue data points) together with the expectation from visible matter (dashed line). The x-axis, showing the distance to the center of the galaxy, is aligned to the image in the background depicting the galaxy M33. Including a dark matter halo yields the solid line, which is in agreement to the measured data. Illustration taken from [23] with data from [24].

The dashed line in figure 1.2 is given by the expectation from luminous matter which clearly contradicts the measured data. However, expectation and observation agree when

one includes a spherical dark matter halo extending well beyond the visible disk (solid line).

Obviously, for earth-bound direct detection the local dark matter density and the velocity of potential dark matter particles is of major interest. However, measuring rotation curves from inside the galaxy (or more precise the Milky Way) is considerably more challenging then from the outside. In the top part, figure 1.3 shows a recent compilation of measured rotation curves of the Milky Way (taken from [25] with references for the individual measurements given therein). The bottom plot shows expectations assuming only baryonic matter, for different models of the structure of the galaxy (bulge, disk and gas). At the distance of the Sun to the center of the galaxy, which is roughly 8 kpc, a velocity of $v_0 = 230\,\mathrm{km/s}$ is measured (top). All baryonic models (bottom), however, predict a much lower velocity which proves the existence of local (at earth) dark matter with more than $5\,\sigma$ confidence level [25].

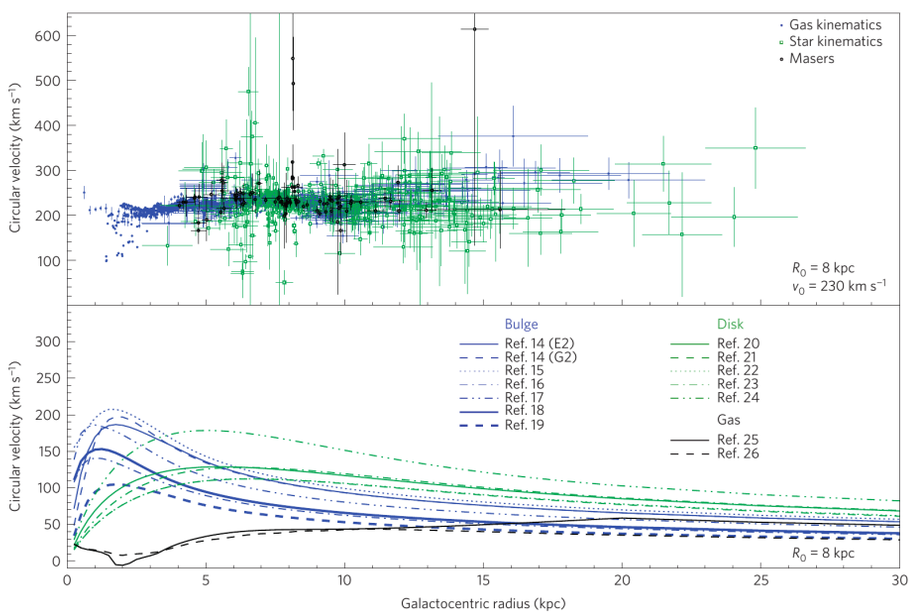

Figure 1.3.: Top: Measured rotation curves of the Milky Way. Bottom: Prediction of baryonic models for different structure of the Milky Way (Plot from [25] with references to measurements and model calculations given therein). $R_0 \sim 8\,\mathrm{kpc}$ corresponds to the distance of the sun to the center of the Milky way, where in average a velocity of $v_0 = 230\,\mathrm{km/s}$ is measured.

1.3. Particle Candidates

While the last section presented selected observations providing convincing evidence for dark matter, this section will introduce possible models explaining its underlying nature. All aspects discussed in the following assume a particle nature for dark matter, which is

natural in the light of ordinary matter being composed of particles. In addition, all evidence is based on the gravitational interaction and explanations with an altered law of gravity seem to be strongly disfavored by various observations, in particular by the Bullet Cluster. If, however, dark matter is made of particles those particles have to fulfill certain requirements:

- The dark matter particles must be cold at the time of structure formation which means that the particles were and, thus, still are non-relativistic. With simulations of the structures seen in the Universe today it is possible to infer back to the structure in the early Universe. However, if there were relativistic (hot) dark matter particles in the early Universe, structures would have been washed out. Thus, in the presence of hot dark matter structures in the early Universe would be far too small to explain the structures in the Universe today.

- Dark matter cannot be baryonic, as this strongly contradicts the observations from the CMB and Big Bang Nucleosynthesis (see subsections 1.2.1 and 1.2.2). In this work the term dark matter always refers to non-baryonic dark matter. However, in the past baryonic dark matter in the form of massive compact halo objects (MACHOS) was considered a viable dark matter candidate (e.g. neutron stars, black holes or brown dwarfs). Indeed, studies using gravitational lensing found suchlike objects, however with only little overall contribution to the energy density of the Universe [26].

- From various observations, in particular from the Bullet Cluster, we know that the interactions between dark matter and baryonic matter and self-interaction of dark matter particles, apart from the gravitational interaction, must be very weak or zero. Therefore (among many other reasons), dark matter particles may neither take part in the strong interaction, nor be electrically charged.

- The measurement of the CMB shows that dark matter existed already in the early Universe (380.000 years after the Big Bang); numerous observations prove the existence today. Thus, dark matter particles are usually considered to be stable, or to exhibit lifetimes on the scale of the age of the Universe. However, in principle these constrains could also be brought in line with a decaying dark matter particle and a reproduction mechanism.

- Weak interactions of dark matter particles are neither forbidden, nor strictly needed to explain the astronomic observations. Null-results from direct searches, however, disfavor a possible coupling to $W^{+/-}$ and Z-bosons to be as strong as for Standard Model particles.

1.3.1. Neutrinos

Out of the Standard Model particles, only neutrinos fulfill most of above requirements, in particular as they are color and electrically neutral. They are known to be massive, but

very light. Thus, neutrinos fall into the category hot, relativistic dark matter which rules out Standard Model neutrinos as a single explanation for dark matter. Latest measurements constrain the energy density of neutrinos to be less than $\Omega_\nu \leq 0.0055$ [19].

1.3.2. Axions

The axion was introduced to solve the long-standing *strong CP-problem*, which refers to CP-violation being observed in the weak interaction, but not in the strong interaction - although explicitly allowed by QCD. Currently, the most stringent constraints for the CP-violating term are obtained by measurements of the electric dipole moment of the neutron [27]. A solution to the strong CP-problem was put forward by R. D. Peccei and H. R. Quinn [28] introducing a new global symmetry which is spontaneously broken leading to a new, massive pseudo Nambu–Goldstone boson [29] - the axion. Depending on the particular model, axions can make up for the complete dark matter abundance [30]. Via the Primakoff-effect axions can be converted to photons in strong electromagnetic fields, or vice versa axions may be produced in strong magnetic fields, which opens the possibility of direct detection. Currently, two experiments are leading the field of direct axion searches: CAST searching for axions produced in the sun [31] and ADMX aiming to detect relic dark matter axions [32]. However, up to now no indications for axions could be found.

1.3.3. WIMPs

The abbreviation WIMP stands for Weakly Interacting Massive Particle - a new particle beyond the Standard Model. The main motivation why the dark matter community (still) favors WIMPs as an explanation for dark matter will be sketched in the following. Basically, one assumes WIMPs to be in thermal equilibrium in the early Universe, thus being continuously produced and annihilating to a generic particle f:

$$\chi\bar{\chi} \leftrightarrow f\bar{f} \tag{1.15}$$

However, with the temperature of the Universe dropping, as a consequence of its expansion, the production is not possible any longer, also called freeze-out. From this point in time the abundance of WIMPs will decrease due to annihilation. With further expansion of the Universe, the WIMP distribution gets diluted and the annihilation basically stops, which explains the abundance of WIMPs today (if WIMPs are stable and not destructed in another way). From the abundance today the expected annihilation cross section can be calculated. Assuming dark matter particle masses that are typical for the weak scale $\mathcal{O}(10\,\mathrm{GeV}/c^2)$ one also obtains weak-scale cross sections [33]. This astonishing agreement is often considered the *WIMP miracle*, giving rise for weakly interacting dark matter particles.

If WIMPs existed they could be seen in all three detection channels. This is outlined in the next chapter 2: direct interaction (via the weak interaction) in earth-bound experiments, indirect detection aiming to measure annihilation signals and the production at colliders.

The so-called Lee-Weinberg-bound excludes WIMP masses below $\sim 3\,\mathrm{GeV}/c^2$, for the following consideration. As the annihilation cross section decreases with the WIMP mass, lighter WIMPs would be more abundant today. For masses smaller than $\sim 3\,\mathrm{GeV}/c^2$ the expected relic abundance would be too large leading to an overclosure of the Universe.

WIMPs as a dark matter explanation also became popular, because some models beyond the Standard Model provide viable candidates, in particular the so-called super symmetry (SUSY). In SUSY theories, every Standard Model particle gets assigned a supersymmetric partner. The lightest supersymmetric particle, however, needs to be stable and, therefore, makes up for a viable WIMP candidate [34]. Alternative explanations e.g. arise from Kaluza-Klein-theories introducing extra dimensions with excitation states translating themselves to WIMP candidates in four-dimensional spacetime [35].

1.3.4. Asymmetric Dark Matter Models

In particular from CMB measurements it is known that the dark matter energy density roughly equals five times the baryon density: $\Omega_\chi/\Omega_{\text{baryon}} \simeq 5$. However, in the standard WIMP scenario this relation is not constrained and a sheer coincidence may be doubted, given that the two values are close to each other. This consideration is the starting point of so-called asymmetric dark matter models postulating an asymmetry between dark matter particles and dark matter antiparticles [36, 37]. Furthermore, it is claimed that the dark matter asymmetry is connected to the baryon asymmetry in the early Universe

$$n_\chi - n_{\bar{\chi}} \leftrightarrow n_b - n_{\bar{b}} \tag{1.16}$$

with a separate freeze-out (decoupling) of the two sectors during the evolution of the Universe.

Since the baryon asymmetry is measured to be $\eta = (n_b - n_{\bar{b}})/n_\gamma = 6 \cdot 10^{-10}$ [38] an efficient interaction is needed which annihilates away the symmetric part. A very rough estimate on the mass scale of asymmetric dark matter may be given by the observation that baryonic matter is dominated by the mass of the proton. Thus, with dark matter being five times more abundant than ordinary matter one obtains a dark matter particle mass of $m_\chi \sim 5m_p \sim 5\,\mathrm{GeV/c^2}$. However, the proton is a compound particle and its mass is no fundamental physics quantity which renders this estimate weak without knowledge of the so-called dark sector. More detailed models, as discussed among others in references [36, 37] predict a mass for the dark matter particle of $\mathcal{O}$(0.1-10 GeV/c^2). The interest in asymmetric dark matter models is further augmented as many of them provide possibilities for direct detection via interactions with new dark mediators. If the mass of the new mediator is much larger than the transfered momentum, the scattering can be treated to be point-like (see discussion in section 2.1). Therefore, the exclusion limits (calculated in this thesis) on the dark matter particle - nucleon scattering cross section apply to asymmetric models as well as for WIMP-like dark matter. Indirect detection, in contrast, is more constrained and only possible in partly asymmetric models with some left-over antiparticles.

2. Detection of Dark Matter

Today, one distinguishes between three main approaches to search for dark matter. Indirect detection, searches at colliders and direct detection. Indirect searches mainly aim to find astronomical evidence for dark matter particles annihilating into Standard Model particles, while the goal of collider searches is to produce dark matter particles in the collision of Standard Model particles. Direct dark matter experiments search for interactions of dark matter particles with Standard Model particles in earth-bound detectors.

This chapter starts with a brief comment on dark matter searches at colliders and prospects of indirect detection. The central aspect, however, is direct detection and the expected energy spectrum of dark matter particles interacting in the detector target material. Although focusing on a $CaWO_4$-target, the basic concepts for the commonly used spin-independent scattering also hold for other target materials. Throughout this chapter the term WIMP will be used for any dark matter particle scattering elastically off nuclei, so not only the *classic* WIMP which is thermally produced in the early Universe.

Today, a great variety of experimental techniques is applied in the field of direct dark matter detection. The last section of this chapter introduces the most important technologies currently being used in experiments around the globe.

2.1. Detection at Colliders

Dark matter particles which interact with Standard Model particles might be produced in high-energy collisions of Standard Model particles at accelerators. Today, the LHC, located at CERN, is in the center of interest holding the world-record in collision energy. It should be kept in mind that two questions would remain, even if collider searches found a dark matter particle candidate. Firstly, it would have to be proven that the new particle produced at the collider is the same as present in nature and, secondly, that its lifetime is large enough to fulfill the astronomical constraints. On the other hand, finding a dark matter particle candidate would be of invaluable help for direct dark matter searches, as it would allow for dedicated optimization of the experiments.

Since potential dark matter particles produced in the collision leave the detector unharmed, they induce events of missing energy [39]. Dark matter candidate interactions are most efficiently found by searching for events with the Feynman diagram depicted in figure 2.1, showing the production of a dark matter particle/antiparticle pair $\chi\bar{\chi}$ and initial-state radiation of a gluon [40]. In summary, the characteristic signature for such an event is an energetic jet and high missing transverse momentum.

Figure 2.1a depicts the event in the view of a contact interaction, also referred to as *effective field theory* (EFT). However, EFT is only valid if the momentum transfer is much

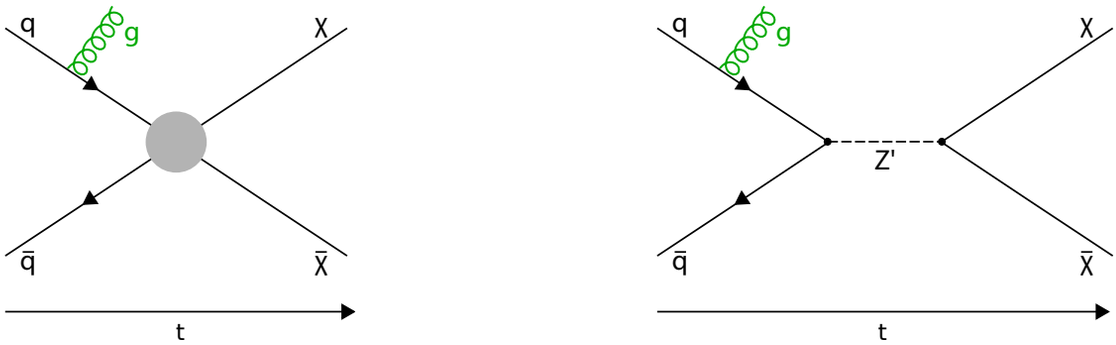

(a) Contact interaction (b) Simplified Model

Figure 2.1.: Feynman graphs for the pair production of dark matter particles $\chi\bar{\chi}$ triggered by initial state radiation of a gluon. Left (a): Contact interaction described by effective field theory. Right (b): Simplified Model mediated by a new vector boson Z'.

smaller than the mediator mass M_{med}. This is certainly fulfilled in direct detection experiments (energy transfer $\mathcal{O}$(keV)), but not necessarily at the LHC. Thus, the LHC experiments more and more switch from EFT to so-called *simplified models* [41], which take into account the mediator (Feynman diagram depicted in figure 2.1b), instead of integrating it out as in EFT. In the limit of large mediator masses M_{med}, EFT and simplified models yield, as expected, identical results [40].

In both cases the observable which is constrained is the so-called suppression scale $M_* \propto \frac{M_{\text{med}}}{\sqrt{g_1 g_2}}$, where $g_{1,2}$ are the two couplings involved in the process. The lower limit on M_* then yields an upper limit on the interaction cross section between nucleons and dark matter particles and, thus, allows for a direct comparison with direct detection results. However, for this comparison assumptions on the a-priori unknown couplings $g_{1,2}$ have to be made, which inevitably introduces a model-dependence in the comparison of results obtained from direct and collider dark matter searches. In the appendix results obtained for certain assumed couplings [39] are shown together with direct detection results. No hint for dark matter is found by the two main LHC experiments - ATLAS [40] and CMS[42] - in data from collisions with a center of mass energy of 8 TeV. This is also confirmed by first, preliminary analyses from 13 TeV-data, as e.g. reported by CMS [43].

2.2. Indirect Detection

Indirect dark matter detection aims to find cosmic rays originating from the annihilation[1] of dark matter particles into pairs of Standard Model particles (e.g. $b\bar{b}$, $\mu^+\mu^-$, $\tau^+\tau^-$, W^+W^-). The Standard Model particles, which are produced in the annihilation, then undergo further processes (in particular hadronization) and create a flux of cosmic rays, such as e^-, e^+, $\bar{p}$, ν, γ. Currently, the search concentrates on three main types of cosmic rays:

[1] Cosmic rays originating from a potential decay of dark matter particles are negligible (or not existent), given the long anticipated lifetime (or the stability) of the dark matter particle

γ-rays, charged leptons and neutrinos.

Gamma Rays Firstly, γ-rays might be produced promptly in the annihilation, either via annihilation of dark matter particles directly into γ-rays, or via virtual internal bremsstrahlung [44]. Both processes result in characteristic γ-ray spectra, in particular the direct annihilation leads to a line-spectrum corresponding to the mass of the dark matter particle. Thus, this signature is often considered a so-called *smoking gun evidence*.

Furthermore, γ-rays may also be produced in processes following the actual annihilation which leads to a rather continuous spectrum and, thus, is much harder to disentangle from γ-rays of *ordinary* (= non dark matter) origin.

Charged Leptons Secondly, finding an excess of charged leptons can be evidence for dark matter. Obviously, the spectrum strongly depends on the Standard Model particles initially created in the annihilation, however in general a bump in the spectrum is expected with a hard cut-off at the mass of the dark matter particle. This hard cut-off may be used to set such a signature apart from other, ordinary origins.

Neutrinos The third channel is the detection of neutrinos. Of particular interest in the context of this thesis are neutrinos from the center of the Sun, since they provide a signature directly comparable to direct detection experiments, as will be explained in the following. The basic idea is that dark matter particles might be captured in the gravitational potential of the sun. Captured dark matter particles then loose energy in scatterings with Standard Model particles and, thus, accumulate in the center of the Sun causing a locally enhanced rate of annihilations and neutrinos originating therefrom can reach earth-bound detectors. In equilibrium state between capture and annihilation, the rate of annihilations in the sun becomes a function of the interaction cross section $\sigma_{\chi\leftrightarrow\mathrm{SM}}$ between dark matter and Standard Model particles and explicitly becomes independent of the annihilation cross section $< \sigma_A v >$. Since the cross section $\sigma_{\chi\leftrightarrow\mathrm{SM}}$ is the same one as for direct dark matter searches, a direct comparison is possible. Due to the high abundance of hydrogen in the sun, these searches exhibit a high sensitivity for spin-dependent scattering of dark matter particles off nuclei [45, 46, 47].

For all indirect searches, it is a-priori unclear which regions in the sky provide the highest sensitivity. On the one hand, regions of high gravitational potential and, thus high dark matter density, such as the Sun or the galactic center, are preferred for obvious reasons. On the other hand, one has to consider backgrounds from ordinary sources of cosmic rays, which, in general, constitute a major uncertainty in the indirect dark matter search.

2.3. Direct Detection

The third pillar of dark matter searches is the direct detection in earth-bound experiments, aiming to measure dark matter particles interacting in the respective target material. Thereby, dark matter particles are most commonly expected to scatter elastically

(and coherently) off nuclei. This section will outline the anticipated dark matter recoil spectrum, discussing the relevant inputs from astronomy (dark matter halo and velocity distribution) and from the target material (form factor). As will be shown, the main challenges in direct detection are a small expected scattering rate and typical recoil energies of a few keV at most. Consequently, these requirements force highly-sensitive devices operated in a low-background environment. The last section of this chapter will give a brief tour on the various experimental approaches currently realized in direct dark matter detection.

2.3.1. Expected WIMP Recoil Spectrum

The total interaction rate (equation 2.1, [33]) expected for WIMPs in an ideal detector is a product of three main factors:

$$R = \frac{M_{\text{Target}}}{m_N} \cdot \frac{\rho_\chi}{m_\chi} v \cdot \sigma(v) \tag{2.1}$$

The first factor is the total number of nuclei in the target given by the total target mass M_{Target} divided by the mass of one nucleus m_N. For a multi-element target, like $CaWO_4$, one obviously has to take into account its exact composition of the various nuclei. The WIMP flux penetrating the earth makes up for the second factor and is given by the local dark matter density ρ_χ, the WIMP mass m_χ and its velocity v. For equation 2.1 it is assumed that all WIMPs travel through the galaxy with the same speed. The final multiplication factor is the WIMP-nucleus cross section $\sigma(v)$ which, in general, depends on the velocity. As will be discussed in the following, astrophysics, as well as nuclear physics provide inputs to evaluate these factors.

In practice not the total rate, but rather the differential interaction rate (equation 2.6, [48]), so the number of counts per kg target material and keV energy, is of major interest. The WIMP-nucleus cross section σ in general consists of two contributions, a spin-dependent and a spin-independent one. The spin-independent term accounts for all scalar couplings and scales quadratically with the atomic mass. The spin-dependent term describes an interaction of WIMPs with the net spin of the nucleus which is practically zero for all nuclei with an even number of nucleons. For $CaWO_4$ the sensitivity to spin-dependent interactions is orders of magnitudes suppressed compared to spin-independent scattering and, thus, neglected. Commonly, the coupling strength f is assumed to be identical for neutrons and protons. [2]

The differential cross section of WIMPs scattering elastically off nuclei is given by [49]:

$$\frac{d\sigma}{dE_R} = \frac{2m_N A^2 f^2}{\pi v^2} F^2(E_R) \tag{2.2}$$

Directly visible in equation 2.2 is the aforementioned quadratic dependence of the cross section on the atomic mass number A. The last element relevant to describe the scattering

[2] Models giving up this assumption are called isospin-violating (although there is no actual violation of isospin). They gained interest in the past years; however, for the framework of this work those models will not be considered.

process is the structure of the nucleus encoded in the form factor $F(E_R)$ (details will be discussed in subsection 2.3.3). Equation 2.2 can be rewritten by defining the point-like WIMP-nucleus cross section σ_0 [48]:

$$\frac{d\sigma}{dE_R} = \frac{\sigma_0}{E_r^{\max}(v)} F^2(E_R) \tag{2.3}$$

with the maximum possible energy transfer $E_r^{\max}$ for a WIMP of velocity v and the reduced mass μ_N:

$$E_r^{\max}(v) = \frac{2v^2\mu_N^2}{m_N} \qquad\qquad \mu_N = \frac{m_\chi m_N}{m_\chi + m_N} \tag{2.4}$$

Since the quantity σ_0 describes the scattering off a specific nucleus it is not suited to compare different target materials used by different experiments. Thus, the community uses the material-independent WIMP-nucleon cross section σ_{WN}, the cross section normalized to one nucleon [48]:

$$\sigma_{\mathrm{WN}} = \frac{1 + m_\chi/m_N}{1 + m_\chi/m_p} \cdot \frac{\sigma_0}{A^2} \tag{2.5}$$

with m_p being the mass of the proton.

Using all of the information above and giving up the oversimplified assumption of a constant WIMP velocity v (as was done for equation 2.1) one finds the following final formula for the differential scattering rate:

$$\frac{dN}{dE_R} = \frac{\rho_\chi}{2m_\chi\mu_N^2}\sigma_0 F^2(E_R) \underbrace{\int_{v_{\min}(E_R)}^{v_\infty = v_{\mathrm{esc}}} d^3v \frac{f(\vec{v})}{v}}_{I(v_{\min})} \tag{2.6}$$

The velocity distribution of WIMPs in the rest frame of the earth $f(\vec{v})$ (see subsection 2.3.2) has to be integrated from the minimal velocity able to induce a recoil of energy E_{r}:

$$v_{\min} = \sqrt{(E_R m_N)/(2\mu_N^2)} \tag{2.7}$$

The upper limit of the integral is the galactic escape velocity v_{esc}, the maximum velocity possible for WIMPs bound in the galaxy.

2.3.2. Dark Matter Halo Model

Usually dark matter is expected to form a spherical halo around the center of the galaxy (see figure 2.2). The dark matter particles are assumed to be thermalized, thus following a Maxwellian distribution of the dark matter particle velocities[3] . However, to calculate the

[3]For an isothermal dark matter halo the density is given by $\rho(r) = \frac{\rho_c}{(1+(r/r_c)^2}$ with the core radius r_c and the density at the center ρ_c. Other slightly different profiles, as e.g. the well-known NFW profile [50] derived from N-body simulations, are usually not considered to maintain comparability between different results.

velocity distribution in the rest frame of the detector, the movement of the sun around the center of the galaxy, the orbit of the earth around the sun and, in principle, the rotation of the earth have to be taken into account. Often the effect of the earth moving in the dark matter halo is referred to as facing the *WIMP wind*, as illustrated in figure 2.3. A more detailed view will be given in the following.

For an isotropic and spherical distribution of dark matter and assuming no self-interaction of the dark matter particles, one obtains a Maxwellian distribution function $f(v)$ in the rest frame of the galaxy and truncated at the galactic escape velocity v_{esc} for the velocity v [48]:

$$f(v)dv = \frac{1}{\mathcal{N}}\left(\frac{3}{2\pi v_{\text{rms}}^2}\right)^{\frac{3}{2}} \exp\left(-\frac{3v^2}{2v_{\text{rms}}^2}\right)\theta(v - v_{\text{esc}})dv \tag{2.8}$$

with the normalization $\mathcal{N}$ given by:

$$\mathcal{N} = \text{erf}(z) - \frac{2}{\sqrt{\pi}} z \exp(-z^2) \qquad \text{with:} \qquad z := \frac{v_{\text{esc}}}{v_\odot} \tag{2.9}$$

In the above equation $v_\odot$ denotes the velocity of the sun and for the isothermal dark matter halo the root mean square velocity v_{rms} is simply given by: $v_{\text{rms}} = \sqrt{3/2}v_\odot$.

Evaluating $I(v_{\text{min}})$ with above equation yields an exponential proportionality which reveals the basic shape of the WIMP spectrum - a multiplication of an exponential with the form factor F:

$$I(v_{\text{min}}) \overset{eq.(2.8)}{\sim} \exp(-v_{\text{min}}^2) \overset{eq.(2.7)}{\sim} \exp(-E_R) \xrightarrow{eq.(2.6)} \frac{dN}{dE_R} \sim F^2(E_R) \cdot \exp(-E_R) \tag{2.10}$$

The movement of the solar system around the galactic center is taken into account via a Galilei transformation. Additionally including the earth orbiting around the sun leads to an annual modulation of the WIMP signal [51] with its peak in June 2nd, where the speed of the earth with respect to the dark matter halo (the WIMP wind) is at its maximum (see figure 2.3). Neglecting the elliptic shape of the earths orbit, the annual variation of the WIMP velocity with respect to the earth is given by the following expression:

$$v(t) = v_\odot + v_{\text{earth}} \cos(\gamma) \cos \omega(t - t_0) \tag{2.11}$$

The plane in which the earth moves around the sun is tilted with an angle of $\gamma = 60°$ with respect to the galaxy. A graphical illustration of the earths motion in the so-called WIMP wind is depicted in figure 2.3.

The velocity of the earth v_{earth} is roughly 30 km/s the one of the sun $v_\odot$ around 220 km/s, which yields a variation of the WIMP velocity in the order of $\mathcal{O}(\leq 10\%)$. As a real detector is not sensitive to the full velocity distribution, but only to velocities high enough to produce a recoil above threshold (see equation 2.7) the modulation of the scattering rate can be significantly different from the value of $\mathcal{O}(10\%)$. A potential WIMP signal will also have a day-night modulation because of the earth's rotation, however at present this is far beyond experimental reach.

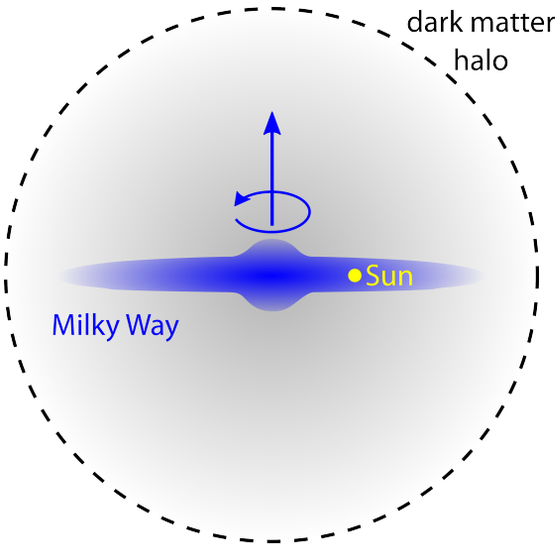

Figure 2.2.: Schematic drawing illustrating the isotropic dark matter halo spherically extending from the center of the Milky Way. The sun rotates around the center of the galaxy, indicated by the blue arrow.

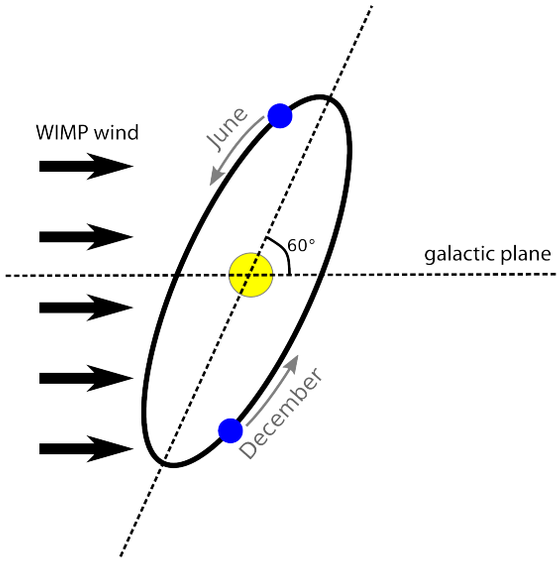

Figure 2.3.: Illustration of the movement of the earth (blue) with respect to the *WIMP wind* originating from the movement of the sun (yellow) around the center of the Milky Way (see left). The orbit of the earth is tilted by $60°$ with respect to the galactic plane.

An observation of the modulation signal with the correct phase is usually considered a *smoking gun evidence*. However, in practice it has to be disentangled from other seasonal effects, like e.g. a variation in the atmospheric muon flux due to the density of the atmosphere being a function of temperature. Since typical runs of CRESST last more than one year we average over the annual modulation (analytic expression for $I(v_{\text{min}})$ can e.g. be found in [48]). The value used for the speed of the sun $v_{\odot}$ as well as all other relevant parameters for the dark matter halo used are summarized in table 2.1.

The direction of the impinging dark matter particle is another information not accessible by current dark matter searches. Directional information might become even more relevant once experiments start to see coherent neutrino-nucleus scattering (CNNS). CNNS is a process predicted by the Standard Model and presents an irreducible background for direct detection experiments since it can neither be actively discriminated (from WIMP-nucleus scattering) nor passively shielded. However, because it is solar and/or atmospheric neutrinos causing this background directional information might yield a suppression to some extent [52]. Since CNNS depends on the target material (calculation for $CaWO_4$ may be found in [53]) complementarity between different target materials might be another handle to enhance the WIMP discovery potential in the regime of CNNS background [54].

Practically all direct dark matter searches use the so-called standard halo model (SHM), as well as the parameters in table 2.1, although slightly outdated: more recent studies, e.g. suggest a slightly higher velocity of the sun of $v_{\odot} = 230\,\text{km/s}$ (see subsection 1.2.4). In addition, the SHM has some theoretical drawbacks. For example, possible substructures

Parameter	Symbol	Value	Reference
Galactic escape velocity	v_{esc}	544 km/s	[55]
Solar velocity	$v_{\odot}$	220 km/s	[56]
Local dark matter density	ρ_{DM}	0.3 GeV/cm^3	[56]

Table 2.1.: Parameters of the standard dark matter halo model used in this work.

of the dark matter halo are not taken into account [57, 58]) and the SHM is in a strict sense only valid for a halo of infinite size [59],[60]. The dark matter velocity distribution extracted from N-body simulations [61] is often considered as a more precise estimate of the true distribution (also confirmed by a new non-parametric approach [62]).

On the one hand, one could argue that experiments should report their results with the best halo model available at the time of the analysis. Best in this case means the model which is closest to nature with current knowledge. This is relevant, because experiments might be influenced by, in particular, a change of the velocity distribution to a quite different extent depending on their target material and their energy threshold. On the other hand, such an approach would make comparisons between experiments, or even between different analyses of the same experiment, extremely difficult or even impossible; at least without a constant update of old analysis results obtained with *outdated* assumptions. For this reason and because the SHM and the parameters used are not substantially different to current knowledge, the dark matter community sticks to them. However, one should always keep in mind this issue when comparing experiments. If WIMPs will be discovered one day the question of the *correct* velocity distribution will be of major importance to determine properties of WIMPs like, e.g. their mass. [4]

2.3.3. The Form Factor

For high momentum transfers ($q = \sqrt{2m_N E_R}$) in WIMP scatterings off nuclei, a point-like approximation of the respective nucleus is not valid any more, but its substructure has to be taken into account. This is done by introducing so-called form factors $F(E_R)$ (see equations 2.2 et. seq.). Although this work centers around the search for light dark matter particles, where form factors play a negligible role only, the basic concepts will be sketched.

A form factor basically describes the distribution of nucleons inside the nucleus and, thus, is given by a Fourier transform of its density distribution. Most commonly used is the parametrisation introduced by Helm [65] and confirmed by Engel [66, 67] for the application in the field of direct dark matter searches. The basic idea behind this model is to introduce a fading density at the edge of a solid sphere. Using a Gaussian function to model this decreasing density one obtains the following equation:

$$F(q) = 3\frac{j_1(qR_0)}{qR_0}e^{-\frac{1}{2}q^2s^2} \tag{2.12}$$

[4] As e.g. [63, 64] point out it would also be possible the other way around, namely to derive the velocity distribution from a WIMP measured with sufficient statistics and on several target materials.

In the above equation R_0 denotes the radius of the solid sphere (= the nuclear radius), j_1 is the first Bessel function and s is the width of the Gaussian function ($s \sim 1$ fm). As one can see, the Helm parametrization allows to analytically calculate the form factor for any nucleus of known radius R_0. In [66] the author has shown that - despite its simplicity - this model provides a very good approximation of the density distribution of nuclei, which is in particular true for light nuclei. Very recently results from shell-model calculations performed for ^{129}Xe were published [68] finding good agreement with the Helm parametrization and with previous shell-model calculations [69]. It should be noted that the small differences seen for various parametrizations hardly play any role for spin-independent scattering. For the spin-dependent case, instead, even small deviations potentially have a significant impact on the scattering cross section and, thus, on the final result.

To overcome the need for the nuclear radius R_0 as an input parameter Lewin/Smith [56] derived the following approximation from experimental scattering data:

$$R_0 = \sqrt{c^2 + \frac{7}{3}\pi^2 a^2 - 5s^2} \tag{2.13}$$

The parameters thereby are:

$$c = 1.23 \cdot A^{1/3} - 0.6\,\text{fm} \qquad a = 0.52\,\text{fm} \qquad s = 0.9\,\text{fm} \tag{2.14}$$

The main advantage of the Lewin/Smith approach is that it provides a good analytic approximation for any nucleus. However, enhanced precision can be achieved by an individual treatment for the nucleus of interest. In [70] the authors put forward a *model-independent* form factor. Experimental data from electron scattering are used as input parameters assuming that charge and mass distribution inside the nucleus are proportional to each other. The charge distribution is then modelled by fitting a sum of Bessel functions to the data. For a sufficiently large number ($\mathcal{O}$(10-20)) of summed Bessel functions a good agreement between data and model was found. In this work the form factors for oxygen and calcium were calculated using this model-independent approach (details on the concrete implementation are presented in [71]).

The main drawback of the model-independent formalism is the need of electron scattering data, which is not available for tungsten. Among others, the authors of [70] suggest to use a Wood-Saxon description for the nuclear potential

$$\rho(r) = \frac{\rho_c}{\exp(\frac{r-c}{a}) + 1} \tag{2.15}$$

with the surface thickness a, the radius of half density c and being $\rho_c = 2 \cdot \rho(r = c)$. On the one hand, this parametrization is, just like the Helm form factor, very generic and oversimplified. On the other hand values for a and c are also available for heavy nuclei like tungsten providing at least some level of flexibility to account for individual features of the substructure. Since ^{184}W is by far the most abundant tungsten isotope the values $a = 0.353$ fm and $c = 6.51$ fm (from [70]) are used for the analysis presented in this work.

2.3.4. Result for an Ideal Detector

The result of the expected differential WIMP scattering rate off $CaWO_4$ as a function of recoil energy is shown in figure 2.4 for a WIMP mass of 100 GeV/c^2. The colored lines correspond to the rate off the individual target elements, red for oxygen, cyan for calcium and green for tungsten (weighted according to their mass fraction in $CaWO_4$). The black line corresponds to the total rate seen for a $CaWO_4$-target given by the sum of the rates for the individual elements.

For very low recoil energies, thus small momentum transfers, impacts of the form factor are negligible. In this regime recoils off tungsten completely dominate, because of its high mass $A_W = 184\,u, A_{Ca} = 40\,u, A_O = 16\,u$ and the expected A^2-dependence of the scattering cross section. When going to higher energies the form factors cause a steep drop of the rate. The highest impact is seen for recoils off tungsten manifesting itself as two pronounced dips in the differential scattering rate. As a result the total expected rate significantly decreases with energy; from 20 keV to 50 keV by two orders of magnitude.

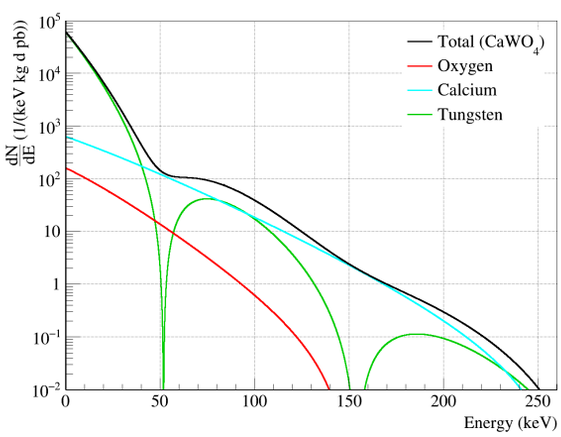

Figure 2.4.: Differential recoil rate as a function of energy for a WIMP with a mass of 100 GeV/c^2 seen on the target nuclei, oxygen (red), calcium (cyan) and tungsten (green). The black line is the sum of the three rates, thus corresponding to the differential recoil rate expected per kg of $CaWO_4$.

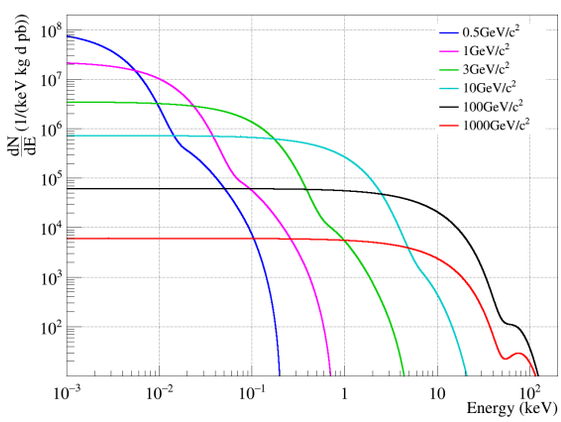

Figure 2.5.: Differential recoil rates for WIMPs of different masses (see legend) scattering off $CaWO_4$. The black line depicting the rate for a 100 GeV/c^2 WIMP corresponds to the black line of figure 2.4.

Figure 2.5 shows the differential rate for several WIMP masses in addition to the black 100 GeV/c^2-spectrum, already plotted in figure 2.4. As one can see the spectra get considerably steeper when going to lower WIMP masses. Two effects come into play. Firstly, the expected number density of WIMPs is indirectly proportional to the WIMP mass, as the total dark matter energy density is fixed to the value of $\rho_{DM} = 0.3\,\mathrm{GeV/cm^3}$. Secondly, the energy transferred in a scattering decreases with decreasing WIMP mass. The second effect becomes more clear in the next chapter including a finite energy threshold.

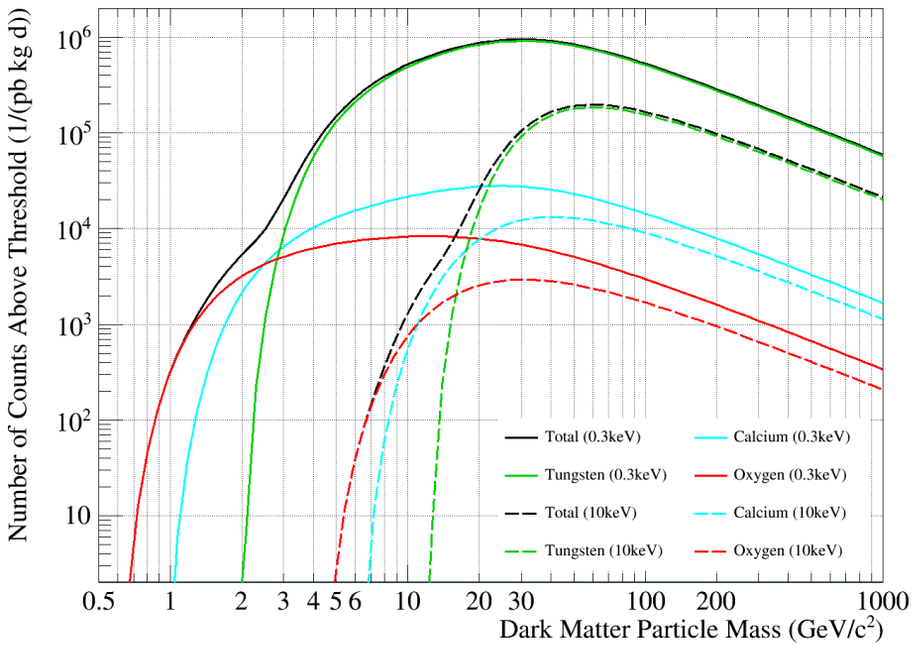

Figure 2.6.: Expected WIMP recoil rate as a function of WIMP mass in the energy range from 0.3-40 keV (solid lines) and from 10-40 keV (dashed lines). The rate is shown in total (black) and separately for the three target nuclei: Ca (cyan), W (green) and O (red).

2.3.5. Finite Energy Threshold

One main innovation of the analysis in this work is the use of data down to the energy threshold of the detector. While the following chapters will deal with the challenges of this approach, the motivation will be given here. The effects of the threshold will be discussed using $CaWO_4$ as target material, but the results also hold for any other target. Figure 2.6 shows the expected count rate (normalized to a cross section of 1 pb and per kg day of exposure) as a function of WIMP mass. The rate is shown separately for the three different nuclei (Calcium (cyan), Tungsten (green) and Oxygen (red)). The dashed lines correspond to a threshold of 10 keV which roughly equals the analysis thresholds set in CRESST-II phase 1 [72]. Lowering the threshold to 0.3 keV - the lowest threshold achieved in phase 2 - yields the solid lines. Both energy ranges are limited to 40 keV since above this region the count rate quickly drops because of the tungsten form factor (see the last subsection 2.3.4).

All spectra share a common shape with the maximum count rate reached for a few 10 GeV/c^2. The decrease of the count rate right of the maximum is caused by the reduced WIMP number density. Left of the maximum an increasing fraction of scatterings is below the threshold of the detector. For (mainly) this reason current direct dark matter searches reach their best sensitivity - in terms of cross section - in this WIMP mass regime.

For both thresholds, when going from higher to lower WIMP masses one can see that the rate drops quickly as the threshold sets in. However, the lighter the nucleus is, the later this drop appears, which is expected as more energy is transferred in scatterings off

light nuclei. Consequently, the light elements present in $CaWO_4$ extend the sensitivity of CRESST down to lower WIMP masses - a unique feature in the family of direct dark matter searches.

Comparing the dashed and the solid lines reveals the importance of a low threshold in the low WIMP-mass regime. For example for a WIMP of 10 GeV/c^2 the difference in the count rate between the two threshold settings is more than two orders of magnitude, a WIMP of 3 GeV/c^2 is completely below the 10 keV-threshold, even for recoils off oxygen. However, the benefit of low thresholds is not only the access to very low WIMP masses, also at higher WIMP masses the count rate is enhanced, as can be seen by comparing the dashed and the solid line at e.g. 100 GeV/c^2. This is a simple consequence of the fact that the WIMP spectrum is probed (integrated) over a larger energy range.

2.4. Direct Detection Experiments and their Techniques

This section gives a very brief overview over the most common techniques used by the current state-of-the-art dark matter search experiments, without discussing them in detail. The main challenge for all experiments is the low anticipated WIMP scattering rate, rendering background reduction a crucial issue. The first step is to shield the experiment against cosmic radiation by placing the experiment in a deep underground site. Most experiments have passive and active layers of shielding to suppress environmental backgrounds as well as the remaining cosmic radiation under ground. Obviously, all materials of the experiment and, in particular of the detectors, have to fulfill high standards in terms of radiopurity to be suited for this kind of low-background experiments. Depending on the target material different signals may be induced by a particle interaction, in general, and a nuclear recoil, in particular. In solid state materials (e.g. Ge, Si, $CaWO_4$) a particle interaction induces a temperature rise (phonon signal) and/or may induce either an ionization signal (Ge, Si), or scintillation light ($CaWO_4$). Liquid noble gases (Ar, Xe) emit scintillation light. Applying an electric field can provide an ionization signal, in addition.

The first direct dark matter searches usually used one channel, e.g. CRESST-I [73] measuring the phonon signal induced in sapphire (Al_2O_3). The current experiments are often referred to as second generation, since most of them combine two channels to discriminate backgrounds from a possible signal, which often is mandatory to achieve the required background level. Typically, beta and gamma interactions are the dominant background source, often also referred to as *electron recoils*. Today most one-channel experiments aim to measure the annual modulation (see 2.3.2). The idea behind is that one can tolerate some level of over-the-year-constant background and still see the modulating WIMP signal on top.

Figure 2.7 shows exclusion limits and allowed regions for the WIMP-nucleon cross section as a function of WIMP mass. A line corresponds to an exclusion of the parameter space above with 90 % confidence level. Typically exclusion limits quickly rise towards low WIMP masses because of the finite energy threshold of the detector under consideration. The moderate rise towards high WIMP masses ($>$100 GeV/c^2) results from a reduction in WIMP number density. Figure 2.7 only shows results from the experiments discussed be-

low, projections for experiments under construction may be found in the references given. The plot widely follows a color coding for exclusion limits (red/blue for CRESST, green for Ge/Si-based experiments and magenta for liquid noble gases).

2.4.1. Liquid Noble Gas Experiments

Over a wide WIMP-mass range liquid noble gas experiments report the best exclusion limits (DarkSide [82], LUX [83], PandaX [84] and Xenon100 [85]) and further improvements in sensitivity are expected to be seen within the next years (e.g. by Xenon1T[89], LZ [90] and DEAP-3600 [91]).

The concept of most of these experiment is a so-called dual phase time projection chamber (TPC), as depicted in figure 2.8. Most of a TPC is filled with a liquid noble gas with some gaseous layer on top. A particle interaction in the liquid produces scintillation light which is measured with photomultipliers (PMTs) on top and on bottom of the TPC (S1 Signal). The PMTs are arranged in an array which allows to reconstruct the position in the xy-plane (the z-axis being the rotation axis of the cylindrical TPC). An electric field drifts electron-hole pairs created by the particle interaction along the TPC. Across the gaseous phase a high electric field is applied accelerating the electrons that emerge from the liquid causing a second light signal proportional to the charge (S2 Signal). Recoils on electrons induce more charge than nuclear recoils of the same deposited energy allowing for a discrimination by the ratio S2/S1 of the two signals. Their time difference yields the z-position of the interaction. These experiments use the 3D-position reconstruction for the so-called fiducialization, which in this case means to reject events close to the walls of the TPC. Since most backgrounds originate from the outside of the TPC, fiducialization provides an efficient background suppression. Remaining intrinsic backgrounds in the liquid are approached by continuous purification - a technique used by many low-background experiments with liquid target, not only in the field of dark matter, but also for neutrino detectors (e.g. Borexino [92]).

In addition to the ratio S2/S1, particle discrimination is, in principle, also possible via the pulse shape of the prompt scintillation signal S1, especially for liquid argon. Apart from dual phase also single phase detectors with only liquid are being used. Either without discrimination (XMASS [93]) or using the pulse shape discrimination method (DEAP-3600 [91], Mini-Clean [94]). Single phase detectors can use a spherical geometry (4π-setup), which makes a 3D-position reconstruction possible without the need of an S2 signal.[5]

In summary, the rapid progress in sensitivity seen for liquid noble gas experiments is a result of a large target mass with a low background achieved by purification, fiducialization and discrimination. In the next years further gains in sensitivity are expected with the step to target masses of one tonne and more.

[5] DarkSide uses the pulse shape difference of the S1 signal for background discrimination, but nonetheless sticks to a TPC layout, since the position reconstruction of a TPC is better than for single phase detectors like e.g. DEAP. A better position reconstruction obviously facilitates fiducialization.

2.4.2. Ge and Si-based Experiments

Germanium detectors are used in a variety of applications, for dark matter detection either by only measuring ionization (CoGeNT [87], CDEX [95], TEXONO [96]), or by measuring heat/phonon and ionization (EDELWEISS [97], (Super)CDMS [79]). All germanium-based experiments benefit from the extremely low level of intrinsic backgrounds, which can hardly be achieved by most other solid state materials. The mass of the crystals usually is around several hundred grams.

P-Type Point Contact Detectors

CDEX, CoGeNT and TEXONO use so-called p-type point contact detectors (PPC, [98]) made of germanium. In such a detector a particle interaction creates electron-hole pairs which are drifted to the point-like electrode by the applied electrical field. Via the rise time of the ionization signal, surface events can be rejected (fiducialization), however no particle discrimination is possible. Typically, PPCs exhibit a very low noise level leading to low energy thresholds ($\mathcal{O}(< 1\,\mathrm{keV})$). PPCs do not need cryogenic temperatures, but may be operated at liquid nitrogen temperature. They have proven to exhibit excellent long-term stability which makes them well suited for WIMP modulation analyses.

Cryogenic Detectors

EDELWEISS and (Super)CDMS belong to the family of cryogenic detectors with operating temperatures of $\sim 20\,\mathrm{mK}$ and $\sim 50\,\mathrm{mK}$, respectively . The basic idea behind those detectors is that a particle interaction will induce a very small temperature rise $\mathcal{O}(\mu\mathrm{K})$. Such a thermal pulse is measured with either a transition edge sensor (TES) in the case of CDMS, or a neutron transmutation doped thermistor (NTD) for EDELWEISS. This so-called phonon signal is a precise measure of the deposited energy, independent of the type of particle. Cryogenic detectors are connected to a heat bath causing a relaxation back to the original temperature after a particle interaction. Since also CRESST is a cryogenic experiment, details will be given in chapter 3. Via a weak electric field the induced ionization is measured. Also for this experiments beta and gamma interactions are the dominant background, but they create more electron-hole pairs than the sought-for nuclear recoils. Thus, an excellent background discrimination is achieved via the ionization yield, which is defined as the ratio of ionization signal to phonon signal.

The first generation of these detectors used large electrodes on top and bottom of the germanium crystal creating a rather homogeneous electric field. The advantage of simplicity was given up due to the finding that events near the surface have little or no ionization signal. Such a degradation of the ionization yield might lead to a misidentification of beta or gamma events as nuclear recoils. Different strategies were carried out over time, only the latest one shall be discussed here. The left side of figure 2.9 shows a schematic drawing of the interleaved Z-sensitive Ionization Phonon (iZIP) detector as used by SuperCDMS[6] - a design based on developments from EDELWEISS. The resulting electric field is illustrated

[6] SuperCDMS is the successor of CDMS-II

on the right side of figure 2.9. The field lines are drawn in red, lines of equal potential in blue. The basic idea behind this electric field configuration is that for a near-surface event the electron as well as the hole will drift to the same face of the crystal, whereas for an event in the bulk both faces will be reached.

In addition, the outer charge electrodes are read out separately to gain information on the radial event position which is also possible via the layout of the phonon sensors: Top and bottom face of the crystal each are equipped with four phonon sensors, three central ones (three segments of a circle) and an outer ring enhancing the precision on the radius measurement. The information on the radius of an event allows to veto events near the mantel surface of the cylinder. In total, the combination of the layout of the phonon sensors with the electric field configuration, rejecting events on only one face of the crystal, enables to define a fiducial volume which is free of surface-related ionization degradation.

SuperCDMS also operates iZIP detectors with a high bias voltage ($V_b \sim 70\,\mathrm{V}$) to amplify the phonon signal via the Neganov-Luke effect - then called the CDMSlite experiment [100, 78]. The basic idea of the rather strong field is that the work done by drifting electron-hole pairs adds to the phonon signal induced by the initial recoil (E_R):

$$E_{\text{total}} = E_R + N_{\text{eh}} e V_b \tag{2.16}$$

As already pointed out, the number of electron-hole pairs N_{eh} depends on the type of recoil allowing for a particle identification via the ionization signal in the normal operation mode. Thereby, $\epsilon = 3\,\mathrm{eV}$ are needed in average to create one electron-hole pair for an electron recoil in germanium. However, if a large bias voltage ($V_b \gg \epsilon$) is applied the phonon signal E_{total} will be dominated by the heat originating from the drift of the electron-hole pairs. Thus, in CDMSlite the phonon signal effectively becomes an amplified measurement of the ionization induced by a particle interaction, which prevents particle discrimination via the ionization yield. The advantage of Neganov-Luke-amplification, however, is a better signal to noise ratio and, thus, enhanced energy resolution and threshold ($\sim 60\,\mathrm{eV_{ee}}$)[7]. In summary, CDMSlite extends the sensitivity of CDMS detectors to WIMP masses below $\mathcal{O}(10\,\mathrm{GeV/c^2})$ where scatterings would be below threshold ($\sim 2\,\mathrm{keV}$) in the normal operation mode.

The CDMS collaboration also reports on results using silicon instead of germanium as target material. For kinematic reasons rather light WIMPs ($\mathcal{O}(10\,\mathrm{GeV/c^2})$) transfer more energy to the silicon nucleus, compared to the heavier germanium nucleus, which enhances sensitivity to low WIMP masses. For high WIMP masses germanium is the better choice, because of the A^2-dependence of the coherent scattering cross section. CDMS-Si uses the ZIP layout the predecessor of the iZIP design. The main difference between iZIP and ZIP is that surface events in the ZIP design are rejected via a pulse shape discrimination of the phonon signal.

Compared to PPC detectors CDMS and EDELWEISS detectors are by far more complex and they need to be cooled and stably operated at cryogenic temperatures which is a major technological effort. However, their advantages concerning fiducialization and particle discrimination make them the most sensitive germanium/silicon detectors for a

[7] ee is an abbreviation for *electron equivalent*, so denotes the energy for an electron recoil.

wide range of WIMP masses. Since all germanium/silicon based experiments use crystals with at maximum a few hundred grams, large target masses require many detectors which is often considered more challenging than to scale up liquid noble gas experiments. However, because of their superior energy resolution and threshold germanium/silicon detectors play an important role in the lower WIMP mass regime $\mathcal{O}(10\,\mathrm{GeV/c^2})$.

2.4.3. NaI-based Experiments

DAMA (DAMA/NaI followed by DAMA/Libra) uses scintillating NaI-crystals. The current setup houses 25 crystals with a mass of 9.7 kg each. They are arranged in an array of 5 times 5 crystals. The scintillation induced by a particle interaction is measured with two PMTs per crystal. Dark matter particle candidate events are required to scatter in only one crystal, since multiple scatterings of WIMPs are practically excluded in view of their small interaction rate. The energy range of interest is set to 2-6 keV_{ee}. Figure 2.10 shows the modulation of events fulfilling above requirements over 13 annual cycles. The final result ([101]) includes 14 annual cycles with a statistical significance of 9.3 σ. The amplitude and the phase of the modulation is compatible with the prediction from the standard halo model. To compare DAMA with other direct dark matter searches requires certain assumption on the interaction of WIMPs with matter (see 2.3.1). For standard assumptions the claim of DAMA is ruled-out by other experiments by several orders of magnitude, as put forward by [102].

No convincing explanation other than dark matter, like e.g. seasonal variations of the muon flux, was found up to now for the modulation observed. It is widely accepted that a NaI-experiment performed on the southern hemisphere has great potential to clarify the nature of the modulation. Using NaI excludes material-dependent effects. Carrying out the experiment on the southern hemisphere reverses seasonal background effects. One collaboration following this approach is DM-Ice [104]. Two detectors of a first small demonstrator experiment (DM-Ice17, [105]) were deployed in the ice of the south pole, below the IceCube neutrino observatory. To approach the DAMA sensitivity DM-Ice250 is being planned with 250 kg target mass, split in two detectors, one on the northern and one on the southern hemisphere. Key requirement for all NaI-based experiments is to achieve a background level as low as in the DAMA experiment. A slightly different approach is to operate NaI as a cryogenic detector which would provide particle discrimination via the ratio of scintillation light to energy measured in the phonon channel (light yield), similar to CRESST-II detectors. In a recent measurement we proved particle discrimination for a CsI-crystal [106], which is supposed to have similar properties to NaI as both belong to the family of alkali halides.

2.4.4. Bubble Chambers

Bubble chambers can be used for the search for dark matter, as it is currently done by PICO [107], merged from PICASSO and COUPP. In such a bubble chamber a liquid (CF_3I or C_3F_8) is heated to a temperature above boiling temperature (superheated). Particle interactions then may nucleate a macroscopic bubble recorded from different angles by digital

cameras. Since the bubble will form at the place of the particle interaction this allows for fiducialization. Two requirements have to be fulfilled for a macroscopic bubble to form, the deposited energy has to be above a certain threshold, as has to be the energy loss per unit length (dE/dx). The latter is too small for beta and gamma events, so no bubble will be nucleated. Alpha-particles will create bubbles, however, they can be discriminated from nuclear recoils via a different high-frequency acoustic signal [108]. Basically, the acoustic signal measures pressure changes in the bubble chamber, thus recording the formation of the bubble. For an alpha event the alpha as well as the daughter nucleus form so-called proto-bubbles which then merge into a big bubble. Nuclear recoils, instead, are supposed to create a single proto-bubble only, making a discrimination possible. In [107] PICO reports the first background-free measurement with a bubble chamber. Due to their target material, bubble chambers have a high sensitivity for spin-dependent scattering and currently set the most stringent limits.

2.4.5. Dark Matter Search with CCDs

Relatively new in the field of direct dark matter searches is DAMIC [109, 110] using charge-coupled devices (CCDs) as detectors. CCDs are used in common digital cameras[8], the ones used by DAMIC were optimized for near-infrared measurements in telescopes (for *The Dark Energy Survey* (DES)). Similar to detectors discussed before, a particle interaction in the silicon bulk material of a pixel creates electron-hole pairs drifting to electrodes on top and bottom of the pixel. Just like for a digital camera the charge is accumulated at the electrodes until readout. Currently, DAMIC operates with exposure lengths of several hours. The depth of the interaction can also be reconstructed by the signal height in the neighbouring pixels. The deeper the interaction was, the more the charge carriers will diffuse to the adjacent pixels causing a higher signal height therein. Background discrimination is possible via the different clusters; a muon or a high-energy electron will lead to a track, an alpha particle will be point like, however spreading over many more pixels than the sought-for nuclear recoil, also leaving a point-like signature in the detector. Figure 2.11 shows a sector of an image with various event clusters.

The main advantage of a CCD is its very low energy threshold ($\sim$0.5 keV for nuclear recoils) making CCDs competitive detectors for low WIMP masses. A decent sensitivity in the high WIMP mass region seems unrealistic in the view of the target mass of a few grams per CCD, only.

[8] However, today most cameras use CMOS sensors.

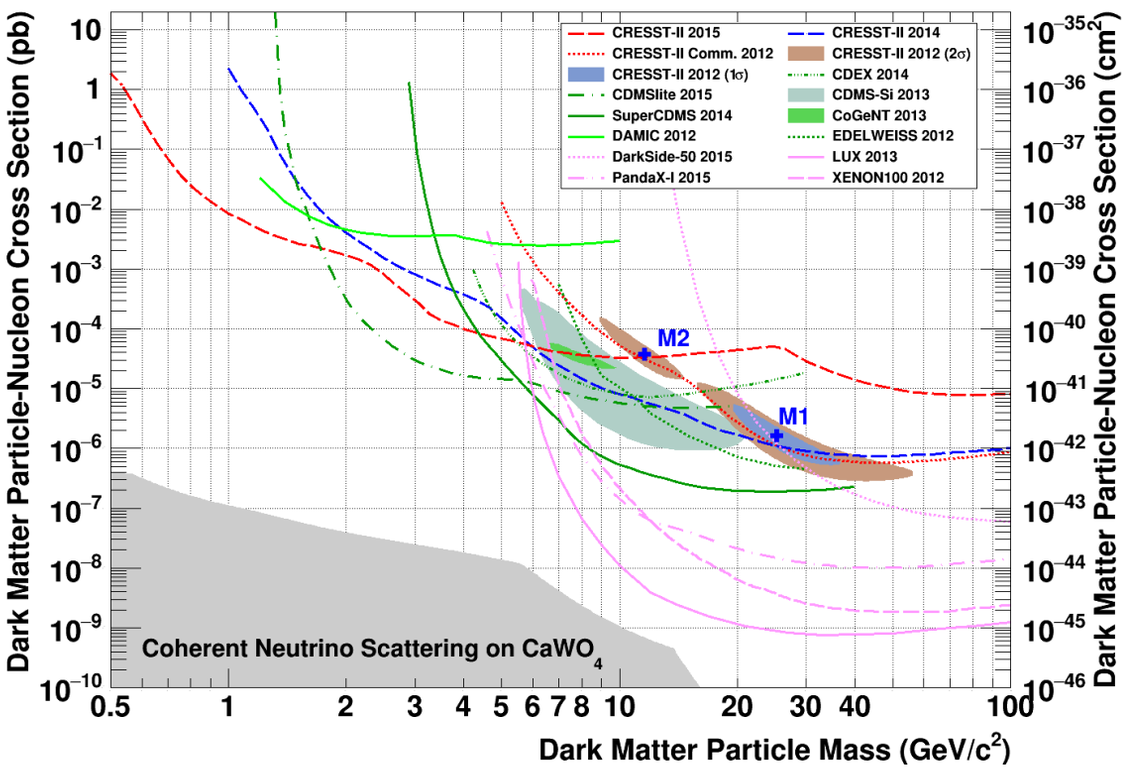

Figure 2.7.: Cross section for spin-independent dark matter particle - nucleon scattering as a function of the mass of the dark matter particle. Included are published results (until February 23, 2016) from direct dark matter searches, with lines corresponding to exclusion limits (all with 90 % confidence level). Exclusion limits obtained with data from the latest CRESST-II measurement campaign (phase 2) are drawn in dashed red [74] and dashed blue [75]. The exclusion curve resulting from previous CRESST-II commissioning run data is depicted as dotted red line [76]. Green exclusion limits correspond to Ge/Si-based experiments [77, 78, 79, 80, 81] and magenta curves to experiments based on liquid noble gases [82, 83, 84, 85]. Shaded in color are regions of parameter space compatible with excess signals observed in the previous CRESST-II phase 1 [72], CDMS-Si [86] and CoGeNT [87]. For a $CaWO_4$-based experiment coherent neutrino-nucleus scattering (CNNS, [53]) represents an irreducible background once approaching the area shaded in gray.

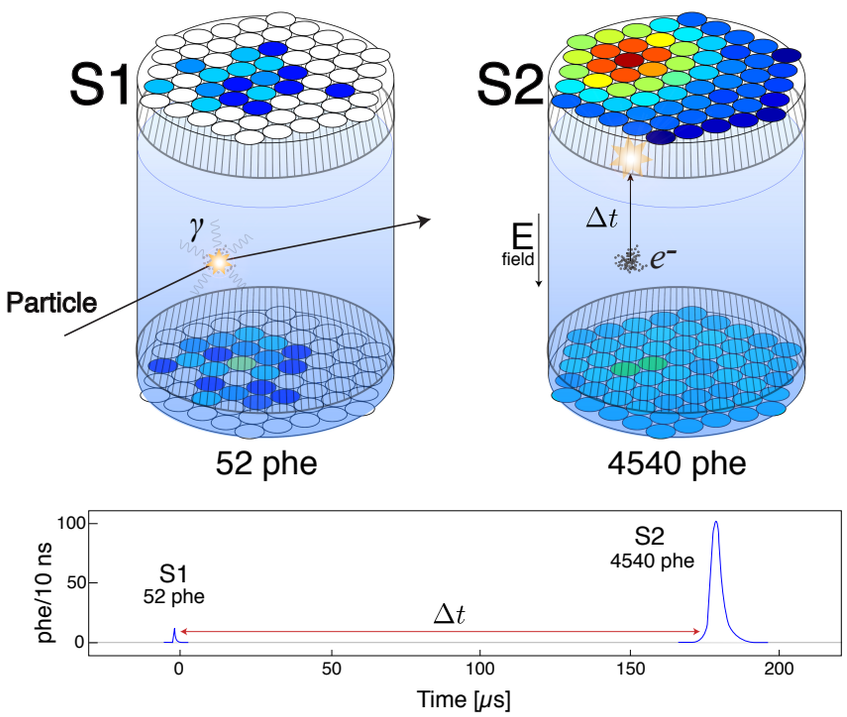

Figure 2.8.: Schematic drawing of a double phase time projection chamber (TPC) as used, in particular, by the DarkSide, LUX, PandaX and Xenon collaborations. The TPC is equipped with PMTs on top and bottom first measuring the primary scintillation light signal S1. By applying an electric field a second light signal S2 is induced on the negative charges emerging from the liquid. Via the time difference of S1 and S2 and the layout of the PMTs a 3D space reconstruction is possible, allowing to use the self-shielding effect of the target (fiducialization, see text). Illustration taken from [88], values quoted for the number of photo electrons (phe) correspond to the LUX detector.

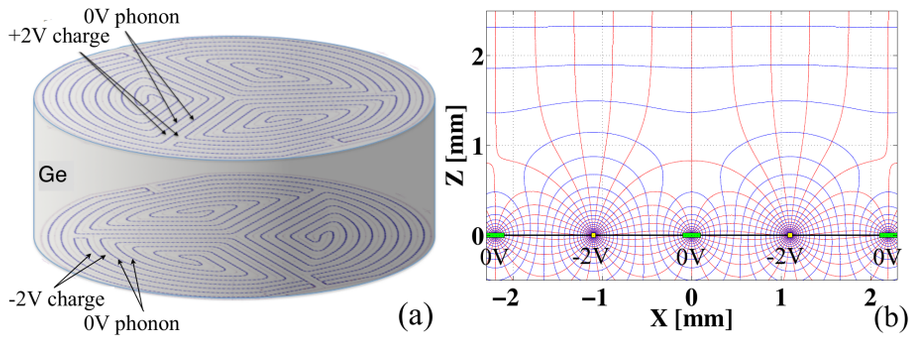

Figure 2.9.: On the left an iZIP detector as used by the SuperCDMS collaboration is shown, including the layout of the electrodes (blue lines). On the right the resulting field lines are drawn in red, lines of equal electrical potential in blue. This sophisticated layout causes electron-hole pairs created near the surface to drift to the same face of the crystal, while bulk events will be drifted to both faces. This technique allows to reject surface events exhibiting a reduced ionization yield. Plot taken from [99].

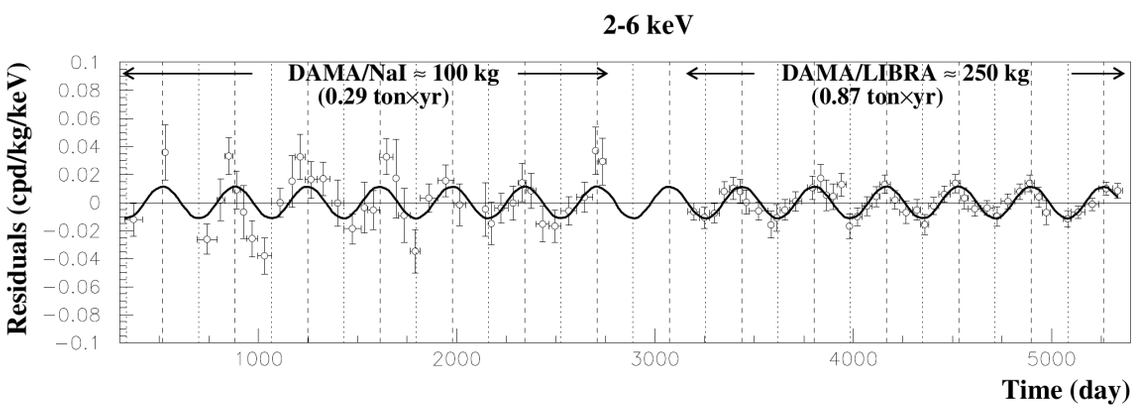

Figure 2.10.: Modulation of events in the range of 2-6 keV$_{ee}$ measured over 13 annual cycles by the DAMA collaboration [103]. The gap corresponds to the time of the upgrade from DAMA/NaI to DAMA/LIBRA.

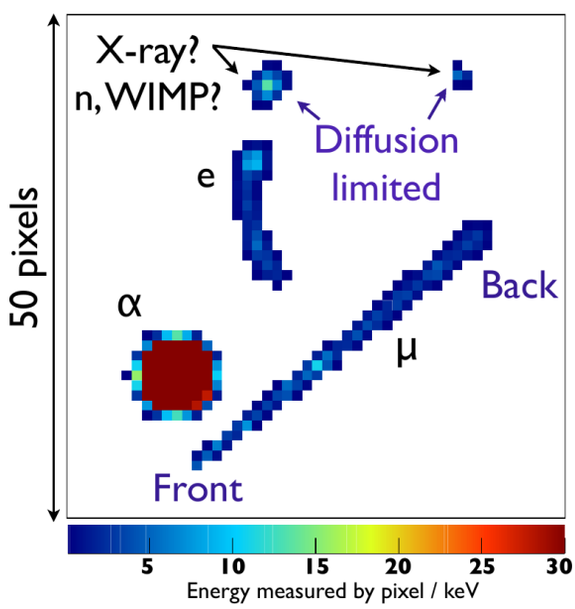

Figure 2.11.: Part of an image taken by a DAMIC CCD [109]. Shown are clusters caused by different particles. The direction of the muon can be extracted from the broadening of the track. Slim corresponds to little lateral diffusion and thus to an interaction point close to the surface.

3. The CRESST-II Experiment

This chapter will present the CRESST-II experiment in detail, starting with the experimental setup, then explaining the working principle of the detectors.

3.1. Nomenclature of the Experimental Stages and Phases

The construction of the Cryogenic Rare Event Search with Superconducting Thermometers (CRESST) began in 1995. The first stage, named CRESST-I, used sapphire (Al_2O_3) as target material. As sapphire is not scintillating only one channel, the phonon signal, was measured. Results may be found in [73]. Afterwards CRESST-I was upgraded to CRESST-II with a two-channel readout (phonon plus light) using scintillating $CaWO_4$ crystals. This thesis concentrates on CRESST-II phase 2 (2013-2015), however results from phase 1 (2009 - 2011) will be shortly summarized in the next chapter. There will be no phase 3, but the experiment will be renamed to CRESST-III to express the major upgrades in detector design undertaken to explore the low dark matter particle mass regime. Table 3.1 gives an overview over the various stages and phases.

Stage	Phase	Data taking	Comment	References
CRESST-I	-	2000	Al_2O_3, phonon signal only	[73]
CRESST-II	Comm.	2007	$CaWO_4$, phonon and light	[111, 76]
	Phase 1	2009-2011	first extensive physics run	[72]
	Phase 2	**2013-2015**	**upgraded detector module(s)**	[75, 74]
CRESST-III	Phase 1	2016	optimized for light dark matter	[112]
	Phase $\geq$2	$\geq$ 2017	improved crystals (radiopurity)	[112]

Table 3.1.: Overview over the stages of the CRESST experiment subdivided into phases. At the time of writing CRESST is in its transition from CRESST-II to CRESST-III. The analysis presented in this work uses data taken in 2013-2015 during CRESST-II phase 2. The comment column very briefly points out the key innovations to previous phases. Further information may be found in this work and in the references given.

3.2. Experimental Setup

In the field of low-background rare event searches shielding against cosmic radiation is mandatory. Thus, nearly all experiments are placed deep under ground. CRESST-II is located in hall A of the *Laboratori Nazionali del Gran Sasso* (LNGS) in the Abruzzi mountains in central Italy. The LNGS is one of the largest underground laboratories world-wide, housing a variety of different experiments. It has an overburden of 1400 m of rock in each direction which equals 3800 m water equivalent [113], providing an efficient reduction of cosmic radiation background.

Figure 3.1 shows the experimental setup of the CRESST-II experiment. The following subsections will explain the working principle and purpose of the various components.

3.2.1. Cryostat

CRESST is a cryogenic experiment requiring operating temperatures of $\leq$10 mK provided by a commercial dilution refrigerator circulating a He^3/He^4 mixture (details e.g. given in [115, 116]). For the operation liquid nitrogen and liquid helium are needed and have to be refilled three times per week. Detectors cannot be operated stably during and shortly after refilling. Thus, data taking is switched off for two to three hours per refill, which makes up for a substantial fraction of the dead time of the experiment. The detectors are mounted in the so-called carousel which is held by the cold finger. The latter also provides the thermal coupling between cryostat and the carousel.

3.2.2. Backgrounds and Shielding

Muon Background

The main component of the primary cosmic radiation are protons interacting with nuclei of the earth's atmosphere creating mainly pions and to a minor extent kaons. The pions then decay to muons and muon neutrinos. Thus, at sea level muons make up for the dominant part of charged particles induced by the cosmic radiation [117] with a rate of roughly 1 $\mathrm{cm^{-2}min^{-1}}$ ($= 1.7 \cdot 10^2\,\mathrm{m^{-2}s^{-1}}$). Muons are the only charged component penetrating deep under ground, due to their rather long lifetime and their low interaction cross section. In the LNGS underground lab Borexino measured the muon flux to be $(3.41 \pm 0.01) \cdot 10^{-4}\,\mathrm{m^{-2}s^{-1}}$ [113] which corresponds to a reduction of $\mathcal{O}(10^{-5} - 10^{-6})$ compared to the rate at sea level. The muon flux modulates throughout the year with a relative amplitude in the order of 1 %, due to seasonal fluctuation of the temperature of the atmosphere and, thus, its density.

Muons themselves are no background for the dark matter search, however they can induce secondary particles in interactions with material in the vicinity of the detectors (like e.g. in the rock or in the shielding of the experiment). Thus, CRESST is surrounded by plastic scintillator panels (depicted in blue in figure 3.1), each equipped with a photomultiplier to detect muons reaching the experiment. Taking into account the hole on top which

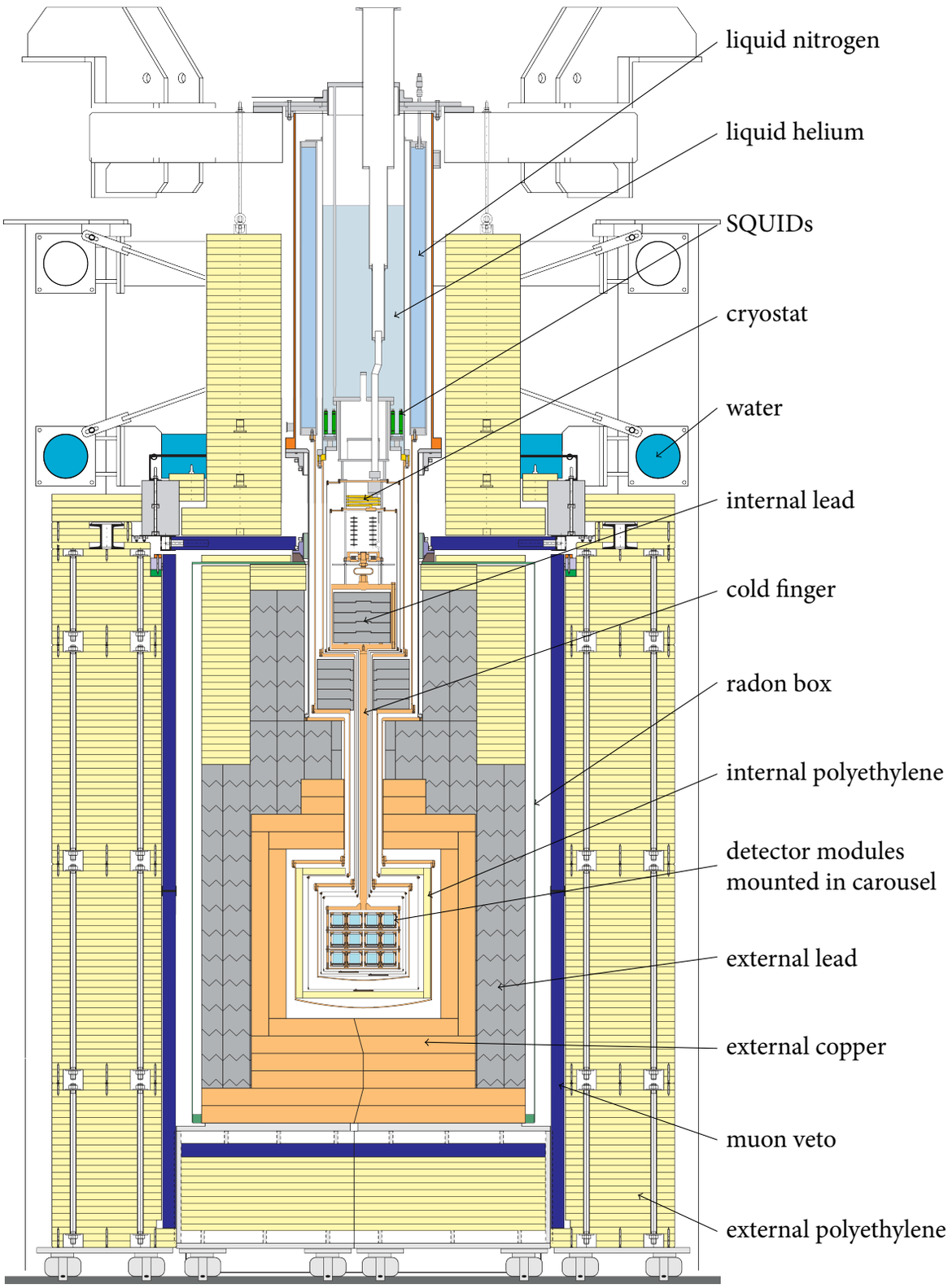

Figure 3.1.: Schematic drawing of the CRESST experimental setup. Adopted from [114].

is needed for the cryostat the geometrical coverage is 98.6% [1]. In phase 2 the overall trigger rate of the muon veto is $\sim$ 20 Hz causing a dead time of $\sim$8 % (as will be discussed in subsection 6.7.1). Obviously, the rate of the veto by far exceeds the rate of muons. This is a result of gamma radiation in the vicinity of the photo multipliers causing signals above threshold. Dedicated studies on the CRESST muon veto may be found in [118].

Gamma Background

The rock overburden provides an efficient suppression of the cosmic radiation. However, additional layers of passive shielding are required to protect the detectors against the remaining cosmic radiation and natural radioactivity originating mainly from ^{40}K and the decay chains starting with ^{238}U and ^{232}Th. Measurements of the gamma flux were undertaken in several places in the LNGS underground lab in [119]. For hall A (near the CRESST experiment) the authors report a gamma flux of 0.25 cm^{-2}s^{-1} in an energy range of (7.4-2734.2) keV.

To shield against the gamma background the detectors are surrounded by 20 cm of low-background lead (24 tons in weight, see figure 3.1). Lead provides a high stopping power for the gamma background due to its hight atomic number density. The drawback using lead as shielding material, however, is its rather high intrinsic radioactive background, mainly originating from the isotope ^{210}Pb. This isotope is part in the ^{238}U-chain which ends with the stable isotope ^{206}Pb. During the decay from ^{210}Pb to ^{206}Pb α, β and γ-radiation is emitted. Thus, 14 cm of copper are installed in between the lead and the detectors (see figure 3.1). In contrast to lead, copper can be produced with a minimal amount of radioactive contaminations. Therefore, it is also the material-of-choice for all support structures in the vicinity of the detectors.

Neutron Background

Neutrons represent a dangerous background for any dark matter search, since their experimental signature equals that of dark matter particles; both will induce a nuclear recoil.

To protect against neutrons the outermost layer of shielding consists of 40 cm Polyethylene (see figure 3.1). Polyethylene is a chemical compound with a large number of light hydrogen atoms. For kinematic reasons light elements are preferred in terms of energy transfer in scatterings with neutrons making Polyethylene an efficient moderator for neutrons. Where no Polyethylene could be installed for technical reasons, water is used instead. However, neutrons might also be produced in the lead and copper shielding located inside the Polyethylene, through α-n-reactions as well as by muons (which might be missed by the muon veto). Thus, in phase 2 we installed an additional layer of Polyethylene closed to the detectors inside all other shielding. From simulations a reduction of one order of magnitude or more is expected [120]. A dedicated analysis of all detectors using the full data set will be needed to compare this prediction with the measurement.

[1] The geometrical coverage might not exactly match the rejection power for muons as the direction of the muons is not uniformly distributed, but depends on the shape of the mountain.

Neutrons have a certain probability to scatter in multiple detectors, whereas this probability is practically zero for dark matter particles. If the ratio of multiple to single scatters is known an estimation of the neutron background (single scatters) can be achieved by the number of multiple scatterings observed in the data set under consideration.[2]

However, this ratio differs for the two origins of neutrons: muon-induced neutrons and neutrons from α-n-reactions. For muon-induced neutrons higher multiplicities are expected since muons may produce showers with more than just one neutron. The time resolution of cryogenic detectors is by far not capable to distinguish between one neutron scattering in more than one detector, or several neutrons hitting multiple detectors. The multiplicity spectra for muon-induced neutrons is acquired by events with detectors and muon veto triggering coincidently. For source-like neutrons, calibrations with AmBe-sources yield the multiplicity distribution.

3.3. CRESST Detectors

3.3.1. Working Principle

This section will give a brief overview over the working principle of a CRESST-II detector module (depicted in figure 3.2).

Any particle interaction in the $CaWO_4$ target crystal will mainly induce a heat/phonon signal. While this phonon signal yields a precise measurement of the energy deposited, the simultaneously produced scintillation light is used for particle discrimination. Phonon and light detector are then referred to as a detector module.

To measure the phonon signal a special thermometer is used, a transition edge sensor (TES). The scintillation light leaving the crystal is guided to the light detector by a reflective and scintillating foil enclosing the detector module. A light detector usually consists of a silicon-on-sapphire (SOS) disk providing high absorption for the blue scintillation light produced by a $CaWO_4$ crystal [121]. The absorbed light then leads to an energy deposit in the light detector read out by a second TES. Strictly, also the signal from the light detector is a phonon signal. However, in contrast to the signal read from the TES of the crystal it is not directly induced by the particle interaction, but by the absorbed light. Thus, the crystal with its TES will be called phonon detector and the term light detector will refer to the light absorber and the corresponding TES.

The discrimination of different types of particle events is done on the light yield parameter. It is defined as the ratio of the energy measured in the light channel (E_l) to the energy measured in the phonon channel (E_p):

$$\text{Light Yield} = \frac{E_l}{E_p} \tag{3.1}$$

The energies E_p and E_l are given in electron equivalent which means that an electron recoil of energy E results in measured energies of $E_l = E$ and $E_p = E$ in the light and phonon

[2] In practice not only the ratio is used, but the full multiplicity spectrum.

detector, respectively. Thus, electron recoils, which are induced by betas or gammas, have a light yield of one. All other types of events exhibit a lower light output, referred to as quenching.

Figure 3.3 depicts the regions in the light yield versus energy plane for various event classes. Inside each of these bands 80 % of the events corresponding to the respective class are expected (another 10 % above and below, respectively). As already mentioned e^-/γ-events (blue band) have a light yield of one by calibration.[3] The mean of the other bands (α-particle interactions in magenta, nuclear recoils off oxygen and calcium in red and green) can then be calculated using the corresponding quenching factor which quantifies the reduction in light output. The width of the bands is caused by the finite resolution of light and phonon detector.

Since the sought-for dark matter particles scatter off nuclei the region of interest (ROI) includes all three nuclear recoil bands. Usually, energies above 40 keV are not considered due to the tungsten form factor significantly reducing the expected scattering rate (see section 2.3.3).

As one can see in figure 3.3 the discrimination power between different event classes depends on the energy. For higher energies even scatterings off different nuclei can be distinguished on an event-by-event basis. In the regions of overlapping bands an event-by-event discrimination is not feasible any more, but it might still be possible to derive information on the event class on a statistical basis.

3.3.2. Transition Edge Sensors

Figure 3.4 shows the electrical resistance of a typical thin tungsten film evaporated on the target substrate ($CaWO_4$ for the phonon detector and silicon-on-sapphire for the light detector) as a function of temperature. This particular film is superconducting for temperatures below $\sim$17.8 mK. Within 1.2 mK it undergoes the transition to the normal conducting state[4]. The base temperature of the cryostat is well below the transition temperature of the films used, allowing to precisely heat each film to its individual operating temperature. Due to the steepness of the transition even a small temperature change (induced by a particle interaction) of $\Delta T = \mathcal{O}(10\,\mu K)$ provides a measurable large change in resistance $\Delta R = \mathcal{O}(10\,m\Omega)$. Today, these so-called transition edge sensors provide extremely precise temperature measurements in the field of cryogenic particle detectors.

3.3.3. Pulse Formation in the Target Material $CaWO_4$

Naively, one would expect that an energy deposition ΔE will lead to a temperature rise ΔT of the thermometer (thermometer and TES refer to the same thing, namely the thin

[3] When going to low deposited energies, the light output of e^-/γ-events is no longer proportional to the deposited energy, causing the e^-/γ-band to bend down. This so-called non-proportionality effect is not observed for nuclear recoils. Details are given in chapter 7.

[4] Typical normal conduction resistances are in the order of 200 mΩ.

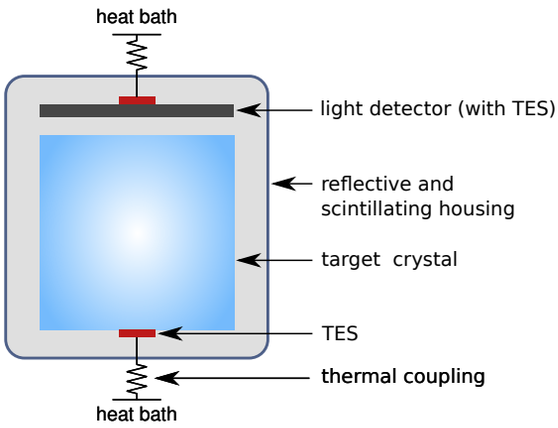

Figure 3.2.: Schematic drawing illustrating the working principle of a CRESST-II detector module. The phonon signal induced by a particle interaction in the $CaWO_4$ target crystal is measured with the TES (red). Scintillation light emitted by the crystal is guided to the light detector via a scintillating and reflective foil surrounding the crystal. The light detector consists of an absorber equipped with a TES measuring the phonon signal induced by the absorbed light. Both TESs are weakly coupled to the heat bath of the cryostat, thus relaxing back to the operating temperature after a particle interaction.

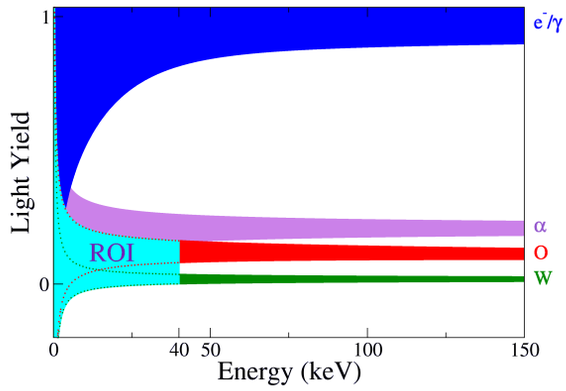

Figure 3.3.: Typically CRESST-II-data is presented by plotting the light yield as a function of deposited energy. The light yield is defined by the energy measured in the light channel (E_l) divided by the energy measured in the phonon channel (E_p). e^-/γ-events exhibit the highest light yield set to one. Inside each band (shaded areas) 80% of the events of the respective event class are expected (10% below and 10% above). The region of interest (ROI) expands over all three nuclear recoil bands (Ca-band not drawn for clarity) from threshold energy up to 40 keV.

tungsten film) following the equation

$$\Delta T = \frac{\Delta E}{C} \tag{3.2}$$

with the heat capacity C. For dielectric materials like $CaWO_4$ the heat capacity at low temperatures scales with the third power of the temperature divided by the Debye temperature Θ_D:

$$C \sim \left(\frac{T}{\Theta_D}\right)^3 \tag{3.3}$$

The above equation is the main motivation to operate at temperatures as low as ~ 10 mK. Even a slightly higher operating temperature would lead to a significant loss of temperature rise and, thus, signal. However, in reality equation 3.2 is oversimplified, in particular because of not taking any couplings of the thermometer into account.

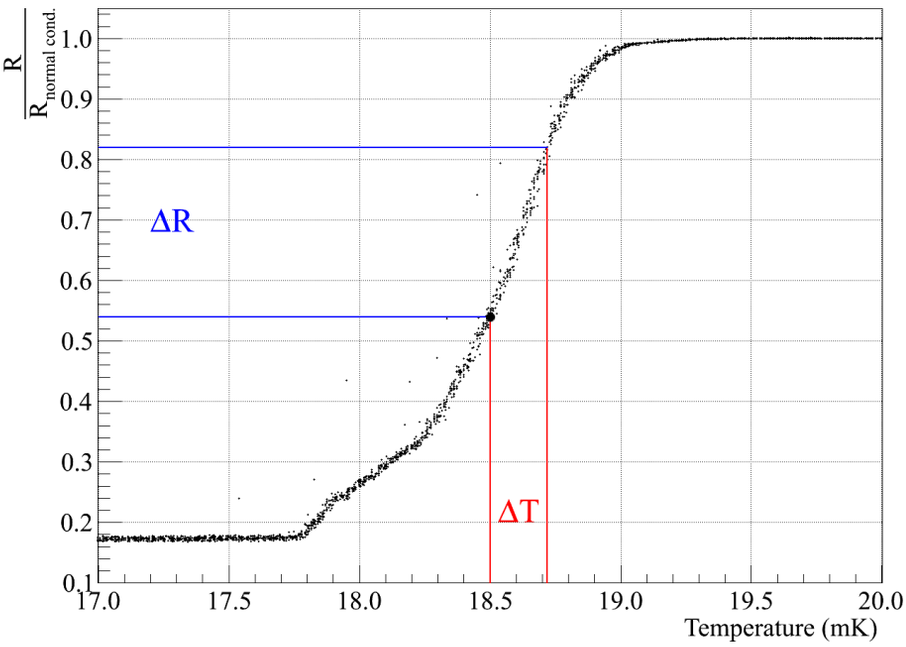

Figure 3.4.: Transition between the super and the normal conducting state of a typical thin tungsten film. The resistance is normalized to the resistance in the normal conducting regime. The temperature rise from the operating point (black dot) induced by a particle interaction yields a detectable large change of electrical resistance thanks to the steepness of the transition.

In 1994 Pröbst et. al. developed a model for cryogenic detectors with TES readout [122], which at that time was verified with measurements of a silicon crystal, but it proved to be valid for other materials like $CaWO_4$. The most relevant aspects of this model will be discussed in the following.

Any particle interaction depositing energy in the crystal will create high-frequency phonons decaying within nanoseconds to acoustic phonons of half the Debye frequency ν_D:

$$\frac{\nu_D}{2} = \frac{k_B \Theta_D}{2h} \tag{3.4}$$

In the above equation, k_B and h denote Boltzmann's and Planck's constant, respectively. The Debye-temperature Θ_D is around 350 K for $CaWO_4$ [123]. Lattice anharmonicities cause a rapid degradation from the $\mathcal{O}$(10 THz) to the $\mathcal{O}$(100 GHz) regime. The conversion rate scales with the fifth power of the frequency: $\Gamma \sim \nu^5$. However, the associated energy of a 100 GHz phonon ($E = h\nu \simeq 0.4$ meV) is still well above the thermal regime $E = k_B T \simeq 0.9\,\mu$eV. Thus, these phonons, which uniformly fill the absorber after a few reflections, are called *non-thermal*.

Two mechanisms of thermalization have to be considered. Firstly, non-thermal phonons may be experience a thermalization in the thermometer via their strong interaction with the free electrons therein. This process provides a fast heating of the electron system of the thermometer and is denoted the *non-thermal* component.

Phonons remaining in the absorber (crystal) will be thermalized therein (mainly on the surface) making up for the second, slow component which is referred to as *thermal* component.

The TES Response $\Delta T_e(t)$

A detailed description on how to derive the thermometer response $\Delta T_e(t)$ after an energy deposition ΔE may be found in [122], only the result will be given here.

As already mentioned there are two components contributing to the thermal pulse. A *non-thermal* one originating from phonons which are thermalized directly in the thermometer and a *thermal* component from non-thermal phonons being thermalized in the absorber.

The fraction of phonons not yet thermalized at the time t is given by the exponential function e^{-t/τ_n} with τ_n being the lifetime of non-thermal phonons. The temperature change ΔT in the thermometer then takes the form

$$\Delta T_e(t) = \Theta(t)[A_n(e^{-t/\tau_n} - e^{-t/\tau_{\text{in}}}) + A_t(e^{-t/\tau_t} - e^{-t/\tau_n})] \tag{3.5}$$

with the thermal relaxation time given by τ_t and the thermometer intrinsic time constant τ_{in} (which is basically given by its heat capacity divided by the sum of the couplings to the absorber and the heat bath). The step function $\Theta(t)$ accounts for an instantaneous uniform distribution of non-thermal phonons after an energy deposit ΔE. A_n and A_t are the amplitudes of the non-thermal and the thermal component, respectively.

Depending on the relation between the intrinsic time constant τ_{in} and the lifetime of the non-thermal phonons τ_n, one distinguishes two operation modes. For $\tau_{\text{in}} \ll \tau_n$ the thermometer effectively measures the flux, referred to as *bolometric mode*. The opposite case, namely a setup with $\tau_{\text{in}} \gg \tau_n$, integrates the power input and is, therefore, called *calorimetric mode*. Technically, a large τ_{in} can be realized with a weak coupling to the heat bath.

Verification on a Standard Pulse

Figure 3.5 verifies the applicability for the model of pulse formation discussed above for the phonon detector Lise. To obtain a noise-free description of the pulse shape in a detector we average over a large number of pulses induced by the same energy deposition in the detector. The averaging cancels out any randomly distributed noise component. This so-called standard event is shown as solid black line in figure 3.5. Then the model of pulse formation is fit to the standard event with the outcome depicted by the red dashed curve. The blue and the green dashed lines visualize the contribution of the non-thermal and thermal component, respectively. All parameters of equation 3.5 are unconstrained in the fit and additional parameters are introduced to account for a non-zero baseline level and a shift of the template in time.

In table 3.2 the values determined by the fit including the statistical uncertainties are listed. The small uncertainties observed confirm the visual impression of figure 3.5, namely an excellent agreement between model and data. From τ_{in} being much smaller than τ_n one

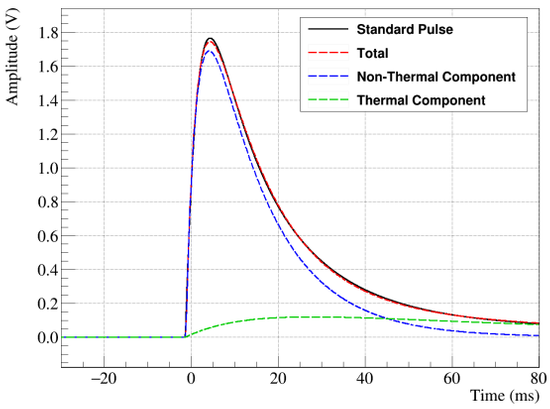

Figure 3.5.: Standard pulse of the phonon detector Lise (solid) black together with the result of a fit of the model of pulse formation given in equation 3.5. The description of the pulse as a function of time is given by the sum (dashed red) of a thermal component (dashed green) and a non-thermal component (dashed blue). The resulting fit parameters including their statistical uncertainties are given in the table on the right.

Parameter	Fit Result
Baseline Level	1.6 mV $\pm$ 0.1 mV
t_0	-1.310 ms $\pm$ 0.001 ms
A_n	3.071 V $\pm$ 0.003 V
A_t	0.210 V $\pm$ 0.002 V
τ_{in}	2.628 ms $\pm$ 0.004 ms
τ_n	13.90 ms $\pm$ 0.02 ms
τ_t	78.2 ms $\pm$ 0.5 ms

Table 3.2.: Values resulting from a fit of equation 3.5 to the standard event depicted on the left. Additional to the parameters in equation 3.5, a constant but non-zero baseline level is included as a free fit parameter. To allow for a shift in time the onset t_0 is also fit, thus the time t in equation 3.5 becomes: $t \rightarrow t - t_0$.

concludes that this detector, as all other phonon detectors installed in phase 2, is operated in bolometric mode measuring the flux.

3.3.4. Glued TES Carriers

Both phonon detectors analyzed in this work use a so-called composite design. In the composite design the TES is not evaporated directly onto the absorber crystal, but onto a small $CaWO_4$-carrier crystal which is in turn glued to the main absorber. This design was introduced to avoid exposing the main crystal to high temperatures during the evaporation process. It was found that the high temperatures lead to oxygen vacancies causing a decreased light output [114, 124] and, therefore, a smaller discrimination power.

A photograph of the detector TUM40 including the TES-carrier is shown in figure 3.6. $CaWO_4$ is a quite brittle material and easily cracks when a too high pressure is applied. To study the stress originating from a different shrinking of the glue and $CaWO_4$ during cool-down dedicated FEM-Simulations[5] were carried out in [114]. These simulations showed that the stress can be reduced by a thin layer of glue and by matching the orientation of the crystal axis of carrier and absorber. Based on this findings CRESST optimized the fabrication process and succeeded to reliably produce detectors of composite design. Twelve out

[5] Finite Element Method

Figure 3.6.: Photograph of the detector TUM40 during assembling. Clearly visible is the small $CaWO_4$ carrier with the TES (black structure) evaporated on top. While the carrier is polished, the absorber is roughened on all sides, except of the contact points with the holding sticks, as can be seen on the front side.

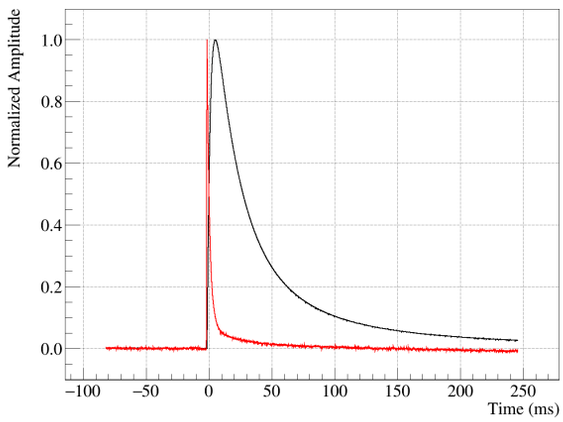

Figure 3.7.: Pulse shapes for an energy deposition in the main absorber crystal (black) and in the carrier crystal (red) for the detector TUM40. To emphasize the differences in shape both pulses are normalized to an amplitude of one.

of the eighteen phonon detectors installed in phase 2 use a glued TES carrier.

However, the carrier inevitable introduces an additional class of events from direct hits of the TES carrier. These *carrier events* exhibit faster rise and decay times. Figure 3.7 depicts the pulse shapes for events in the carrier (red) and in the absorber (black) for the detector TUM40. To provide a direct comparison the amplitude of both standard events are scaled to one. On the one hand, the standard events exhibit a pronounced difference in pulse shape. On the other hand a clear discrimination becomes unfeasible when approaching very small pulses slightly above the baseline noise. The analysis presented in this work shows that the carrier events diminish the sensitivity of CRESST detectors for scatterings of light dark matter particles. Thus, the next-generation detectors for CRESST-III will not use glued carriers any more, as the benefit of eliminating the carrier events clearly outweighs a potentially reduced discrimination power due to a slight degradation of the light signal.

3.4. Data Acquisition

3.4.1. Readout Circuit

As discussed already, an energy deposition in the crystal or the light detector manifests itself as a change of electrical resistance in the TES. To measure this resistance change

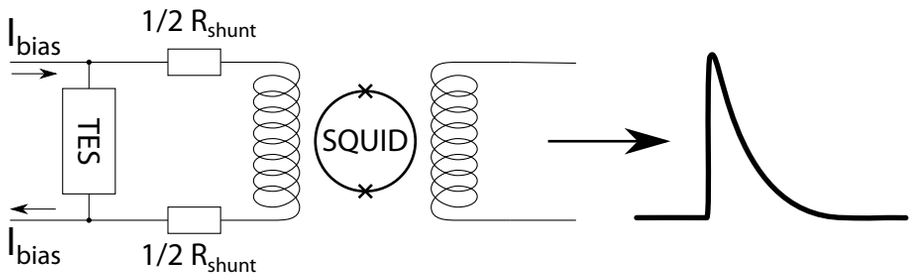

Figure 3.8.: Readout circuit for a TES with a SQUID.

the TES is connected in a parallel circuit to a coil in series with a resistance R_{shunt}, as can be seen in figure 3.8. For symmetry reasons the circuit is realized using two resistors of $\frac{1}{2}R_{shunt}$ =20 mΩ. We apply a constant current I_{bias} with $\mathcal{O}(\mu A)$, individually adjusted for every sensor. A resistance change of the TES modifies the splitting of the current in the parallel circuit causing a variation of the magnetic field induced by the coil. To measure this change of magnetic field CRESST uses Superconducting QUantum Interference Devices (SQUIDs). The output of these extremely precise devices is a voltage signal proportional to the change of magnetic flux. Going back the chain from `SQUID output` $\leftrightarrow$ `magnetic flux` $\leftrightarrow$ `electrical current through coil` $\leftrightarrow$ `electric resistance of TES` $\leftrightarrow$ `temperature rise in TES` $\leftrightarrow$ `energy deposition in detector` reveals that the amplitude of the recorded pulse is in first (and good) approximation proportional to the energy deposition in the detector.

Figure 3.9 shows the technical realization of this readout principle. The bias current is injected via the parts marked in purple. The blue circuit on the left is connected to the heater of the detector. Each detector is equipped with its own heater serving two purposes. First of all, a quasi-constant current is applied to keep the detector at a well-defined operating point in the transition between super and normal conducting state. Technically, the desired current is set by the data acquisition (DAQ) via a digital-analog converter (DAC). Secondly, a pulser yields the possibility to inject artificial pulses to the heater. Signals from pulser and DAC are summed up ($\sum$) and passed to the square-rooter ($\sqrt{}$). The latter establishes a direct proportionality between the voltage V of the initial signal and the electric power P injected to the heater (R_h): $P \sim 1/R \cdot (\sqrt{V})^2$. Two current-defining resistors are connected in series to the heater. Three different sets of resistors together with the setting of amplifier after the square-rooter allow to individually adjust the dynamic range of the circuit for each heater.

The heater may either be directly connected to the TES or be completely separate. Separate heaters proved to reduce electric noise, thus improving the energy resolution of a sensor. Currently, separate heaters are used for most of the light detectors but not for the phonon detectors. However, since the detection of tiny energies requires excellent sensitivity of the phonon detectors also those will be equipped with separate heaters in the future. The main advantage of non-separated heaters is that the TES is heated directly and not the complete detector. Thus, for certain applications directly connected heaters will remain without alternative.

3.4.2. Recorded Pulses

The red part in figure 3.9 shows the *signal path* beginning from the input coil of the SQUID in parallel with the TES. After the SQUID electronics the voltage signal is split. One part (left) is connected to a transient digitizer. This digitizer uses a so-called ring buffer to constantly record the signal in time samples of 40 μs with 16 bit each. Once the buffer is full (one round) the digitizer overwrites samples, beginning with the oldest one. The second part of the signal is filtered, amplified and shaped to achieve a high trigger efficiency even for small pulses on the one hand, and a low level of false triggers on the other hand. After a trigger the DAQ awaits the so-called post-trigger time before reading out the transient digitizer (illustrated in figure 3.10), including samples before the trigger. Storing also this pre-trigger samples to disk is crucial to precisely determine the baseline and, thus, the amplitude of a pulse. In addition, the pre-trigger samples are needed to compensate for the *trigger walk* - the dependence of the trigger time on the amplitude (rise time) of the pulse.

Eight transient digitizers are enclosed in one digitizer module. Detectors from the same detector module (phonon and light) are always read out together, even if only one of them triggered. For all other detector modules on the same digitizer module a trigger is required to toggle readout. However, this secondary triggers have to appear shortly after the initial trigger (usually in the first half of the post-trigger time). Afterwards, the trigger is blocked and only reactivated after the time needed for readout and a full pre-trigger region (see figure 3.10). By blocking the second post-trigger region and one pre-trigger region CRESST avoids pulses very late in the record, or very early in the next record, respectively. In both cases a precise reconstruction of the pulse amplitude and, therefore, the energy of the event would not be feasible.

Figure 3.10 graphically shows the pulse recording scheme, table 3.3 gives the parameter values used in CRESST-II phase 2.

3.4.3. Control and Heater Pulses

To infer from the amplitude of a recorded pulse to the energy deposited in the detector, a very precise stabilization of the TES in its assigned operating point is mandatory. The base temperature of the cryostat is not constant over time and a variety of events, such as e.g. construction works in the tunnel or earth quakes, may induce short-term temperature rises. Therefore, the heating current has to be adjusted over time.

The first step of this regulation is to inject large pulses - a large amount of energy - to the heater. Such *control pulses* lead to a signal quickly rising until the normal conducting state of the TES is reached. In the normal conducting regime further heat input will hardly increase the electric resistance, thus not contributing to the signal. As a result, the pulse height recorded from a control pulse is a direct measure of the distance from the normal conducting state to the point in the transition (the temperature) before the injection of the pulse. A pulse height smaller than the nominal set point means that the constant heating has to be reduced in order to go deeper into the transition and vice versa. Control pulses are injected every six seconds and a software Proportional-Integral-Differential (PID) loop

keeps the TES at the desired temperature. The pulse heights of these control pulses are also saved to disk allowing to mark time periods with the TES out of the operation point as unstable in the offline analysis and, thus, to discard them from the dark matter analysis.

Additionally, also pulses of much smaller energy - the so-called *test pulses* - are sent to the heater serving two main purposes. Firstly, constantly injecting a well defined amount of energy to the TES allows to correct for drifts of the detector response over time. For a perfectly linear transition the height of a pulse is directly proportional to the energy deposited. In a real world small deviations from this linearity cannot be avoided. Thus, the second purpose is to measure these small deviations by the injection of test pulses of different energies. In summary, the test pulses are a key ingredient for a precise energy calibration from the sub-keV to the MeV regime.

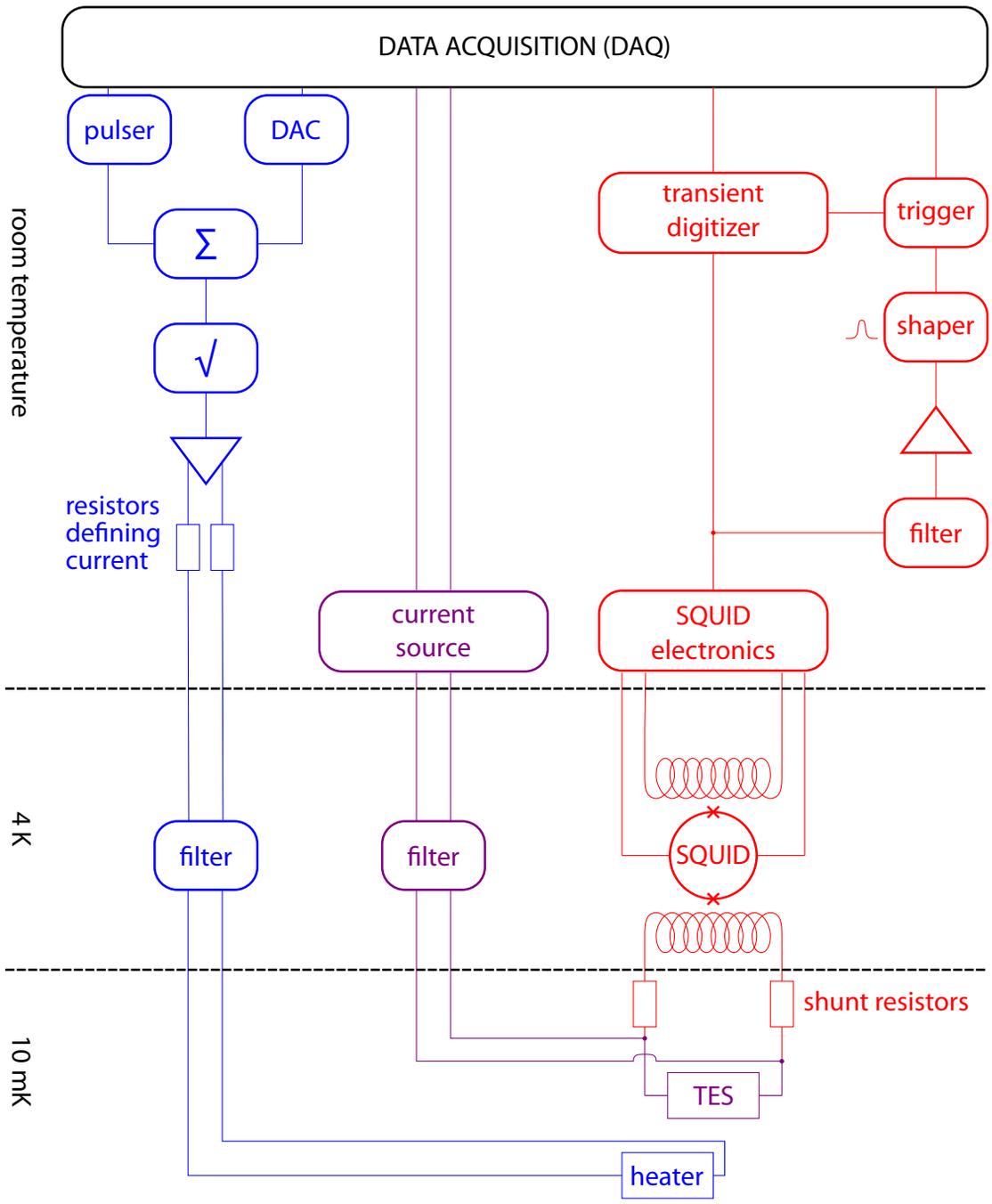

Figure 3.9.: Simplified scheme of the CRESST detector readout. The heater part used to stabilize a detector in its operating point and to inject heater pulses is drawn in red. The purple part corresponds to the bias circuit, the blue part to the SQUID readout including the trigger. The dashed black lines mark the operating temperatures of the various parts.

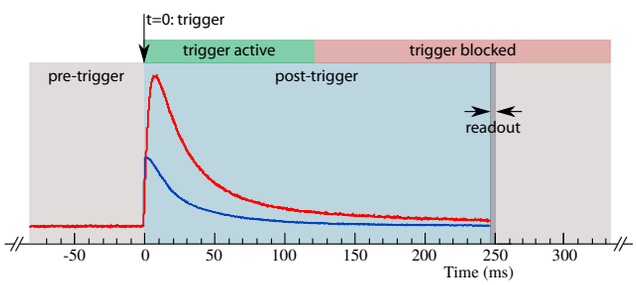

Figure 3.10.: Illustration of the readout scheme. After a trigger the post-trigger time is awaited before the readout of all detectors of a module. A record consists of the pre and the post-trigger time (gray and blue). Triggers from other detectors on the same transient digitizer are accepted in the first half of the post-trigger time (green bar). Afterwards the trigger is blocked for the second half of the post-trigger time, the time needed for readout and for the duration of one pre-trigger time.

Parameter	Duration	
	samples	(ms)
Record	8192	327.68
Pre-Trigger	2048	81.92
Post-Trigger	6144	245.76
Readout time		$\mathcal{O}(2)$

Table 3.3.: Values for the time parameters illustrated on the left as used in CRESST-II phase 2. The sampling rate is 25 kHz, so one sample corresponds to 40 μs.

4. Results of CRESST-II Phase 1 and Implications for Phase 2

In this work data from CRESST-II phase 2 is analyzed. In the previous phase 1 an excess above the known backgrounds was observed in a maximum likelihood analysis, which will be summarized in the beginning of this chapter. For phase 2, several measures were undertaken aiming at a reduction of the background level. Additionally, new fully-active detector modules were installed which are immune to certain backgrounds induced by, in particular, surface α-decays. Those new, upgraded detector designs will be presented in the last section of this chapter.

4.1. The Maximum Likelihood Analysis of Phase 1

This section will briefly review the analysis of CRESST-II phase 1 presented mainly in [72] with additional details given in [71, 125]. In phase 1 eighteen modules have been installed out of which eight could be used for the dark matter analysis. These modules collected 730 kgd of net exposure after cuts in the years from 2009 to 2011. Figure 4.1 depicts a scheme and a photograph of the detector design used for all those eight dark matter modules.[1] Today, this design is called *conventional* detector design. The working principle of such a detector was already discussed in the previous chapter. The core component is a polished, cylindrical $CaWO_4$ crystal with 40 mm in height and in diameter; the mass is 300 g.

For phase 1 a maximum likelihood analysis found an excess of events above the known backgrounds. Details on the maximum likelihood framework will be given in chapter 10. The basic ingredient for a maximum likelihood analysis is a model of all known backgrounds including uncertainties. The parameters of the model are then varied to find the parameter values maximizing the likelihood function which are those values for the parameters yielding maximal agreement between model and observed data. As a second step a potential dark matter signal is added to the model and, again, the maximum of the likelihood function for this background plus signal model is calculated. By investigating how well the latter fits the data in comparison to the background-only model one can infer the statistical significance of a potential signal.

[1] One module was equipped with two light detectors. However, both light signals were combined and apart from that no extra treatment of this module in the analysis was needed. More information may be found in [114, 126].

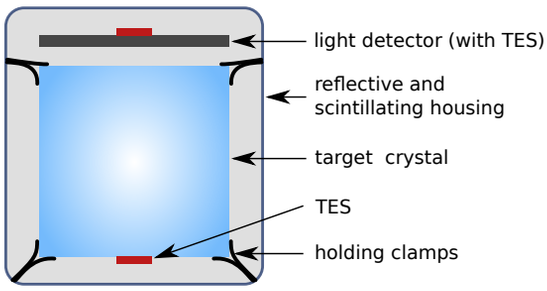

(a) Schematic drawing of a conventional detector module design.

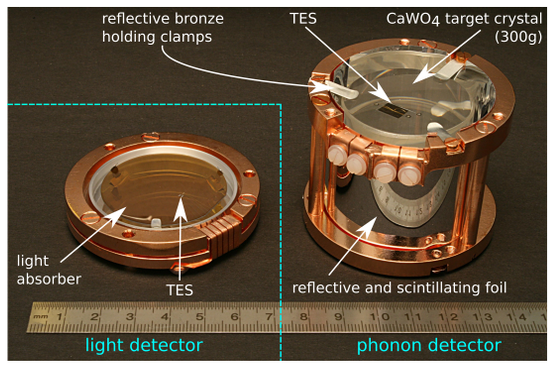

(b) Photograph of an opened detecor module with light and phonon detector mounted in their copper holders.

Figure 4.1.: Shown are a schematic drawing of the conventional detector module design (a) and a corresponding photograph (b). The conventional design houses cylindrical $CaWO_4$ crystals with a height and diameter of 40 mm and a mass of 300 g. To hold the crystal bronze clamps are used (covered with aluminum or silver to increase their reflectivity). The light absorber is made of a silicon-on-sapphire disk with 40 mm diameter. Additionally, the reflective and scintillating foil enclosing the module can be seen in (a) and (b).

4.1.1. Backgrounds

In the following the backgrounds considered in the model of this analysis will be discussed: leakage from the e^-/γ-band, neutron scatterings, degraded alphas and lead recoils. All backgrounds, as well as the potential signal are modeled two-dimensionally making full use of the energy and light yield information of the measured events.

Leakage from the e^-/γ-Band

The shape of the bands in the light yield-energy plane (mean and width, both dependent on energy) for the various event classes (see figure 3.3) is described by a model thoroughly discussed in chapter 7. This model is then fit to the data, individually for each detector module. From the band and the energy spectrum of events seen therein one can calculate the leakage of the e^-/γ-band into the ROI, i.e. the nuclear recoil bands. As can been seen in figure 3.3 the overlap of the bands and, thus, the leakage will be higher for lower energies. In this analysis the leakage was limited to one expected e^-/γ-event per detector module by defining a lower limit, referred to as analysis threshold, on the accepted energies. We call the region from the analysis threshold up to 40 keV, spreading over all three nuclear recoil bands, the acceptance region.

The leakage of e^-/γ-backgrounds into the nuclear recoil bands basically depends on the e^-/γ-background level and on the width/overlap of the bands (the discrimination power). Most of the e^-/γ-background is known to result from intrinsic contaminations of the crystal [127, 128] with large variations among different crystals. The width of the bands de-

pends on the amount of light reaching the light detector and its resolution. Both factors show a large spread between different crystals [114, 126] and between different light detectors. Considering all these arguments render an individual treatment of each detector module mandatory. As a result the analysis thresholds for the acceptance regions vary from 10 to 19 keV with a total of 67 events observed in eight detector modules. Data and the resulting bands for one detector module are shown in figure 4.2 (see caption for detailed description).

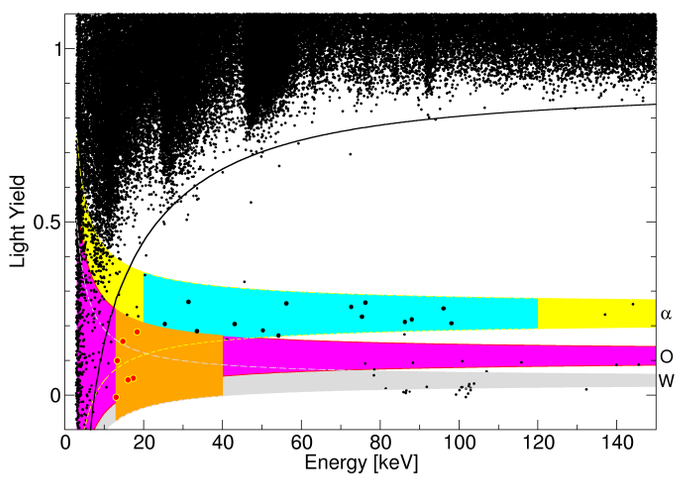

Figure 4.2.: (Plot from [72]) Data of the detector module Verena (Ch20) recorded in CRESST-II phase 1. The dominant e^-/γ-background has a light yield of around one by calibration and 99.9 % of all e^-/γ-events are expected above the solid black line. The α-band is depicted in yellow, with the alpha reference region highlighted in cyan (see text for explanation). The magenta and gray shaded areas correspond the nuclear recoil bands of oxygen and tungsten, respectively (the calcium band which would be in between the two is not drawn for clarity reasons). The acceptance region is drawn in orange with the events therein highlighted in red.

Neutron Background

While a single scattering of a neutron cannot be distinguished from a potential dark matter signal an estimation of the neutron background is possible via the multiplicity spectrum for muon-induced neutrons or neutrons from a source (see subsection 3.2.2). The multiplicity is defined as the number of detector modules triggering in coincidence with an event in the acceptance region of one detector. No selection criteria are imposed on the coincident events; a single scattering gets assigned a multiplicity of one. Three multiple scatterings were found in the background data (not coincident with the muon veto). A simple estimate by the ratio of multiple to single scatterings yields an expected neutron background of 1.5 events for all neutrons being muon-induced and of 11.4 events for all neutrons being from a source. However, the likelihood analysis has access to the multiplicity spectra of muon-induced neutrons (measured by coincidences between the detectors

and the muon veto), of neutrons from source (measured with a neutron source) and for the three observed multiple scattering events. The ratio between the two origins is treated as a nuisance parameter[2].

Backgrounds Induced by the α-Decay of ^{210}Po

All remaining backgrounds considered in the analysis arise from the α-decay of ^{210}Po to ^{206}Pb . The Q-value of this decay is 5407.46 keV, directly converted to kinetic energies of 5.3 MeV for the α-particle and 103 keV for the ^{206}Pb recoil in almost 100 % of the cases. In a negligible fraction (0.001 %) of decays ^{206}Pb is left in an excited state emitting a gamma of 803 keV (all energy values from [129]); the corresponding energy of the α-particle and the ^{206}Pb daughter nuclide then are 4.5 MeV and 86 keV.

Degraded Alphas An alpha decay taking place in a surface-near layer of detector material surrounding the crystal may result in a so-called degraded alpha event. The term *degraded* refers to the fact that the alpha might lose part of its energy in the starting material and, thus, reach the detector with less than the nominal energy of 5.3 MeV. For low energies the alpha-band overlaps with the nuclear recoils bands (see figure 3.3) leading to a direct contribution of degraded alphas to the events in the acceptance region. We define a range of 100 keV of the overlap-free part of the alpha band as the reference region for alpha events (cyan-shaded area in 4.2). The lower limit of this reference region is chosen upon the expected e^-/γ-leakage into this region which was allowed to be no higher than 0.1 expected events. From the spectrum of the events seen in this reference region we model the contribution of degraded alphas to the signal region.

Lead Recoil Background For the lead recoil background two different scenarios have to be distinguished, depending on where the α-decay takes place, both illustrated in figure 4.3.

^{210}Po-Decay on Crystal Surface The top part of figure 4.3 refers to a decay on the surface of the crystal where the ^{206}Pb recoil will be fully absorbed in the crystal, thus depositing its full energy of 103 keV. In addition, also the alpha might deposit some energy before leaving the crystals for decays taking place slightly below the surface.

^{210}Po-Decay on Surface of Surrounding Material For decays on surfaces of surrounding materials, in particular the metal holding clamps, the ^{206}Pb-recoil might lose part of its energy in the surrounding material and then hit the crystal with an energy smaller than 103 keV (bottom part of figure 4.3). A similar strategy was carried out as for the alpha decays. We find a rather flat distribution in the lead recoil reference region (see green shaded area in figure 4.4) expanding over the band expected for lead recoil events from 40 to 90 keV. SRIM simulations [130] validated a constant extrapolation from the reference to

[2] A nuisance parameter is a parameter included in the model and fit to the data which is not of primary interest.

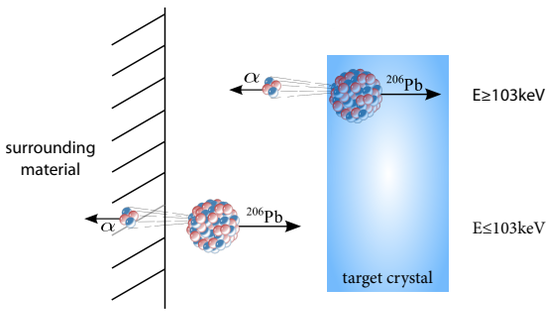

Figure 4.3.: Illustration of backgrounds induced by ^{210}Po on or slightly below surfaces. Picture adapted from [72].

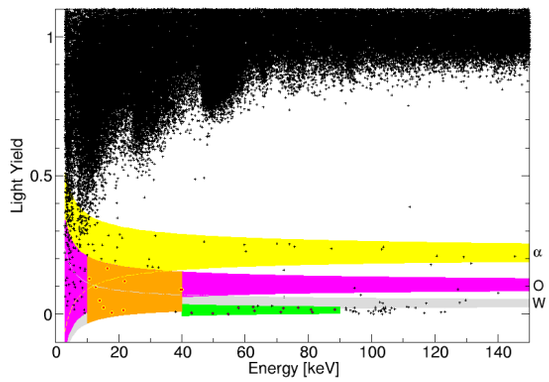

Figure 4.4.: Data from one detector module operated in phase 1. The color coding follows figure 4.2 with the control region for lead recoil events shaded in green. Remarkable is the accumulation of events at the full recoil energy of 103 keV and a leackage down to the acceptance region (orange). As one can see lead recoils have an average light yield slighly below the tungsten band. Plot from [72].

the signal regions. However, in [131] the authors show that the surface roughness, which is not included in SRIM, might lead to a rise of this background towards lower energies by so-called sputtering events. Sputtering describes the process of atoms being kicked out of a material in collisions with heavy ions. The CRESST collaboration repeated this simulation and could reproduce the results [132]. However, many unknown parameters like the implantation depth and profile have crucial impact on the result. Thus, it could not be clarified whether these effects are the origin of the excess of events observed [132].

4.1.2. Result

The result of this maximum likelihood analysis is summarized in table 4.1, showing the number of expected events for all backgrounds discussed above and a potential signal. The model for the potential signal takes into account the different acceptance regions of the modules and the three different target nuclei. Two maxima were found for the likelihood function, the global maximum M1 corresponding to a dark matter particle mass of 25 GeV/c^2 and a local maximum M2 with 12 GeV/c^2 (see also figure 2.7). The presence of two maxima with comparable statistical significance of more than 4 σ is not surprising in the light of the different target nuclei. As discussed in chapter 2, the expected dark matter particle scattering rate scales quadratically with the atomic mass number. However, for light dark matter particles, scatterings off the heavy tungsten would have energies below the acceptance region. The finite resolution of the light channel prevents a strong constraint of the light yield distribution of a potential signal. Therefore, a light dark matter

particle scattering mainly off oxygen (high light yield, M2) is a model of the data almost as good as a dark matter particle of twice the mass mainly scattering off tungsten (low light yield, M1). This discrepancy could only be resolved with a higher discrimination power between the three target nuclei.

	M1	M2
e/γ-Events	8.00 ± 0.05	8.00 ± 0.05
Neutron Events	$7.5\,^{+6.3}_{-5.5}$	$9.7\,^{+6.1}_{-5.1}$
α-Events	$11.5\,^{+2.6}_{-2.3}$	$11.2\,^{+2.5}_{-2.3}$
Pb recoils	$15.0^{+5.2}_{-5.1}$	$18.7\,^{+4.9}_{-4.7}$
Signal Events	$29.4\,^{+8.6}_{-7.7}$	$24.2\,^{+8.1}_{-7.2}$
m_χ (GeV/c^2)	25.3	11.6
σ_{WN} (pb)	$1.6 \cdot 10^{-6}$	$3.7 \cdot 10^{-5}$
Statistical Significance (σ)	4.7	4.2

Table 4.1.: Results of the maximum likelihood analysis [72]. Listed are the various background and signal contributions for the two maxima of the likelihood function M1 & M2. The last three columns contain the corresponding mass and cross section for a potential dark matter signal and its statistical significance.

On the basis of the global maximum M1 allowed regions in the dark matter mass versus cross section plane with $1\,\sigma$ (brown shaded area in figure 2.7) and $2\,\sigma$ (shaded in blue-gray) confidence level (C.L.) were calculated. Figure 2.7 also shows that already at the time of the release other direct dark matter searches put strong constraints on the M2-solution and completely ruled out the M1-maximum. However, as was discussed already, a direct comparison of different experiments using different target materials is always subject to certain assumptions, for example on the velocity distribution of dark matter particles. Since no other experiment uses $CaWO_4$, a model-independent comparison is only possible with the reanalysis of CRESST-II commissioning run data [76]. While previous analyses of commissioning run data included scatterings off tungsten only, the analysis in [76] made full use of all three nuclear recoil bands - just like the likelihood analysis discussed right now. On the one hand, this limit excludes most of the $2\,\sigma$-allowed parameter space, on the other hand the sensitivity of the experiment was increased only moderately between the commissioning run and phase 1. Thus, a potential signal would naturally appear close to the former exclusion limit.

4.2. Background Reduction for Phase 2

Based on this result from phase 1 the aim of the CRESST collaboration for phase 2 was to clarify the origin of this excess. Reaching this goal requires to significantly lower the background level, since table 4.1 reveals that the sum of all backgrounds roughly equals

Background	Origin	Measure
e/γ	intrinsic crystal contamination	crystal growth in house [133], enhanced discrimination power
Neutrons	missed by muon veto and α-n reactions	additional neutron shielding
α	contaminations in clamp material	cleaner material or fully-active detector designs
Pb Recoils	^{210}Po from ^{222}Rn and silver coating	radon prevention, no silver coating or fully-active detector designs

Table 4.2.: Backgrounds observed in CRESST-II phase 1, their origin and measures undertaken for their reduction in phase 2.

the possible signal contribution. Prerequisite to succeed in reducing backgrounds is the identification of their origin. Table 4.2 summarizes the background origins of phase 1 and the measures taken for phase 2, which will be briefly discussed here.

4.2.1. Electron/Gamma and Neutron Background

Most of the e^-/γ-background originates from intrinsic radioactive contaminations of the crystals. In phase 2 the CRESST collaboration could, for the first time, also use crystals grown within the collaboration by the Technische Universität München (TUM) [133]. Out of the eighteen crystals installed, four crystals were grown at TUM reducing the background level by a factor of 2-6 compared to typical commercial crystals used for the remaining twelve modules [128].

It should be mentioned that the impact of the e^-/γ-background for the dark matter search depends on the leakage of the e^-/γ-band into the nuclear recoils bands. The latter is given by the product of the total level of events inside the e^-/γ-band and its overlap with the nuclear recoil bands. So even for crystals of a given contamination, improvements are possible by increasing the separation between the bands. Therefore, CRESST is constantly optimizing the light channel (crystal light output, module geometry and light detector resolution). Obviously, optimal results may by achieved combining both measures.

For phase 2, 5 cm of high-purity Polyethylene were installed as the innermost shielding layer (see figure 3.1). The main motivation was to better shield the detectors against neutrons created by reactions in the lead and copper shielding, in particular from muons which are penetrating the experiment and missed by the veto. Simulations predict a reduction of the neutron background by roughly one order of magnitude due to the additional inner Polyethylene shield [120].

4.2.2. Alpha and Lead Recoil Background

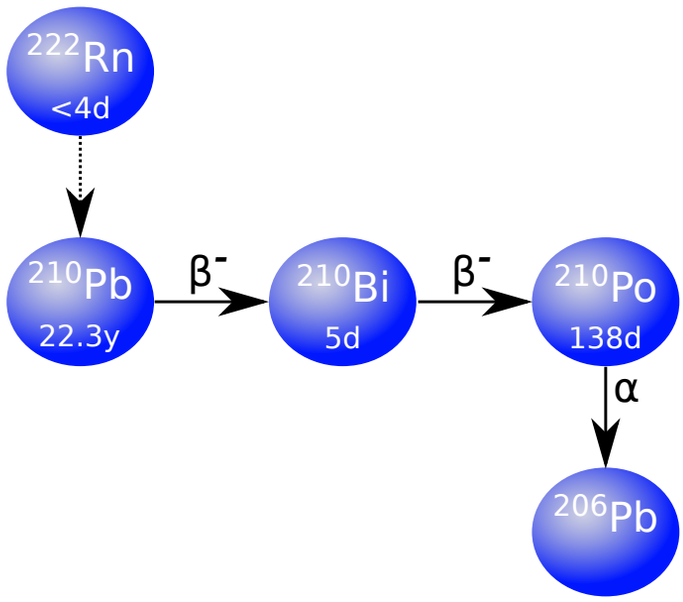

Figure 4.5.: Illustration of the relevant part of the uranium (^{238}U) decay chain, staring with the gaseous ^{222}Rn quickly decaying (in several steps) to the first long-lived isotope ^{210}Pb . The latter undergoes two $\beta-$decays, before the alpha decay of ^{210}Po which was identified as main source for degraded alphas as well as for the lead recoil background.

As was discussed earlier ^{210}Po α-decays inside the bulk of the clamp material (CuSn6) were identified as the origin of degraded alphas. No other parts of the detector may be the source of this kind of background, since the alpha would produce an additional light signal, either by scintillation or by direct absorption in the light detector. ^{210}Po is part of the ^{238}U decay chain after ^{210}Pb with two beta decays in between (see 4.5). In [134] a higher ^{210}Pb contamination was observed than expected from the typical content of the isotope ^{210}Pb in lead. This excess was understood after finding graphite remnants from the production process of the CuSn6 clamp material. Graphite is known to efficiently adsorb gaseous radon and ^{210}Pb is a progeny of ^{222}Rn (figure 4.5). Thus, adsorption of radon will lead to an enhancement of degraded alphas over the level expected from lead contaminations in CuSn6 alone.

The lead recoil background also originates from the alpha decay of ^{210}Po , however this decay has to take place on or very near the surface. In subsection 4.1.1 it was pointed out that decays on the surface of the crystal or a surrounding material will lead to recoil events with the full energy of 103 keV. However, decays slightly below the surface of the clamps will result in recoil events with less than the full energy. In [134] two main processes for a contamination of ^{210}Po were identified. Firstly, the direct deposition of ^{210}Po at the end of the electrolytic silver deposition process applied to increase the reflectivity of the clamps. Secondly, the implantation of ^{210}Pb via the adsorption of radon. These two processes can be disentangled via the time distribution of the recoil events. For events with the full energy of

103 keV a decreasing rate was observed, pointing to a direct deposition of ^{210}Po with a half-life of 138 days. For recoil events between 40-90 keV an increasing rate was found which is expected for a contamination induced by radon adsorption: radon and its daughter nuclei will quickly (4 days) decay to ^{210}Pb. The latter, however, has a long half-life of 22 years causing a slow build-up of ^{210}Po.

Time and energy distributions are consistent in the light of the two processes. Since ^{222}Rn undergoes a series of alpha decays, ^{210}Po from this origin is expected to be slightly implanted, in contrast to the direct surface deposition of ^{210}Po at the end of the silver coating process [134].

Three main measures were taken to improve the clamps in terms of radioactive backgrounds for phase 2. First, an even more radiopure material with a thoroughly surveillance of all production steps was used to avoid degraded alphas. Secondly, after fabrication the surface layer was etched and any exposure to radon-contaminated air was avoided - storage in vacuum or nitrogen, assembling of detector modules in de-radonized air. Thirdly, no electrolytically deposited silver was used any more (direct ^{210}Po-deposition), but sputtered aluminum. For phase 2 twelve of the eighteen modules were equipped with these improved clamps relying on passive background reduction. However, also an active strategy was carried out which is described in the following.

The Benefit of Fully-Active Modules

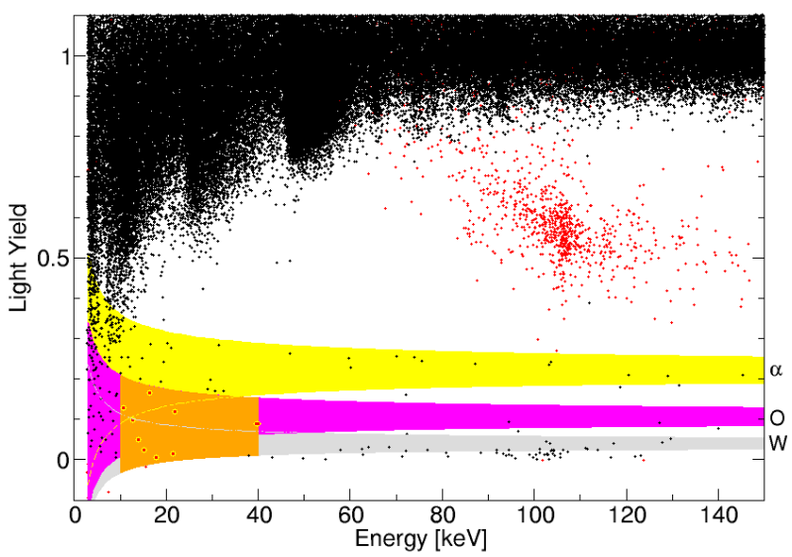

Figure 4.6.: Data from the detector module Rita/Steven (Ch51/52) taken in phase 1 [135]. Marked in red are events originating from ^{210}Po α-decays with the ^{206}Pb recoil hitting the crystal and the alpha hitting a scintillating part of the module housing.

The degraded alpha and in particular the lead recoil backgrounds may leak into the region of interest since the clamp is a non-active material not providing any information about energy depositions therein. Figure 4.6 illustrates the benefit of the foil enclosing the

module not only being reflective but also being scintillating. The population of events in or slightly below the tungsten band (shaded in gray) from the full energy of 103 keV down to the acceptance region (shaded in orange) corresponds to the previously discussed ^{210}Po α-decay with the ^{206}Pb recoil hitting the crystal and the alpha being absorbed in the clamp. If, however, the alpha reaches the scintillating foil, instead of the clamp, additional light is emitted from the foil and recorded by the light detector.

The scintillation process of the foil is faster than the one of $CaWO_4$ which makes a tagging via the faster rise time of the pulse feasible, as was done for the events marked in red in figure 4.6. However, it should be pointed out that the additional light from the foil by itself acts as a fully-efficient veto since it shifts those events to light yields well above the acceptance region.

In conclusion, it is understood that degraded alphas and lead recoil backgrounds can be vetoed completely in a detector module design with only active surfaces in the line-of-sight to the crystal. Active means that the surface either is instrumented, like the light detector, or produces scintillation light. In such a design the alpha will always be detected and the corresponding event can be distinguished from a potential dark matter scattering event.

Since in the conventional design the holding clamps are the only non-active part it suggests itself to cover the clamps with a scintillator. However, the holding has to fulfill several additional requirements. On the one hand,it has to be restrictive enough to prevent the crystal from moving, since this might cause so-called microphonic noise disturbing the measurement. On the other hand $CaWO_4$ does not stand high pressures. A too high force will lead to small (micro-)cracks of the crystal causing a phonon, but no light signal.[3] Such events might mimic a recoil off tungsten, also producing hardly any light. In [134] it was found that plastic materials in contact with the $CaWO_4$ crystal also cause phonon-only events due to spontaneous stress-relaxations in the material.

For phase 2 the CRESST collaboration opted for a twofold strategy. Twelve modules were equipped with the clamps as well-tested holding scheme relying on passive background reduction. Six additional upgraded modules (discussed in the next section) of three new fully-active designs (two modules per design) were installed to utilize the maximum capacity of eighteen modules.[4]

4.3. Upgraded Module Designs

4.3.1. Upgraded Designs Using a Large Carrier Crystal

Figure 4.7 shows two of the three different upgraded detector designs operated in phase 2. They share the use of a large carrier crystal of the diameter of the main crystal. Pulses in the carrier are discriminated from pulses in the target crystal via their faster rise time.

[3] In [136] the authors show that relaxations of mechanical stress can produce light, however the forces applied are well beyond the forces relevant for CRESST and, moreover, the amount of light produced is very small.

[4] The cryostat could house up to 33 modules of this size, however an upgrade of the SQUID system would be needed to operate more than eighteen detector modules.

In the design depicted on the left, the clamps are only attached to the carrier. Potential stress-relaxation phonon-only events originating from the clamps can be discarded in the analysis due to aforementioned pulse shape difference. The clamps are covered with Parylene C which was found to emit twice as much scintillation light at low temperatures as the VM2002 foil used for the surrounding of the module [137].

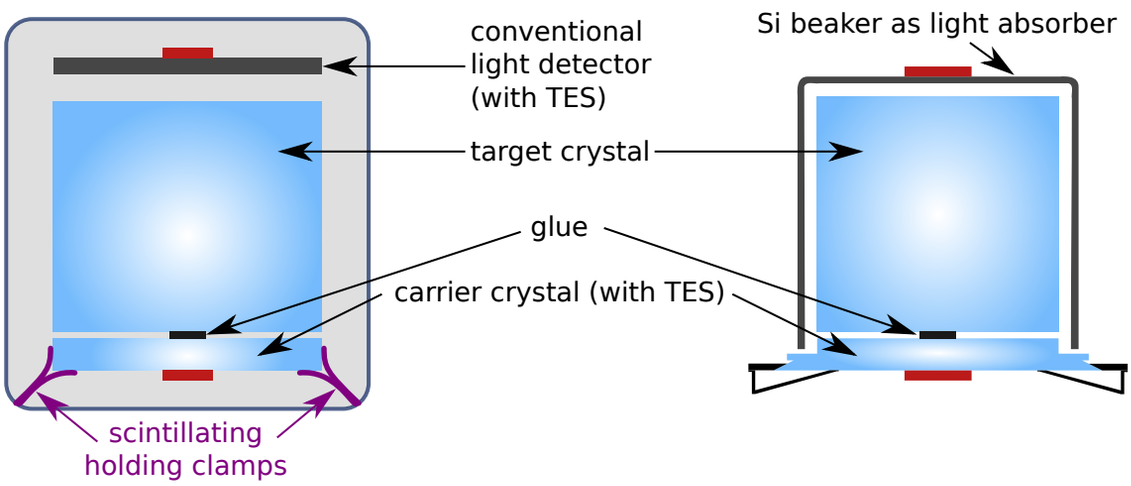

Figure 4.7.: Two upgraded detector designs operated in phase 2 (two modules each). Both designs are fully-active, the left one by a scintillating coating of the clamps, the right one by a beaker-shaped light detector completely surrounding the crystal.

The main innovation of the module shown in the right part of figure 4.7 is a beaker-shaped light detector completely surrounding the target crystal. Since the clamps do not have a line-of-sight to the target crystal non-scintillating clamps are used here. An additional benefit of this design is an enhanced light collection efficiency.

Both designs proved to efficiently veto degraded alphas and lead recoil backgrounds. However, the pulse shape discrimination between carrier and target crystal gets challenging for energy deposits of less than $\sim 5\,\mathrm{keV}$ [138]. Therefore, these modules are not used for the low-threshold analysis presented in this work.

4.3.2. Stick Design

The third upgraded design - shown in figure 4.8 - uses $CaWO_4$-sticks pressed by clamps outside the scintillating housing to hold the target crystal (details may also be found in [139]). Thus, any line-of-sight between the target crystal and any non-active surface is eliminated. To enhance light output the surfaces of the block-shaped target crystal are roughened, except of the contact points of the sticks (see figure 3.6). As was proven in [139] the stick design provides an extremely efficient veto for events induced by the α-decay of ^{210}Po.

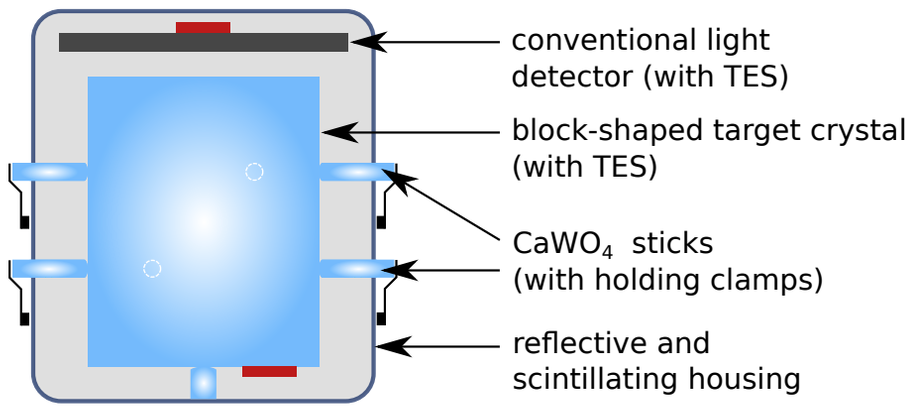

Figure 4.8.: Upgraded detector design (stick design) using $CaWO_4$ sticks pressed to the crystal from clamps outside the scintillating housing. Data from one (TUM40) of the two installed modules is discussed within this work.

4.4. Conclusion

As it was outlined in this chapter, the CRESST-II experiment observed an excess of events above the expected background level in the last measurement campaign (phase 1). To clarify the origin of this excess a lower background level, in particular originating from alpha-decays, was considered mandatory. Two strategies were carried out, firstly a passive reduction by using ultra-pure materials for the holding clamps assembled and mounted into the cryostat in radon-free atmosphere. Secondly, new detector designs actively vetoing those events were installed.

5. Raw Data Processing

The first step of every analysis is the processing of the raw data with the energy calibration being the most important part. This chapter will focus on improvements of the "standard techniques" towards the analysis of small energy depositions (small pulses). However, all relevant steps will be mentioned briefly.

5.1. Detector Modules and Data Sets

This work presents a low-threshold analysis extending the sensitivity of the CRESST dark matter search to light dark matter particle masses. Two detector modules operated in CRESST-II phase 2 are analyzed. The first one is the module TUM40 which is selected, because of its - compared to the other phase 2 modules - superior overall performance in terms of background level, energy resolution and trigger threshold. The module Lise was added, because its trigger threshold is lower than for any other module of phase 2. Table 5.1 summarizes the most important properties of the detector modules TUM40 and Lise.

	TUM40	Lise
Light Detector	Michael	Enrico
Module Design	Stick (subsection 4.3.2)	Conventional (figure 3.2)
TES Fitting	Composite (subsection 3.3.4)	Composite (subsection 3.3.4)
Crystal Material	$CaWO_4$	$CaWO_4$
Crystal Origin	Technische Universität München	Commercial
Crystal Shape	Block-shaped	Cylindrical
Crystal Mass	248 g	306 g

Table 5.1.: Comparison of features of the two detector modules analyzed in this work: TUM40 and Lise.

A blind analysis is carried out by defining a small part of the data set as training data (also referred to as training set). All methods of data preparation (this chapter) and data selection (next chapter) are developed on training data and then applied without any changes (blindly) to the blind data. Figure 5.1 illustrates the partitioning of the data, separately for the two modules. Training data are marked in green, data used for the final dark matter analysis in blue. Data taken in 2013 are used as training data (I) for both detectors. The differences in exposure (see table 5.2 for a detailed breakdown of the exposures of the various data sets) mainly arise from the different masses of the target crystals. All exposure values listed in figure 5.1 and table 5.1 correspond to gross exposures before cuts.

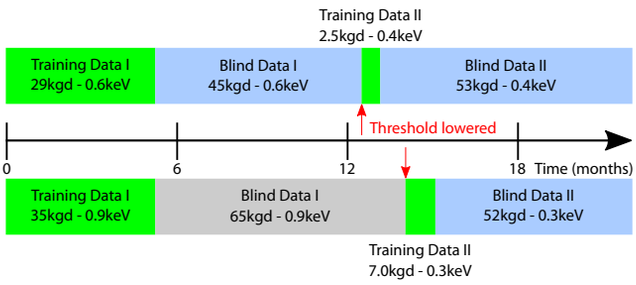

Figure 5.1.: Illustration of the (background) data sets as a function of time for the detectors TUM40 and Lise. For both detectors the thresholds were lowered during phase 2 (red arrows). Training sets are marked in green. The final results for the two detector modules are obtained using the data sets marked in blue.

	Exposure (kgd)	
	TUM40	Lise
Training Data I	29	35
Training Data II	2.5	7.0
$\sum$	32	42
Blind Data I	45	65
Blind Data II	53	**52**
$\sum$	**98**	117
Total $\sum$	130	159

Table 5.2.: Overview on the exposures (before cuts) of the two training and the two data sets for the detector modules TUM40 and Lise. Marked in bold blue are the exposures of the data sets used to derive the final result.

For both detectors the trigger threshold was lowered during phase 2, however at different points in time (red arrows in figure 5.1). Training, as well as blind data, before lowering the threshold is marked with "I", data afterwards with "II".

For TUM40 the threshold was reduced rather moderately from 0.6 keV to 0.4 keV. Thus, a small supplement (training data II) to the main training set (I) is sufficient to adjust the analysis for the new threshold setting. As will be shown later, in the specific case of the detector module TUM40, the benefit of a larger exposure outweighs the benefit from the lower threshold of 0.4 keV. Therefore, the final dark matter results is derived from a combined set of blind data I & II setting an analysis threshold of 0.6 keV for all data.

The threshold for Lise was lowered substantially from 0.9 keV to 0.3 keV, requiring a slightly larger training set II as for TUM40. Since the superior sensitivity for low-mass dark matter particles of the module Lise is driven by the lower threshold setting, only blind data from set II taken with a threshold of 0.3 keV is considered for the final dark matter analysis.

5.2. Event Types

An event consists of two pulses, one from the phonon and one from the light detector. Thus, always both detectors of a module are read out, regardless of which of the two actually triggered. A more detailed description of the structure of the pulses was already given in subsection 3.4.2. In CRESST there are four different types of events tagged by the DAQ:

Control pulses are large pulses injected to the heater needed to measure and stabilize the operating point of the TES. Usually control pulses are injected every few seconds. However, not the complete pulse but only certain parameters which are calculated

on-line by the DAQ are stored to disk.

Test pulses are also injected to the heater, however with smaller and varying amplitudes. Test pulses are used for a precise energy calibration and the measurement of the trigger efficiency. The complete pulse is saved for offline analysis.

Empty baselines are events where the readout was not triggered by the hardware trigger but artificially by the DAQ. They provide a precise measurement of, in particular, possibly time-dependent noise conditions.

Particle pulses are all *real* events causing a hardware trigger, so mostly energy depositions caused by particle interactions.

5.3. Pulse Parameters

In table 5.3 important basic parameters for events and pulses are listed including their determination. These parameters are either directly obtained from the DAQ, or calculated offline with simple algorithms, not including any fit. On the one hand, this allows for a fast processing, on the other hand those parameters often lack the required precision. Therefore, the pulses are further processed with the standard event fit, as will be discussed in the following section.

5.4. Standard Event Fit

The so-called standard event fit or template fit is the by far most important tool to precisely analyze the pulses recorded. It provides information on the pulse amplitude which directly depends on to the deposited energy. Furthermore, it reveals deviations from the nominal pulse shape which is e.g. used to classify events in the TES carrier (3.3.4). Finally, the standard event fit proved to yield the most precise time information on the onset of a pulse [125], which is beneficial to find coincidences between different detectors and/or the muon veto.

5.4.1. Creating the Standard Events

Obviously, the first step of a template fit is the creation of the template which is done by averaging over a large number of pulses of the same deposited energy. Via the averaging the statistically distributed noise is canceled out and a noise-free description of the pulse shape remains. It is important to only sum pulses of the same energy, to be unaffected by the so-called trigger walk. Trigger walk refers to the dependence of the trigger time on the pulse height. Since small pulses rise slower than large pulses, more time elapses between the onset of a small pulse and the trigger time. Thus, small pulses are found earlier in the record (see figure 3.10 for an illustration).

The operating point is set to a regime in the phase transition (see figure 3.4) where the electrical resistance is in good approximation a linear function of the temperature. In this

Parameter Name	Type	Description
Time since Start (h/d)	E	The elapsed time since the beginning of the data set.
Live Time (h/d)		The effective live time during which the detector was in operation.
Test Pulse Amplitude (V)		The injected amplitude of test pulses (not relevant for particle pulses) which is directly proportional to the injected energy (see subsection 3.4.1).
Pulse Height (V)	P	The pulse height is determined using a moving average over 50 channels. It is the difference between the highest obtained value in the record and the baseline level.
Peak Position (ms)		The position in the record with the maximum signal (pulse height).
Pulse Onset (ms)		The pulse onset is determined by going from the peak position backwards in time and finding the time, when the pulse started to rise above the baseline noise. Again an average over 50 channels is used.
Right - Left Baseline (V)		The average of the last 50 channels in the record minus the average of the first 50 channels in the record are saved as the "Right - Left Baseline" parameter.
Trigger Delay (ms)		Each detector of a module can trigger a readout. The first detector, which triggers in a digitizer module, has zero trigger delay. If the signal height in further detectors on the same digitizer module rises above trigger threshold the elapsed time is stored as "Trigger Delay".

Table 5.3.: Main pulse (P) and event (E) parameters (extended and modified from [125]).

so-called linear region the amplitude of a pulse is directly proportional to the deposited energy. As for large energy depositions this linear relation no longer holds, it is crucial to build the template from pulses in the linear range. Since the region of linearity depends on the individual transition curve it has to be determined separately for each detector.

Usually, standard events for particle events are created from the 122 keV γ-line of a ^{57}Co -calibration source. However, for some detectors this energy is already in the non-linear region. Since an external γ-source of lower energy cannot penetrate the shielding, intrinsic (inside the crystal) γ-lines may be used instead.

To achieve templates precisely describing the shape of signal events, the set of pulses has to be cleaned thoroughly, e.g. pile-up events have to be removed. Since already a few ten events are sufficient for a template of appropriate quality [140] one can afford to apply rather strict selection criteria. Analog to the particle pulses, templates are also created for the test pulses.

5.4.2. Basic Working Principle of the Standard Event Fit

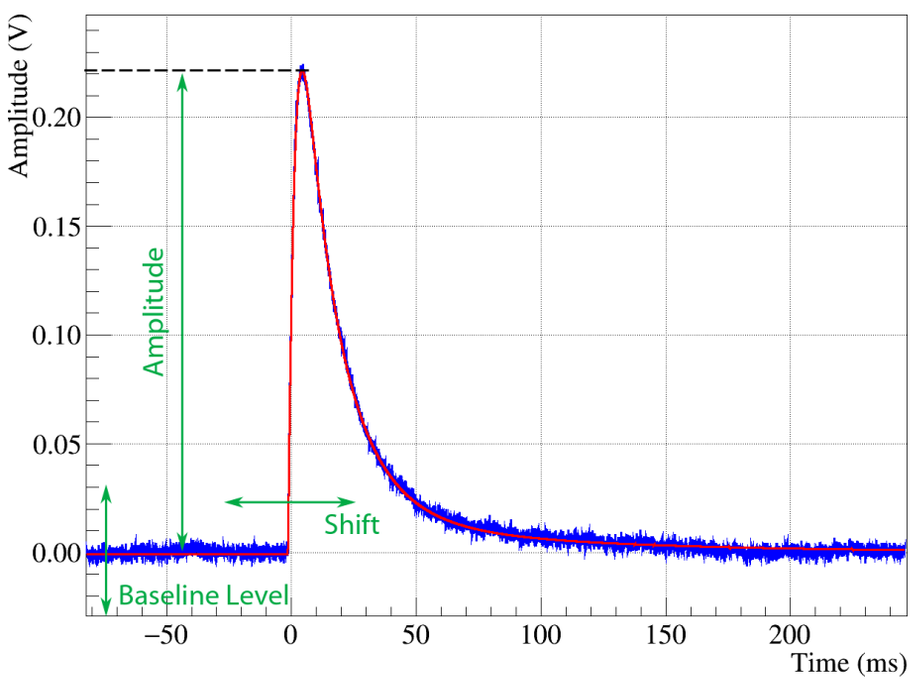

Figure 5.2.: Working principle of the standard template fit. The template (red) is adjusted in amplitude, baseline level and shift (green arrows) to match the recorded pulse (blue).

The basic working principle of the standard event fit is to match the template to the actual pulse by scaling the height (amplitude), aligning the baseline level and shifting the template in time. The green arrows in figure 5.2 illustrate these adjustments to fit the template (red) to the pulse (blue). The three most important parameters determined by the fit are:

Amplitude (V) Amplitude of the pulse (corresponding to upper green arrow) [1]

[1] For large energy depositions, the linear relation between the height of a pulse and deposited energy no

Shift (ms) The shift of the template in time (corresponding to horizontal green arrow)

RMS (V) The Root-Mean-Square of the fit is a measure of the deviation of the template from the pulse.

5.4.3. The Baseline Model

The standard event fit also accounts for the shape of the baseline. In the past mainly two different models with very similar performance were used. A linear function only (used in[71, 125]), or an exponential decay (used in[72]). For the latter the decay time is fixed to the thermal component of the pulse and is, therefore, capable to describe a decaying baseline of a previous large energy deposition in the detector [2].

Detector	Baseline Model	Resolution σ(eV)	$\sigma_x/\sigma_{\text{cubic}}$
TUM40	Constant	-	-
	Linear	112.6 ± 0.5	1.2
	Quadratic	108.5 ± 0.5	1.2
	Cubic	89.2 ± 0.4	1.0
	Exponential*	224.3 ± 1.0	2.4
	Expo. + Quad.*	92.0 ± 0.3	1.0
Lise	Constant	179.5 ± 1.1	2.6
	Linear	84.4 ± 0.4	1.2
	Quadratic	80.9 ± 0.4	1.2
	Cubic	66.0 ± 0.3	1.0
	Exponential*	193.6 ± 0.9	2.8
	Expo. + Quad.*	67.7 ± 0.3	1.0

Table 5.4.: Comparison of the resolution obtained for the 1 keV test pulse using different models for the baseline. Linear, Quadratic and Cubic denote polynomials of degrees 1,2 and 3. The last column corresponds to the fraction of the resolution of the respective column to the value obtained with a cubic baseline model. The cubic baseline model provides the best resolution and, thus, is used in the analysis. The values marked with "$*$" are obtained with a different analysis software, but on the same data set [141]. Using a constant baseline model the fit in many cases does not find the correct pulse. Thus, no value can be given for TUM40. The value given for Lise might be rather regarded as a lower limit for the resolution with a constant baseline.

longer holds. This effect is taken into account by the so-called *truncated fit* (see, among others [71, 125]) linearizing the amplitude. Consequently, then the one-to-one relation between the height of a pulse and the value determined for the amplitude (as illustrated in figure 5.2) is not longer fulfilled. However, for the small pulses analyzed in this work truncated fits are irrelevant.

[2] Technical remark: By fixing the decay time the fit stays linear in its parameters which substantial reduces computation time compared to a non-linear fit.

Within the framework of this work it is observed that baseline fluctuations, mainly caused by mechanical vibrations of the cryogenic facility, are well approximated by a polynomial of third order. In table 5.4 the resolutions of the test pulse equivalent to 1 keV (see section 5.5 for the discussion of the energy calibration) obtained from the same data using the same templates, but different models for the baseline are listed. The 1 keV test pulse is chosen, as it is in the spot light of the energies of interest for the dark matter search.

For a constant baseline the standard event fit does not find the correct shift value (see next subsection) for a large fraction of pulses, in particular for disturbed baselines. Therefore, the value listed for Lise may be regarded as a lower limit for the resolution, which may be achieved with a constant baseline. For Lise the correct shift value is found for only 80 % of the pulses. For TUM40 the situation is even worse, thus no reasonable value can be given.

However, even the previously common linear model for the baseline is found to be at least 20 % inferior to the cubic baseline model used in this work. The energy resolution is a key performance parameter of a dark matter detector, not only in case of the observation of a signal but also to identify backgrounds. Thus, any improvement of the resolution will translate directly into an enhanced sensitivity for the dark matter search.

5.4.4. Determining the Correct Shift in the Correlated Fit

The correct shift of the template is determined by minimizing the RMS value which qualifies the deviation between fitted template and recorded pulse. The smaller a pulse is, the more the RMS is dominated by the noise and the less pronounced its dependence on the shift will be. Since phonon and light signal of a detector module do have a constant and known time relation both templates are always shifted together. This procedure is referred to as *correlated fit*.

RMS Minimization

For an event with pulses in light and phonon detector the minimization of the sum of the RMS of phonon and light detector provides the most precise determination of the correct shift value. However, for example for a low energy nuclear recoil event there will hardly be any light signal and the phonon signal carries all necessary information to find the correct shift. In this work it is found that in such a situation it is beneficial to determine the shift value based on the RMS of the phonon detector only. Basically, the noise of the light signal washes out the minimum of the sum of the RMS values as a function of the shift which complicates its determination.

For direct hits of the light detector the situation is just opposite to a nuclear recoil event, namely a signal in the light detector and a very small or no signal in the phonon detector. On the one hand, such so-called light-only events are not relevant for the dark matter analysis, on the other hand they provide useful information on the light detector performance, in particular for light detectors equipped with a very weak ^{55}Fe-source allowing for an absolute energy calibration.

Since the hardware triggers were adjusted to account for the individual performance of each detector the hardware triggers provide firm information on the absence or presence

of a pulse in the respective channel. Thus, in this work the sum of the RMS was input for the minimum finding only if both, phonon and light detector, triggered. If not, only the detector triggering was used.

Start Value

The second challenge to find the correct shift value is the fact that the correct minimum is not necessarily a global minimum for all allowed shift values. For small pulses, in particular, it might only be a local minimum. This fact is illustrated on the example of the pulse depicted in figure 5.3. This pulse was recorded with the phonon detector TUM40, exhibiting a small but clearly visible pulse slightly shifted left in time ($t = -2.8\,\text{ms}$). In figure 5.4 the RMS of the standard event fit of this pulse is shown in blue as a function of the shift. The minimum possible shift is one channel, corresponding to a time of 40 μs for the data shown here. For the example pulse given here a pronounced local minimum is found around the correct shift value of $t = -2.8\,\text{ms} \equiv -70$ channels, however, another local minimum with even lower RMS is present at a time of $t \simeq 1000$ channels. For shift values larger than $t \simeq 1700$ channels the RMS is constantly below the local minimum corresponding to the correct shift value at $t = -2.8\,\text{ms}$.

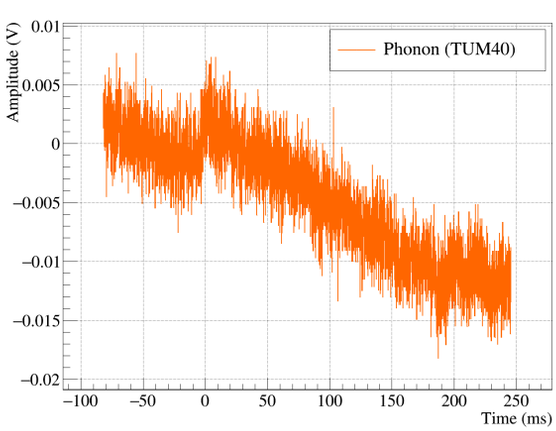

Figure 5.3.: Sample pulse from the phonon detector TUM40.

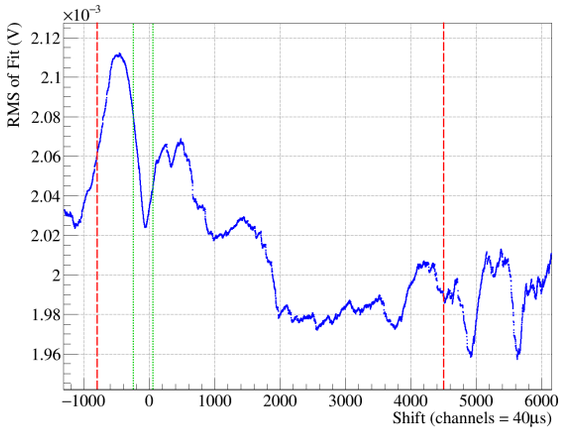

Figure 5.4.: RMS (of the standard event fit of the pulse shown on the left) as a function of the shift in channels. One channel corresponds to a time of 40 μs. The red dashed lines indicate the interval allowed for the choice of the start value. The minimum search is performed within the green dotted lines (search range).

In addition, it is unfeasible to always try all possible shift values, since this is computationally too time-consuming. Based on these two arguments, the following strategy is carried out here: Find a suitable start value and allow a minimum search only in the vicinity of the start value - in the so-called search range.

Mainly two parameters have the potential to provide a suitable start value, namely the hardware trigger time and the peak position relative to the peak position of the standard template (both determined using a 50 channel moving average). Since both parameters are recorded for the phonon and the light detector four potential start values are available for an event.

A coincidence between trigger time and relative peak position is a very good indication for a correct start value in the light of the low probability of random coincidences. In this analysis two times are considered coincident if they differ by less than half the search range.

For this work a search range of $-10\,\text{ms} \leq t_S \leq 2\,\text{ms}$ is used. An asymmetric interval accounts for the fact that small pulses will be found earlier in the record compared to the standard template due to the aforementioned effect of the trigger walk.

In figure 5.5 a scheme of the various coincidence checks and their impact on the final choice of the start values is drawn. First the coincidence check is performed for the phonon and the light detector. If passed for both detectors it is checked whether the relative peak positions of the two detectors match and in case they do their average is used as a start value. Thus, in this situation, which is the case for the vast majority of events, only one start value for the minimum search remains. This leads to a minimization of the computation time needed - absolutely crucial since the standard event fit is the by far most computation time consuming step of the raw data analysis.

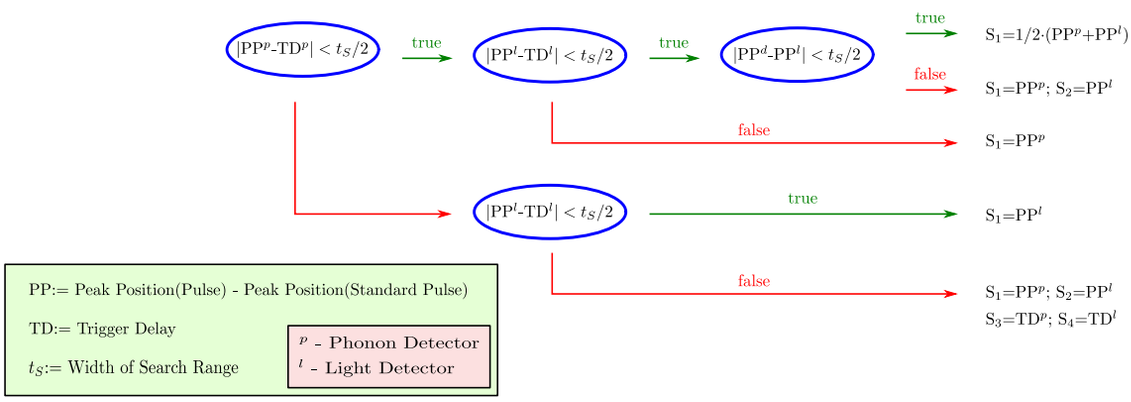

Figure 5.5.: Scheme illustrating the new algorithm to chose the start value for the standard event fit out of the four possible values: shift of the peak position with respect to the standard pulse (PP) and the trigger delay (set by the hardware trigger) both available for the phonon (^{p}) and the light detector (^{l}). Blue bubbles correspond to a check whether two times are found within a certain allowed time range ($1/2 \cdot t_S$ was used in this work). As a result one, two or all four times are considered as start values.

If trigger time and relative peak position do not match for the phonon detector the check is repeated for the light detector. If also this check fails then all four possible start values (trigger and peak position for phonon and light detector) are used and the one with the lowest RMS (or sum of RMS as outlined in the last paragraph) is chosen.

For pulses very early or very late in the record the template fit may result in an imprecise determination of the relevant parameters. Thus start values are only allowed to be 20 ms

before and 180 ms after the trigger time (dashed red lines in figure 5.4). In case no suitable start value is available, the corresponding event is discarded.

5.4.5. Conclusion and Performance Estimate

Quantifying the success rate of the standard event fit to find the correct shift value is subject to many unknowns, however a rough estimate shall be given here using test pulses with an equivalent energy of 1 keV.

For each test pulse the time between the firing of the test pulse by the DAQ and the time of the trigger is saved. The conformity of the time when the pulse was injected with the time when the trigger fired is a firm information that the trigger actually reacted on the pulse sent (and not on any other randomly coincident pulse). Thus, by rejecting all test pulses with an abnormal time difference between sending and triggering results in a set of test pulses where the true time of the pulse is known via the trigger delay parameter.

For test pulses (complete phase 2 data set) selected with the procedure outlined above the correct shift value is found in 98.2 % of the cases for Lise. For TUM40 a slightly lower value of 94.4 % is obtained. However, the standard event fit is more likely to fail for pulses suffering from artifacts, like pile-up or strongly tilted baselines, which are anyhow removed from the dark matter analysis (see chapter 6). Thus, the values given here only serve as a rough estimate of the lower limit for the success rate. The difference between TUM40 and Lise is a manifestation of the increased signal height of Lise compared to TUM40 for the same energy deposition.

In summary it was found that the developments introduced in this work provide a reliable fit, even for very small pulse amplitudes. As the energy is derived from the fitted amplitude, this is a key requirement for the success of a low-threshold analysis.

5.5. Energy Calibration

The first information needed for the energy calibration is the response of the detectors to particle interactions of precisely known type and energy. Usually we use 122 keV γ-rays from a ^{57}Co-source. Two calibrations with ^{57}Co were carried out during phase 2, once at the beginning and once at the end of the run. ^{57}Co decays to ^{57}Fe via an electron capture mainly emitting gammas with energies of 122.06 keV and 136.47 keV (Errors are negligible, values taken from [142] accessed via [143]). In [140] a detailed discussion of the induced Compton background and visible escape peaks may be found.

To quantify the response of the detector we use the amplitude determined by the standard event fit. The amplitude of pulses induced by 122 keV gamma-rays provides the relation between energy deposition and resulting amplitude at 122 keV and for a specific particle. To measure this relation over the whole energy range of interest we inject test pulses with several discrete energies to the heater. Additionally, the test pulses allow to correct for small time-dependent drifts of the detector response.

The amount of scintillation light reaching the light detector not only depends on the type of particle, but also on the crystal (e.g. on the scintillation efficiency) and on the geometry

of the module. Since those factors are a-priori unknown a determination of the total energy deposited in the light detector is impossible with information from a ^{57}Co-calibration. For this reason some light detectors are equipped with an ^{55}Fe-source directly illuminating the light absorber with X-rays of roughly 6 keV. Any improvement of the light signal enhances the discrimination power between the dominant e^-/γ-background and the sought-for nuclear recoils. Thus, the total amount of light reaching the light detector is a crucial aspect for detector development and optimization. However, for the final dark matter analysis only the relative light output of different event types is relevant and, therefore, the reader is referred to [114, 126] for a more detailed analysis of the light channel.

5.5.1. Calibration of Test Pulses

To make use of the test pulses injected to the heater, the relation between injected signal and equivalent energy has to be known. Each heater is equipped with an attenuator. Usually it is adjusted such that an injection of a signal with 1 V results in a pulse in the detector of the same amplitude as a 200 keV γ-particle energy deposition. In section 3.4 it was already pointed out that the injected signal (also referred to as test pulse amplitude) is directly proportional to the injected energy. Thus, a single number, the so-called CPE (convert pulse height to energy) factor quantifies the aforementioned relation.

	CPE Factor (keV/V)
TUM40	203.81
Michael	201.79
Lise	189.69
Enrico	200.26

Table 5.5.: CPE factors for the detectors analyzed in this work.

As the test pulses are fired with the same test pulse amplitude to all detectors a common CPE factor of roughly 200 keV/V is needed to probe the same energy range in all detectors. Obviously, the exact value of the CPE factor has to be known for a precise energy calibration. This is achieved by comparing the average amplitude of test pulses to the average amplitude induced by well known energy depositions, usually the 122 keV gammas from the ^{57}Co-source. Technically this is done by first determining the mean amplitude of the 122 keV peak and of the two - in terms of amplitude - neighbouring test pulses. A linear interpolation between the two test pulses then yields the CPE factor.

5.5.2. Spline Fit - Basic Working Principle

In phase 2 we inject one test pulse every 30 s. In total, up to 15 different amplitudes are injected which corresponds to roughly seven minutes for a complete cycle. A spline fit is used to get an analytic description of the response of the detector, for a specific energy and at any time.

Figure 5.6 shows the fitted amplitude of test pulses (black data points) of TUM40 as a function of the complete measurement time. We inject test pulses with equivalent energies up to 2 MeV, however, the distribution of the test pulses concentrates on the low energies of interest. The highest test pulse depicted in figure 5.6 corresponds to an energy of 102 keV. The fitted splines are show as blue lines. As the mild time-dependent drifts of TUM40 appearing between the refills can hardly be seen in figure 5.6 a zoom-in is depicted in figure 5.7. The lower half shows the lowest test pulses relevant for the energy calibration (equivalent to $\sim$1 keV) for the first two weeks of measurement after the start of their injection. In the upper half the test pulses with the strongest time dependence and a corresponding energy of $\sim$60 keV are shown for the same time period.

The working principle of a (smoothing) spline fit [144] is to perform piece-wise polynomial fits which are continuously connected to each other. They are commonly used in cases of (noisy) measurement data with no or unknown underlying model and not sufficiently approximated by a single polynomial. The smoothness of the fit is set by the smoothing factor ranging from zero to one. The higher this factor the higher the squared deviations of the data points to the spline (residuals) are allowed to be. Thus, a value of one corresponds to no smoothing - to a linear function. For a smoothing factor of zero the residuals have to be zero as well and, thus, the spline will go through every data point. In this limit a spline fit is equivalent to a spline interpolation.

For two reasons a new spline is created whenever a gap larger than one hour appears in the data, which is always the case for the refills of the cryostat, usually done three times a week. The first reason is the aforementioned downward drift of the detector response between the refills (see figure 5.7). Combining the data before and after refill would, thus, results in a non-continuous step, which cannot be approximated by the spline in a satisfying manner. Secondly, smoothing spline fits are known to suffer from numerical instabilities for a too high number of data points.

However, following this strategy produces a huge number of splines ($\sim$200,000 for the whole phase 2 data set and all detectors), rendering an automatic and reliable handling mandatory.

The removal of outliers, as for example caused by pile-up events, is of utmost importance as already a single outlier might have a large impact, as was shown in [125]. To automatically remove outliers an iterative approach is carried out. The first step is to find the data point with the largest residual. If this residual exceeds the average residual by a certain factor (typically between four and five) the respective data point is removed and the spline is fit again. There are two stop conditions for this iteration; either no residual is found above the limit any more or a maximal allowed fraction of points is removed (20 % is chosen for all detectors). Details may be found in [125].

Automatic Determination of the Optimal Smoothing Factor

Within this thesis a further improvement was implemented in cooperation with [145], namely an automatic determination of the smoothing factor. The smoothing factor cannot be a free parameter in the spline fit as a smaller smoothing factor always yields smaller residuals and, thus, mimics an improvement of the fit result. The analog observation that

Detector	Peak	Adaptive σ(eV)	Constant σ(eV)
Lise	^{55}Fe double-peak: (5.9&6.5) keV	99.3±0.6	99.2±0.6
TUM40	^{179}Hf K-Shell: 65 keV	378±10	379±10
TUM40	^{179}Hf M-Shell: 2.6 keV	94±7	95±7

Table 5.6.: Width of certain lines seen in Lise and TUM40 using the automatic algorithm to find the optimum smoothing factor in comparison to a constant factor of 0.98. The uncertainties correspond to statistical fit errors.

the residuals of any (polynomial) fit decrease with an increasing number of free parameters (an increasing order of the polynomial) is often referred to as *overfitting*.

An elegant and powerful solution to automatically set the smoothing factor is to split the data set into a training and a control set which is also commonly used in the framework of machine learning algorithms (like e.g. artificial neuronal networks). In an iterative process the training set is fit with a spline of varying smoothing. At the beginning a rather small smoothing factor (a high smoothing) is chosen. Thus, the fit provides a spline well adapted to the distribution in the training set but badly describing the distribution in the control set. The optimum smoothing factor is then found by minimizing the sum of the residuals of the control data points to the spline determined by the fit of the training set. To avoid any possible periodic effects the points are assigned randomly to the two data sets. Within this thesis the best performance is given by training and control sets of roughly equal size (a 50:50 chance for each data point to be in one or the other set).

The blue numbers in figure 5.7 correspond to the values determined for the smoothing factor for the respective spline. As one can see the lower test pulses hardly show any time dependence and, thus, smoothing factors close or equal to one provide an appropriate description. For the higher test pulses smaller factors are determined. As expected, the smoothing factor gets smaller the larger the deviations from a linear behavior (smoothing = 1) are. Comparing these two different test pulse amplitudes further stresses the benefit of an automatic method to determine the optimal smoothing factor, as the time-dependencies largely differ for different test pulse amplitudes. However, even within one amplitude differences may be observed.

Figure 5.7 clearly illustrates that an adaptive smoothing factor provides an improved approximation of the time dependency of the detector response. However, for Lise and TUM40 hardly any improvement is found for the final energy resolution compared to a spline fit using an appropriate constant smoothing factor. In table 5.6 the width of several lines present in Lise and TUM40 are listed, with and without the automatic smoothing. For the lines tested all widths agree within errors. Nonetheless, there are good reasons to consider the automatic smoothing an improvement. Firstly, larger impacts are expected for detectors were the time-dependence of the detector response is more curved and, thus, not well approximated by a linear function. Secondly, the smoothing factor is chosen in a completely objective way, independent of the analyst and the data set.

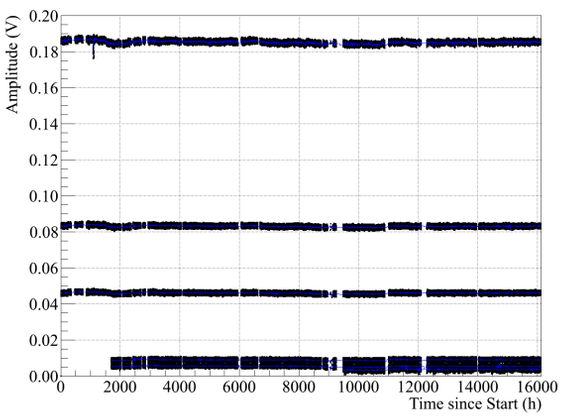

Figure 5.6.: Fitted amplitude of test pulses injected to the heater of TUM40 as a function of time (black data points). During the data taking additional pulses were added to increase the precision at low energies (at 1700 h and 9500 h). The spline fits providing a continuous description of the detector response are draw in blue.

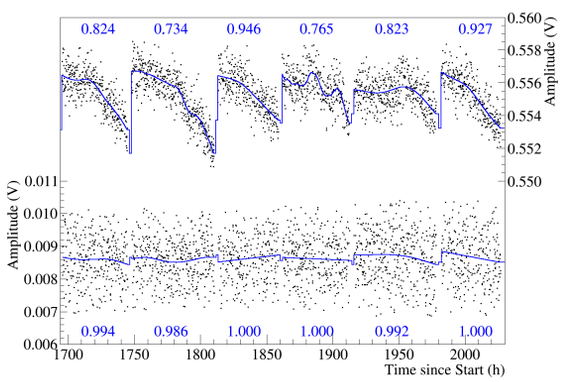

Figure 5.7.: Zoom of the left figure 5.6, for two weeks of measurement time and test pulses with corresponding energies of ∼1 keV (bottom) and ∼60 keV (top). The data points are the fitted amplitudes of the test pulses recorded in the detector, the blue lines depict the outcome of the spline fit. In blue numbers the smoothing factor, as determined by the automatic smoothing, is given for each spline. The gaps in the data and the sharp edges in the spline correspond to the refilling of the cryostat, where no data are taken.

5.5.3. Combining all Information

To get the final electron-equivalent energies $E_{p/l}$ for each pulse a combination of the following information is needed:

- Amplitude for each particle and test pulse derived by a correlated fit with the respective templates (section 5.4)
- Response function to convert amplitude to energy:
  - Amplitude of pulses induced by a well-known energy deposition (usually γ-lines)
  - Description of time-dependence via sectional spline fits (subsection 5.5.2)
  - Interpolation between the response of discrete test pulse energies using a polynomial fit

The procedure of combining all information is outlined for a single event of TUM40 in figure 5.8. The green line thereby marks the response function describing the relation between measured amplitude (x-axis) and energy (right y-axis). The green line is given by a polynomial fit (of order five in this case) interpolating between the blue points. The latter correspond to the values obtained by the spline fits of the discrete injected test pulse energies (left x-axis) at the time of the event (see figure 5.6). Via the ^{57}Co-calibration the relation between injected voltage and corresponding energy (left to right y-axis) is determined to be 203.81 keV/V for TUM40. For the example event given here, the amplitude determined by the fit is 3.35 V. Using the response function one obtains the corresponding energy of 378.3 keV.

As one can see, the response function of TUM40 is well described by a linear function at the time of the example. The linearity (or better to say the deviations thereof) relates to the linearity of phase transition of the TES used and, thus, is an individual feature of every TES, of every detector. To maintain flexibility to account for small deviations from the ideal linear relation, in particular in the low-energy regime, a polynomial of fifth order[3] is used for the fit.

After the completion of the procedure outlined above the energies $E_{p/l}$ are assigned to every pulse, except for the very few pulses were the standard event fit does not converge. However, convergence problems are rare for a reasonably chosen baseline model (see subsection 5.4.3) and are mostly resulting from artifacts strongly distorting the nominal pulse shape.

5.6. Light Yield and Event-Type Independent Total Deposited Energy

As already briefly mentioned in section 3.3 we define the (dimensionless quantity) light yield LY as the ratio of E_l to E_p:

[3] Thereby, the y-intercept is fixed to zero, as zero energy injection corresponds to zero amplitude

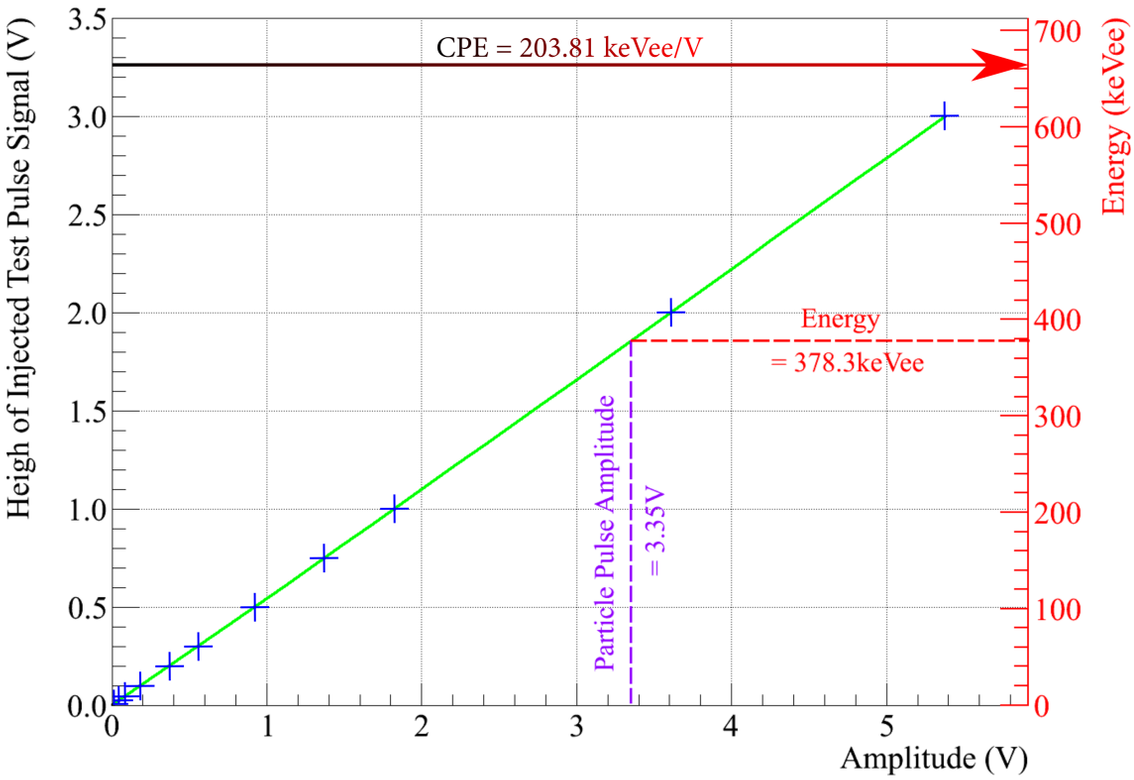

Figure 5.8.: Response function (green) of the detector TUM40 to convert the measured amplitude (x-axis) to energy (right y-axis). The blue points correspond to the splines evaluated at the time of the particle event. The splines describe the time-dependent response of the detector to test pulses injected with discrete energies (right y-axis). The relation between injected signal and corresponding energy is quantified by the CPE factor, determined in a γ-calibration. The idea of the plot follows [71].

$$LY = \frac{E_l}{E_p} \tag{5.1}$$

Since the energy scale is set by the CPE factor which is in turn set by 122 keV γ-rays inducing an electron recoil, $E_{p/l}$ denote an *electron equivalent* energy. Consequently, the light yield of electron recoil events depositing 122 keV get (in average) assigned a light yield of one. The difference between absolute and electron-equivalent energy is in particular relevant for the light detector, as even for electron recoils only 1-2 % of the energy deposited in the crystal is measured in the light detector.

In a cryogenic detector the phonon signal provides a direct measurement of the deposited energy. Thus, the phonon channels is often referred to as *unquenched channel* to set it apart from other channels like scintillation or ionization. In the case of a quenched channel the energy reconstruction relies on model assumptions (see section 2.4), which often are challenging to validate at low energies. The advantage of cryogenic detectors to derive the deposited energy directly from an unquenched channel makes them leading the field in the low dark matter particle mass regime.

Thus, for a CRESST detector the total deposited energy is directly measured in the phonon channel, except of the small fraction emitted as scintillation light (and not reabsorbed by the crystal). For any event where the fraction of the deposited energy emitted as scintillation light is equivalent to the fraction of the 122 keV γ-rays used for calibration - which is the case for every event with a light yield of one - E_p is equivalent to the total deposited energy E. For an event producing more, or in particular less light, E_p will be a slight under or overestimation of E. In simple words: The calibration via the CPE factor implicitly assumes that a certain fraction of the deposited energy is emitted as scintillation light. For an event with less light emitted as scintillation light ($LY < 1$) more energy remains in the crystal and, thus, a slightly too large value will be assigned to E_p. However, as we measure both - the energy remaining in the crystal and the energy emitted as scintillation light - we can correct for this effect with the following relation:

$$E = \eta E_l + (1 - \eta)E_p = [1 - \eta(1 - LY)]E_p \tag{5.2}$$

The scintillation efficiency η quantifies the fraction of energy going into light production. It depends on the crystal with typical values ranging around 6-7 % (for $CaWO_4$).

Additional Remark From the 6-7 % of the deposited energy emitted as scintillation light (for an electron recoil) only about one third is measured in the light detector of a conventional CRESST-II detector module. To derive this information some light detectors in phase 1 and 2 were equipped with ^{55}Fe-sources directly illuminating the light detectors and, thus, enabling an absolute calibration of the light detector (as opposed to an electron-equivalent energy scale). In phase 2, two module designs with a cylindrical $CaWO_4$ target crystal surrounded by a beaker-shaped light detector were installed (see 4.3.1). These light detectors measure roughly twice as much light as standard light detectors, indicating a loss of a substantial fraction of the light produced in the conventional module housing: the light is emitted by the crystal, but never reaches the light detector.

5.6.1. Application for TUM40

To apply equation 5.2 the scintillation efficiency η has to be known. For TUM40 it is possible to derive η by the tilt of intrinsic γ-lines in the energy light yield plane [4]. The tilt arises from statistical (Poissonian) fluctuations in the amount of produced scintillation light. A value of $\eta = 0.066 \pm 0.004$ (statistical uncertainty) is determined by a fit of several γ-lines in the energy region below 100 keV. Figure 5.9a shows the light yield as a function of the uncorrected energy E_p for the data taken with TUM40 in phase 2. The three blue lines correspond to the tilt expected for $\eta = 6.6$ % for three γ-lines with literature values of 11.271 keV, 46.54 keV and 65.35 keV. As one can see expectation and observation are in very good agreement.

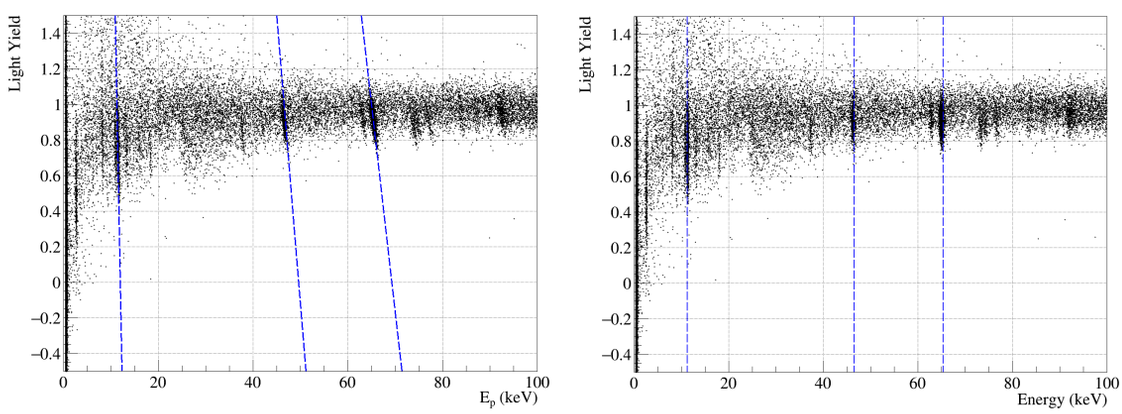

(a) before correction (b) after correction

Figure 5.9.: Data acquired in phase 2 for the detector TUM40 in the light yield-energy plane, before and after the correction (with equation 5.2). The blue lines before the correction (left) correspond to the tilt expected at the given energy for $\eta = 0.066$. Vertical blue lines at the respective energies are drawn for the right plot to illustrate the success of the correction.

The result of applying the correction given in equation 5.2 converting E_p to the total deposited energy (E) is shown in figure 5.9b. Now, the γ-lines are oriented vertically. It should be noted that the scintillation efficiency η can also be derived using different in-situ methods, for example from the offset of the energies of intrinsic α-decays to literature values. However, α-decays typically range in the MeV-regime, while the low-energy gamma lines allow to determine η at the energy of interest. Nonetheless, for TUM40 both methods yield consistent results.

The tilt of the γ-lines leads to a broadening of the respective peaks in the E_p coordinate, which is intuitively clear when thinking of the energy spectrum as a projection of the data in the light yield-energy plane on the energy-axis. For a γ-line with a mean light yield

[4] For technical reasons the fit can be more reliably performed swapping energy and light yield coordinate, compared to the usual light yield - energy plane.

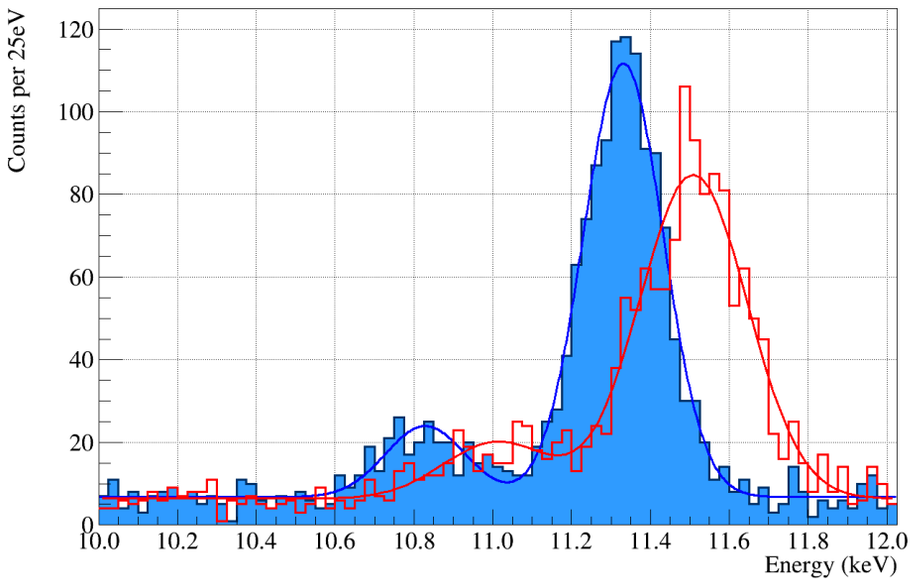

Figure 5.10.: Energy spectra for the electron-equivalent energy E_p (red) and the total deposited energy (blue) for the detector TUM40 in phase 2. The lines correspond to a fit of the double peak using two Gaussian functions plus a constant background level.

	$E_{\text{lit.}}$ (keV)	E_p (keV)	E (keV)
^{179}Hf L1	10.74	11.010±0.020	10.828±0.013
^{179}Hf L2	11.271	11.509±0.005	11.331±0.004
σ	-	0.136±0.005	0.101±0.003

Table 5.7.: Mean values for ^{179}Hf L1 and L2 peaks determined before (E_p) and after (E) application of equation 5.2 in comparison to literature values $E_{\text{lit.}}$ [143]. The last row lists the width of the Gaussian functions for both cases.

different from one[5] the peak will not only be broadened, but its mean energy (in E_p) will also be wrong. This becomes clear considering that events with a light yield of one are not affected by the correction, since the pivot point of the blue lines in figure 5.9b is at a light yield of one.

To illustrate both effects a histogram of the ^{179}Hf double peak (origin will be discussed in section 6.10) is shown in figure 5.10. Red thereby corresponds to the histogram before the correction (E_p) and blue afterwards. Both histograms are fit with two Gaussian functions on top of a constant background level (see equation 6.2 for the complete fit function). The resulting fit values, as well as literature values are given in table 5.7.

With these superimposed histograms the two effects become evident. The unconverted histogram (red) is broader with the smaller peak (L2) being hardly visible. Additionally, it has a significant offset to the literature value of 11.271 keV, a consequence of the mean

[5] Mainly caused by the so-called non-proportionality effect describing a decreased light output at low energy [146].

light yield of this line being at roughly ~ 0.75. Applying the conversion results in an improvement of 26 % in resolution for this double peak.

Despite the success of this correction when applied for the detector TUM40, no conversion is applied for the detector Lise. The light detector Enrico of the module Lise does not meet the performance of the light detector Michael, which is used in TUM40. As a consequence of this modest performance the light signal for low-energy events is completely dominated by baseline noise and, therefore, not a good measure for the amount of the deposited energy emitted as scintillation light. However, the impact on the final dark matter result is proven to be negligible for the detector Lise.

For this work the following convention is used: energies denoted E or "Energy" refer to total event-type independent energies after applying the conversion of equation 5.2. Not converted phonon energies will be denoted E_p.

5.7. Trigger Efficiencies

Obviously, a precise knowledge of the trigger threshold is mandatory for a low-threshold analysis. The trigger thresholds of the detectors are measured by injecting a sequence of test pulses, closely spaced in energy. For each injected energy the trigger efficiency is then given by the fraction of pulses triggering to the number of pulses sent to the heater.

In figure 5.11 two measurements are depicted per detector, once before the reduction of the threshold (Setting I) and once after the threshold was lowered (Setting II). The blue data points correspond to the fraction of test pulses triggering for the respective injected energy. Apart from the low-energy pulses also test pulses with the maximum possible energy ($\sim$2 MeV) were injected. As such pulses will never be missed by the trigger they serve as a reference for the number of test pulses injected.

For a certain injected test pulse the measurement can be regarded as a Bernoulli experiment with outcomes one (pulse triggered) and zero (pulse did not trigger) with N trials (N injected test pulses). Assuming that the true probability for a certain injected energy to fire the trigger (p) was known, the probability to observe a fraction of i/N triggers in the measurement is then given by a Binomial distribution:

$$P(i, p, N) = \binom{N}{i} p^i (1-p)^{N-i} \tag{5.3}$$

Using the binomial distribution the error bars depicted in figure 5.11 are calculated. They illustrate the range of possible outcomes (with a confidence level of 1 σ) under the assumption that the measured fraction is the true efficiency.[6]

As an efficiency can neither be larger than one nor smaller than zero, binomial uncertainties are necessarily asymmetric for any efficiency unequal 1/2. In addition, for an efficiency of 1/2 the binomial uncertainty is maximal, which can be seen in figure 5.11.

[6] This Frequentist probability is equivalent to a Bayesian interpretation with uniform prior.

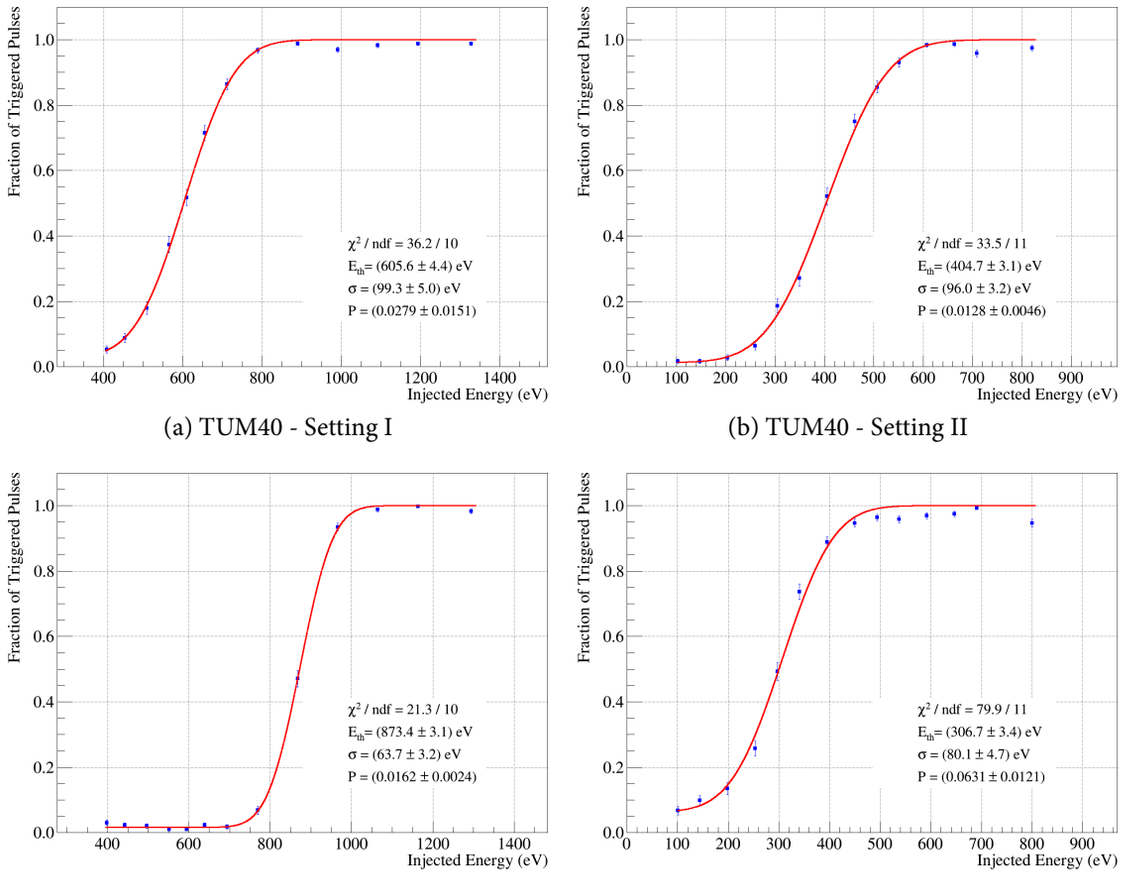

(a) TUM40 - Setting I

(b) TUM40 - Setting II

(c) Lise - Setting I

(d) Lise - Setting II

Figure 5.11.: Trigger thresholds measured for TUM40 and Lise before (I) and after (II) lowering the thresholds. Blue data points depict the fraction of test pulses triggering for the respective injected energy. The error bars correspond to binomial uncertainties, the red lines to the result from a fit of equation 5.5 to the data.

The theoretical description of the trigger efficiency (f) as a function of injected energy (E_{inj}) takes the form

$$f(E_{\text{inj}}) = \frac{1}{2} \cdot \left[1 + \text{erf}\left(\frac{E_{\text{inj}} - E_{\text{th}}}{\sqrt{2}\sigma}\right)\right] \tag{5.4}$$

It is given by the convolution of a step-function, describing an ideal trigger of threshold E_{th}, with a Gaussian function (of width σ) accounting for the finite baseline noise. In the above equation erf denotes the Gaussian error function [7]. The error function is zero if its argument is zero, thus, for $E_{\text{inj}} = E_{\text{th}}$ the efficiency is $f = 50\,\%$.

However, $f(E_{\text{inj}})$ asymptotically approaches zero for $E_{\text{inj}} \ll E_{\text{th}}$ which is in contradiction to the DAQ scheme of tagging test pulses. When a test pulse is fired every pulse which triggered in time window of 0.4 s around the time of the injection will be flagged as

[7] $\text{erf}(x) = \frac{2}{\sqrt{\pi}} \int_0^x e^{-t^2} dt$

Detector	Setting	Threshold E_{th} (eV)	P (%)	$P_{expected}$ (%)
TUM40	I	605.6±4.4	2.8±1.5	0.5±0.1
TUM40	II	404.7±3.1	1.3±0.5	2.0±0.5
Lise	I	873.4±3.1	1.6±0.2	1.5±0.3
Lise	II	306.7±3.4	6.3±1.1	6.2±2.4

Table 5.8.: Threshold and pedestal values determined by the fit of equation 5.5 to the data depicted in figure 5.11 for the detectors TUM40 and Lise. The last column lists the expectation of the pedestal P obtained from the probability of random coincidences between a particle interaction and the firing of a test pulse in the respective data set.

a test pulse. Thus, random coincidences between the firing of a test pulse and a particle interaction causing a trigger in the respective time window result in a pedestal P.

Generalizing equation 5.4 to account for a finite pedestal yields:

$$F(E_{\text{inj}}) = \frac{1-P}{2} \cdot \left[1 + \text{erf}\left(\frac{E_{\text{inj}} - E_{\text{th}}}{\sqrt{2}\sigma}\right)\right] + P \tag{5.5}$$

For $E_{\text{inj}} = E_{\text{th}}$ the efficiency becomes $F = \frac{1+P}{2}$. This may be understood in the following way: The chance to observe a particle pulse above trigger threshold in the time window is given by P. As the probability for the test pulse to trigger is completely uncorrelated to the probability of a random coincidence with a particle pulse, in $P/2$ times the injected test pulse will be above and in $P/2$ times below threshold. However, for the measured fraction the origin of the trigger does not matter. The total probability to observe a trigger for $E_{\text{inj}} = E_{\text{th}}$ is then given by $1/2 + P/2 = \frac{1+P}{2}$.

In figure 5.11 a likelihood fit of equation 5.5 to the data is performed, with E_{th}, σ and P as free fit parameters. Results are given in the legends, as well as in table 5.8.

The values determined for the width of the efficiency curve (σ) are well compatible with the widths of the baselines, as determined by the standard event fit (see section 7.1). This agreement proves that both, the trigger and the energy reconstruction at low energies, are dominated by the baseline noise. However, slightly lower σ-values are determined for the standard event fit. This is expected as the standard event fit, compared to the trigger electronics, compensates better for low frequency fluctuations by the polynomial used to model the baseline (see subsection 5.4.3). [8]

Table 5.8 also lists the expected pedestal P, calculated using Poissonian statistics. The given values account for the time window of 0.4 s and the average rate of particle events in the respective data set. Very good agreement is found for all values, except for TUM40-Setting I. The latter may result from a lack of test pulses well below the threshold energy (see figure 5.11a) causing the pedestal P to be hardly constrained in the fit.

[8] No indications were found for an additional noise contribution induced by the trigger electronics itself.

5.7.1. Long-Term Stability of the Trigger

The trigger thresholds are determined in dedicated measurements injecting many low-energy test pulses to map the entire efficiency curve. However, we inject several low-energy test pulses with equivalent energies of 0.6 keV and 1.0 keV since almost the beginning of the data taking. An additional 0.4 keV was added in parallel to the lowering of the threshold of TUM40. These low-energy test pulses allow to study the long-term stability of the trigger threshold.

In figure 5.12 the fraction of pulses triggering per week live time is shown for the whole phase 2 for the three lowest test pulses (0.4 keV in blue, 0.6 keV in red and 1 keV in green). The gray vertical lines mark the point in time where the threshold was lowered from setting I to setting II for the corresponding detector.

For TUM40 (top, figure 5.12a) fluctuations of up to 20 % are seen for the 0.6 keV test pulse with setting I and the 0.4 keV test pulse with setting II. At first glance this might be a hint for a very unstable trigger threshold, but the injected test pulses energies are very close to the trigger threshold E_{th} where small fluctuations of the energy have a substantial impact on the fraction of pulses triggering. The two dashed lines mark the values determined for the respective test pulses in the dedicated measurement, red for the 0.6 keV test pulse with trigger setting I (figure 5.11a) and blue for the 0.4 keV test pulse with trigger setting II (figure 5.11b). As can bee seen only very few time bins result in an efficiency below this line, rendering the threshold determined in the dedicated measurements conservative.

Also for Lise (bottom, figure 5.12b) the efficiency of the 0.4 keV test pulse as determined in the dedicated measurement (blue dashed line) is always below the efficiency measured in the data set which is used to derive the final result (setting II).

The points drawn with gray squares indicate the pedestal P which is given by the trigger rate in the respective time bin. For both detectors only small variations are seen in the pedestal P. A convincing proof for the validity of the calculation of the pedestal P is given by the agreement of the fraction of triggers for the 0.4 keV test pulse (red) in Lise with the threshold setting I. As the injected energy of 0.4 keV is well below the trigger setting I of 0.9 keV, basically only random coincidences with a particle pulse can cause a firing of the trigger, which is the origin of the pedestal.

For both detectors only small variations in the pedestal P are observed, which excludes changing baseline noise as the origin of the fluctuations in the trigger rate, for the following argument. In particular with the low settings II already a slightly enhanced in baseline noise (e.g. by mechanical vibrations originating from the cryostat) has the potential to substantially increase the overall trigger rate by a high number of noise triggers. A higher overall rate would raise both, the fraction of triggers and the pedestal P. This is, however, not seen in the data which show fluctuations in the fraction of triggers, but a rather constant pedestal P. The argument outlined above points to a small instability of the trigger electronics.

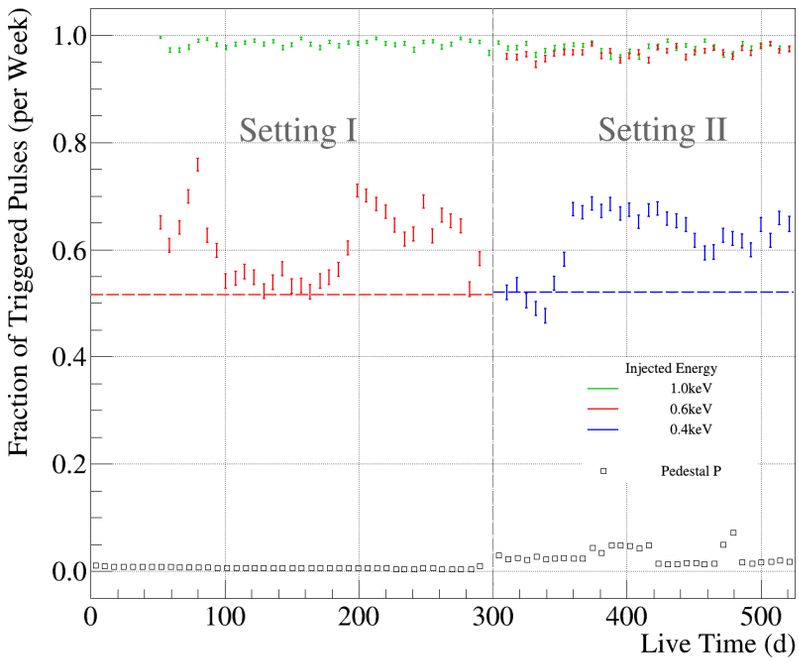

(a) TUM40

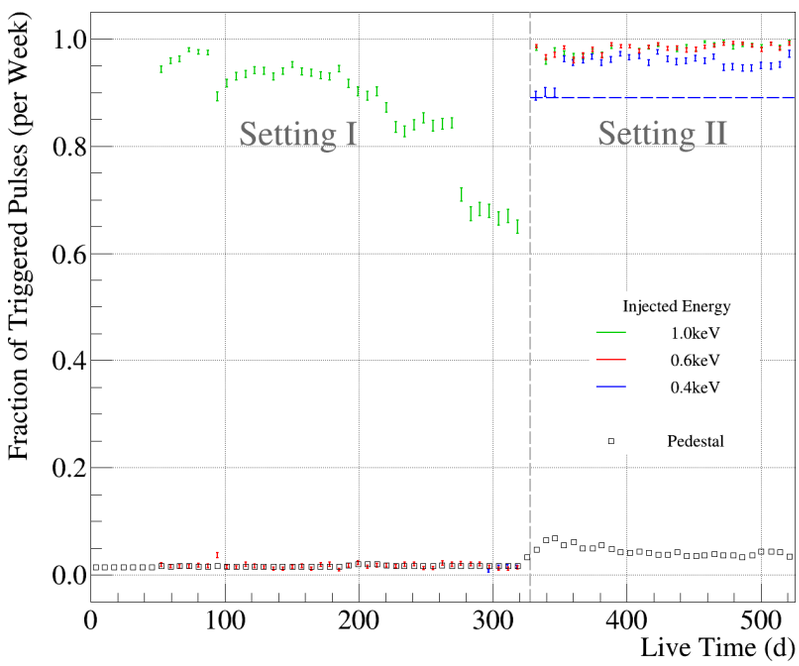

(b) Lise

Figure 5.12.: Fraction of test pulses of different energies (see legend) triggering per week of live time. The point in time where the threshold of the respective detector was lowered is marked with a gray vertical line. The errors bars depict binomial uncertainties, analog to figure 5.11. The horizontal dashed lines correspond to selected efficiencies for the test pulse of the same color as determined in the dedicated threshold measurements in figure 5.11.

5.7.2. Conclusion on the Trigger Threshold

The injection of low energy test pulses to the heater proved to allow for a very precise determination of the threshold E_{th} - a key parameter for the final dark matter analysis. The continuous sampling of low-energy test pulses throughout the whole data taking revealed upwards fluctuations of the trigger efficiency compared to the dedicated measurements. Thus, using the values E_{th} determined by the dedicated measurements (see table 5.8) is conservative.

Outlook for CRESST-III Since the trigger threshold is a key parameter for the sensitivity towards very low dark matter particle masses, CRESST-III will be equipped with a continuous readout of the detectors, avoiding the need of a hardware trigger. This allows to optimize the search for the presence of a pulse, if necessary accounting for individual detectors and/or different time periods.

5.8. Empty Baselines to Monitor the Baseline Noise Over Time

Empty baselines are acquired every few minutes by toggling the readout of the transient digitizers at a certain point in time. Empty baseline serve two main purposes: They are used to monitor possibly time-dependent variations of the baseline noise and they are needed to create artificial events used to evaluate the efficiency of the selection criteria applied to the raw data (discussed in the next chapter). An example empty baseline is depicted in 6.1b.

To monitor possible variations of the noise with time, the empty baselines are fit with a polynomial of third order, which allows a direct comparison with the standard event fit which is also using a third-order polynomial for the baseline model (see section 5.4). Figure 5.13 shows the RMS[9] of this fits as a function of live time.

On the one hand, for the phonon detectors TUM40 and Lise hardly any changes in the noise level are found in the course of phase 2. The light detectors Michael and Enrico, on the other hand, are affected by time-dependent noise changes, in particular in the second half of the data taking. These dependences are mainly caused by mechanical vibrations induced by the cryogenic facility[10]. Despite the small disturbances seen for the light detectors it should be noted that the situation substantially improved compared to phase 1 [125]. In phase 1 the larger time-dependent noise changes required an individual treatment of different periods for most detectors, which is not needed for phase 2.

The absolute noise level is on a comparable level for the light detectors Michael and Enrico. The modest performance of Enrico results from very small pulses. However, for the analysis presented here the resolution of the light detector is only of minor importance compared to the resolution of the phonon detector. To illustrate the differences of the

[9] For a record with N samples, the signal height in each sample being s(i) and the polynomial p evaluated at i the RMS is defined as: RMS = $\sqrt{\frac{\sum_i^N (p(i)-s(i))^2}{N}}$

[10] The so-called 1K-pot was identified as the dominating origin of the disturbances.

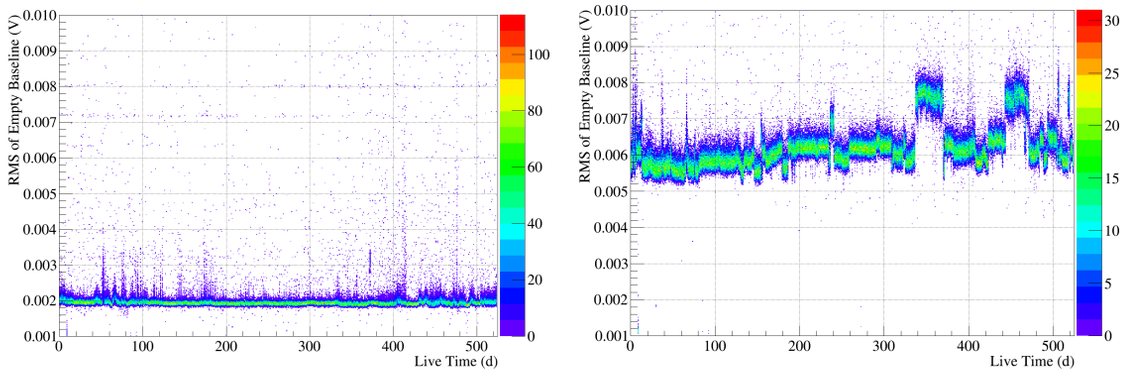

(a) TUM40

(b) Michael

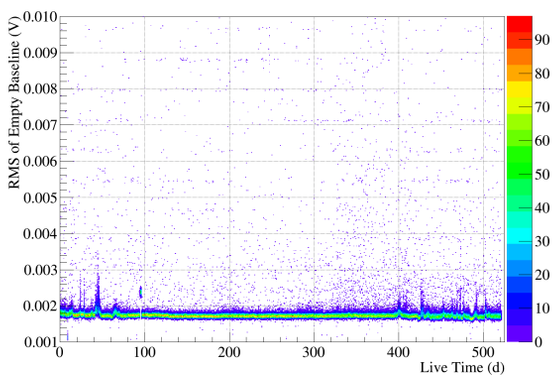

(c) Lise

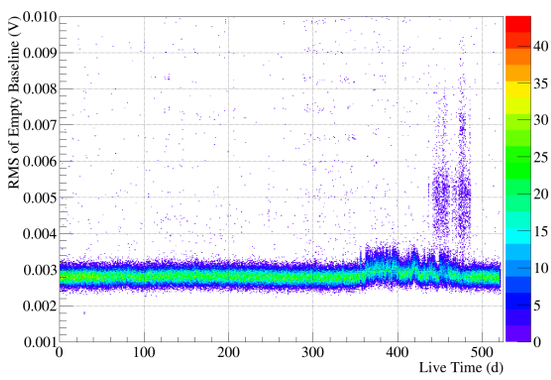

(d) Enrico

Figure 5.13.: RMS of the empty baselines (determined using a polynomial of third order) as a function of live time for the respective detector. Included are data from the whole phase 2.

RMS of the empty baselines for Lise and TUM a histogram is drawn in figure 5.14. The solid lines correspond to the RMS of the empty baselines determined using a polynomial function of order three (cubic, analog to figure 5.13) for Lise in red and TUM40 in blue. Comparing the lines yields the baseline noise level of TUM40 to be roughly 10 % higher than the one of Lise. The dashed lines correspond to the RMS values determined by a linear fit function, underpinning the benefit of a cubic baseline as was already found in section 5.4.3.

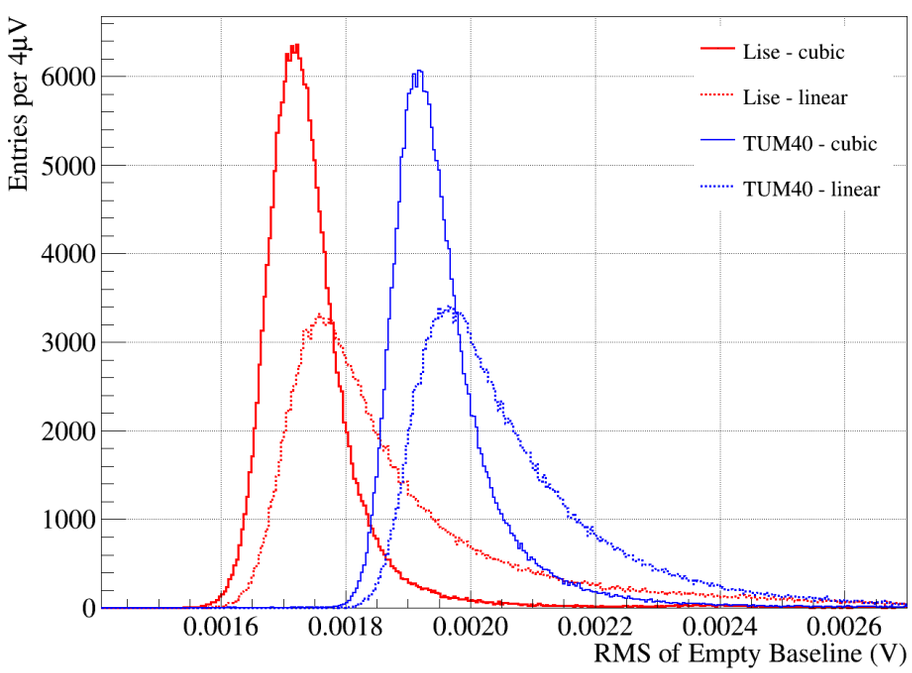

Figure 5.14.: RMS of the empty baselines determined for TUM40 and Lise with different baseline models (see legend).

6. Raw Data Selection

After the processing of the raw data, which was discussed in the last chapter, a set of parameters describing each event and each pulse is available. The most important information thereby is the phonon energy and the light yield, both determined by the standard event fit. Thus, a general guideline for most selection criteria (cuts) discussed in the following is to remove all events where a correct reconstruction of the energy cannot be guaranteed.

6.1. Blind Analysis

A blind analysis is performed by designing all cuts on the respective training sets (see figure 5.1). Then, the cuts are applied without any changes to the blind data set. By choosing the training set to be considerably smaller in terms of exposure, any unwanted bias (knowingly or unknowingly) is avoided, which is the essence of every blind analysis.

For TUM40 the exposure criterion is certainly fulfilled as the exposure of the training data is roughly one third of the blind data set (see table 5.2). For Lise the dark matter result is driven by very low energies, inaccessible in training data I with a threshold of 0.9 keV. Therefore, mainly training set II is relevant, which is seven times smaller than the blind data set II. Thus, also for Lise all requirements for a blind analysis are met.

6.2. Determination of Cut Efficiencies

As the classification of an event as good or bad is not always unambiguous, most selection criteria applied will also remove potential signal events. The probability for a potential signal event to pass a cut is referred to as the efficiency of the respective cut. This chapter begins with a presentation of a general method to estimate the cut efficiencies, then discusses the cuts applied. Finally, results will be shown for the two detector modules Lise and TUM40.

The main innovation of this analysis is to make use of the data down to trigger threshold. However, this approach introduces substantial energy-dependencies for the cut efficiencies, rendering a precise determination of the efficiencies mandatory. The method presented in the following was first used in [134] and adopted to fulfill the requirements of a dark matter analysis.

The basic idea behind this method is to apply all methods of data preparation and selection on a set of artificially created signal events (also referred to as simulated events). The efficiency for a specific cut is then given by the fraction of events surviving the cut. To gather information on the energy dependence, artificial events of a set of discrete energies are created. The simulated events are obtained by superimposing empty baselines

and a standard event representing the shape of a potential dark matter signal. Since empty baselines are affected by any possible artifact in the same manner as an event induced by a particle interaction, this method provides a profound basis for a precise determination of cut efficiencies.

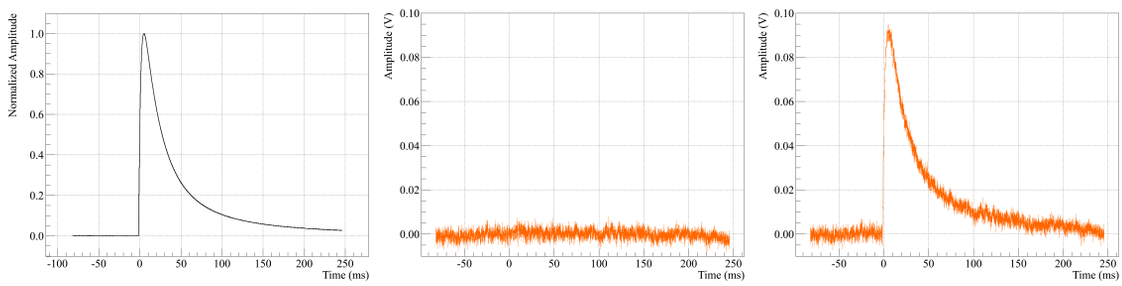

(a) Standard Event (b) Empty Baseline (c) Artificial Pulse

Figure 6.1.: One example for the creation of an artificial pulse for the detector TUM40. First the standard event (a) is scaled to the desired amplitude ($\equiv$ energy), then added to the empty baseline (b) resulting in the final artificial pulse (c).

Two simplifications are introduced for the artificially created events. Firstly, the response function of the detector, describing the relation between the deposited energy and the resulting pulse amplitude (see figure 5.8), is approximated to be linear (with zero y-intercept). As a result energy and amplitude of a pulse are direct proportional to each other, quantified by the proportionality factor C (keV/V). This approximation is well justified, as the energies of interest for this work are in the linear range of the TES.

The proportionality factors C are determined by a linear fit of the energy as a function of fitted amplitude using data from the training set. The resulting values including statistical uncertainties are listed in table 6.1.

Secondly, the small time-dependencies of the detector response are neglected. While these dependencies are taken into account by the test pulses for real particle events (section 5.5), a constant conversion factor C is used for the simulated events. Also this simplification hardly introduces any uncertainty on the final result. Basically no time-dependent effects are present in the relevant detectors for energy depositions below ~ 5 keV. For energies above, small variations in time are observed. However, for these energies the cut efficiencies are practically constant - independent of energy. Thus, a small uncertainty concerning the energy of the simulated events does not impact the result on the efficiency.

A pulse of the desired energy is then created by scaling the standard event according to the inverse proportionality factor 1/C and adding the result to an empty baseline. However, as C is determined using e^-/γ-events, but the potential signals are nuclear recoils, for the light pulse the quenching factor has to be taken into account in addition $(1/(C \cdot QF))$. For two reasons only artificial recoils off tungsten ($QF_W \sim 50 \gg QF_{O,Ca}$) are created, firstly because for a wide range of potential dark matter particle masses, tungsten is the dominant scattering parter. Secondly, efficiencies in general decrease for smaller pulses. Thus, the efficiency for a potential signal on oxygen, or calcium might be marginally higher than for

Detector	C (keV/V)
TUM40	111.24±0.06
Michael	67.92±0.07
Lise	68.29±0.01
Enrico	2227±1

Table 6.1.: Proportionality factors C describing the linear dependence between the amplitude of a pulse and its corresponding energy.

recoils off tungsten. As this analysis sets exclusion limits on the scattering cross section an underestimation of the efficiency is conservative. For the same argument, also the small correction for the phonon energy of events with a light yield below one (see section 5.6) is not performed. Not applying the correction leads to slightly smaller amplitudes for the phonon pulses of simulated nuclear recoils and, thus, is conservative, as well.

Figure 6.1 illustrates the procedure creating one exemplary artificial event for the detector TUM40. The first step is to scale the normalized standard event, which is the same as used in the standard event fit of the particle events. In figure 6.1 the desired simulated energy is 10 keV. Thus, the amplitude of the standard event was scaled to $\frac{10\,\mathrm{keV}}{(C{=}111.24\,\mathrm{keV/V})} \sim 0.09\,\mathrm{V}$. After the scaling the standard event is added to the empty baseline (b) resulting in the artificial pulse (c).

The first step of the analysis of the artificial pulses is to perform the standard event fit. Thus, the artificial events are a powerful tool to study the performance of the standard event fit by comparing the simulated amplitude/energy with the reconstructed amplitude/energy. As a constant factor was used to scale the standard event in the creation procedure of the artificial pulse, the reconstructed energy is given by the multiplication of C for the respective detector with the amplitude of the artificial pulse, as determined by the standard event fit.

Additional Remark on the Proportionality Factors C The values listed in table 6.1 contain information on some aspects of detector performance of the two detector modules analyzed in this work.

Comparing TUM40 and Lise reveals that pulses in Lise are almost a factor of two higher than in TUM40. Obviously, not the signal height but the signal-to-noise level is the relevant quantity for the achievable energy threshold and resolution. However, by comparing the empty baselines for TUM40 and Lise (see figure 5.13) one finds that the noise is on a similar level (10 %) for both detectors, while the difference in signal height is much more distinct. Thus, the better energy resolution and the lower trigger threshold of Lise can be attributed to the signal height rather than to the noise.

The last argument is even more true for the light detectors. While the noise levels of Enrico and Michael are on a comparable level, the pulses seen in Enrico are 30 times smaller than for the same energy deposited in TUM40/Michael. Although a direct comparison is more complex for the light detectors, as the amount of scintillation light also depends on

the crystal and the module design, the large difference in the signal height clearly reveals the poor performance of Enrico compared to Michael. A comparison with other light detectors operated in phase 2 undoubtedly indicates a problem far beyond the variations of performance seen between the light detectors. However, up to now the origin of the problem could not unambiguously be identified.

6.3. Rate and Stability Cut

6.3.1. Rate Cut

The first cut applied is the so-called rate cut removing time periods of unusually high rate, as an increased rate points to the presence of disturbances causing the trigger to fire. Furthermore, a stable detector operation relies on control pulses which are only injected if no other pulse is present.

Figure 6.2 shows the rate as a function of live time for the detectors TUM40 and Lise for the whole phase 2. For both detectors a cut limit of 500 counts per hour live time is chosen. All time periods with a rate above this limit are removed from the analysis, plus the preceding and the succeeding time bin. Compared to Lise, TUM40 exhibits some short-term fluctuations extending over less than one hour. Therefore, for TUM40 a finer binning is used (0.1 h) with the cut limit being adjusted accordingly to 50 counts per time bin.

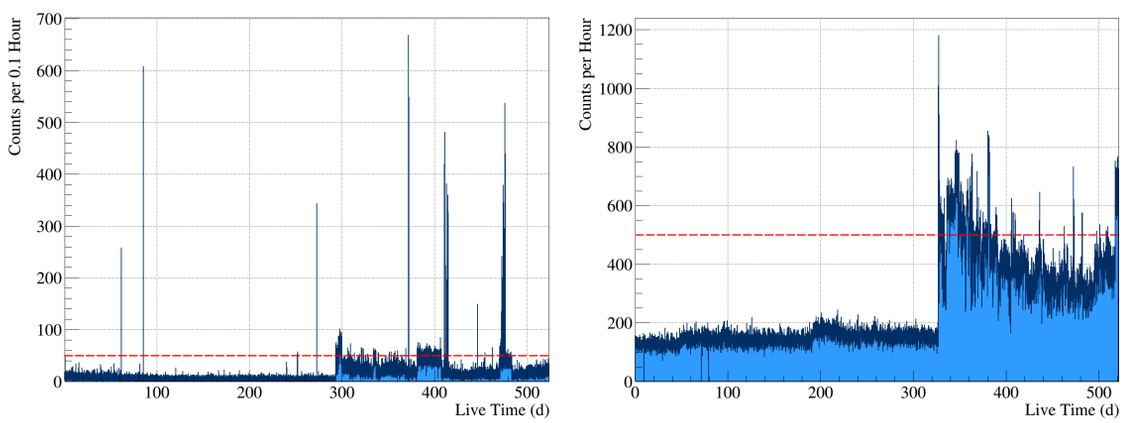

(a) TUM40 (b) Lise

Figure 6.2.: Trigger rates of TUM40 and Lise. The red dashed line marks the cut limit chosen for the respective detector.

Technically, the rate cut is done by removing the control pulses in periods above the allowed limit from the event list of control pulses. As a result, the stability cut, described in the following, will automatically mark the respective time periods as unstable.

The rate cut is the only cut which was adjusted using data from the full data set. However, the cut limit was fixed based on the histograms shown in figure 6.2 before unblinding the data. As the rate contains practically no information on a possible dark matter signal in the data this procedure certainly does not violate the concept of a blind analysis.

6.3.2. Stability Cut

As was already discussed in subsection 3.4.3 control pulses are obtained by injecting a large heater pulse completely heating the TES to the normal conducting regime. Then, the height of a recorded control pulse is a measure of the point in the phase transition of the TES.

Since the phase transition is never perfectly linear, different points in the transition yield different response functions of the detector. Thus, we require a precise stabilization of the TES in its operating point to maintain an accurate energy calibration. The stabilization is done online by the DAQ via adjusting the heating power with a PID-loop with the control pulse amplitude as input parameter. While this method reliably controls long-term drifts, short-term excursion from the operating point induced by disturbances have to be accounted for in the offline analysis. Such disturbances mainly originate from mechanical vibrations causing a dissipation of heat. They may either be produced internally from the cryostat[1] or externally (trucks moving inside the laboratory, earthquakes etc.).

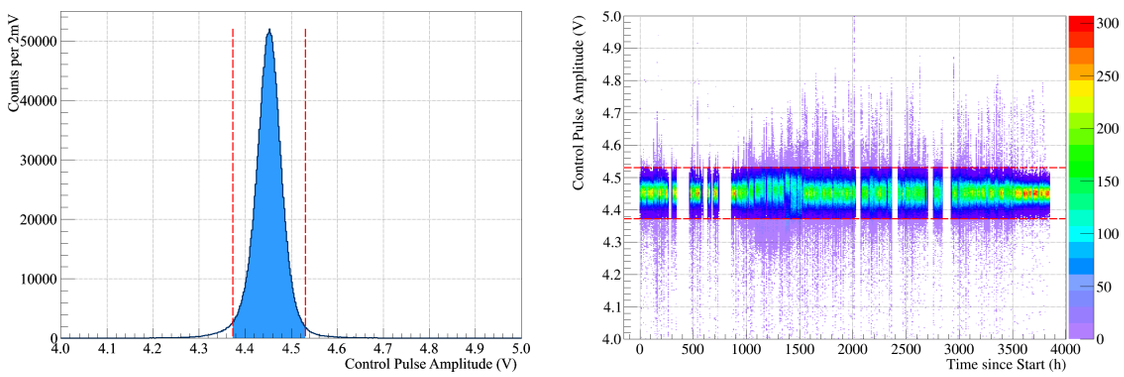

(a) Histogram of the control pulse amplitude

(b) Control pulse amplitude as a function of time since start

Figure 6.3.: Control pulses for Michael in the training set I. The red dashed lines indicate the allowed deviation from the set point of 4.45 V.

The first step of the stability cut is to define an allowed deviation from the operating point, individually for each detector. In figure 6.3a a histogram of the amplitude of the control pulses of the light detector Michael is shown. Close to the set point the distribution can be approximated by the fit of a Gaussian function. For each detector a deviation of $\mu \pm 3\,\sigma$ is allowed (red dashed lines). The operating points, as well as the resulting ranges ($[A_{min}, A_{max}]$) are listed in table 6.2.

Figure 6.3b shows the control pulse amplitudes as a function of time; the allowed range is again marked by red dashed lines. Considering the color coding, one clearly sees the stable detector operation with time, with an improvement given for the last ~ 300 hours. This improvement is observed for most detectors in phase 2. The explanation is that this time period coincides with the Christmas holidays, where the work in the underground laboratory and, thus, the amount of external disturbances, is reduced to a minimum.

[1] More precise: from the 1K-pot.

	Operating Point (V)	A_{min} (V)	A_{max} (V)
TUM40	8.90	8.723	9.092
Michael	4.45	4.373	4.531
Lise	7.35	7.150	7.564
Enrico	0.128	0.121	0.135

Table 6.2.: Operating points (2nd column) for the detectors analyzed in this work. Control pulses inside the interval [A_{min}, A_{max}] are considered stable.

	Data Set	Fraction (%) removed by			Overlap (%)
		Rate Cut	Stab. Cut	Rate + Stab. Cut	
TUM40	Blind Data I&II	5.86	3.62	8.90	0.58
Lise	Blind Data II	17.3	6.73	21.8	2.23

Table 6.3.: Fraction of exposure removed by the rate cut only, the stability cut only and the combined application of rate and stability cut. The overlap is the sum of the individual fractions for rate and stability cut minus the fraction of both cuts applied (column three).

A period is considered unstable if two consecutive control pulses are either missing[2] or are outside the allowed range. The latter criterion is applied to be immune to single outliers, e.g. caused by pile-up events. Since control pulses are injected very frequently (6 s in phase 2) real deviations from the operating point cause more than one control pulse to be outside the allowed range. If an unstable period is found all data from the last stable control pulse before this period to the next stable control pulse after this period are tagged as unstable.

In summary, the stability cut discards all data where the phonon and/or the corresponding light detector are not operating stably.

Results of the Stability Cut

As the stability cut removes time periods only, the remaining live time (=exposure) after the cut can also be calculated analytically (without the artificial events).

For the dark matter data sets the fraction of exposure removed by the rate cut, by the stability cut and by stability cut plus rate cut are listed in table 6.3. One cannot simply add the fractions removed by rate and stability cut, since periods of high rate and unstable detector operation might overlap. The last column of table 6.3 depicts the overlap which is given by the sum of the fraction when applying rate and stability cut individually minus the fraction of combined application. Thus, the values in the last column mark the fraction of exposure being above the rate limit and violating the stability criteria.

For TUM40 hardly any overlap is observed and also for Lise the majority of removed periods by the two cuts is not overlapping. This result further motivates the need for both, the rate and the stability cut.

[2] Thus, periods where the control pulses were removed by the rate cut are automatically marked unstable.

In particular for Lise the rate cut removes a significant amount of exposure. However, for the low-threshold analysis of Lise the exposure is hardly limiting the dark matter sensitivity (see section 9.3). Thus, a rather strict cut can be used without a negative impact on the final result.

6.4. Energy and Amplitude

CRESST detectors typically offer a large dynamic range, from the sub-keV region up to typical α-energies of several MeV (see [127, 128] for recent α-analyses of CRESST-II data). However, to make full use of the complete dynamic range requires some adjustments for the high-energy scale, in particular for the energy calibration. The response function in the low-energy regime is very well modeled by a polynomial of fourth or fifth order, as was shown in figure 5.8. However, for high energies this is no longer given as less test pulses are injected in the high-energy region, which leads to a lack of supporting points for the polynomial fit (details may be found in [125]). The low-threshold analysis presented here is tuned for optimal performance in the low-energy region. Thus, all events with with an amplitude too large to be precisely converted to energy are discarded. Thereby, the actual value depends on the individual detector.

Additionally, all events with an energy lower than the trigger threshold (see section 5.7) are discarded. This cut is irrelevant for the dark matter data set, as events below the energy threshold are anyhow not considered for the calculation of exclusion limits. However, the cut has to be included in the calculation of the signal survival probability (= cut efficiency) to account for events where the standard event fit fails to find the correct pulse position. In such a case the standard event fit might search for the pulse in a part of the simulated record where no pulse is present and return a very small amplitude. Such an event gets assigned an energy well below the threshold energy and will, therefore, be removed by the cut on the energy. As those events typically would not be removed by any other cut (if not affected by artifacts), they would be considered as *surviving* in the determination of the signal survival probability. However, this would represent an overestimation of the signal survival probability, as events with an energy smaller than the threshold energy are not considered for the final dark matter analysis. Obviously, the probability of the standard event fit to find the correct pulse increases with increasing pulse amplitude and, thus, energy. In summary, removing all events with an energy smaller than the threshold energy accounts for the energy-dependent probability of the standard event fit to not find the correct pulse.

6.5. Quality Cuts

The guideline for all cuts described in this section, denoted quality cuts, is to discard events affected by well-known artifacts. In principle most of these events could also be tagged by an increased RMS of the standard event fit, which is sensitive for any deviation from the nominal pulse shape. However, as will be discussed in the next section, the RMS cut is

based on an algorithm automatically discarding events outside the RMS distribution given for artifact-free (good) events. To clearly identify the RMS-distribution for good events requires to remove the majority of events affected from artifacts from the data set before applying the RMS cut.

Obviously, the quality cuts address very specific issues and can, thus, only be designed for known classes of invalid pulses which appear frequently, in particular considering the limited statistics of a training set. As opposed to the quality cuts, the RMS parameter reveals any deviation from the nominal pulse shape. A simplified view would be to see the quality cuts as dedicated cuts removing pulses affected by well-known artifacts prior to the RMS cut which removes any left-over event where the correctness of the energy reconstruction is in danger.

Figure 6.4 depicts the most frequent invalid event classes targeted by the quality cuts described in the following.

Delta Voltage - RMS The characteristic signature of the so-called delta-spikes (see figure 6.4a) is an obviously unreasonable signal in a very few samples only. Such a quasi-instantaneous change of the signal cannot be connected to a real change of temperature but may only be induced by electric disturbances. Usually, delta-spikes appear in multiple detectors, further underpinning an electric origin. These events are removed by the *Delta Voltage - RMS* parameter, which is defined as the maximum change between two samples divided by the RMS of the baseline (as sampled in the pre-trigger region).

On the one hand, rather large spikes, as the one depicted in figure 6.4a, can easily be identified by the *Delta Voltage - RMS* parameter. On the other hand small spikes might survive the cut and also the RMS cut. However, such small spikes have no negative impact on the precision of the standard event fit and, thus, there is no need for removal.

Right - Left Baseline The *Right - Left Baseline* (RLB) parameter is calculated by subtracting the average of the first 50 channels in the record from the average of the last 50 channels. This cut aims at multiple invalid event classes.

The first one are so-called losses of flux quanta (two examples are depicted in figures 6.4b and 6.4c) which appear for pulses rising too fast for the SQUID to follow, thus resulting in a change of baseline level. Obviously, the correct amplitude of the pulse cannot be reconstructed in a reliable manner. Therefore, these pulses have to be discarded. Figure 6.4d depicts another class of events removed by the RLB parameter, namely so-called decaying baselines. They follow a very large energy deposition in the previous record, if the pulse did not yet relax back to equilibrium after the reactivation of the trigger.

Also so-called stick events in TUM40 are removed by a cut on the RLB parameter. Stick events arise from energy depositions in the $CaWO_4$-sticks holding the crystal (see subsection 4.3.2). They feature longer rise and decay times than events in the absorber crystal, since the phonons do have to pass the crystal-stick interface. For the same reason also the amplitude of a pulse is significantly suppressed (by a factor ~ 50 for TUM40 [147]) than for the same energy deposition in the main crystal. The light produced in the stick is comparable to the light produced in the absorber (for the same deposited energy) resulting in

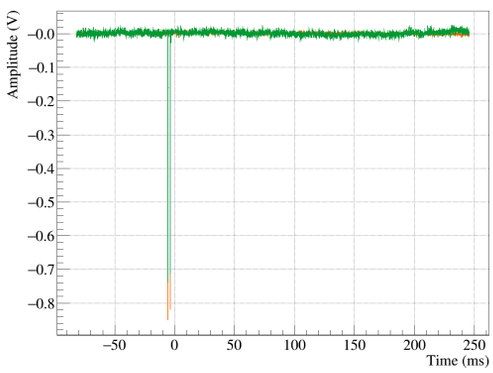

(a) Delta Spike

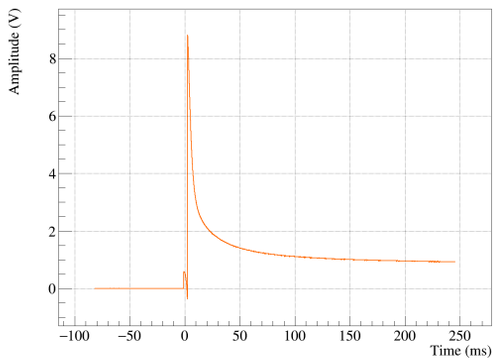

(b) Flux-Quantum Loss I

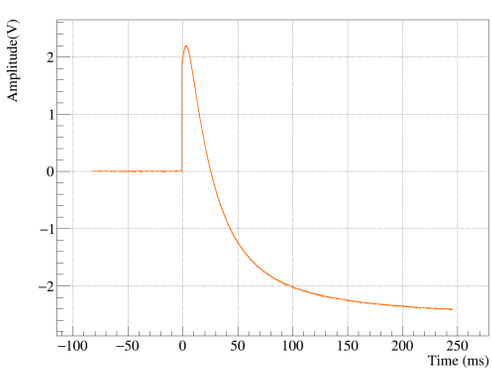

(c) Flux-Quantum Loss II

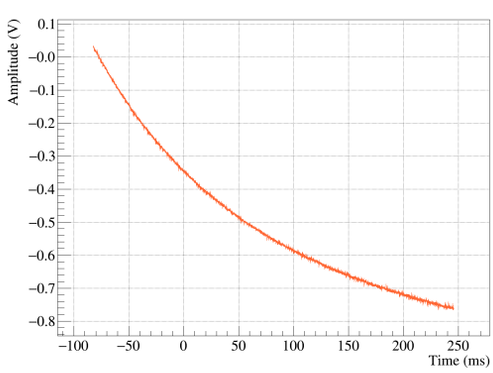

(d) Decaying Baseline

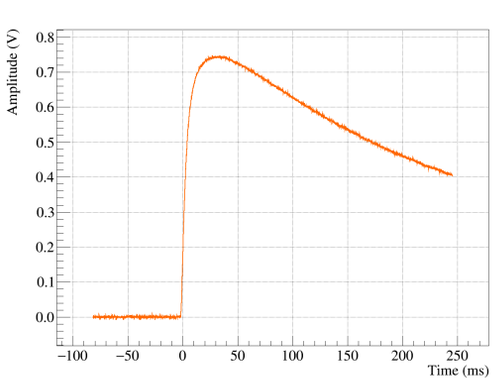

(e) Stick Event

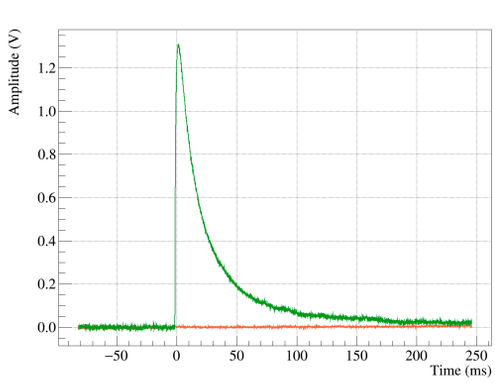

(f) Light-Only Event

Figure 6.4.: Selection of invalid pulses to be discarded by quality cuts. Orange pulses were recorded with TUM40, green pulses with the corresponding light detector Michael.

very high light yields for interactions of α, β, γ-interactions in the stick. Information on stick events may be found in [147, 139].

Shift and Peak Position For the detector Lise two additional cuts on the peak position, as determined by the moving average, and the shift, as determined by the standard event fit, are applied. As for Lise pulses slightly above the baseline noise are analyzed, fluctuations of the noise might be misidentified as a pulse. Such a misidentification in the middle part of the record generally leads to an event with a reconstructed energy below threshold and, thus, is discarded by the cut on the energy (and also taken into account in the calculation of the efficiency). However, if the standard event shifts the template very early or very late in the record, the baseline level might not be constrained enough, leading to wrongly fitted amplitudes. Therefore, these events are removed from the final analysis.

6.6. Carrier Cut

Both detectors analyzed in this work feature a glued thermometer carrier (see section 3.3.4). Events in the carrier exhibit faster rise and decay times than events in the absorber, resulting in a different pulse shape, as was shown on the example of TUM40 in figure 3.7. The strategies to discriminate absorber and carrier events differ for TUM40 and Lise, therefore the following subsection applies for TUM40 only.

6.6.1. Linearized RMS Difference

To make use of the full difference in pulse shape each pulse is fitted twice, once with the standard template for absorber events and once with a template created from carrier events. Then absorber and carrier events are discriminated via a cut on the *linearized RMS difference* defined as

$$\text{RMS lin. Diff.} = \frac{\text{RMS}^a - \text{RMS}^c}{\text{RMS}^a + \text{RMS}^c} \tag{6.1}$$

with RMS^a and RMS^c being the RMS values obtained by the fit with the absorber and the carrier template, respectively. The interpretation of this parameter is straight-forward. For an absorber event the pulse shape of the absorber template will fit the pulse much better, thus: $\text{RMS}^a \ll \text{RMS}^c$ and the *RMS lin. Diff.* parameter will approach -1. Vice versa, a carrier event will result in a positive value for the parameter *RMS lin. Diff.*. If both templates are an equally good (or bad) description of the pulse, then a parameter value around zero will be determined. This starts to be the case when approaching very small pulses, as for those pulses the RMS is dominated by the influence of the baseline noise, rather than by the impact of the pulse shape.

For the above reason the distributions obtained for carrier and absorber events overlap for small energies, which complicates the design of an appropriate cut based on real data. Therefore, simulated events are used to study the distributions for carrier and absorber events separately. The distribution of the linearized RMS difference for absorber events as

a function of energy is depicted in figure 6.5a with the chosen two-dimensional cut accepting all events below the solid red line. The energy thereby is derived from the amplitude determined by the standard event fit of the absorber template and thus corresponds to the energy which would be assigned to a carrier event found in the real data set. However, one should keep in mind that this energy does not relate to a real deposited energy for carrier events.[3]

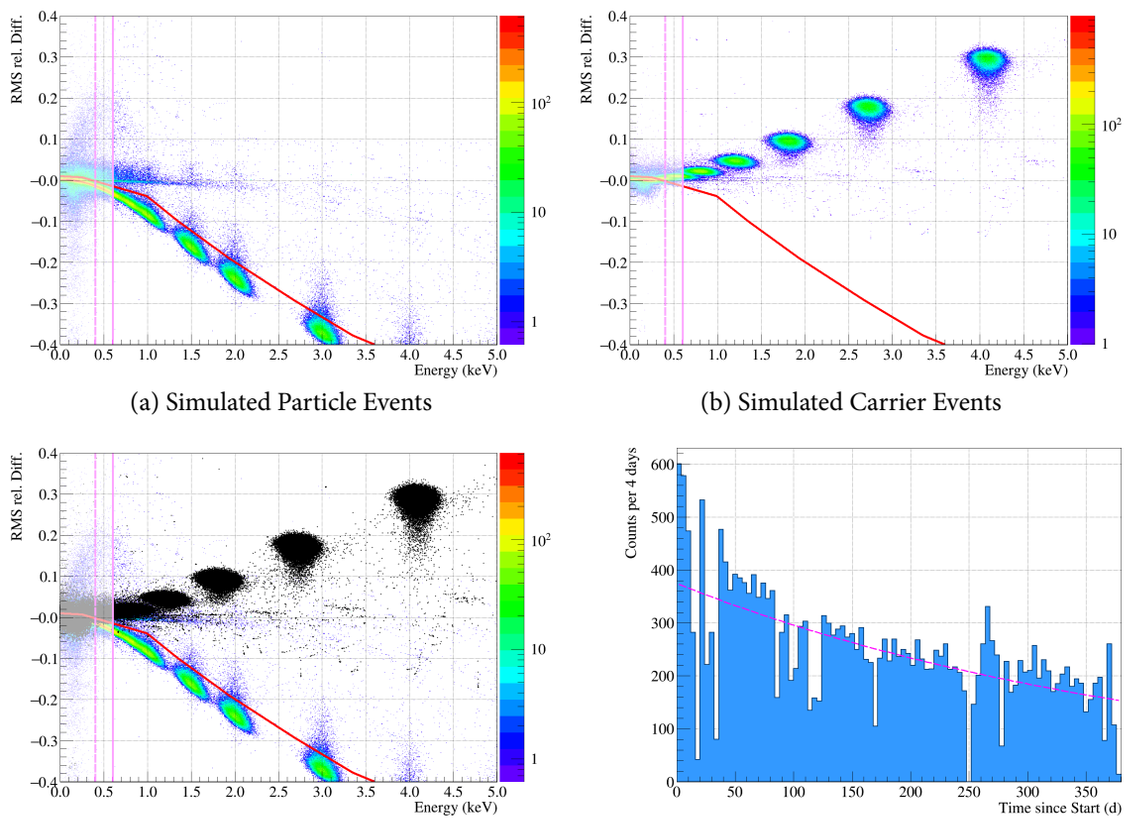

(a) Simulated Particle Events

(b) Simulated Carrier Events

(c) Overlay

(d) Events removed by the cut as a function of time since start, fitted with an exponential decay (magenta dashed line).

Figure 6.5.: The plots a-c show the distributions of the linearized RMS difference obtained for different event classes. The chosen cut is indicated in solid red. The vertical magenta lines correspond to the trigger threshold settings of TUM40: setting I (0.6keV) as solid line and setting II (0.4keV) with a dashed line. In plot (d) the decrease of the number of events removed by the cut is illustrated. The time period chosen corresponds to all data taken with trigger setting I (0.6keV) - see section 5.1.

The magenta lines in figure 6.5a indicate the threshold of TUM40 (solid for setting I,

[3] Calibrating the carrier events might provide additional insight on their origin, However, due to the small size of the carrier, statistics are far too low to identify the 122 keV-peak of the ^{57}Co γ-calibration source. A stronger source, on the other side, cannot be used, as it would increase the trigger rate of the detectors above the limit for stable detector operation.

dashed for setting II). As one can see, the cut is allowed to slightly cut into the distribution of absorber events. The need for a rather strict cut becomes evident looking at the distribution for carrier events depicted in figure 6.5b revealing that a less strict cut clearly would result in a reduced rejection power for low energies (in particular for trigger setting II). This conclusion is further illustrated by figure 6.5c showing both distributions in the same histogram, black for simulated carrier events and colored for artificial absorber pulses.

The two main quantities classifying the performance of a cut are the efficiency and the rejection power. The efficiency describes the probability for a valid event to survive the cut and, thus, should ideally be as high as possible. The probability for an invalid event to be removed by the cut is referred to as rejection power and should also be as high as possible. However, the study of the carrier events illustrates that it might not be possible to fulfill both criteria at the same time. In such a case the analyst has to balance the cut between the removal of exposure on the one side and the leakage of background, due to invalid pulses surpassing the cut, on the other side. Obviously, an optimal choice is then only possible, comparing the distribution in light yield and energy of the background leakage to the distribution expected for a potential dark matter signal. However, taking into account the anticipated signal introduces a dependence of the cut on the mass of the dark matter particle. While such an approach optimizes the sensitivity of an analysis to a wide range of dark matter particle masses, the benefit for a low-threshold analysis aiming for maximum sensitivity for light dark matter particles is very limited. In addition, it should be mentioned that this kind of cut optimization is solely possible if the features of the background under consideration and thus, the rejection power can be determined precisely. For the specific case of the carrier events in TUM40 this study can be performed since a large number of the carrier events is present allowing to create a - in terms of noise contribution - high quality standard template which is the fundamental requirement to simulate artificial carrier events.

Naively one would expect the relation between the number of events in the carrier and in the absorber to scale with the ratios of the respective masses/volumes (given the same level of radioactive contaminations in both crystals). Following this simple argument, the rate of carrier events in TUM40 should roughly be $2\,\mathrm{g}/250\,\mathrm{g} \simeq 2\,\%$, however, in reality the carrier events make up for $\mathcal{O}(20\,\%)$ of events with a reconstructed energy above threshold. The origin for this excess could up to now not be finally clarified. The most probable explanation are stress-relaxation events in the glue interface between absorber and carrier crystals. For two reasons a particle-induced origin, e.g. by an extraordinary high radioactive contamination, seems unlikely. Firstly, the vast majority of these carrier events has very small pulses in the phonon detector, but no associated light signal. Secondly, the rate of carrier events substantially decreases since the beginning of the measurement campaign which is illustrated in figure 6.5d showing the number of events removed by the cut in time bins (real time = Time since Start) of four days. Fitting an exponential decay yields a lifetime of 294 ± 7 days. Although this is an oversimplified model to reconstruct the decay time, since it does not take into account any differences of live time per real time bin, the fit illustrates the visual impression of a decreasing rate with time. Since TUM40 was equipped with

its carrier long before the measurement campaign[4], crystal-intrinsic contaminations with such a rather short lifetime can be excluded. An external contamination introduced during mounting, however, should affect both carrier and absorber and most-probably also other detector modules.

In summary, these observations render a particle-origin for a significant fraction of the carrier events unlikely.

6.6.2. Peak Position - Onset

As outlined in the last subsection, TUM40 has an excess above the normal level of carrier events. To some extent this drawback can be compensated by the use of the linearized RMS parameter as selection criterion. For most detectors this is difficult, since only few carrier events of the same pulse amplitude are available, thus hindering to produce a carrier standard template of decent quality. In this case the cut is based on the *Peak Position - Onset (ms)* (PPO) parameter defined as the difference between the *Peak Position (ms)* and the *Pulse Onset (ms)* (see table 5.3), thus describing the rise time of the pulse from onset to peak.

As will be shown in section 6.9 the discrimination power of the PPO parameter is in general not as high as the one of the linearized RMS difference. However, a more robust discrimination via the PPO parameter was found for pulses of mixed shape, which appear for particles interacting very close to the glue interface between absorber and carrier, thus depositing energy in both crystals. Therefore, the PPO cut is not only done for Lise, where it is the only cut for carrier events, but also for TUM40 in addition to the linearized RMS difference cut.

Figure 6.6 shows the PPO parameter as a function of pulse height for TUM40 and Lise based on data from the training set I with everything below the red line being discarded by the cut, since carrier events rise faster and, thus, get assigned smaller PPO values.

For TUM40 the population of carrier events surviving the cut on the linearized RMS difference can be seen as a band with PPO-values around 2 ms most populated at low energies but extending over the complete energy range depicted. A further investigation of these events reveals that they are mostly associated with a light signal, thus mostly induced by particle interactions. In addition, the rate of the events removed by the PPO cut is roughly compatible to the mass ratios between carrier and absorber. This further argues for a non-particle induced population of carrier, or better to say carrier-like events in TUM40, in addition to real particle-induced events in the carrier.

[4]The module TUM40 was used to commission the stick design in the test facility of the MPI in the LNGS underground laboratory [147].

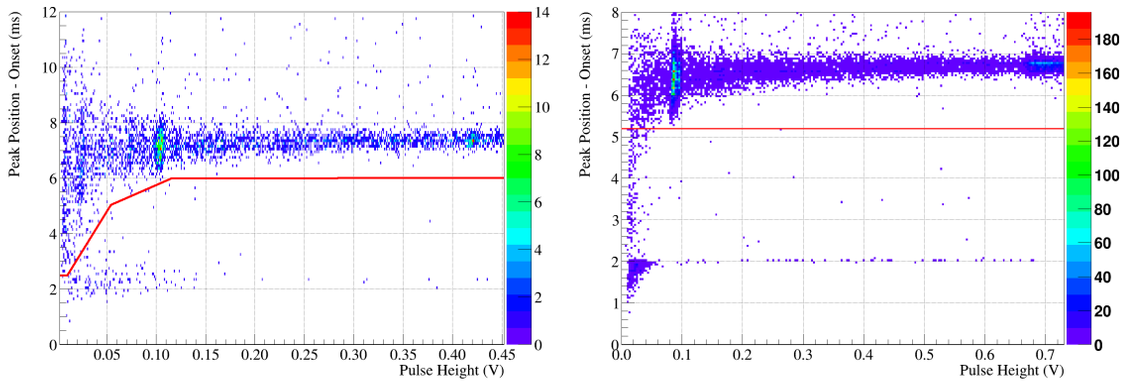

(a) TUM40 (after applying a cut on the linearized RMS difference)

(b) Lise (no cut on linearized RMS difference)

Figure 6.6.: Histograms of the *Peak Position - Onset* parameter as a function of *Pulse Height*, roughly corresponding to an energy range of 0-50 keV. All events below the red lines are discarded.

6.7. Coincident Events

6.7.1. Muon-Coincident Events

The muon flux in the Gran Sasso underground laboratory is suppressed by roughly six orders of magnitude compared to sea level (see section 3.2.2). To tag the remaining muons CRESST is surrounded by a veto made of plastic scintillator panels equipped with photo multipliers (see figure 3.1). Thus, the task of the muon veto cut is to discard events in the detectors coincident with the muon veto. The main challenge of this cut is to precisely determine the time of the energy deposition in the cryogenic detectors. Compared to the cryogenic detector, the uncertainty induced by the finite time resolution of the scintillation light signal in the muon veto panels is negligible.

Most of the triggers of the muon veto are not caused by muons, but by γ-rays interacting in the vicinity of the photo multipliers with no chance to reach the cryogenic detectors. Thus, the vast majority of coincidences between a detector and the muon veto are random coincidences. The choice of the time window marking an event coincident with the muon veto and, thus, being removed from the analysis has therefore to be chosen in the light of two competing requirements: On the one hand, the window should be as small as possible to reduce the number of random coincidences and, consequently, the amount of removed exposure. On the other hand, it has to be ensured that no real coincidences survive the cut, as in particular muon-induced neutrons may mimic a potential dark matter signal. The following subsection will discuss the precision of the time reconstruction, which was the basis for choosing a coincidence window of ± 2 ms.

Precision of the Time Reconstruction

In [125] it was shown that the shift parameter of the standard event fit provides the most precise determination of the onset of a pulse and, therefore, the time of the energy deposition. Real coincidences between muon veto and cryogenic detector(s) have a fixed time and, therefore, manifest themselves as a peak on top of the Poissonian distribution describing the random coincidences. This can be seen in the histogram depicted in figure 6.7, showing the time difference between the muon veto trigger and an exemplary phonon detector operated in the previous phase 1.

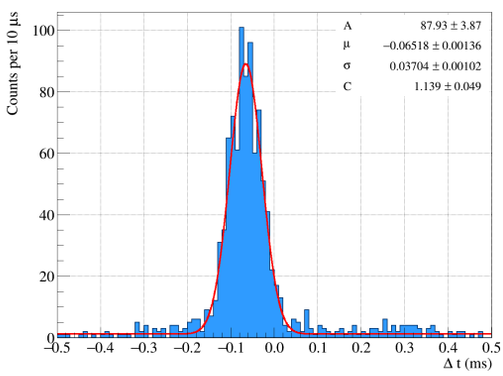

Figure 6.7.: Histogram of the time difference Δt given by the trigger time of the muon veto minus the time of the event in the cryogenic detector, as determined using the shift parameter. The red line corresponds to a fit using a Gaussian function (A,μ,σ) plus a constant level C. Data from phase 1, [125], fit values for μ and σ given in ms in the legend.

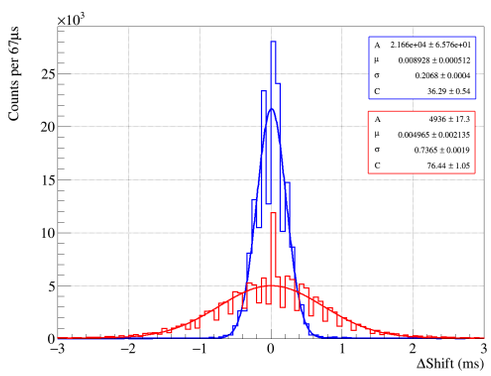

Figure 6.8.: Difference between the nominal and the reconstructed value for the shift parameter (ΔShift) for simulated pulses for Lise with equivalent energies of 0.3 keV in red and 1 keV in blue. The legend lists the parameters for the fits (solid lines) of a sum of Gaussian function (A,μ,σ) and a constant C. Fit values μ and σ are given in ms in the legend.

The red curve corresponds to a fit using a Gaussian function describing the shape of the peak on top of a constant C. In the narrow time window analyzed, a constant level is a very good approximation for the Poissonian distribution. This fit suggests that a cut of (65$\pm$185) μs would tag muon coincident events with a certainty of 5 σ. However, as will be shown in the following, the precision of the time reconstruction decreases for the small pulses analyzed in this work, requiring a substantially larger coincidence window.

For two reasons the study of [125] cannot be repeated for phase 2. Firstly, the sensitivity of the muon veto was increased, leading to a rise in trigger rate of the muon veto of roughly a factor of four compared to phase 1. Secondly, the new inner PE shielding substantially reduces the probability for muon-induced neutrons (e.g. by reactions of the muon in the rock or the Pb/Cu-shielding) to reach the detectors. Both effects cause the peak of real coincidences to hardly emerge from the level of random coincidences, making a precise analysis unfeasible.

Nevertheless, a performance estimate on the time determination by the shift parameter may be given using simulated pulses (see section 6.2). For these simulated pulses the time of the artificial energy deposition is known by the shift of the signal template superimposed with the empty baseline. Figure 6.8 shows histograms for ΔShift which is defined as the time difference between the nominal and the reconstructed shift; in blue for pulses with a simulated energy of 1 keV and in red for an energy of 300 eV.

Both histograms are fit with a Gaussian function which serves as an approximative description of the distribution observed. For both energies the time bin with ΔShift=0 which corresponds to the standard event fit finding exactly the correct shift is significantly above the Gaussian function, in particular for an energy of 300 eV. Therefore, the true fraction of events being inside the allowed limit is higher than suggested by the parameters of the Gaussian fit. For this study no cleaning (except for a cut for so-called delta spikes, see section 6.5) of the data is involved to give a lower limit on the performance of the standard event fit. Applying cuts would remove pulses affected by certain artifacts which also hamper the finding of the correct shift value for the standard event shift. This results in the very small constant value C which accounts for events were the shift value is not dominated by the simulated pulse, but e.g. a pile-up pulse.

Obviously, the precision of the shift parameter decreases for smaller energy depositions (for smaller pulses). At 1 keV an interval of ± 1 ms roughly equals $\pm 5\,\sigma$ for the Gaussian fit function. At 300 eV "only" $\pm 3\,\sigma$ of events are inside the chosen interval of ± 2 ms. However, $\pm 3\,\sigma$ still corresponds to a rejection power of 99.7 % which is clearly sufficient given the low anticipated rate of neutrons. No results for TUM40 are shown here, mainly because the lowest energy analyzed for TUM40 is 0.6 keV where the precision of the reconstruction of the shift parameter is better than for Lise at 0.3 keV, even when taking into account the enhanced energy resolution of Lise.

The effect of this generous choice for the coincidence window is a significant decrease in exposure due to random coincidences between the muon veto - which triggers with an average rate (throughout the whole data taking) of roughly 20 Hz - and events in the detectors. For the given rate one calculates a probability of 7.7 % using Poissonian statistics (details are e.g. given in [125]). It should be mentioned that muons generally lead to much higher signals in the PMTs of the muon veto panels than γ-rays. Thus, neglecting low signals in the muon veto panels as potential veto events would significantly reduce the rate of random coincidences and consequently increase the net exposure. However, for example for muons hitting the very edge of a panel, the signal height in the PMT will also be substantially smaller. To reduce the number of potentially unidentified muon-induced events as far as possible, all triggers of the muon veto are considered, regardless of their signal height.

6.7.2. Coincidences Between Detectors

Given the low expected interaction probability of dark matter particles with ordinary matter, scatterings of WIMPs in multiple detectors can be excluded. Thus, the so-called coincidence cut removes any event with any of the other detectors in coincidence. Thereby, no criteria are set for the secondary pulses in the other detectors. As the time difference be-

tween two (or more) detectors is determined using the shift parameter for both detectors [5] a larger time interval of ± 5 ms is used. However, the rate of the detectors is more than one order of magnitude lower, than for the muon veto. Thus, the reduction of exposure due to random coincidences clearly is negligible, even for an interval of ± 5 ms.

In phase 1 the multiplicity, defined as the number of detectors triggering in coincidence, was used to estimate the level of the neutron background, as well as its origin (see section 4.1.1). However, due to the new inner PE-shielding not enough statistics is available to perform such a study based on Lise and TUM40, only.

6.8. Automatic RMS Cut

From the standard event fit we derive the RMS which quantifies the deviation between the standard event and the pulse. The main difference between the quality cuts and the RMS cut is that the former requires an awareness for the presence of a certain artifact while the latter acts as a "general-purpose" cut removing all events with a deviation from the nominal pulse shape.

Two major challenges have to be met when designing an appropriate event selection based on the RMS. Firstly, for most detectors the RMS exhibits a dependence on energy which is in general of arbitrary shape. Secondly, the RMS is directly influenced by the baseline noise, which is in turn not completely stable over time. Consequently, training set data can only be used to design the cut assuming that the baseline noise level in the training and in the final data set is comparable, which is unknown a priori.[6] Additionally, it should be considered that the RMS cut removes a significant fraction of potential signal events which argues for an objective selection criterion. For the outlined reasons an automatic RMS cut was implemented within this thesis, which is done in three steps:

Step 1 Split the events in bins of energy.

Step 2 Fit a Gaussian function to the RMS distribution separately for each energy bin.

Step 3 Remove all events from the data set where the RMS value exceeds a predefined distance (in terms of σ) from the mean of the Gaussian of the corresponding energy bin.

The outcome for the detector Lise is shown in figure 6.9 showing the RMS as a function of energy, including the cut values chosen for the energy bins. As one can see, the binning allows the cut to follow the energy-dependent RMS distribution. The width of the bins is chosen a-priori on the training set and has to be balanced between being large enough for a sufficient number of events in each bin and being small enough to appropriately follow the energy dependence.

[5] If the shift parameter is not available for a secondary pulse the peak onset determined using a moving average is used instead. However, these cases are rare.

[6] In phase 1, the variations of the baseline noise with time were much more severe [125] which forced the splitting of the data set in different periods of similar noise level.

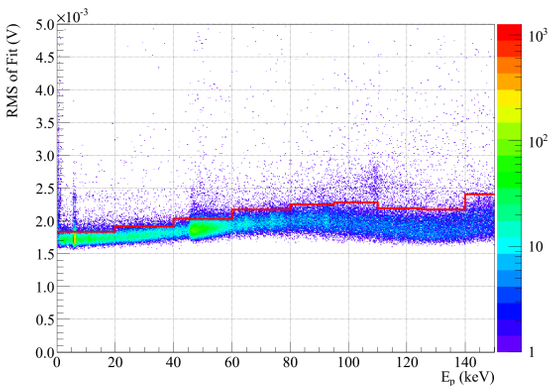

Figure 6.9.: RMS distribution of Lise in the dark matter data set as a function of energy. All events above the red line are discarded by the automatic RMS cut.

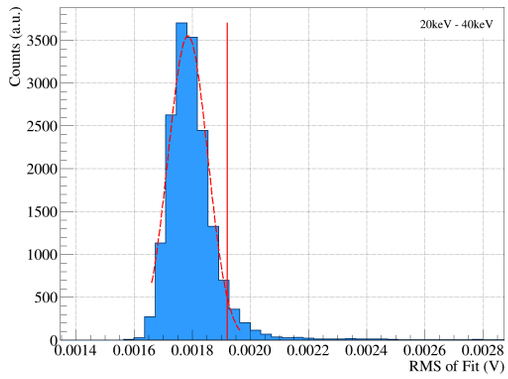

Figure 6.10.: Data in the energy bin from 20 keV to 40 keV for the detector Lise, including the Gaussian fit function (dashed red) and the resulting cut limit (solid red) for the respective energy bin.

The RMS distribution in each bin, as shown on the example of the bin from 20 keV to 40 keV in figure 6.10, would follow a Gaussian distribution, if it was solely affected by baseline noise. Any deviation from the pulse shape of the standard event results in an additional contribution to the RMS and, thus, ends up in the right tail seen in figure 6.10. Therefore, the aim of fitting a Gaussian is to describe the RMS distribution caused by the baseline noise and discard any event incompatible with fluctuations of the baseline noise only. The result of this fit is depicted in dashed red in figure 6.10. For a sufficiently cleaned data set (by the quality cuts applied before) no convergence problems for the Gaussian fit are observed for reasonably chosen start values and fit ranges.

For this work every event with an RMS value being $2\,\sigma$ above the mean of the fitted Gaussian is discarded for all phonon and light detectors with the cut on the light detector being done on the basis of events surviving the cut in the phonon detector. For the example bin depicted in figure 6.10 the cut value determined with this procedure is drawn as solid red line. Finally, all cut values are saved and used later on to determine the efficiency of the RMS cut.

6.9. Final Signal Survival Probability

To maintain a blind analysis all cuts are designed using training set data only and then are applied without any change to the final data set. However, the efficiency of a cut may be different between training and data set, e.g. in the presence of changing noise conditions. Thus, the empty baselines from the dark matter data set are used to create artificial signal events, closely spaced in energy. All cuts that are applied on the real data are then also applied on the artificially created data set. The cut efficiency of a cut at a certain energy is then given by the fraction of artificial pulses surviving the respective cut.

Figure 6.11 shows the cut efficiencies for TUM40 and Lise on the dark matter set after

cumulative application, again with the respective energy thresholds marked as vertical magenta lines. The energy (x-axis) corresponds to the simulated energy of the artificial pulses sampled at discrete energies (marked by circles in the efficiency curves). Simulated and reconstructed energy in general differ, mainly caused by the finite resolution of the standard event fit.[7] Due to the finite resolution an artificial pulse with a simulated energy below threshold might get assigned a reconstructed energy above threshold (above the energy cut, see section 6.4) which is the reason for the efficiencies not dropping to zero immediately at threshold energy. Obviously, also the other direction is possible, namely that an event with a simulated energy above threshold might get assigned an energy below threshold and, hence, be removed by the cut on the energy which is evaluated in combination with the quality cuts (yellow curve). This effect is the one reason for the energy-dependence of the yellow curve, especially evident for Lise in figure 6.11b.

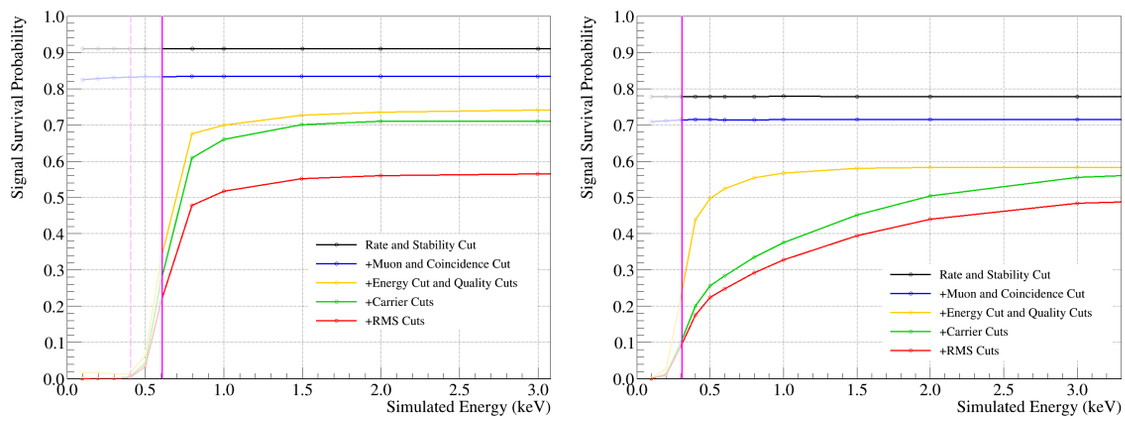

(a) TUM40 (b) Lise

Figure 6.11.: Cumulative cut efficiencies (=signal survival probabilities) as a function of simulated energy. The solid vertical magenta lines mark the energy thresholds used in the dark matter set.

The first cut applied is the rate & stability cut (black line) which acts on the rate of particle pulses and on the control pulses and, therefore, is energy-independent. The rather stringent rate cut applied for Lise causes a larger removal of exposure compared to TUM40 (see section 6.3). Since the vast majority of events coincident with the muon veto (or other detector modules) are random coincidences, the blue line depicting the efficiency of the corresponding cuts is also constant over the whole energy range above threshold energy. The first family of cuts introducing an energy dependence are the quality cuts (yellow line). However, comparing the carrier cuts (green) for Lise and TUM40 reveals a much stronger dropping efficiency for Lise than for TUM40 which is mainly a result of the aforementioned superior discrimination power of the linearized RMS difference compared to the one-dimensional cut on the *Peak Position - Onset* parameter. The strong decrease in Lise is to some extent lessened by the RMS cut (red line) which removes a smaller fraction at

[7] In rare cases there might also be pile-up events between an empty baseline and a real particle interaction.

very low energies than for slightly higher energies. The most viable explanation is that the *Peak Position - Onset* already removes many events which would otherwise be removed by the RMS cut. At threshold energy the final signal survival probability (red line = all cuts applied) is roughly 10 % for Lise and 22 % for TUM40 (with trigger setting I: 0.6 keV).

Using artificially created events to determine the signal survival probabilities for the cuts was used for the first time in the framework of the analysis presented in this work (first published in [75]) arising from the requirements of a low-threshold analysis. In previous analyses (e.g. in [72]) lower energy boundaries of > 10 keV were set for the energy range of interest for the dark matter search. In those analyses the signal survival probability was estimated by classifying the cuts in two categories: those which only remove artifacts (e.g. quality cuts) and those which remove unwanted background and part of the signal (e.g. the RMS cut). While this estimation was found to be roughly compatible with the much more precise determination presented here, a look at figure 6.11 reveals that the simple estimate no longer holds for very low energies, where a strong energy dependence of the efficiency is evident.

Obviously, for the rate & stability cut and the coincidence cuts the amount of removed exposure can be calculated analytically, thus the empty baseline method presented here does not yield a gain in precision. However, the empty baseline procedure is much more straight-forward reducing error-proneness.

6.10. Results

This section will present the low-energy spectra for the detectors TUM40 and Lise, beginning with an investigation of the full data set obtained in the whole phase 2 (see table 5.2). Afterwards, the discussion will focus on the dark matter data set, which are the data relevant for the final dark matter result.

6.10.1. Complete Phase 2 Data Set

Figure 6.12 depicts the energy spectra for TUM40 and Lise in the complete phase 2 data set (see section 5.1) equally binned with a bin size of 25 eV and cropped at a maximal bin content of 120.

An observation is that TUM40 has a drastically lower background level. Using a simple estimate by counting the number of events in the energy range between 1 keV and 40 keV and dividing by the exposure weighted with the average cut efficiency for this energy range one obtains a level of 3.7 counts/(keV kg day) for TUM40 and 15.4 counts/(keV kg day) for Lise. However, a substantial part of the background in this energy range in Lise arises from a double peak at 6 keV which originates from an accidental illumination with an ^{55}Fe-source installed to calibrate the light detector of an adjacent detector module. Subtracting this external background contribution results in a value of 9.6 counts/(keV kg day) for Lise which is more than a factor of two higher than for TUM40.

Both, the significant lower background level in the region of interest, as well as the absence of a crystal-intrinsic ^{210}Pb-contamination in TUM40 shows the substantial improve-

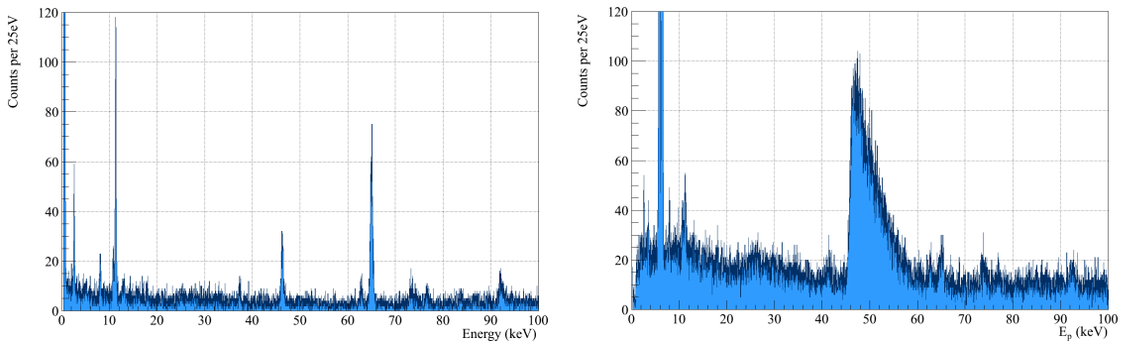

(a) TUM40 - 130kgd (before cuts)

(b) Lise - 159kgd (before cuts)

Figure 6.12.: Energy spectra for TUM40 and Lise in the complete data set of phase 2.

ment concerning background level for crystals grown at TUM (Technische Universität München) to commercially available crystals (see references [127, 128] for a more detailed discussion).

However, not only the total level of background differs, but also the features seen in the spectrum. For Lise a prominent β-spectrum starting at 46.5 keV is evident which can clearly be assigned to an intrinsic contamination with ^{210}Pb , where the γ-ray with an energy of 46.539 keV as well some additional energy from the accompanying β-particle is deposited in the crystal making up for the characteristic triangular shape. For TUM40, instead, only a rather symmetric and much less intense peak at 46.5 keV is observed pointing towards an external origin.

In both crystals, lines at 2.6 keV, $\sim$ 11 keV and 65 keV are present, however with different intensities in the two modules. These lines originate from cosmogenic activation of the crystal material. The reaction in detail is a proton capture on ^{182}W which decays to ^{179}Ta which in turn undergoes an electron capture. The experimental signature is then an energy deposition in the crystal with the full binding energy of the ^{179}Ta electron shells (K, L1, L2, M) (for a detailed description the reader is referred to [128]). Table 6.4 lists the literature energy values, the energy values determined in the data, the relative difference between the two and the width of the Gaussian fit function.

All single peaks in table 6.4 are fit with a Gaussian function superimposed with a constant background level, for the double peaks - ^{179}Hf (L1,L2) and Mn K$_{\alpha,\beta}$ (originating from the external ^{55}Fe X-ray source) - the following model function is used:

$$A_\alpha \exp\Big[-\frac{1}{2}\Big(\frac{E-\mu_\alpha}{\sigma}\Big)^2\Big] + A_\beta \exp\Big[-\frac{1}{2}\Big(\frac{E-\mu_\beta}{\sigma + c(\mu_\beta - \mu_\alpha)}\Big)^2\Big] + P_0 \tag{6.2}$$

Basically the above equation describes two Gaussian functions with means $\mu_{\alpha,\beta}$, amplitudes $A_{\alpha,\beta}$ and a common width σ. However, as the single peaks in table 6.4 show, σ is linearly dependent on the energy which is taken into account by the term $c(\mu_\beta - \mu_\alpha)$. The constant c is determined by a fit of the width of single peaks and a fixed parameter in the fit of the double peaks. The validity of this approach was verified by fitting the highly

populated ^{55}Fe double-peak using two uncorrelated fits yielding compatible results within errors.

The outcome of this fit for the ^{179}Ta in TUM40 was already shown in figure 5.10 (blue histogram), while figure 6.13 depicts the ^{55}Fe double-peak as measured by Lise.

The relative difference of the determined values to the corresponding literature values (second to last column in table 6.4) shows a slight overestimation for TUM40 in the energy range of interest (< 40 keV), however always below 1 %. For Lise the overestimation of the energy of the ^{179}Hf-line at 2.6 keV is 1.6 % which results from not correcting for the reduced relative light output for electron recoils at low energies (non-proportionality effect, see section 7.2). As a reminder, the correction cannot be applied, since the light signal in the light detector Enrico is completely dominated by baseline noise at low energies, not allowing for a precise measurement of the scintillation light produced (see section 5.6). However, it is checked that the impact on the final dark matter result is negligible.

The spectrum of TUM40 exhibits a rise towards the threshold energy starting at around 0.8 keV, which will be extensively discussed in the next subsection.

Detector	Origin	E_{lit} (keV)	E_{fit} (keV)	$\frac{E_{\text{fit}}-E_{\text{lit}}}{E_{\text{lit}}}$ (%)	σ (eV)
TUM40	^{179}Hf (M1)	2.601	2.614 ± 0.007	0.5	95.2 ± 6.9
	Cu	8.041	8.104 ± 0.014	0.8	117 ± 13
	^{179}Hf (L1)	10.74	10.828 ± 0.013	0.8	101 ± 3
	^{179}Hf (L2)	11.271	11.331 ± 0.004	0.5	102 ± 3
	^{210}Pb	46.54	46.293 ± 0.012	-0.5	226 ± 12
	^{179}Hf (K)	65.35	64.993 ± 0.008	-0.5	250 ± 6.8
Lise	^{179}Hf (M1)	2.601	2.643 ± 0.009	1.6	70.3 ± 7.9
	Mn K_α	5.895	5.891 ± 0.001	-0.07	99.3 ± 0.6
	Mn K_β	6.490	6.469 ± 0.002	-0.3	104 ± 0.6
	^{179}Hf (L1)	10.74	10.79 ± 0.03	0.5	141 ± 12
	^{179}Hf (L2)	11.271	11.29 ± 0.02	0.2	145 ± 12

Table 6.4.: Peaks observed in TUM40 and Lise with fitted peak positions E_{fit} and widths σ in comparison to the corresponding literature values E_{lit} (from [143]).

6.10.2. Phase 2 Dark Matter Data Set

Figure 6.14 shows a zoom-in to the low-energy spectrum in the dark matter data sets for TUM40 and Lise, respectively. Including the cut efficiency - red solid line, rescaled to the constant level (=without peaks) - illustrates the different behaviors of TUM40 and Lise close to threshold energy. For Lise good agreement is found between the measured spectrum and the decreasing cut efficiency indicating a roughly constant background level down to threshold. For TUM40, on the other hand, a strong rise is found, despite the dropping cut efficiency. The origin of this peak could not be clearly identified in the framework of this analysis. Using data taken with the low threshold setting (0.4 keV) indicates a mean

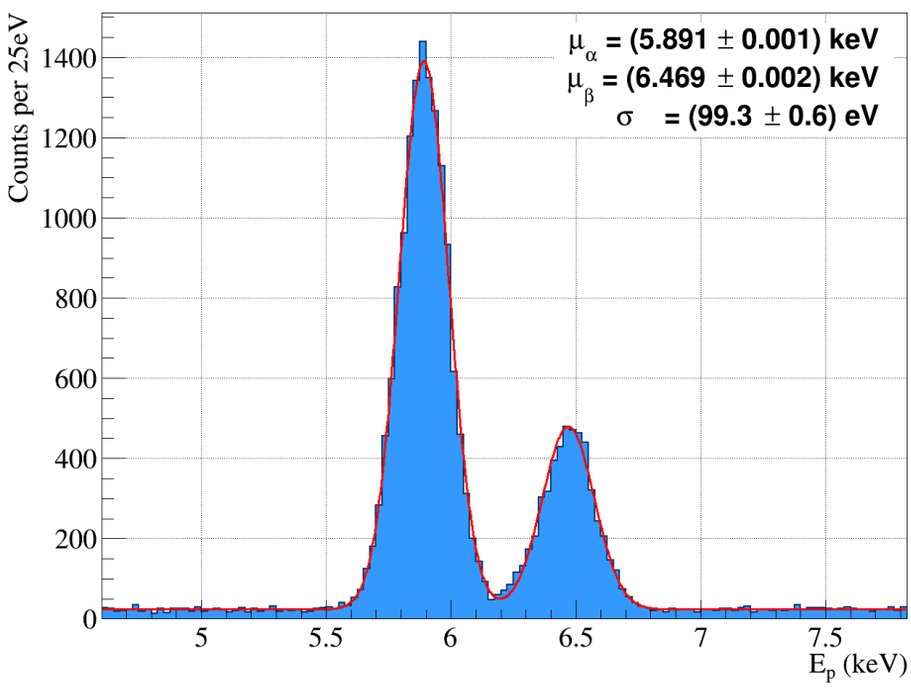

Figure 6.13.: Double peak caused by the illumination of the detector Lise with an ^{55}Fe-source. The red line corresponds to a fit with two Gaussian functions with a correlated width (see equation 6.2) on top of a constant background level. Relevant fit parameters are given in the legend.

light yield larger than zero pointing to a partly particle-induced origin. However, no other of the detectors operated in phase 2 with a low threshold (see appendix, section A.1.2) observes an excess at that energy. Since none of those other detectors is equipped with a crystal grown at TUM, future measurements may give further insight on the origin of the rise. Additional complications arise from the fact that also misidentified carrier-like events and possibly noise-triggers contribute to this rise. Thus, further investigations (on TUM40 and phase 2 data) are done in [145] using an artificial neural network aiming for a higher discrimination power for carrier events and, thus, a better separation of the potential contributions. As will be shown later, the presence of this rise limits the sensitivity for very low-mass dark matter particles as it introduces an *effective threshold* at about 1 keV significantly above the hardware trigger threshold of 0.6 keV.

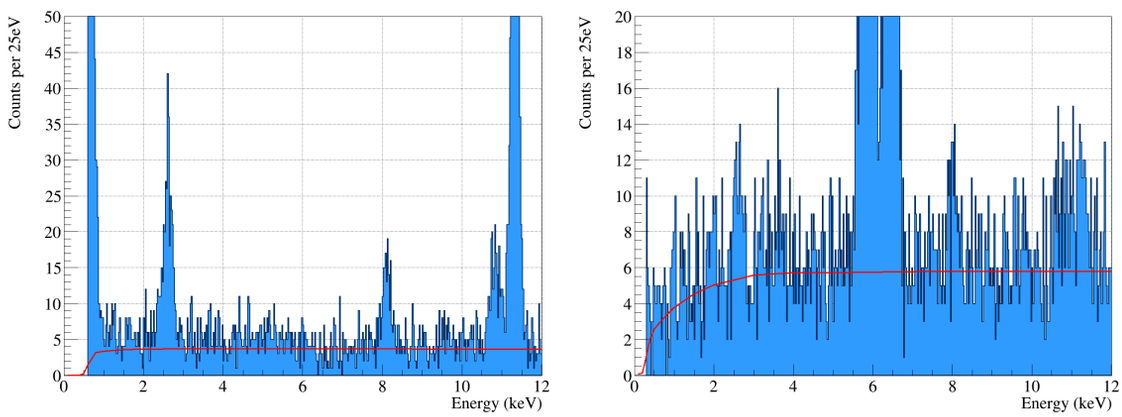

(a) TUM40 (b) Lise

Figure 6.14.: Low-energy spectra of TUM40 and Lise of data from the respective dark matter sets. The red line corresponds to the final cut efficiency, as determined in section 6.2.

6.10.3. Long-Term Stability

The high statistics given for the ^{55}Fe double-peak allows to verify the long-term stability of the energy calibration. Figure 6.15a shows the events (gray dots) in the relevant energy range as a function of live time for the detector Lise in the whole phase 2. To study possible time-dependencies of the energy scale and/or the energy resolution the fit done in figure 6.13 (using equation 6.2) is repeated separately for time bins of two weeks. Two weeks are chosen to guarantee sufficient statistics in almost all time bins. However, a few bins with less than 200 events have to be excluded.

The outcome of each fit is drawn in blue for the peak position of the Mn K_α-line and in magenta for Mn K_β line. The error bars indicate the statistical uncertainty derived from the fit. The solid lines depict the values obtained for the fit of the whole data set (see figure 6.13). As one can see, the vast majority of bins is within errors compatible to the mean value, in particular for the higher populated K_α-line.

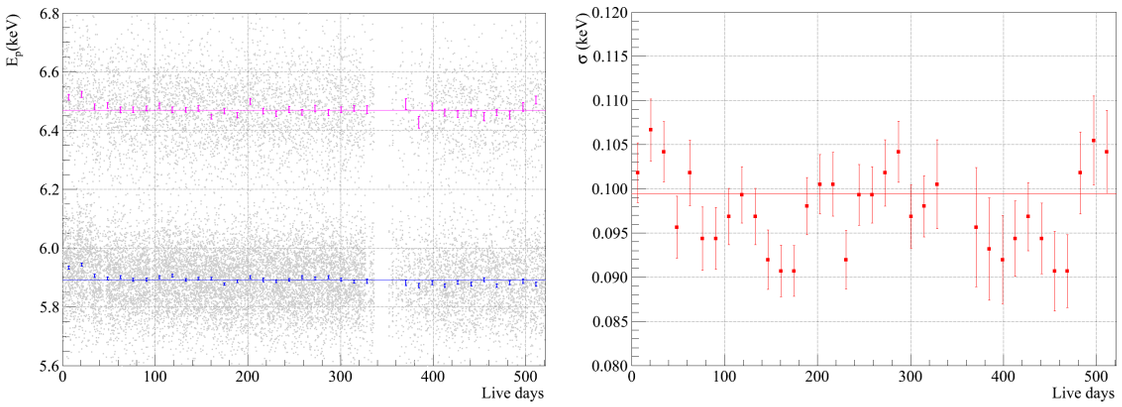

(a) Mn-lines (magenta: K_α, blue: K_β)

(b) Width (σ)

Figure 6.15.: Data (gray, left plot) taken in phase 2 for the detector Lise as a function of live time (in days). The double ^{55}Fe-peak is fit in time bins of two weeks with two Gaussian functions of the same width on top of a constant background level. For each time bin the fitted peak positions for the Mn K_α and K_β lines are shown on the left in blue and magenta, respectively. The width of the Gaussian functions (in σ) is shown on the right. In both plots horizontal lines depict the mean value for the whole data set for the corresponding parameter, as determined in figure 6.13. The error bars indicate statistical fit uncertainties.

Figure 6.15b shows that not only the absolute energy scale exhibits an excellent stability, but also the resolution. The correlated width (σ) of the Gaussian functions is depicted in red points for the same time bins as in figure 6.15a with all bins showing a deviation of less than 10 % from the mean value (solid red line).

In summary this analysis of the double peak originating from X-rays emitted by an ^{55}Fe-source proves an excellent long-term stability, even for time scales beyond one year. This is in particular remarkable in the light of the rather low energy of the X-rays, where the impact of a potentially unstable baseline noise (see section 5.8) is more pronounced than for higher energies.

7. Resolution, Bands and Signal Expectation

This chapter will discuss the modelling of the bands corresponding to different event classes in the light (yield) energy plane. The width of the bands is dominated by the resolution of the light detector, however also the finite resolution of the phonon detector has some impact, which is the starting point of this chapter.

7.1. Resolution and Baseline Noise

The resolution of the phonon detector mainly depends on the finite baseline noise. An additional contribution arises from the shape of the transition, depending on the pulse height and, thus, affecting particle as well as test pulses. The resolution for particle events may furthermore be influenced by potential position dependencies, proportional to the energy deposited. In conclusion, neither test nor particle pulses provide clean and isolated information on the impact of the baseline noise on the energy resolution.

Therefore, the artificially created events are used instead (as utilized for the determination of the cut efficiencies, see section 6.2), by fitting the reconstructed energy of each simulated energy with a Gaussian function. Thereby, small simulated energies, for which the cut efficiency is not constant in energy, are excluded because the non-constant cut efficiency leads to an asymmetric peak: events with a lower reconstructed energy (left side of Gaussian) have a higher probability to be removed by a cut than events in the right side of the peak. To get a statically robust information on the resolution at zero energy the values are obtained by averaging several simulated energies.

Both detectors analyzed in this work reach a value well below 0.1 keV; details are listed in table 7.1.

	Resolution: $\sigma =$
TUM40	(74.1 ± 0.2) eV
Lise	(60.7 ± 0.3) eV

Table 7.1.: Baseline noise, equalling the phonon energy resolution at zero energy, determined by evaluating the width of peaks in reconstructed energy originating from monoenergetic simulated events.

7.2. Description of the e^-/γ-Band

The first step to derive the bands for the different event classes is to fit a model of the e^-/γ-band to the data in the light (L) - energy (E) plane acquired with each detector module. It shall be emphasized that L is the energy measured in the light channel ($E_l = L$) which should not be confused with the light yield LY. Figure 7.1 shows the bands of e^-/γ-events and recoils off oxygen and tungsten for TUM40, left in the light (L) - energy (E) plane and right in the light yield (LY) - energy (E) plane.

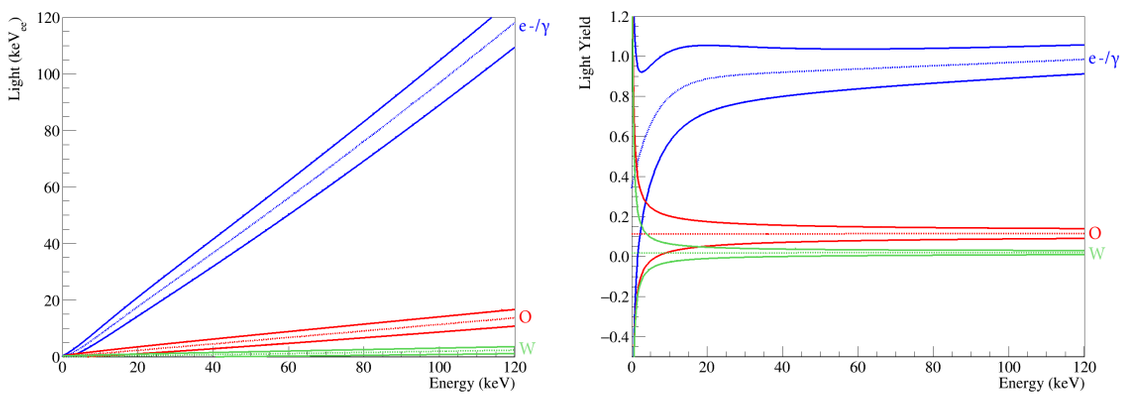

(a) Light vs. energy (b) Light yield vs. energy

Figure 7.1.: Bands determined for TUM40, blue for e^-/γ-events, red and green for recoils off oxygen and tungsten, respectively. The dashed lines mark the mean of the corresponding band, the solid lines the corresponding 90 % upper and lower boundaries.

Once the e^-/γ-band is known, all other bands can be calculated with the corresponding quenching factor and its energy dependence, as will be described throughout this chapter. The notation and fit procedure presented here largely follows [71].

Mean The mean light output of an e^-/γ-event L_γ as a function of energy is parametrized by the following equation:

$$L_\gamma = (L_0 E + L_1 E^2)[1 - L_2 \exp\left(\frac{-E}{L_3}\right)] \tag{7.1}$$

with L_{0-3} being free parameters in the fit. The amount of scintillation light produced linearly depends on the energy deposited which is accounted for by the proportionality factor L_0 usually close to one by calibration. To allow for small deviations from this direct proportionality the empirical factor L_1 is added as it generally improves the fit result. Due to a saturation effect in the amount of energy lost per unit path length (dE/dx), the e^-/γ-band starts to bend down towards low energies (best visible in the light yield coordinate, see figure 7.1b). This behavior, which is common for inorganic scintillators, is referred to as non-proportionality effect [146]. The second term in equation 7.1 models this effect, with L_2 quantifying the strength of the non-proportionality effect and L_3 describing the curvature of the downward bending.

Width The width of the e^-/γ-band is a Gaussian function centered around its mean L_γ:

$$\sigma_\gamma(L_\gamma) = \sqrt{S_0 + S_1 L_\gamma + S_2 L_\gamma^2} \tag{7.2}$$

In the equation above S_0 denotes the resolution at zero energy (the baseline noise), which is typically dominated by the baseline noise of the light detector, in particular for the modules analyzed in this work featuring highly performing phonon detectors. A finite phonon resolution ($\sigma_p(E)$) leads to a mismatch between the true energy deposited in the crystal and the reconstructed energy E. Thus, even for an ideal light detector with zero resolution, bands of finite width would appear in the light-energy plane. The impact of the uncertainty $\sigma_p(E)$ on the width of the e^-/γ-band depends on its slope dL_γ/dE. However, for the e^-/γ-band the slope is practically one (see figure 7.1a), thus S_0 is given by:

$$S_0 = \sigma_{l,0}^2 + \left(\frac{dL_\gamma}{dE} \cdot \sigma_{p,0}\right)^2 \simeq \sigma_{l,0}^2 + (1 \cdot \sigma_{p,0})^2 \tag{7.3}$$

It deserves to be mentioned that the baseline resolution of typical CRESST-II light detectors in absolute scales is $\mathcal{O}$(5-10 eV)[1] which is substantially better than for phonon detectors ($\geq$60 eV, as was shown in section 7.1). However, $\sigma_{l,0}$ and $\sigma_{p,0}$ are given in electron-equivalent and, since for the stick or the conventional detector design only $\sim$1-2 % of the energy deposited in the crystal are measured in the light detector, $\sigma_{l,0}^2$ dominates over $\sigma_{p,0}^2$.

In principle, S_0 can be treated as a free fit parameter in the fit of the e^-/γ-band, however, this often hinders convergence. In such a case S_0 is derived from the baseline noise of phonon and light detector and then fixed in the fit.

The second term ($S_1 L$) in equation 7.2 accounts for the quantization of the scintillation light by the number of photons produced (N), thus leading to Poisson fluctuations scaling with $\sqrt{L} \propto \sqrt{N}$. The quantity S_1 is the energy which has in average to be deposited in the crystal to measure one photon in the light detector.

To allow for an additional contribution to the width of the bands scaling with energy, as e.g. position dependencies, the term $S_2 L^2$ is added. Typically very small values ($\mathcal{O}(10^{-4} - 10^{-5})$) are assigned by the fit for S_2.

Excess Light Events The term "excess light" labels events exhibiting a light signal larger than e^-/γ-events which in turn exhibit the highest light output compared to all other particles producing scintillation light in the crystal. The underlying nature for excess light events could not be tracked down with full certainty, however, the most viable origin is external electrons penetrating the module and thereby producing scintillation light in the foil surrounding the detector before being absorbed in the crystal. This idea is further supported by two observations. Firstly, excess light events exhibit a slight deviation from the nominal light pulse shape indicating a second, faster mechanism of light production apart from scintillation in $CaWO_4$. Secondly, no excess light events are present in the two

[1] This value indicates that the performance of CRESST light detectors is not too far away from single-photon detection, as the mean photon energy for the blue $CaWO_4$ scintillation light is roughly 3 eV.

prototype modules where the crystal is fully surrounded by a beaker-shaped light detector, preventing external electrons to reach the crystal. Thus, the non-existence of excess light events in the beaker modules indicates a dominantly external origin of the excess light events.

To account for the contribution of the excess light events to the e^-/γ-band an empirical model is used. The data show a decrease of the density of excess light events with increasing energy which is modelled by an exponential decay with decay constant E^{el}_{decay}. The energy-dependent fraction of excess light events is given by

$$X(E) = X_0 \exp\left(\frac{-E}{E^{el}_{\text{decay}}}\right) \tag{7.4}$$

with X_0 denoting the fraction of excess light events at zero energy. Consequently, $1-X(E)$ is the fraction of normal (not excess light) events in the e^-/γ-band at energy E. It should be noted that the densities (in the light-energy plane) of excess light events and the normal e^-/γ-events are a-priori not correlated, as excess light events are supposed to mainly be of external origin and normal e^-/γ-events dominantly from crystal-intrinsic origin. Thus, parametrizing the excess light events as a fraction of the normal e^-/γ-events is only valid for a constant and featureless energy spectrum of the e^-/γ-events. This is to a good extent fulfilled for Lise, but not for TUM40, exhibiting pronounced γ-lines. However, a cross-check with a model parametrizing the excess light contribution completely independent from the e^-/γ-events proved this simplification to have negligible impact for the e^-/γ-band fits of Lise and TUM40.

In the light coordinate an exponential decay (with decay constant L^{el}_{decay}) is used to describe the observed decrease starting at the mean (L^{γ}) of the e^-/γ-band. To obtain the final model for the e^-/γ-band the contribution of the excess light events has to be convolved with the finite width of the e^-/γ-band. For the empirical model chosen here, it is possible to derive an analytic expression for this convolution, as given in [71].

7.2.1. Likelihood Fit

In total, the model of the e^-/γ-band contains eleven parameters which are fit to the data using a maximum likelihood fit. While maximum likelihood methods will be discussed in detail in chapter 10, the basic idea shall be sketched here. Prerequisite for a maximum likelihood fit is a model (often referred to as likelihood function) assigning a likelihood value ($\mathcal{L}_i(E_i, L_i)$) to each data point in the parameter space which spans over the energy E and the light L for the given application. In other words, the likelihood value $\mathcal{L}_i(E_i, L_i)$ equals the probability to observe an event with observables E_i, L_i.

The likelihood function $\mathcal{L}_i(E_i, L_i)$ for the fit of the e^-/γ-band is composed of the mean line L_γ (equation 7.1) and the width $\sigma_\gamma(L)$ (equation 7.2) convolved with the contribution of the excess light events. The full analytic expression may be found in [71].

In a second step the individual probabilities for all events observed are multiplied

$$\mathcal{L} = \prod_{i=0}^{N} \mathcal{L}_i(E_i, L_i) \tag{7.5}$$

yielding a single likelihood value $\mathcal{L}$ quantifying the probability to observe the distribution of data in the parameter space given the underlying model was true. Now, the idea of a likelihood fit is to find those values for the fit parameters yielding the maximum value $\mathcal{L}$ and, thus, the maximal achievable agreement between data and model.

In practice, $\mathcal{L}$ is not maximized, but instead the $-\log\mathcal{L}$ is minimized.[2] Firstly, because powerful function minimizers are commonly available and secondly, because taking the logarithm avoids too large numbers for $\mathcal{L}$ which are easily obtained for data sets with a large number of events.

7.3. Results of the Band Fit

Table 7.2 lists the fit parameter values obtained for TUM40 and Lise with the maximum likelihood fit. The corresponding e^-/γ-bands for TUM40 and Lise are depicted in figure 7.2. Thereby, the solid lines denote the 90 % boundaries, thus 80 % of the e^-/γ-events are expected in between. The dashed line marks the mean of the e^-/γ-band. It should be noted that the bands drawn in figure 7.2 show the e^-/γ-band for TUM40 and Lise, without the contribution of the excess light events.

Additionally, figure 7.3 shows projections on the light yield-coordinate for the exemplary energy slice from 7.5 keV to 12.5 keV for TUM40 (a) and Lise (b). Included are the contributions from the excess light events (dotted green), the e^-/γ-events (solid) blue and the sum of both (dashed red).

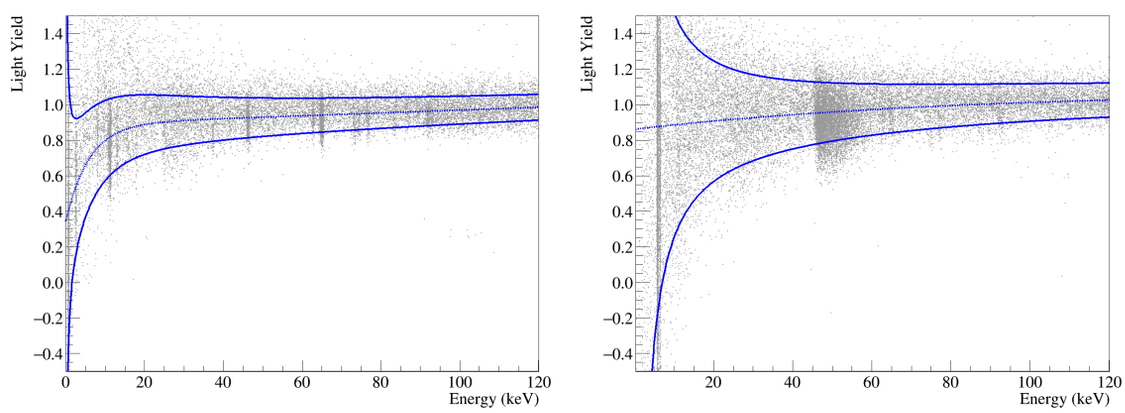

(a) TUM40 (b) Lise

Figure 7.2.: Results for the fits of the e^-/γ-band depicting the 90 % upper and lower boundaries of the band as solid blue lines, the mean line in dashed blue and the data in gray dots.

The information contained in the plots and the corresponding fit parameters will be outlined in the following with a special emphasis on the differences between the two detector modules.

[2] Since the logarithm is a strictly monotonically increasing function, the maximum found for $\log\mathcal{L}$ also maximizes $\mathcal{L}$.

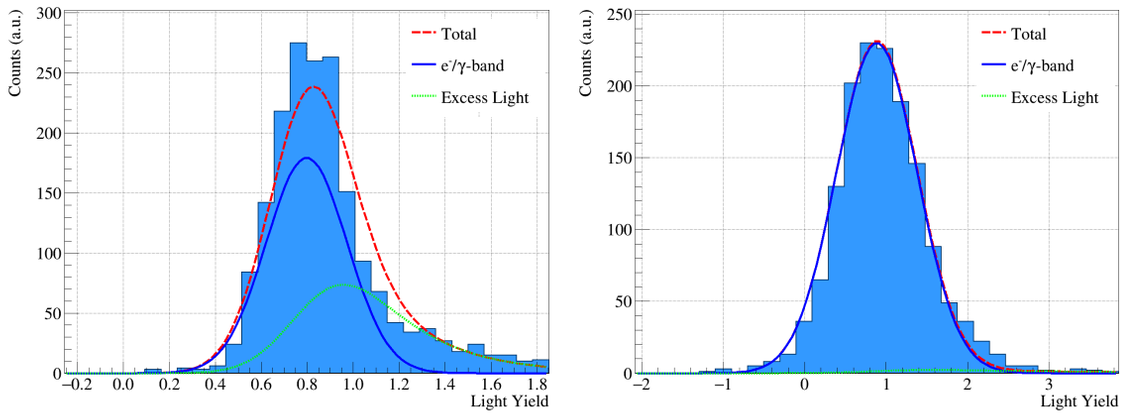

(a) TUM40 (b) Lise

Figure 7.3.: Light yield distribution in the energy range of 10 ± 2.5 keV for TUM40 and Lise. In each plot the red dashed line depicts the total model consisting of contributions from the e^-/γ-band (solid blue) and the excess light events (dotted green).

The already extensively discussed differences in the background spectra of TUM40 and Lise (see section 6.10) are also clearly evident in the light yield-plots, in particular, with TUM40 exhibiting several γ-lines and the prominent β-spectrum starting at 46 keV for Lise.

As already discussed in section 5.5, by calibration the light yield of a γ-event with an energy of 122 keV is set to one with the CPE-factor of the light detector being the decisive parameter. Looking at L_0 and L_1 indicates a slight tilt of the e^-/γ-bands for Lise and TUM40, however in opposite direction. It should be emphasized that the tilts found have small impact in the low-energy range which is relevant for the dark matter analysis.

The non-proportionality effect, which causes the bands to bend down towards lower energies described by the parameters L_2 and L_3, is much more pronounced in TUM40 than in Lise. As one can see in figure 7.2a the mean light yield for an e^-/γ-event at 1 keV in TUM40 is only around 0.5, while for Lise it is still at 0.85 (see figure 7.2b).

Both, Enrico (light detector of Lise) and Michael (light detector of TUM40) are CRESST-II light detectors of standard design. While Michael exhibits a typical performance in terms of energy resolution, Enrico clearly falls back by roughly one order of magnitude. This statement is reflected by the largely differing S_0-parameter (the influence of the slightly different phonon detector performance is negligible for this comparison). The large S_0-value obtained for Lise results in the pronounced broadening of the e^-/γ-band observed towards low energies. For high energies, instead, the widths of the bands become similar, since in this regime the photon-statistic term $S_1\sqrt{L}$ dominates over the baseline noise quantified by S_0 and the parameter S_1 is almost equal for both modules.

As was already mentioned, the performance of CRESST light detectors is not too far away from the ultimate limit, namely single photon detection, although, further performance improvements obviously become more and more challenging when approaching this limit. However, for the case of TUM40 the statistic term $S_1\sqrt{L}$ is already larger than S_0

	Parameter	TUM40	Lise
Mean	L_0	0.888	1.10
	L_1 (keV^{-1})	$7.97 \cdot 10^{-4}$	$-1.25 \cdot 10^{-4}$
	L_2	0.616	0.221
	L_3 (keV)	5.82	92.2
Width	$\sigma_{p,0}$ (keV)	0.0741*	0.0607*
	S_0 (keV$^2_{ee}$)	0.0661*	21.2
	S_1 (keV$_{ee}$)	0.379	0.363
	S_2	$8.86 \cdot 10^{-5}$	$9.35 \cdot 10^{-4}$
Excess Light	X_0	0.384	0.0273
	E^{el}_{decay} (keV)	$4.60 \cdot 10^6$	91.4
	L^{el}_{decay} (keV$_{ee}$)	2.83	20.9

Table 7.2.: Values for the parameters describing the position of the e^-/γ-band in the light yield - energy plane for TUM40 and Lise with the baseline resolution of the phonon detector $\sigma_{p,0}$ listed in addition. To express that $\sigma_{p,0}$ is not a fit parameter of the maximum likelihood the corresponding parameter values are marked with *, as is the S_0-value for TUM40, since for this detector S_0 is calculated using equation 7.3 and fixed in the fit.

at threshold energy (for e^-/γ-events). This implies that further improvements in the absolute baseline resolution of the light detector will hardly yield slimmer bands and, thus, enhanced discrimination power. Optimizing the amount of measured light, however, bears great potential for further improvements, as it affects S_0 and S_1 (both are electron equivalent quantities). Doubling the measured light, which seems feasible considering that less than one third of the scintillation light produced is actually detected for the module designs analyzed in this work [126], would reduce S_1 by a factor of two and $\sigma^2_{l,0} \sim S_0$ by a factor of four. In any case, an increase of, in particular, position dependencies should be avoided, since a non-negligible S_2-term would have a strong impact on the width due to its linear dependence on L.

Another striking difference between TUM40 and Lise is in the parameter determined for the excess light contribution. While for Lise their contribution is determined to be ~ 3 % at zero energy and a decay constant of ~ 90 keV, for TUM40 a practically constant contribution of almost 40 % is obtained with the fit. This observation is also optically visible in figures 7.2a and 7.3a with a significantly higher event density above the band than below. At first glance one could think that this effect may result from a wrong fit, which underestimates the width of the band and compensates by a large contribution of excess light events. However, looking at the γ-lines, which are nicely centered within the band boundaries, disproves this hypothesis (the slight offset of low energy gamma lines is discussed in the next paragraph). To some extent the difference of the fraction of excess light events is explained by the lower level of intrinsic radioactive contaminants in TUM40 than in Lise, however a detailed analysis including Monte Carlo simulations, which is beyond the scope of this work, will be needed to resolve the remaining discrepancy.

Figure 7.2a also shows that certain γ-lines, in particular evident for the 11 keV double-peak, are not perfectly centered in the e^-/γ-band, but rather exhibit a slightly lower light yield. This effect is referred to as gamma-quenching [146, 134] and arises from the different interaction properties for gammas and electrons and the presence of the non-proportionality effect. While an electron directly excites the scintillation process, the energy of a γ-ray is transferred to multiple electrons. As each of those low-energy electrons is affected by the non-proportionality effect the overall light output is decreased for a gamma distributing its energy to multiple electrons compared to single electron of the same energy. However, since the e^-/γ-band is fit in a wide energy range the slightly lower light yield of the γ-lines has only negligible impact on the outcome of the fit parameters.

7.4. Quenched Bands

At this stage, position and shape of the e^-/γ-band in the light-energy parameter space are precisely known. A second ingredient, namely the so-called quenching factor, is needed to calculate a band in the light-energy plane corresponding to another particle interacting in the detector. Thereby, the quenching factor is defined as the light output L_x produced by the particle x relative to the light produced by a γ-particle at the same energy deposit E' in the crystal:

$$QF_x = \frac{L_x(E')}{L_\gamma(E')} \qquad \left(\equiv \frac{LY_x(E')}{LY_\gamma(E')} \right) \tag{7.6}$$

For convenience reasons, very often the inverse quenching factor $QF^{-1} = 1/QF$ is quoted, which is also done in this work.

7.4.1. Energy-Dependent Quenching Factors

Today, the commonly used term "quenching factor" might be misleading, since it is known that quenching - in general - depends on energy. As no framework is available which allows to calculate the quenching factors (or even their energy dependence) for arbitrary materials, the required information have to be obtained experimentally. Using a fast neutron beam the energy dependencies of oxygen and calcium in $CaWO_4$ were measured for the first time within the CRESST collaboration [147, 148]. In general, the energy-dependence of the quenching factor is stronger for light particles. No energy-dependence could be observed for tungsten in this measurement, however the constant value could be determined with unprecedented precision compared to previous measurements. Thus, the quenching factors for all three nuclear recoil bands (oxygen, calcium and tungsten) used in this work are taken from [148].

The implementation of the energy-dependence of the quenching factors for nuclear recoils represents a novelty of the analysis of this work.[3] Thereby, the quenching factors for

[3] We also used this implementation in [148] to show that the results obtained for phase 1 are only mildly affected by the energy-dependent quenching factors.

Nucleus	L_0^{ref}	LY^{∞}	f	λ
O	1.07	0.07908 ± 0.00002	0.7088 ± 0.0008	567.1 ± 0.9
Ca	1.07	0.05949 ± 0.00078	0.1887 ± 0.0022	801.3 ± 18.8

Table 7.3.: Parameters describing the energy-dependent quenching factors for oxygen and calcium (values from [148]).

Event Type / Nucleus	QF^{-1}	Reference
e^-/γ	1.00	
α	4.63	(determined with phase 1 data, [72])
O*	8.03 ± 0.32	[148]
Ca*	15.2 ± 1.0	[148]
W	51.0 ± 5.7	[148]
Pb	70.0	(estimated from phase 1 data)

Table 7.4.: Inverse quenching factors used in this work. The energy-dependent quenching factors (marked with *) are averaged over the energy range of interest: $[E_{th} \sim 0.5$,40 keV]. Differences arising from the different thresholds of Lise and TUM40 are smaller than the precision of the quoted values. The uncertainties, which are dominated by systematics, are based on the errors given in [148]. For a detailed discussion see [147].

oxygen and calcium are parametrized in the following way:

$$QF_x^{-1}(E) = \frac{L_0^{\text{ref}}}{LY_x^{\infty}[1 + f_x \exp(-E/\lambda_x)]} \tag{7.7}$$

with the index x denoting the respective nucleus (oxygen or calcium). The denominator in equation 7.7 basically describes an exponentially decreasing light yield (amplitude f_x, decay length λ_x) which asymptotically approaches LY_x^{∞} - the light yield for the particle x depositing an *infinite* amount of energy. Since the quenching factor is defined relative to the light produced by an e^-/γ-event the parameter L_0^{ref} is added, denoting the L_0-parameter of the reference module used in [148] (L_1^{ref} is negligible). The corresponding parameter values including their statistical uncertainty are listed in table 7.3.

In [147, 148] it was found that the absolute scale of the quenching factors varies between different crystals ($\mathcal{O}(10\,\%)$). To correct for this effect the authors suggest to introduce a crystal-specific scaling factor ϵ, which is also done in this work:

$$QF_x(E) \rightarrow \epsilon \cdot QF_x(E) \tag{7.8}$$

The factor ϵ is precisely determined with neutron calibration data. For kinematic reasons mainly neutrons scattering off oxygen deposit energies well above 100 keV. Thus, measuring the light yield of events in the energy range between 150 keV and 200 keV provides the light yield (averaged over the given energy range) of oxygen scatters, denoted $\overline{LY_O^*}$. The

	ϵ	ϵ^{-1}
TUM40	0.88	1.14
Lise	0.85	1.18

Table 7.5.: Values for ϵ and its inverse for TUM40 and Lise.

average quenching factor for the specific module is then known by $\overline{QF_O^*} = \overline{LY_O^*}/\overline{LY_\gamma}$ and consequently ϵ is given by

$$\epsilon = \frac{\overline{QF_O^*}}{\overline{QF_O}} = \frac{\overline{LY_O^*}/\overline{LY_\gamma}}{\overline{QF_O}} \tag{7.9}$$

with $\overline{QF_O}$ given by averaging the energy-dependent quenching factor for oxygen (equation 7.7 with values of table 7.3) in the given energy range.

Table 7.5 contains the resulting values for TUM40 and Lise, showing a very similar behavior of both detectors.

The above rescaling via equation 7.8 basically decouples the quenching factors (and their energy-dependence) from crystal-specific behavior of light quenching of nuclear recoils. Thus, for both aspects the best information available can be used: On the one hand, the external measurement allows a much more precise determination of the quenching factors than neutron calibration data, in particular for scatterings off tungsten. On the other hand crystal-specific effects can only be determined in the actual measurement campaign with neutron calibration data. This procedure relies on two main implicit assumptions, firstly that the same scaling factor ϵ applies for all three nuclear recoil bands (oxygen, calcium and tungsten) and secondly, that the energy-dependence is independent of the specific crystal. However, for the modules analyzed in this work those potentially simplified assumptions are clearly beyond the resolution power of the light detector dominating the width of the bands. Furthermore, good agreement is found between prediction and neutron calibration data as will be shown in section 7.5.

Measurements of α-particles also indicate a rising relative light output towards lower energies [134] for α-particles hitting the crystal. However, since basically no degraded α-background (see section 4.1.1) is present in phase 2 the energy-dependence of the corresponding quenching factor is irrelevant for this work.

7.4.2. Calculation of the Quenched Bands

Analog to the e^-/γ-band the quenched bands are characterized by a mean line and a Gaussian function describing the energy-dependent width.

Mean Experimentally the non-proportionality effect is only observed for e^-/γ-events and, thus, it is irrelevant for the quenched bands. In other words, the non-proportionality effect may be considered a quenching factor for electrons arising from the increasing dE/dx towards low energies (see section 7.2). The mean light of a quenched band is then given by neglecting the corresponding term in equation 7.1 and accounting for the respective

quenching factor:

$$L_x(E) = QF_x(E) \cdot (L_0 E + L_1 E^2) \tag{7.10}$$

Width Basically, the width of the quenched bands is derived from the width of the e^-/γ-band. Via the fit parameters $S_{0,1,2}$ the e^-/γ-band accounts for the influence of the phonon detector, as well as for the light detector. However, the impact of the phonon detector (as already discussed in section 7.2) depends on the slope of the corresponding band in the light - energy plane and, thus, differs for the quenched bands and the e^-/γ-band. Based on this consideration the procedure to calculate the width of the quenched bands presented in the following is based on three main assumptions:

1. The e^-/γ-band contains both, the resolution of the phonon and the light detector.

2. The resolution of the phonon detector and its energy-dependence $\sigma_p(E)$ are known.

3. E and L are statistically independent quantities and, thus, knowing $\sigma_p(E)$ allows to extract the light resolution $\sigma_l(L)$ from the width of the e^-/γ-band.

A statistical independence between E an L is only approximately true as a slight correlation arises from the sharing of the deposited energy between phonon and light detector (see section 5.6). However, for the given purpose of calculating the width of a quenched band, an independent treatment of E and L is well justified in the light of the smallness of the correlation.

The energy which would have to be deposited for an e^-/γ-event to produce the same amount of light L as the quenched event can, to good approximation, be calculated with: $QF_x(E) \cdot E$. This yields

$$\sigma_l(L)^2 = \sigma_\gamma^2(L) - \sigma_p^2(QF_x(E) \cdot E) \tag{7.11}$$

for the light detector resolution $\sigma_l(L)$ at the light energy L.

At this point $\sigma_l(L)$ and $\sigma_p(E)$ are known and since the slope of the quenched bands (at energy E) is approximatively the respective quenching factor ($dL_x/dE(E) \simeq QF_x(E)$), the width of the quenched band is, in analogy to equation 7.3, given by

$$\sigma_x(L) = \sqrt{\sigma_l(L)^2 + [QF_x(E) \cdot \sigma_p(E)]^2} \tag{7.12}$$

In this work the slight energy dependence of the resolution of the phonon detector is neglected, thus $\sigma_p(E) \rightarrow \sigma_{p,0}$ (values given in table 7.2). This simplification is well justified, since equation 7.12 shows that the phonon detector influences the width of the quenched nuclear recoil bands even less than the e^-/γ-band, although it is almost negligible for the latter already.

7.5. Verification with Neutron Calibration Data

To validate the calculation of the quenched bands from the fitted e^-/γ-band with the procedure outlined above, figure 7.4 shows data from a neutron calibration (AmBe-source) performed during phase 2. The magenta lines depict the nuclear recoil bands (including scattering off all three target nuclei) calculated from the fitted e^-/γ-band (solid blue lines). The energy range shown corresponds to energies relevant for dark matter sensitivity.

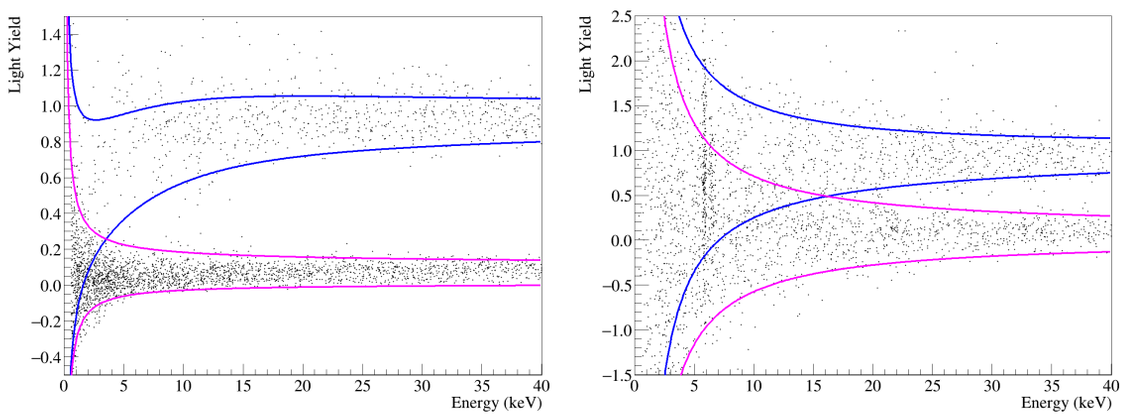

(a) TUM40 (b) Lise

Figure 7.4.: Neutron calibration data (black) taken in phase 2 with Lise and TUM40. Solid blue lines: 90 % upper and lower boundaries of the e^-/γ-band. The solid magenta lines mark the nuclear recoil bands: the upper line corresponds to the 90 % upper boundary of oxygen band and the lower line to the 90 % lower boundary of the tungsten band.

Clearly visible for both modules is the excellent agreement of the model of the quenched bands with the data measured. Additionally, the higher discrimination power of TUM40 due to the better performance of the light detector Michael (TUM40) becomes evident as the nuclear recoil bands are separated from the e^-/γ-band down to an energy of ~ 4 keV which is more than 10 keV below the overlap-free energy found for Lise.

Figure 7.4 indicates that the energy-dependence of the quenching factors is hardly relevant in the energy range of interest ((0-40) keV). However, it should not be forgotten that the factor ϵ is determined for energies above 150 keV and without the energy-dependence the excellent agreement between data and calculation could not be achieved.

In summary, this comparison with neutron calibration data shows that potentially existing inaccuracies in the modelling of, in particular the quenched bands, are negligible in the light of the resolution power of TUM40 and even more Lise.

7.6. Signal Expectation for a Real Detector

The starting point of any dark matter analysis is the calculation of the anticipated signal in the given detector which is based on the recoil spectrum expected for dark matter particles

scattering off nuclei, as already discussed in subsection 2.3.1. Included are effects from the dark matter halo, the form factors and it accounts for the three constituents of the $CaWO_4$ target material. However, this idealized spectrum neglects the performance of the individual detector, in particular its energy resolution and threshold. This section will explain the steps which have to be undertaken to calculate the spectrum as the detector would *see* it starting from the spectrum of an idealized detectors. Using this spectrum the experimental signature, induced by a dark matter particle corresponding to the excess seen in the previous phase 1, can be simulated. In the appendix A.2 simulations for TUM40 are presented.

The calculation of the dark matter recoil spectrum, as expected in a real detector, is done in the following steps:

1. Calculate the energy spectrum for an idealized detector (see section 2.3.1)
2. Convolve the spectrum with a Gaussian function (σ = baseline noise of the phonon detector (see section 7.1)) to account for the finite energy resolution of the phonon detector
3. Apply the cut efficiency (see section 6.9)
4. Cut spectrum below trigger threshold energy E_{th} (see section 5.7)
5. Calculate the distribution in the light yield coordinate
6. Integrate light yield distribution in acceptance region (only needed for Yellin methods, as discussed in chapter 8)

In the following some of these steps are illuminated in more detail.

Step 2: Convolution The convolution of the differential recoil rate $\frac{dN(E_R)}{dE_R}$ with a Gaussian function $g(E_R)$ is given by:

$$\left[\frac{dN}{dE_R} * g\right](E_R) = \int_0^{E_R} \frac{dN(\epsilon)}{dE_R} \cdot g(E_R - \epsilon)d\epsilon \tag{7.13}$$

Solving this convolution integral is straight-forward by binning the expected spectrum, because the integral then simplifies to a summation. However, bins of constant size are not well suited for a low-threshold analysis. The reason is, that the exponential rise towards low recoil energies requires small bins the low-energy region to maintain the needed accuracy. To use a very fine binning over the complete energy range (up to 40 keV), however, implies a very large overall number of bins which leads to unpractical long computation times. Thus, for this work an adaptive bin size has been implemented, where the bin size is continuously increased: the size of the (n+1)-st bin is given by multiplying the size of the n-th bin with a certain factor f (analog to a compound interest calculation in economics). This procedure, ensures small bins in the low-energy region where the spectrum steeply

rises and simultaneously allows for large bins at higher energies where the spectrum only moderately changes.

The factor f is set according to the desired number of bins; for this work 10,000 bins are used, which includes a high safety margin against any binning effects. Additionally, the validity of this approach is verified obtaining identical results with a different software package using an unbinned numerical integration.

Step 3: Cut Efficiency The cut efficiencies, as determined in section 6.9, are taken into account by multiplication with the convolved spectrum. This procedure, however, is not strictly valid, since the cut efficiencies are given as a function of simulated energy while the convolved energy spectrum is a function of reconstructed energy. At first glance this issue could easily be solved by determining the cut efficiencies as a function of reconstructed energy.[4] However, as was discussed in section 6.4, the cut efficiencies implicitly account for the (energy-dependent) probability of the standard event fit failing to find the correct pulse. Obviously, this probability would not be included any more when determining the cut efficiencies as a function of reconstructed energy, as the energy itself is derived from the standard event fit. In other words, it is not possible to describe the probability of the standard event fit to fail as a function of energy determined with the standard event fit.

For *high* energies it is anyhow irrelevant whether the cut efficiencies are determined as a function of simulated or reconstructed energy, since a small difference in energy will not result in a different value for the cut efficiency. For low energies, on the other side, the effect of the standard event fit failing to find the correct pulse is more relevant than the small differences between simulated and reconstructed energy, justifying the simple multiplication of the convolved spectrum and the cut efficiencies (as a function of simulated energy).

Additionally, it should be mentioned that part of the energy-dependence of the cut efficiencies results from the finite energy resolution (also consider discussion in the subsequent paragraph). The explanation is that an event with a simulated (=perfectly known) energy above threshold can, due to the finite energy resolution, get assigned a reconstructed energy below threshold, which is removed by the cut on energy neglecting all events with a reconstructed energy below threshold energy (see section 6.4). This effect, however, is already implicitly taken into account be the convolution of the energy spectrum. Therefore, by the simple multiplication of the cut efficiency one takes the finite resolution into account again.

This argument can most easily be understood for the simple cut at the threshold energy E_{th} (see section 6.4). The efficiency curve of this cut as a function of simulated energy takes the form of an error function with its mean (50 % efficiency) at E_{th}. The error function results from a convolution of step function with Gaussian accounting for the baseline noise. Thus, the efficiency is overestimated below the cut value ($< E_{th}$) and underestimated above. Since, as will be explained in the next subsection, the spectrum is cut at threshold energy, the efficiency for this particular cut is underestimated in total which is

[4] This would require to simulate a flat, continuous energy spectrum instead of certain discrete energies (see section 6.9).

conservative. Obviously, this simple argument might not completely hold for other cuts, however the general tendency will remain. In summary, the treatment of the cut efficiency as a function of simulated energy is conservative, in particular considering that the effect of the standard event fit failing to find the correct pulse is the dominating effect for very small pulses.

Step 4: Trigger Threshold The measured efficiency curves, as discussed in section 5.7 describe the deviation from a perfect step-function induced by the finite baseline noise of the detector. Thus, multiplying the efficiency curves with the convolved spectrum would take the baseline noise into account twice. Instead, the convolved spectrum is cut at threshold energy E_{th} which equals the threshold energy for an ideal trigger.

This procedure is backed by the following consideration. The finite width of the trigger efficiency curves arises from random background fluctuations adding up to the measured signal height which is the decisive input signal for the trigger. This means that a particle interaction depositing an energy slightly below the threshold E_{th} can cause a trigger, if an upward baseline fluctuation lifts the total signal height above the threshold. However, if the signal height is large enough to cause a trigger signal, also the reconstructed energy will be above the threshold energy E_{th}.

Obviously, the argument above only holds if the pulse processing of the trigger electronics and the energy reconstruction with the standard event fit feature an equal performance. Comparing the widths of the trigger efficiency curves (figure 5.11) with the energy resolution of section 7.1 reveals a better resolution of the energy reconstruction on the level of $\leq 30\,\%$. The improvement compared to the trigger electronics mainly arises from the cubic baseline model in the standard event fit taking baseline fluctuations into account more accurately. This implies that there is a certain chance to observe events depositing an energy smaller than E_{th}. Vice versa, there is also the equal chance for a particle interaction with an energy above E_{th} to be missed by the trigger. However, the small inaccuracy by a hard cut at E_{th} is conservative when setting exclusion limits, for the following reason. The expected recoil spectrum rises exponentially towards low energies and, thus, upward baseline fluctuations shifting an event above threshold would be more frequent than downward fluctuations causing an event to be missed. This means that in total the expected recoil spectrum is slightly underestimated which leads to a slightly weaker exclusion limit.

Step 5: Light Yield Distribution Up to now only the one-dimensional energy recoil spectrum of dark matter particle scattering was discussed. Even without explicit statement the energy recoil spectrum is always a sum of the contributions from scatterings off the three different target nuclei. The extension to a two-dimensional spectrum is then simply given by the nuclei-individual energy spectra distributed in the light yield-energy plane according to the corresponding nuclear recoil bands. [5]

[5] An illustration may e.g. be found in [71].

8. Calculating Exclusion Limits Using Yellin Methods

This chapter will discuss Yellin methods, which are one of the two possibilities presented in this work, to derive exclusion limits on elastic scattering of dark matter particles. The methods presented in the following were developed by Steve Yellin, first published in a paper entitled *"Finding an upper limit in the presence of an unknown background"* [149]. This title already highlights its main feature, namely to provide strong and statistically correct exclusion limits for data sets including background events of unknown (or not precisely known) origin. For this reason Yellin methods quickly became very popular, in particular in the field of direct dark matter searches and they are still frequently used today. If, on the other hand, the background is precisely known, Yellin methods may result in too conservative exclusion limits. Today, most dark matter searches achieved a very detailed understanding of their detectors and their backgrounds, motivating the use of maximum likelihood methods, which will be discussed in chapter 10.

8.1. Yellin Maximum Gap and Optimum Interval

8.1.1. Maximum Gap

Two ingredients are needed for the maximum gap method: Firstly, the signal expectation for a certain dark matter particle mass (and normalized to a certain cross section) as a function of deposited energy. Secondly, the energy distribution of the events measured by the detector. This is illustrated in figure 8.1 with an imaginary signal expectation in red and an imaginary distribution of measured events in blue. A gap x_i thereby is defined as the integral of the expected signal in-between two consecutive events or between an event and the start or end point of the energy interval allowed:

$$x_i = \int_{E_i}^{E_{i+1}} \frac{dN}{dE} dE \tag{8.1}$$

For N events seen in the detector the index i runs from 0 to N+1: E_i denote the energies of the individual events whereas E_0 and E_{N+1} correspond to the lower and upper limit of the energy range. As a second step the maximum gap x_{max}, shaded green in figure 8.1, out of all gaps $x_{i=0..N+1}$ is used to derive the limit on the cross section. In other words, the maximum gap corresponds to the energy range where maximal discrepancy between the number of expected events to zero observed events is found.

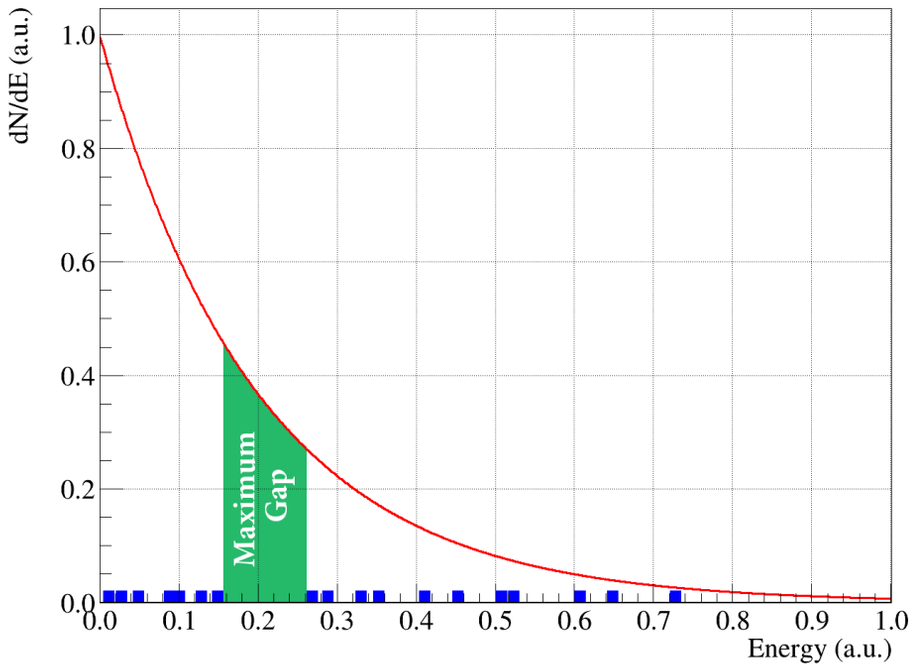

Figure 8.1.: Illustration of the Yellin maximum gap method. The red line corresponds to the expected number of events per unit energy as a function of energy. The blue squares are measured event energies. The maximum gap (the maximum integral below the red curve in-between two consecutive events) for the given example is drawn in green.

Once the maximum gap (x_{max}) is determined, an upper limit on the cross section of dark matter particle scattering (σ_{ul}) is calculated. Upper limit means that any cross section larger than the limit can be excluded with a certain confidence level which usually is set to 90 %. The confidence level is interpreted in a frequentist framework (as opposed to Bayesian statistics): Assuming dark matter was existing and the true cross section was σ_{ul}. Now, if many completely identical experiments were performed, then in 90 % of the experiments a limit on the cross section larger than σ_{ul} would be calculated. Or, more specific for the Yellin method: If the true cross section was σ_{ul}, the maximum gap would be smaller than the one found for the given data set in 90 % of the cases.

Obviously, the size of the maximum gap x_{max} by itself is meaningless, but has to be put into relation to the total number of events μ expected in the energy interval $[E_0, E_{N+1}]$ for a certain cross section σ:

$$\mu = \int_{E_0}^{E_{N+1}} \frac{dN(E,\sigma)}{dE} dE \tag{8.2}$$

In [149] it was shown that the probability C_0 for the maximum gap being smaller than x_{max} for a given set of x_{max} and μ can be calculated analytically using the following equation:

$$C_0(x = x_{\text{max}}, \mu) = \sum_{k=0}^{m} \frac{(kx-\mu)^k \exp(-kx)}{k!} \left(1 + \frac{k}{\mu - kx}\right) \tag{8.3}$$

In the equation above, m is the largest integer number with $m \leq \mu/x$. In an iterative

process the cross section σ is increased, which affects both x_{max} and μ. The iteration is stopped if C_0 reaches a value of 0.9 (for a 90 % confidence level).

To conclude the main benefits of the Yellin maximum gap method are:

Robustness to Background Events In contrast to setting a limit based on Poissonian statistics, where the exclusion limit is simply given by comparing the number of observed events to the number of expected events, the Yellin maximum gap method also utilizes differences between the shape of the expected spectrum to the observed energy spectrum.

This makes the result to suffer less from a few background events, in particular if those appear in energy regions of small sensitivity. Small sensitivity in this case refers to energy ranges where either the number of observed events is high, or the expectation is low (or both). For the example given in figure 8.1 adding another event at energies below or above the maximum gap found would not affect the exclusion limit at all.

No Binning The energy information of the measured events is used unbinned, thus no binning effects appear.

Analytic Calculation As already pointed out all quantities, in particular C_0, can be calculated analytically for arbitrary numbers of observed and expected events.

8.1.2. Optimum Interval

The maximum gap method performs best in cases of few background events, or for special cases where the background events are distributed in a very non-uniform way (e.g. a detector triggering in noise causing a high number of events at very low energies). For most situations with a larger number of events it pays out to generalize the maximum gap method to the optimum interval method. The latter seeks to find the optimum interval allowing at n events inside. The number of events inside the interval n may thereby take any value between 0 and the total number of observed events N: $n \leq N$.

In analogy to the maximum gap method, $C_n(x_{\text{max}}, \mu)$ is the probability for a certain cross section σ to find only intervals (containing n events) of smaller size than the largest interval x_{max}. Thus, the higher $C_n(x_{\text{max}}, \mu)$ is, the more unlikely is the existence of dark matter with a scattering cross section σ. However, n is not chosen a-priori, but the optimum interval methods selects the value for n resulting in the best exclusion limit for the cross section, that is the largest value

$$C_{\text{max}} = \max_{n=0..N} C_n(x_{\text{max}}, \mu) \tag{8.4}$$

In general, the value obtained for C_{max} does not correspond to the confidence level for the exclusion of a certain cross section σ. This is because one has to compensate for the freedom to chose the optimum value for n based on the measured data. Thus, the function $\bar{C}_{\text{max}}(\text{C.L.}, \mu)$ is defined as the probability for a random experiment with μ observed events to yield a value for $C_{\text{max}} \leq \bar{C}_{\text{max}}(\text{C.L.}, \mu)$ for the given confidence level. Consequently, a 90 % confidence limit is obtained by finding the value $C_{\text{max}} = \bar{C}_{\text{max}}(0.9, \mu)$. Figure 8.2 shows the function $\bar{C}_{\text{max}}$ as a function of the number of expected events μ.

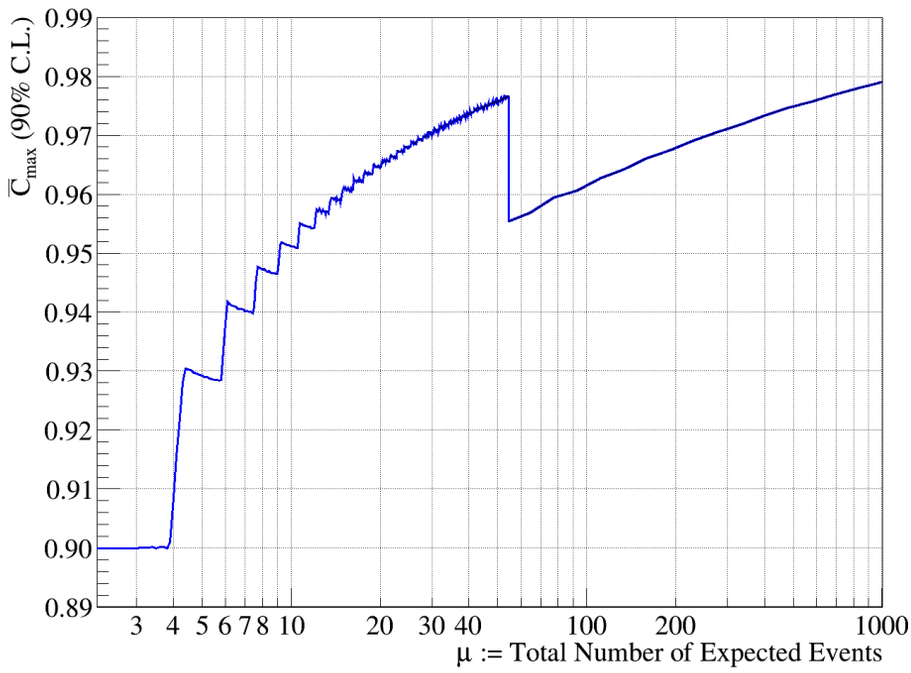

Figure 8.2.: $\bar{C}_{\text{max}}$ calculated for a 90 % confidence level as a function of the number of expected events μ. See text for a detailed explanation.

While $\bar{C}_{\text{max}}(0.9, \mu)$ is discussed in detail in [149], some special features shall be mentioned here.

The first peculiarity of $\bar{C}_{\text{max}}(0.9, \mu)$ is the step-wise behavior pronounced, in particular, for low μ. Thereby, every step corresponds to an increase of possible values for n by one when calculating $C_n(x_{\text{max}}, \mu)$ and, thus, C_{max}.

In contrast to the calculation of C_0 for the maximum gap method, $C_n(x_{\text{max}}, \mu)$ (and C_{max}) and $\bar{C}_{\text{max}}(0.9, \mu)$ cannot be calculated analytically, but have to be tabulated from Monte Carlo simulations. Since these simulations are computationally expensive, tabulated values only exist for $\mu < 54.5$ and $n \leq 50$. To allow dealing with a large number of expected events, S. Yellin developed an analytic continuation in [150] which causes the discontinuity seen at $\mu = 54.5$ in figure 8.2. However, in [150] it was ensured that the resulting limit also maintains its 90 % confidence level near the discontinuity. For this work the implementation available at [151] is used which automatically switches between tabulated values for $\mu \leq 54.5$ and the analytic continuation for larger numbers of expected events.

To verify the 90 % C.L. of both Yellin methods for the given application, upper limits were calculated from simulated data sets for different dark matter particle masses and for both detectors (10,000 data sets each). All test performed yield a positive result finding exclusion limits above the true (simulated) cross section in at least 90 % of the cases.

8.1.3. Similarities and Differences Between Yellin Methods

In subsection 8.1.1 three main benefits of the maximum gap were named: robustness to some level of background events, no binning and a completely analytic calculation. The last one does not hold for the optimum interval method as both, $C_n(x_{\max}, \mu)$ and $\bar{C}_{\max}(0.9, \mu)$ require numeric determination using Monte Carlo methods. However, all values needed are tabulated with high precision, rendering this issue irrelevant in practice.

There is no hard criterion on an a-priori choice of one method over the other. In general, the optimum interval method is better suited for situations with a high number of background events, while the maximum gap method has its best performance for a few background events only. However, a final answer which method provides the better exclusion limit cannot be given without taking the measured data into account. For this work the optimum interval method is used as it was found to perform slightly better on training set data.

Neither do both methods require any knowledge of the background, nor do they offer the possibility to take any information of the background into account, except at least some part of the background is precisely known. In this case the respective background contribution can be included in the expected spectrum dN/dE leading to a stronger exclusion since the expectation is raised with respect to the observation. However, for rare event searches in general, and low threshold analyses in particular, a known and entirely understood background usually is not the case. Thus, other methods like a maximum likelihood analysis, might be a better choice if one wants to take a background model including its uncertainties into account.

8.2. Acceptance Region

Both, the maximum gap and the optimum interval method work with one observable only. Thus, to exploit the discrimination power of CRESST detectors via the scintillation light, potential dark matter candidate events are extracted by defining an acceptance region in the light yield-energy plane.

8.2.1. Definition of the Acceptance Region

In light yield, all events above the 99.5 % lower boundary of the tungsten band and below the mean of the oxygen band are accepted. Due to the form factor of tungsten, substantially suppressing the anticipated count rate for higher recoil energies (see subsection 2.3.3), the acceptance region is limited to energies of up to 40 keV. A novelty of this work, however, is to include all energies starting from threshold. The resulting acceptance regions in the light yield energy plane are shaded in light magenta in figures 8.3a and 8.3b, events therein are highlighted in blue.

At first glance the particular choice of the acceptance region might seem arbitrary. However, it should be noted that any choice of the acceptance region is perfectly valid if the choice is not based on the data used to derive the exclusion limit. Otherwise, the choice

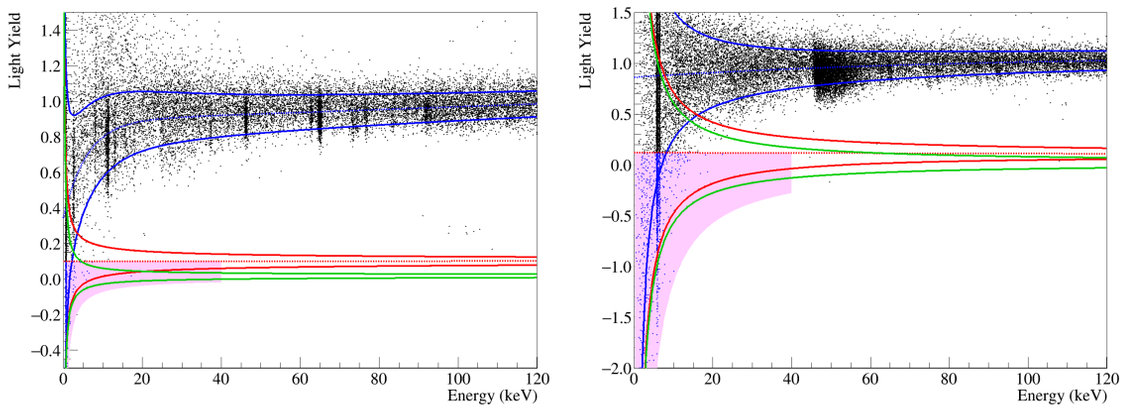

(a) TUM40 (b) Lise

Figure 8.3.: Light yield energy data from TUM40 and Lise including the acceptance region in light magenta with events inside highlighted in blue. The acceptance region includes all energies from threshold to 40 keV and spans from the 99.5 % lower boundary of the tungsten band to the mean of the oxygen band (dashed red). The solid lines correspond to the bands for recoils off tungsten (green), off oxygen (red) and the e^-/γ-band (blue).

is endangered to be biased exploiting statistical fluctuations of the data without properly accounting for the freedom to base the choice on the outcome of the exclusion limit. Thus, for this work the definition of the acceptance region is done on training set data which fulfills the requirement of a blind analysis.

While the energy limits and the lower light yield bound are an obvious choice, the upper light yield boundary deserves a more detailed discussion. With training set data it is found that limiting the acceptance to the mean of the oxygen band yields the best sensitivity over a wide dark matter particle mass range, since it is a very good balance between including as much as possible of the nuclear recoil bands on the one hand, and reducing the leakage from the e^-/γ-band into the acceptance region on the other hand. Limiting the leakage is crucial considering that the Yellin methods used in this work are one-dimensional only and, therefore, cannot exploit differences in the light yield distribution between the dominant e^-/γ-background and nuclear recoils induced by a potential dark matter signal. Results obtained with differently defined acceptance regions will be discussed in section 9.6.

8.2.2. Expected Signal Composition

Since the acceptance region in general does not include the full nuclear recoil bands, this has to be considered in the calculation of the anticipated energy spectrum for dark matter particles (dN/dE) interacting in the target material. This requires to integrate dN/dE for each target nucleus over the yield range of the acceptance region. It should be noted that the composition of the signal on the three target nuclei depends on the dark matter particle mass. For a very light particle, where only scatterings off oxygen induce energy

deposits above threshold, choosing the mean of the oxygen band as an upper boundary results in a 50 % reduction of the expected count rate. In contrast, for very heavy dark matter particles where scatterings off tungsten dominate the expected count rate is reduced much less, as most of the tungsten band is contained in the acceptance region. This is in particular evident for a detector with good discrimination power, like TUM40 (see figure 8.3a). The figures 8.4a and 8.4b show the expected count rate of accepted events, normalized to a cross section of 1 pb and as a function of dark matter particle mass, for TUM40 and Lise, respectively. Thereby all detector-specific effects, as e.g. exposure, cut efficiency and energy resolution (see section 7.6) are taken into account. The colored lines correspond to the rate expected on the individual nucleus; their sum yields the total rate depicted as dashed black line. Going from high to low masses, both rates show the expected rise of the rate resulting from the increasing number density of dark matter particles. As soon as a significant part of the recoil spectrum is below the energy threshold the rate starts to drop, more quickly for tungsten, because less energy is transferred in the scattering process than for the much lighter elements oxygen and calcium (also see subsection 2.3.5).

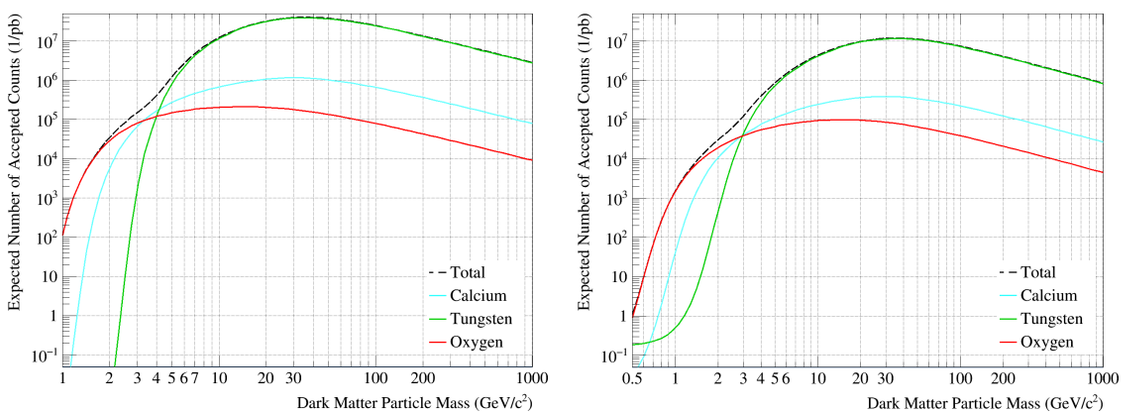

(a) TUM40 - 98kgd (b) Lise - 52kgd

Figure 8.4.: Expected dark matter particle count rate for a cross section of 1 pb, shown separately for the three target nuclei (colored lines, see legend) and the sum thereof (dashed black line). The spectra include the choice of the acceptance region, as well as all detector-specific properties (threshold, resolution, exposure etc.). The exposure quoted correspond to the dark matter data sets (see section 5.1).

Comparing TUM40 and Lise allows to study the benefit of the threshold of Lise being roughly two times lower than the one of TUM40 (0.3 keV vs. 0.6 keV). For TUM40 tungsten is the dominant scattering partner down to a mass of about 4 GeV/c^2, while for Lise calcium and oxygen only take over for masses below 3 GeV/c^2. At 1 GeV/c^2 the total expected count rate for Lise is one order of magnitude higher than for TUM40, although the exposure of TUM40 is roughly twice as much as for Lise.

Due to the finite escape velocity of dark matter particles in our galaxy there is a maximal energy which can be transferred to the target nucleus by a dark matter particle of a given mass. Thus, for an ideal (arbitrarily good energy resolution) detector with a finite thresh-

old the expected count rate will also be sharply cut at a certain particle mass. For a real detector with finite energy resolution, on the other hand, the finite baseline noise has to be taken into account, since an upward fluctuation of the baseline may shift an event above the energy threshold of the detector, or vice-versa a downward fluctuation may shift an event below threshold. Mathematically this effect is accounted for with the convolution of the recoil spectrum for an ideal detector with a Gaussian function describing the baseline noise. However, this approach strictly holds only under the assumption that the trigger electronics is affected by the baseline noise in exactly the same manner as the energy reconstruction. In other words, an event shifted above the trigger threshold by an upward baseline fluctuation gets assigned an energy value being the sum of the energy deposition and the random upward fluctuation. Comparing the energy resolution of the trigger, given by the widths of the trigger efficiency curves (see section 5.7), with the baseline resolutions (see section 7.1) proves that this assumption is well justified. Nonetheless, in order not to heavily rely on the validity of this assumption the calculation of the exclusion limits is stopped at particle masses of 0.5 GeV/c^2 for Lise and 1 GeV/c^2 for TUM40. For scatterings off oxygen a dark matter particle of 1 GeV/c^2 may transfer up to 0.75 keV, which is already above the threshold of TUM40. The maximum energy transfer for a dark matter particle of 0.5 GeV/c^2 is only 0.20 keV, which is below the threshold of Lise (0.30 keV). However, with the baseline resolution of Lise being $\sigma = 60.7$ eV an upward baseline fluctuation of less than two σ is needed to trigger. This represents a mild use of the baseline noise only, in particular considering that the trigger threshold turned out to be considerably better in the dark matter data set than in its dedicated measurement (see subsection 5.7.1).

Going to very low dark matter particle masses another effect can be seen for Lise, namely that the rate expected on tungsten (figure 8.4b) starts to drop less rapidly until it almost stays constant with decreasing mass. This phenomenon is a consequence of the aforementioned convolution with the Gaussian function to account for the finite baseline noise, leading to two competing effects which nearly compensate each other. On the one hand, the energy transferred in the scattering process decreases for lower masses which leads to a smaller fraction of the recoil spectrum being above threshold and, thus, to a lower count rate. On the other hand, the number density increases the lighter the dark matter particle is. In other words, when going to lower dark matter particle masses the expected spectrum gets pushed to lower energies on the one hand, but increases more steeply, on the other hand. In summary, the fraction of events expected above threshold decreases when going to lower masses, but the total number stays roughly constant.

However, it should be emphasized that the count rate at the lowest mass considered in this analysis (0.5 GeV/c^2) stays clearly dominated by recoils off oxygen, exceeding the rate for scatterings off tungsten by more than a factor of five.

8.2.3. Events in Acceptance Region

Energy spectra for the events in the acceptance regions of TUM40 and Lise are shown in figures 8.5a and 8.5b, respectively. Both plots, show all events in the acceptance region with a logarithmic scale and a zoom-in to the most-relevant low-energy part in linear scale the inlay.

For TUM40 the aforementioned rise below 1 keV is also clearly evident in the spectra of accepted events. Going to higher energies the spectrum quickly drops with one outlier event at about 17 keV. As the light yield plot (see figure 8.3a) shows, this event is in the nuclear recoil bands and is incompatible with leakage from the e^-/γ-band (by more than $6\,\sigma$). Investigating this particular event shows a clear light signal correctly fitted by the standard event fit and no peculiar behavior in any other respect which strongly argues for a particle origin, as e.g. a neutron-induced nuclear recoil.

Comparing the spectrum of accepted events of Lise and TUM40 once again demonstrates the superior discrimination power of TUM40, as the spectrum for Lise is rather densely populated up to 14 keV with additional events seen for even higher energies. Furthermore, the ^{55}Fe-induced double peak at 6 keV clearly makes up for a considerable number of events in the acceptance region. For very low energies, however, hardly any rise is seen for Lise which is a key factor driving the enhanced sensitivity of Lise compared to TUM40 regarding very light dark matter particles.

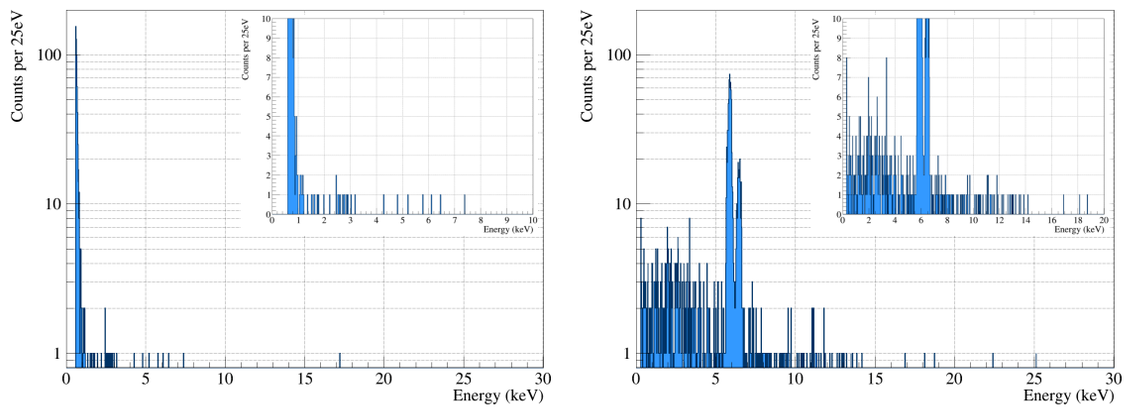

(a) TUM40 (b) Lise

Figure 8.5.: Events in the acceptance regions of TUM40 and Lise (see figure 8.3). While the insert shows a zoom-in (linear scale) to the low-energy part, the main plot shows all accepted events in logarithmic scale.

The two spectra shown are input to the Yellin limit calculation, without any background subtraction. Thus, all events observed in the respective acceptance regions are conservatively considered as potential dark matter particle interactions.

8.3. Maximum Gaps and Optimum Intervals for the Given Data

To visualize the working principle of the Yellin optimum interval and the maximum gap methods on the basis of the measured data, figure 8.6 shows the optimum interval (the maximum gap) for different dark matter particle masses, in red for Lise and in blue for TUM40.

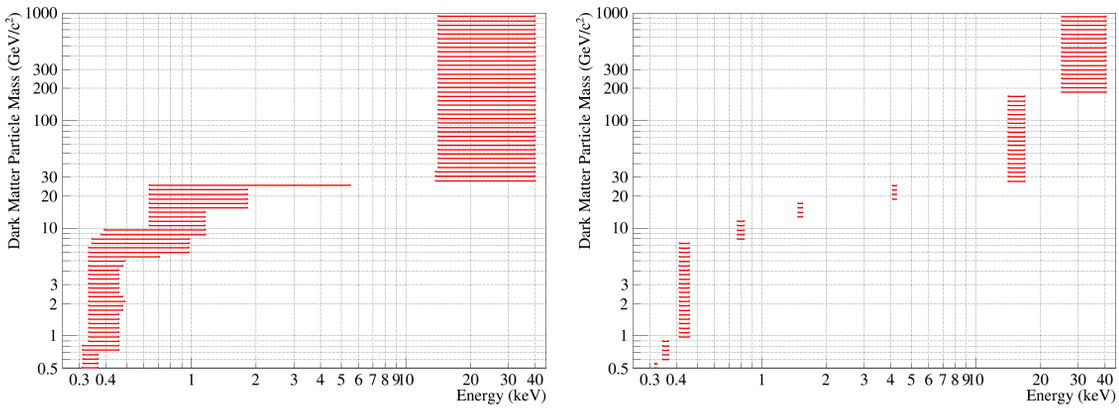

(a) Lise - Optimum Interval

(b) Lise - Maximum Gap

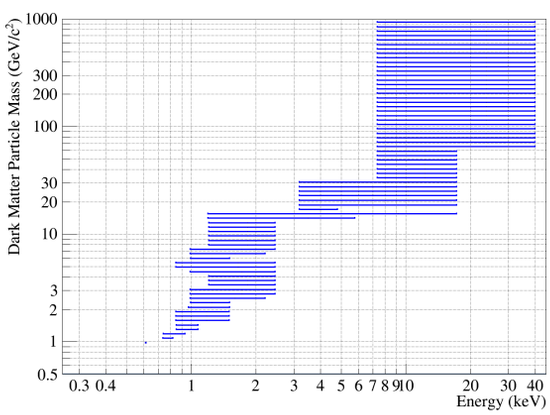

(c) TUM40 - Optimum Interval

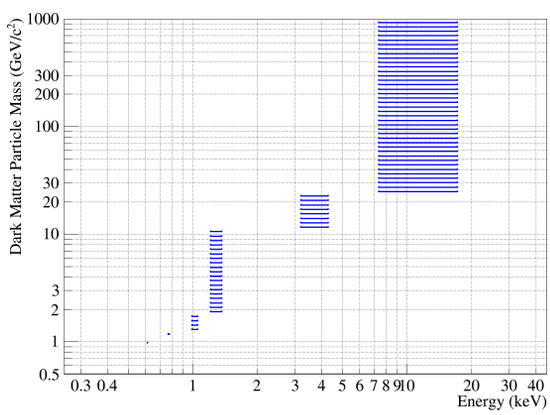

(d) TUM40 - Maximum Gap

Figure 8.6.: Depicted are the energy ranges of the optimum interval and the maximum gap method for Lise and TUM40 for different masses of the dark matter particle.

Comparing optimum interval to maximum gap shows that the former uses a wider energy interval to derive the result which in general makes it more robust against a higher number of events. However, for the given application only small differences are found between the two methods, as will be shown in section 9.4.

For TUM40 it becomes evident that the rise below 1 keV limits the sensitivity for light dark matter particles as for both methods the interval (the gap) is found substantially above threshold, despite the high expectation at near-threshold energies. For Lise, in particular the optimum interval method choses energy ranges very close to threshold, thus resulting in a higher sensitivity for low-mass dark matter particles, as will be shown in the next chapter.

9. CRESST-II Phase 2 Results on Low-Mass Dark Matter

The previous chapter introduced Yellin methods forming the basis for the central result of this work which is presented in this chapter. Exclusion limits are derived from CRESST-II phase 2 low-threshold data for dark matter particles scattering off nuclei in the target material. Additionally, studies are undertaken on the influence of the exposure, the chosen Yellin method, the threshold and the particular choice of the acceptance region.

9.1. Result on Low-Mass Dark Matter

The exclusion limits obtained for TUM40 (solid blue) and Lise (solid red) for the respective dark matter data set are depicted in figure 9.1. In figure 9.1, as well as in all upcoming figures, results obtained within this work are marked with a star. The limits are calculated using the Yellin optimum interval method as discussed in the previous chapter. Both exclusion limits are very similar to the ones already published in [75] for TUM40 and in [74] for Lise (direct comparison shown in figure A.2). The small remaining differences mainly arise from a different data set for TUM40 and a different choice of the selection criteria for Lise. Additionally included in the plot are previous results from CRESST-II, as well as results from competing experiments. Indicated in gray is the limit for a background-free $CaWO_4$-based experiment arising from neutrinos coherently scattering off nuclei [53].

At the time of publication in 2014, the exclusion limit for TUM40 explored new parameter space for dark matter particle masses below 3 GeV/c^2, now for a large mass range overtaken by the new results from the CDMSlite collaboration. Today, the exclusion limit obtained with Lise provides the highest sensitivity in the field of direct dark matter detection for masses lighter than 1.7 GeV/c^2. With this result, parameter space in the sub-GeV/c^2-region is explored for the first time - a mass region currently inaccessible to competing experiments.

Compared to other direct dark matter searches the exclusion limits of CRESST-II usually show some kinks. This phenomenon originates from the multi-element target $CaWO_4$. The kinks for Lise seen at roughly 2-3 GeV/c^2 and for TUM40 at 4-5 GeV/c^2 mark the transition region between the expected recoil spectra being dominated by scatterings off tungsten above and oxygen below this mass, which is best seen considering the count rates expected for the target nuclei as shown in figure 8.4. For Lise a second kink is observed at $\sim 28\,\mathrm{GeV}/c^2$ which follows an untypical, almost constant exclusion curve. Both observations are explained by the high leakage of events from the e^-/γ-band into the acceptance region caused by the presence of the ^{55}Fe-double peak ($\sim$ 6 keV) and the modest dis-

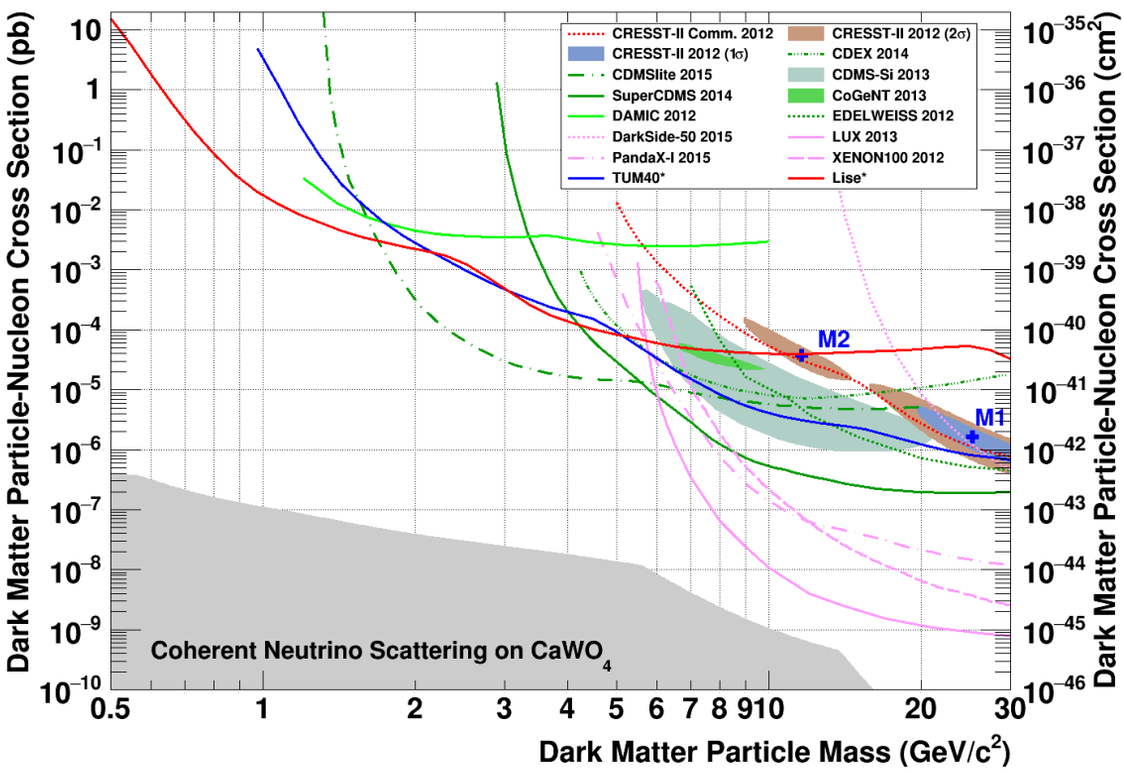

Figure 9.1.: Main results of this work (marked with '*') depicting exclusion limits for TUM40 (solid blue) and Lise (solid red) on the elastic scattering of dark matter particles as a function of the mass of the dark matter particle. Additionally shown are previous CRESST-II results, as well as results from other direct dark matter searches. In the gray region a $CaWO_4$ -based experiment is expected to be affected by the irreducible background originating from neutrinos coherently scattering off the target nuclei. References are given in the caption of figure 2.7.

crimination power of Lise. Thus, for masses below $\sim 28\,\mathrm{GeV}/c^2$ the optimum interval is found at rather low recoil energies, below the ^{55}Fe-line (see figure 8.6a). For masses above $\sim 28\,\mathrm{GeV}/c^2$ the expected recoil spectrum extends to recoil energies large enough to find the optimum interval above the ^{55}Fe-line causing an increase in sensitivity again and, thus, a more stringent exclusion limit.

Comparing TUM40 and Lise clearly shows that the substantially lower background leakage of TUM40 results in a superior sensitivity for masses of 5 GeV/c^2 and more. However, only the detector Lise yields sensitivity for sub-GeV/c^2dark matter particles, driven by the lower trigger threshold and the constant background level down to threshold. For the mass regime in between (2-5 GeV/c^2), the advantages of a low background level in TUM40 and of a low threshold in Lise hold the balance leading to similar sensitivities for both detectors.

9.2. Statistical Fluctuation

To estimate the statistical fluctuation of the exclusion limits, 10,000 data sets[1] are simulated for each detectors starting from the energy spectrum in the e^-/γ-band and distributed in the light yield-energy plane according to the analytic model of the e^-/γ-band (as discussed in chapter 7). Additionally, the lower light yield observed for γ-lines (in particular for TUM40 due to the pronounced non-proportionality effect, see section 7.3) is taken into account.

The result is shown in figure 9.2 with bands corresponding to confidence levels of 1 σ and 2 σ, blue colors for Lise and yellow colors for TUM40.[2]

For TUM40, excellent agreement between simulation and exclusion limit (solid blue line) is found in the most relevant low-mass regime. Above a few 10 GeV/c^2 the simulations predict slightly stronger limits than resulting from data. The main reason is the aforementioned potential neutron event observed in the oxygen-band at 17 keV which is obviously not included in the simulation where solely e^-/γ-background is considered. The impact of this particular event is illustrated with the blue dotted exclusion limit which one obtains from the TUM40 dark matter data set, but with the event under consideration being removed. As can bee seen removing this special event substantially reduces the tension of data and simulation.

In contrast to TUM40, data and simulation are consistent for Lise over the whole dark matter particle mass range. For low masses, simulations tend to be slightly stronger than data. This could be an indication for an underestimation of the e^-/γ-background in the simulation, in particular at small energies. On the other hand, the limit obtained from data always stays inside the 2 σ-bound, which corresponds to 95 % confidence only, thus leaving a realistic chance for a statistical fluctuation to be at the edge or even beyond the 2 σ-bound.

[1] The limit calculation was parallelized using the software tool GNU Parallel [152].

[2] For both detectors it is checked that the resulting limits, for a given dark matter particle mass, follow a Gaussian distribution.

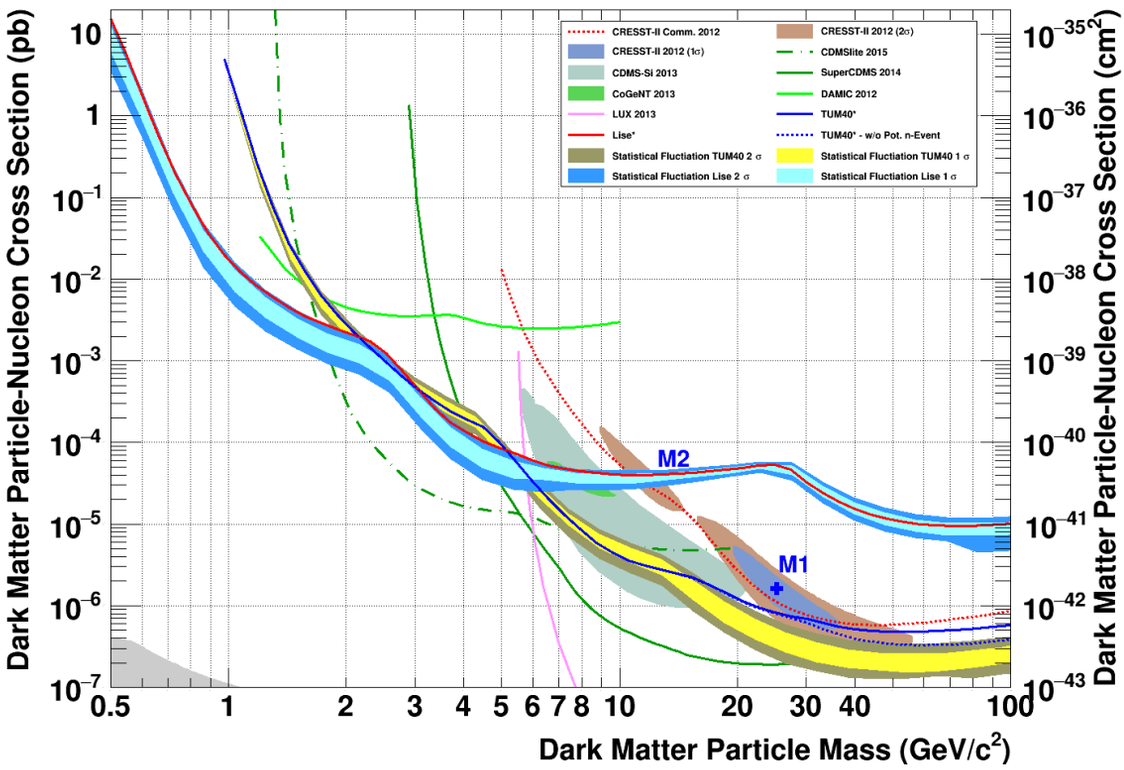

Figure 9.2.: Exclusion limits obtained in this work together with a reduced set of other results. The yellow and blue colored bands correspond to the statistical fluctuations (dark = 2 σ, light = 1 σ) expected for the corresponding exclusion limits obtained from a data-driven simulation of the e^-/γ-background leakage. The blue dotted line corresponds to the limit one would obtain for TUM40, if the potential neutron scattering at 17 keV was not present in the data.

9.3. Influence of the Exposure

To investigate the influence of the exposure on the final result two tests are performed for each detector. Once the data are randomly split in two sets of equal size and once data sets of one tenth of the size of the complete set are created. For each test data set one is randomly selected and the resulting exclusion limits are depicted in figure 9.3.

Comparing the halved data sets (dotted lines, corresponding to 49 kgd for TUM40 and 26 kgd for Lise) to the complete data set (solid lines) reveals the same trend for both detectors. While hardly any difference is seen for low dark matter particle masses, the exclusion power at higher limits benefits from additional exposure.

This effect becomes even more evident when taking the data sets of one tenth of the full exposure into account, which also hardly differ at very low masses. However, a clear improvement of the limit can already be seen for dark matter particles with masses of a few GeV/c^2. Thus, one often refers to the low-mass regime as being performance-limited, in contrast to the exposure limitation for higher particle masses.

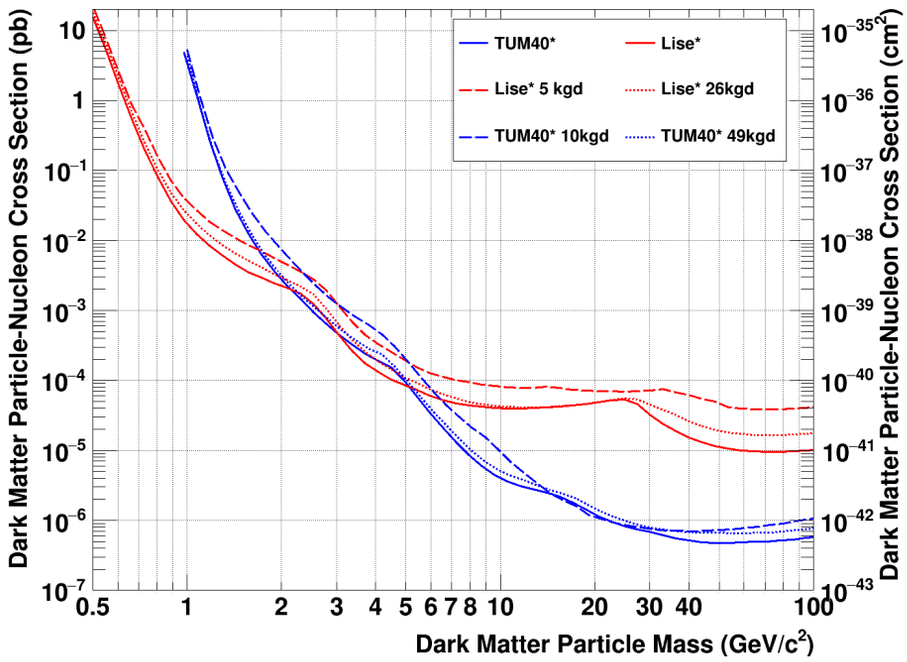

Figure 9.3.: Exclusion limits for Lise (red) and TUM40 (blue) with the full exposure (solid), the half exposure (dotted) and one tenth of the exposure (dashed).

A-priori it is hard to predict how the sensitivity of an experiment scales with exposure, except for the background-free case, where one obtains a direct proportionality between sensitivity (= exclusion limit) and exposure.

In case of background the relation depends how *signal-like* the background is, which shall be explained considering two extreme cases. The first one is to perform a limit calculation in a case where there actually is a dark matter signal. In this case the sensitivity will not improve with increasing exposure.[3] In the other extreme case, where the background is completely different to the signal, the sensitivity will still scale linearly with exposure, since Yellin methods exploit differences in the shape of the measured energy to the expected signal spectrum.

A third case which deserves to be mentioned is a background which induces a similar experimental signature as dark matter particles would, but the *cross section* of the background and signal differ. This is e.g. the case for the region marked gray in figure 9.1) where the coherent neutrino nucleus scattering (CNNS) becomes relevant. This irreducible background process is expected to induce events which cannot be distinguished from dark matter particles scattering in the detector on an event-by-event basis. However, a discrimination can be performed on a statistical basis. In other words, if there was a dark matter signal one expects to observe the sum of events induced by CNNS and by dark matter, which obviously differs from the number of events originating from CNNS alone. In such a situation one obtains a sensitivity scaling with the square-root of the exposure, as e.g. shown in [54].

The comparison in figure 9.3 shows, as expected, that neither of the two extreme cases

[3] However, for a positive analysis the significance for a signal will benefit from additional exposure.

apply for the given data. The enhancement seen for high dark matter particle masses is considerably smaller than expected for a direct proportionality between exposure and sensitivity. However, some level of improvement is seen over the whole dark matter particle mass regime. Admittedly, for very low dark matter particle masses the differences between the expected spectrum and the measured spectrum fade away causing less benefit from a larger exposure.

9.4. Optimum Interval Versus Maximum Gap

For the analysis presented in this work the optimum interval method was chosen a-priori, based on data from the respective training sets. Nonetheless, figure 9.4 shows a comparison between the optimum interval method (solid lines, red for Lise and blue for TUM40) and the maximum gap method (dashed lines). Over the whole dark matter particle mass range no substantial differences are observed. The general tendency of the maximum gap method being better for a small number of events can be seen comparing the TUM40-limits at masses of 30 GeV/c^2 and more, where the sensitivity originates from recoil energy regimes with few background events only. Also the opposite may be seen, as the optimum interval method yields slightly better exclusion limits over almost the whole mass range for the detector Lise where numerous leakage events are observed in basically the entire acceptance region. In general, exclusion limits calculated with the maximum gap method exhibits additional kinks corresponding to a change of the maximum gap (compare to figures 8.6b and 8.6d).

In summary, the performances of the maximum gap and the optimum interval method are practically identical for the given data.

9.5. Impact of the Threshold

To emphasize the importance of a low energy threshold for the sensitivity to very light dark matter particles figure 9.5 shows exclusion limits calculated for TUM40 (blue) and Lise (red) with different energy thresholds. For TUM40 very similar exclusion limits are obtained when increasing the energy threshold from 0.6 keV to 1 keV, which is caused by the already discussed steep energy-rise below 1 keV for TUM40. For the same reason, the limit for Lise with a threshold setting of 0.6 keV (red dotted line) is better for low dark matter particle masses, despite the otherwise significantly larger background level of Lise compared to TUM40. Finally, only considering energies of more than 1 keV in both detectors (dashed lines) yields an evidently superior performance of TUM40 for all masses of the dark matter particle.

In conclusion the study in this section once again points out the importance of a low energy threshold for the sensitivity in the low-mass regime. However, it also becomes evident that the ideal detector should combine both, a low background level in the acceptance region as well as a low trigger threshold.

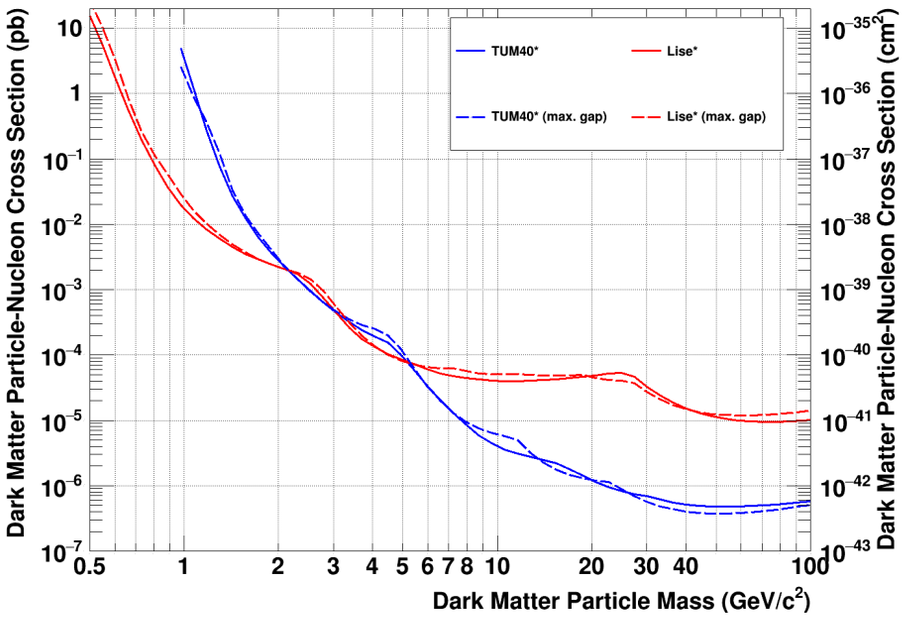

Figure 9.4.: Comparison of the exclusion limits obtained for Lise (red) and TUM40 with the optimum interval (solid) and the maximum gap method (dashed lines).

Upper Acc. Boundary	Nr. of Acc. Events	
	TUM40	Lise
Oxygen band: 50 %	615	1381
Oxygen band: 90 %	1317	4828
Tungsten band: 50 %	482	1178

Table 9.1.: Number of events in the acceptance region for different upper acceptance boundaries.

9.6. Results Using Different Acceptance Regions

Analog to the choice of the Yellin method, no hard criterion can be established to find the optimal definition of the acceptance region a-priori; without considering the data measured. Thus, also the choice of the acceptance region, in particular the upper light yield boundary, was fixed before unblinding the data. Subsection 8.2.1 already motivated the use of the mean of the oxygen band as an upper light yield boundary. However, figure 9.6 additionally shows limits obtained with acceptance bounds set to the mean of the tungsten band (dotted) and the upper 90 % boundary of the oxygen band. These two examples are chosen as they reflect two different extremes: using the mean of the tungsten band limits the leakage from the e^-/γ-band into the acceptance region at the cost of signal expectation, while including almost the complete oxygen band maximizes the signal expectation at the cost of accepting a high number of leakage events. Table 9.1 lists the number of events inside the different acceptance regions.

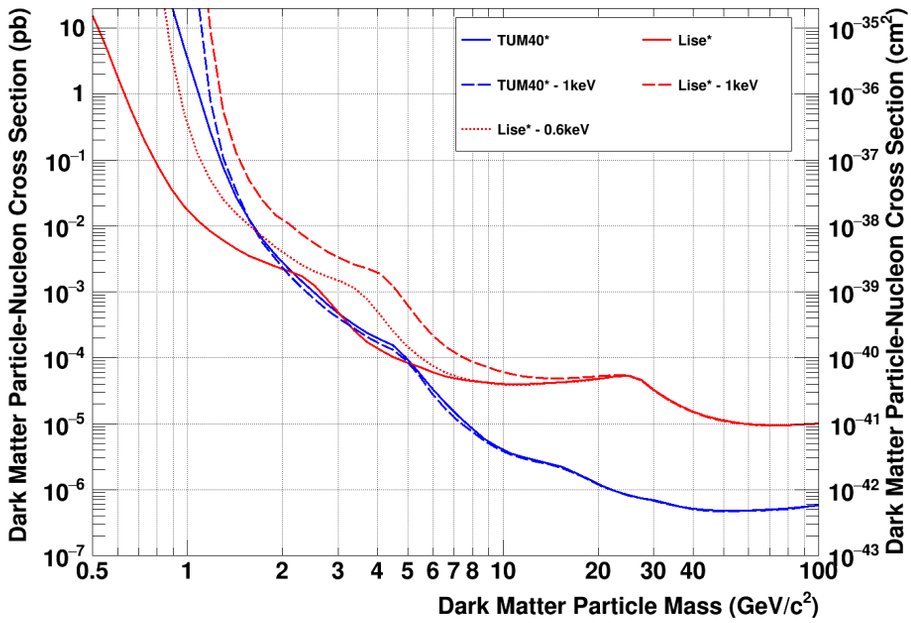

Figure 9.5.: Solid lines: exclusion limits with the hardware trigger threshold (0.6 keV for TUM40 (blue) and 0.3 keV for Lise (red)). Dashed and dotted lines: Exclusion limits with analysis thresholds as specified in the legend.

It is observed that the choice of the acceptance region has negligible impact for the sensitivity for low-mass dark matter particles, which is the main interest of this work. However, for masses above a few GeV/c^2 differences appear. Obviously, a 90 % oxygen band upper boundary is a suboptimal choice for both detectors for the following arguments. Firstly, the signal for these masses is completely dominated by scatterings off tungsten and, thus, including the almost complete oxygen band does not significantly increase the signal expectation. Secondly, the leakage from the e^-/γ-band is increased since the overlap of the oxygen band with the e^-/γ-band is larger in comparison to the other nuclear recoil bands.

For Lise and TUM40, an acceptance region limited to the mean of the tungsten band would yield a slightly better exclusion limit (dotted lines). This can be understood, as for both detectors some events with comparably high recoil energies drop out of the acceptance region when lowering the light yield bound (see figure 8.3), in particular the aforementioned potential neutron event seen in TUM40 at a recoil energy of 17 keV which considerably weakens the limit for higher masses. Thus, removing this event outweighs the drawback of practically halving the signal expectation with an upper boundary set at the mean of the tungsten band. However, for both detectors the relevant events are very close to the mean of the tungsten band which rather points to a by-chance-fortunate light yield distribution of these events than to a general advantage of this particular definition of the acceptance region.

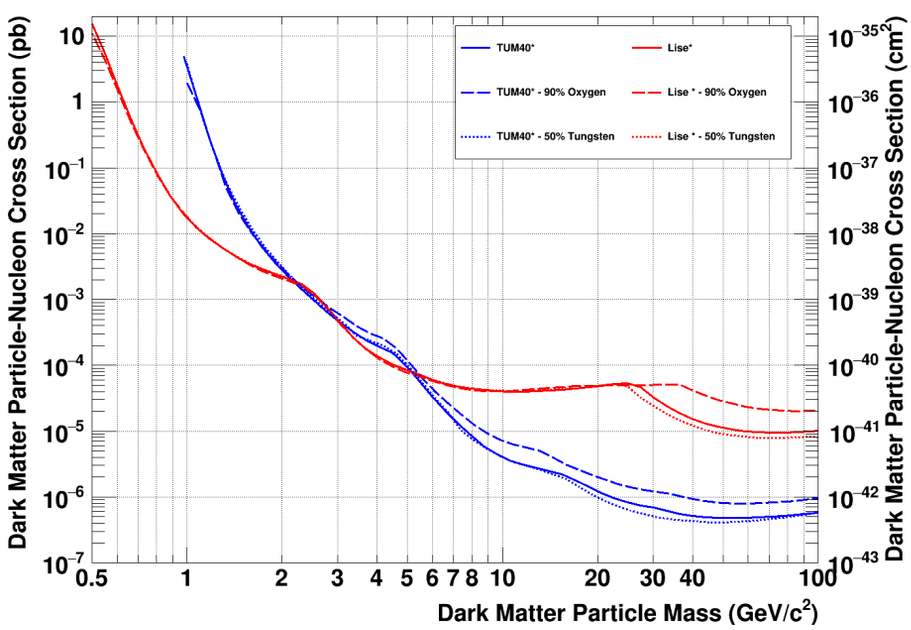

Figure 9.6.: Results obtained in this work for Lise and TUM40 with the mean of the oxygen band as upper light yield boundary (solid lines) compared to upper boundaries corresponding to the mean of the tungsten band (dotted) and the 90% upper boundary of the oxygen band (dashed).

10. Calculating Exclusion Limits Using Likelihood Methods

In the last chapter the main results of this work were presented: Exclusion limits obtained with Yellin methods. The main advantage of Yellin methods, namely to find powerful exclusion limits in the presence of an unknown background [149], may also be regarded as their main drawback as they offer hardly any possibility to include knowledge of the background. This chapter will present exclusion limits obtained within the framework of a maximum likelihood fit. This framework allows to include a model of the background and the uncertainties thereof. While these methods were already successfully used in CRESST-II phase 1 to characterize the observed excess [72, 71] the results presented here for the first time utilize likelihood methods to derive exclusion limits from CRESST-II data, in particular within of a low-threshold analysis.

10.1. Construction of the Extended Likelihood Function

While for the Yellin methods only a model for the expected signal is needed, the aim of a likelihood analysis is to build a complete, parametrized model including contributions from a potential signal and background. The central part thereby is the so-called likelihood function $\mathcal{L}(\boldsymbol{\Theta}|\boldsymbol{x})$ depending on the parameters of the model $\boldsymbol{\Theta}$ and the measured data $\boldsymbol{x}$. $\mathcal{L}(\boldsymbol{\Theta}|\boldsymbol{x})$ then is the likelihood that the model, with parameter values $\boldsymbol{\Theta}$, describes the measured data $\boldsymbol{x}$. The connection to a probability is straight-forward:

$$\mathcal{L}(\boldsymbol{\Theta}|\boldsymbol{x}) = \mathcal{P}(\boldsymbol{x}|\boldsymbol{\Theta}) \tag{10.1}$$

with $\mathcal{P}(\boldsymbol{x}|\boldsymbol{\Theta})$ being the probability to measure the data $\boldsymbol{x}$ for a given model with parameters $\boldsymbol{\Theta}$ [153]. Thus, the goal of a likelihood fit is to determine those values for the parameters $\boldsymbol{\Theta}$ which maximize the likelihood and, thus, to find the best possible agreement between the model and the measured data.

The construction of the model in this work to a large extent follows [72]. Each event in the measured data carries two relevant observables, the energy E and the light yield LY. Similar to the Yellin methods an acceptance region in the light yield-energy plane is defined. However, while for the Yellin methods the upper light yield boundary was set to the mean of the oxygen band, an acceptance region including all three nuclear recoil bands (90 % boundaries) is used for the likelihood analysis. Then, the first step in the construction of the model is to define a two-dimensional probability density function (pdf) ρ for signal and background contributions inside the acceptance region. The total pdf for

a single detector is given by:

$$\rho(E, LY|\mathbf{\Theta}) = \rho_\chi + \rho_\gamma \quad (+\rho_\alpha + \rho_{\mathrm{Pb}} + \rho_{\mathrm{n}}) \tag{10.2}$$

Its individual components, which will be discussed in more detail in the following, are:

ρ_χ potential dark matter spectrum, as extensively discussed in section 7.6.

ρ_γ leakage from the e^-/γ-band into the acceptance region

(ρ_α) contribution from degraded alphas

(ρ_{Pb}) Pb-recoil background

(ρ_{n}) neutron background

The three last components are put in brackets to illustrate that they are included in the model, but lost their importance compared to the likelihood analysis done for phase 1 [72]. The reasons, as well as a description of each pdf, will be given in the following.

ρ_χ The calculation of the spectrum expected for dark matter particles interacting with the detector was already outlined in section 7.6 and used for the Yellin methods in the previous chapter. The only difference for the signal expectation between the Yellin methods and the likelihood methods is that the former is one-dimensional only working on the energy spectrum, while the latter also makes use of the light yield information.

ρ_γ The leakage from the e^-/γ-band into the acceptance region is calculated in a straightforward approach. Firstly, the energy spectrum of events observed in the e^-/γ-band is binned and, secondly, the leakage is calculated using the analytic description of the e^-/γ-band (as presented in chapter 7). While for the likelihood analysis in [72] the lower energy limit of the acceptance region was set according to a desired e^-/γ-leakage of one event per detector module, the likelihood methods in this work use all data starting from trigger threshold (up to 40 keV). The slightly smaller light yield of certain γ-lines (section 7.3, references [146, 134]), which is particularly evident for the 11 keV double-peak in TUM40, is not accounted for in the calculation of the leakage. Thus, the leakage may be slightly underestimated. However, an underestimation of a background contribution leaves more room for a potential signal contribution and, thus, is conservative when calculating exclusion limits.

ρ_α As was already discussed in subsection 4.1.1, α-decays in near-surface layers of the metal crystal holding clamps may introduce so-called degraded α-events. Degraded refers to the α-particle loosing parts of its energy inside the clamp material an then reaching the crystal with energies down to the energies of interest. As the α-band at low energies overlaps with the nuclear recoil bands this background has, in principle, to be taken into account. However, for TUM40 this background is not present at all, as the fully-scintillating

module design, using $CaWO_4$-sticks instead of bare metal clamps to hold the crystal, vetoes this background (see section 4.2.2). Also for the detector Lise, which is of conventional detector design, the degraded-α background is negligible, as the holding clamps in phase 2 were produced from an ultra-radiopure clamp material [134].

ρ_{Pb} The Pb-recoil background arises from α-decays (in particular of ^{210}Po) with the recoiling Pb-nucleus hitting the crystal and the α-particle being absorbed in the metal holding clamps and, thus, staying undetected. The light yield of such events is comparable to recoils off tungsten ($QF_{Pb}^{-1} \sim 70$) and the energy ranges from the full energy (103 keV for a ^{210}Po-decay) down to the energies of interest. Although the Pb-induced recoil background in the conventional modules could not be reduced as much as the degraded α-background, the level of Pb-recoil events in Lise is negligible compared to the leakage from the e^-/γ-band, in particular in the view of the modest discrimination power of Lise.

Obviously, just like for degraded alphas this background is not present for TUM40, as there is no line-of-sight between the crystal and any non-scintillating surface in the stick design. Thus, the α-particle will always produce additional scintillation light which allows to identify such events.

For the stick design a second-order effect induced by the ^{210}Po -decay is imaginable, as a small part of the sticks is outside the scintillating housing and, thus, has a line-of-sight to non-active surfaces. This might result in ^{206}Pb ($E \leq 103\,\mathrm{keV}$) hitting the stick, which would then lead to a reconstructed energy of $E_P = 1/50 \cdot 103\,\mathrm{keV} \simeq 2\,\mathrm{keV}$, with a light yield comparable to a nuclear recoil. The factor $1/50$ arises from the phonon propagation between the interface of stick and crystal as determined for TUM40 [147, 139]. However, given the small surface of the sticks outside the housing the rate of such events is negligible, in particular compared to the expected leakage from the e^-/γ-band at the relevant energies of $\leq 2\,\mathrm{keV}$.

Above argument might not hold for the upcoming CRESST-III, firstly because the interface between the sticks and the crystal will be changed, potentially leading to a smaller suppression factor. Secondly, the new detectors will increase discrimination power between nuclear and electron recoil events, thus this class of events will no longer be negligible compared to e^-/γ-leakage. To overcome this issue, the CRESST collaboration foresees to equip all sticks with a dedicated TES. With this instrumented sticks (iSticks) the place of the primary energy deposition is known and, therefore, events in the sticks can be excluded from the analysis. Information on stick events may be found in [147, 139] and on the new iStick detector modules in [154].

ρ_n Neutrons are a dangerous background for any dark matter search as neutrons induce nuclear recoils, thus mimicking potential dark matter signals. However, in contrast to dark matter particles, neutrons have a certain probability to scatter in multiple detectors. If the ratio of multiple to single scatters is known, the neutron background can be estimated by the number of measured multiple scatterings. Thereby, one has to distinguish neutrons emitted from some radioactive contaminant (in or outside the experiment) from neutrons induced by muons (which are missed by the muon veto). In the latter case higher multiplic-

ities - defined as the number of detector modules triggering in coincidence - are expected, since muons rather induce particle showers than single neutrons, as in the case of a neutron emitter. The time resolution of cryogenic detectors, however, is not capable to disentangle a single neutron scattering in multiple detectors from multiple neutrons coincidently interacting in several detectors. Thus, in the phase 1 analysis [72] two multiplicity spectra were derived, one for source-like neutrons using neutron calibration data acquired by irradiating the experiment with an AmBe-source, and a second one using events coincident with the muon veto. However, for phase 2 an additional layer of high-purity polyethylene was installed (see figure 3.1), which significantly reduced the neutron background. In the dark matter data sets of Lise and TUM40 no multiple-scattering events in the nuclear recoil bands are observed. Thus, no estimation of the neutron background is included in the analysis.

In summary, for the analysis of this work the components ρ_α, ρ_{Pb} and ρ_{n} are forced to zero, leaving only the densities ρ_χ and ρ_γ to contribute in the likelihood.

It should be noted that neither the individual components ρ_x, nor the sum $\rho(E, LY|\mathbf{\Theta})$ are probability density functions, as their normalization depends on the variable parameters $\mathbf{\Theta}$. The number of events N' expected for a single detector in the acceptance region, is given by the two-dimensional integral of $\rho(E, LY|\mathbf{\Theta})$ over the acceptance region:

$$N'(\mathbf{\Theta}) = \int\int_{\text{acceptance region}} \rho(E, LY|\mathbf{\Theta}) dE dLY \tag{10.3}$$

For this analysis the so-called extended maximum likelihood (EML) is used [155], where the number of events N' also is a free parameter. Therefore, the EML formalism allows a deviation between the number of expected and the number of observed events, which is mandatory as the number of observed events is subject to Poissonian fluctuations. Thus, $\rho(E, LY|\mathbf{\Theta})$ does not have to be normalized, but may be used directly to construct the likelihood function evaluated for all accepted events with energies E_i and light yields LY_i:

$$\mathcal{L}'_{\text{acc.}} = \left[\prod_i \rho(E_i, LY_i|\mathbf{\Theta})\right] \exp[-N'(\Theta)] \tag{10.4}$$

Another advantage of the likelihood formalism is the straight-forward combination of different data sets, in particular of data from different detector modules. The combination is done by calculating signal expectation as well as the expected background contribution individually for each detector d (or more general, each individual data set). The total density gets assigned an index d ($\rho^d(E, LY|\mathbf{\Theta})dEdLY$), thus the total number of accepted events N and the total likelihood function $\mathcal{L}_{\text{acc.}}$ become:

$$N(\mathbf{\Theta}) = \sum_d \left[\int\int_{\text{acceptance region}} \rho^d(E, LY|\mathbf{\Theta}) dE dLY\right] \tag{10.5}$$

$$\mathcal{L}_{\text{acc.}} = \left[\prod_d \prod_i \rho^d(E_i, LY_i|\mathbf{\Theta})\right] \exp[-N(\Theta)] \tag{10.6}$$

10.1.1. Nuisance Parameters and Profile Likelihood

Up to now the vector $\boldsymbol{\Theta}$ contained all free parameters of the model. The most important parameter thereby is the dark matter-nucleon cross section σ_χ. Other free fit parameters, which are not of primary interest, are referred to as nuisance parameters and denoted with the letter $\boldsymbol{\theta}$. Therefore, $\boldsymbol{\Theta}$ may be written as $\boldsymbol{\Theta} = (\sigma_\chi, \boldsymbol{\theta})$. Building a model of parameters of interests (only σ_χ for the given application) and additional terms in the likelihood accounting for the uncertainties of nuisance parameters is often referred to as *profile likelihood* (e.g. in [156]), as the influence of the nuisance parameters will be profiled-out later on.

10.2. Discovery Versus Exclusion

For the construction of the likelihood function it is irrelevant whether one aims to claim a discovery (positive analysis) or to set an exclusion limit (negative analysis). Thus, the likelihood formalism is ahead of Yellin methods in terms of versatility, as the latter only allow to set upper limits. This fact was, among many others, pointed out by the authors of [157] whose notation shall be used here.

10.2.1. Discovery

To derive the significance of a process a so-called (profile) likelihood ratio test is performed, comparing the null-hypothesis to the best-fit value:

$$\lambda(0) = \frac{\mathcal{L}(0, \hat{\hat{\boldsymbol{\theta}}})}{\mathcal{L}(\hat{\sigma_\chi}, \hat{\boldsymbol{\theta}})} \tag{10.7}$$

The numerator is referred to as null hypothesis, since it is given by maximizing the likelihood under the condition of no signal expectation ($\sigma_\chi = 0$). The values for the nuisance parameters maximizing this so-called *conditional likelihood function* are labeled with a double hat: $\hat{\hat{\boldsymbol{\theta}}}$. The denominator includes a potential signal (free $\sigma_\chi \rightarrow$ *free likelihood* or best fit) and the resulting values yielding the maximum value for the likelihood function are labeled with a single hat: $\hat{\sigma_\chi}, \hat{\boldsymbol{\theta}}$. Thus, in simple words the likelihood ratio compares the null hypothesis to the best fit value, thereby profiling-out the influence of the nuisance parameters $\boldsymbol{\theta}$. The more evident the signal contribution is in the data, the higher will be the discrepancy to the null hypothesis. Correspondingly, $\mathcal{L}(0, \hat{\hat{\boldsymbol{\theta}}})$ will be small, as will be the likelihood ratio $\lambda(0)$. For the opposite case, namely that no signal contribution is found in the data, the best fit value will be a cross section close or equal to zero, thus free and conditional likelihood will result in very similar values and $\lambda(0)$ will be close to one. As in the free likelihood fit any value for σ_χ is allowed, explicitly also $\sigma_\chi = 0$, $\mathcal{L}(\hat{\sigma_\chi}, \hat{\boldsymbol{\theta}})$ will always be equal or larger than $\mathcal{L}(0, \hat{\hat{\boldsymbol{\theta}}})$ which consequently forces: $0 \leq \lambda(0) \leq 1$.

It should be kept in mind that the (profile) likelihood test provides powerful information on the question of how much better the data is described by a model including a potential

signal contribution than a model without this contribution. However, for a signal claim this implies the need for a precise knowledge about the background contribution, in quantity as well as in the distribution in the observables. Thus, for direct dark matter searches the neutron background ρ_n typically is of major interest. Since neutrons leave a similar experimental signature as dark matter particles would, a potential underestimation of ρ_n would leave room for a non-zero signal contribution ρ_χ.

To break down the outcome of the likelihood ratio test to a single observable which provides the significance of a signal in a frequentist interpretation, a so-called test statistics q_0 is used, most commonly the following one:

$$q_0 = \begin{cases} -2\ln\lambda(0) & \text{if} \quad \hat{\sigma_\chi} > 0 \\ 0 & \text{if} \quad \hat{\sigma_\chi} < 0 \end{cases} \tag{10.8}$$

Since $\lambda(0)$ takes values between zero and one and the logarithm is a continuously increasing function the term $-2\ln\lambda(0)$ is larger the smaller $\lambda(0)$ is. Negative values for the maximum likelihood estimate of the cross section $\hat{\sigma_\chi}$ are obviously non-physical and, consequently, q_0 is limited to 0 which corresponds to no rejection of the null-hypothesis.

At this stage a single observable q_0 is available, which quantifies the agreement between data and signal, or equivalently the non-agreement between data and null-hypothesis. To translate the quantity q_0 into a statistical significance, which describes the probability of a statistical fluctuation to fake a signal, we define the so-called p-value:

$$P_0 = \int_{q_{0,\text{obs}}}^{\infty} f(q_0|0)dq_0 \tag{10.9}$$

In the formula above $f(q_0|0)$ is the pdf of q_0 assuming that the true cross section σ_χ is zero (no signal). Thus, integrating $f(q_0|0)$ from the observed value $q_{0,\text{obs}}$ to infinity provides the probability that one obtains a value for q_0 equal or larger than $q_{0,\text{obs}}$, given that the data does not contain a signal (= the null-hypothesis is true). Figure 10.1a shows an illustration of equation 10.9.

Obviously, the statistical significance of a potential signal is of major interest, which is usually quoted in terms of standard deviations of a Gaussian-distributed variable. In this case the relation between p-value P_0 and significance Z is given by:

$$Z = \Phi^{-1}(1 - P_0) \qquad (= \sqrt{2}\,\text{erf}^{-1}(2P_0 - 1)) \tag{10.10}$$

with $\Phi(x)$ denoting the first quantile of the normal distribution, which may be interpreted in the following way: For a randomly distributed variable X the probability to obtain a value equal or smaller than the first quantile $Q_X(p)$ in a random draw is p. Thus, in a fraction p of random draws the variable X will be smaller or equal to $Q_X(p)$. For the specific case of the normal distribution $Q_X(p) = \Phi(x)$, which is often referred to as Probit-function and can be analytically calculated using the Gaussian error function erf. The relation between significance and p-value is illustrated in figure 10.1 with the red line illustrating the normal distribution and the blue shaded area the p-value. The one-sided definition of the p-value implies that $Z(P_0 = 0.5) = 0$. Today, the particle-physics community considers a statistical significance of $Z \geq 5$ mandatory for a particle discovery

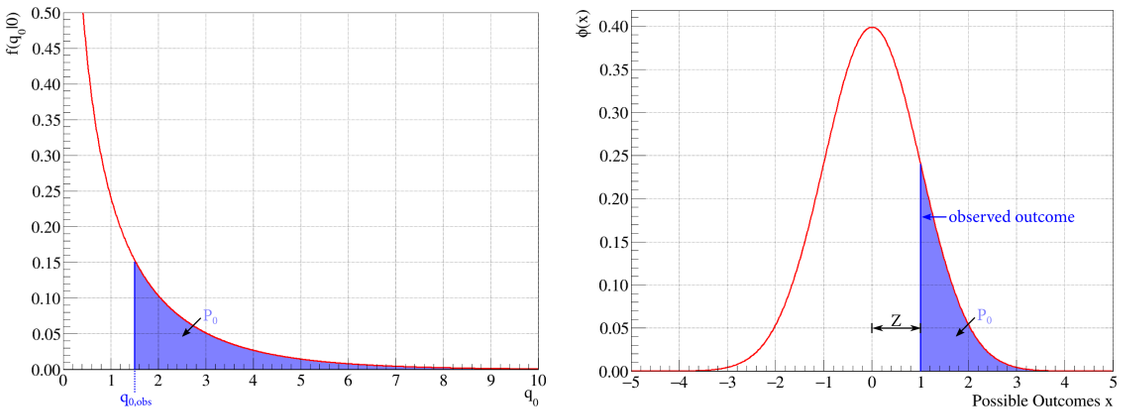

(a) Calculation of the p-value

(b) Calculation of the significance Z with the normal distribution: $\phi(x) = \frac{1}{\sqrt{2\pi}} \exp(\frac{-x^2}{2})$

Figure 10.1.: Plots to illustrate the calculation of the p-value from the observed value q_0 for a test statistics distributed according to the pdf $f(q_0|0)$ (left). Using the normal distribution the obtained p-value P_0 is converted to a significance Z (right). Plot idea adopted from [157].

(as most recently for the discovery of the Higgs-boson), which corresponds to a p-value of $P_0 \leq 2.87 \cdot 10^{-7}$.

The last component needed to test the significance of a signal in the likelihood framework is Wilk's theorem [158], which postulates that the probability density function $f(q_0|0)$ follows a χ^2-distribution with one degree of freedom (for large N) for the test statistics q_0 specified in equation 10.8. A detailed review, including validity tests of this theorem may e.g. be found in [157]. By applying the Wilk's theorem the significance for a signal is simply given by:

$$Z = \sqrt{q_{0,\text{obs}}} \tag{10.11}$$

To summarize, the following three steps have to be carried out for a positive (discovery) analysis using the (profile) likelihood framework:

1. Find maximum likelihood $\mathcal{L}(\hat{\sigma_\chi}, \hat{\boldsymbol{\theta}})$ with all parameters (signal + nuisance) left free
2. Find maximum likelihood $\mathcal{L}(0, \hat{\hat{\boldsymbol{\theta}}})$ with the cross section (signal) fixed to zero and all nuisance parameters left free
3. Calculate significance for a signal with the (profile) likelihood ratio test using equations 10.7, 10.8 and 10.11

10.2.2. Exclusion Limit

Calculating an exclusion limit in the likelihood framework is conceptionally similar to the discovery case, although the underlying question is different. For a discovery the data are investigated to which extent including a potential signal improves the compatibility of data

and model compared to the null hypothesis. The latter is not relevant for the limit setting case, where the question to be addressed is: To which extent (significance) can the existence of dark matter scattering with a given cross section σ_χ be excluded, given the data and the model. Thus the (profile) likelihood ratio test used to set an exclusion limit is

$$\lambda(\sigma_\chi) = \frac{\mathcal{L}(\sigma_\chi\text{=fixed}, \hat{\hat{\boldsymbol{\theta}}})}{\mathcal{L}(\hat{\sigma_\chi}, \hat{\boldsymbol{\theta}})} \tag{10.12}$$

In the formula above the denominator equals the discovery case and reflects the best fit value obtained by maximizing the likelihood with all parameters free. The numerator changed with respect to a positive analysis and is not the null-hypothesis any more, but the conditional maximum likelihood for a fixed cross section σ_χ.

Consequently, the test statistics q_0 becomes q_{σ_χ}:

$$q_{\sigma_\chi} = \begin{cases} -2\ln\lambda(\sigma_\chi) & \text{if} \quad \hat{\sigma_\chi} > 0 \\ 0 & \text{if} \quad \hat{\sigma_\chi} < 0 \end{cases} \tag{10.13}$$

The calculation of the significance Z remains unchanged and can be written as:

$$\begin{aligned} Z &= \sqrt{q_{\sigma_\chi}} \\ &= \sqrt{-2\ln\lambda(\sigma_\chi)} \\ &= \sqrt{-2[\ln\mathcal{L}(\sigma_\chi\text{=fixed}, \hat{\hat{\boldsymbol{\theta}}}) - \ln\mathcal{L}(\hat{\sigma_\chi}, \hat{\boldsymbol{\theta}})]} = \Phi^{-1}(1 - P_{\sigma_\chi}) \end{aligned} \tag{10.14}$$

At this stage another difference arises between discovery and exclusion limit case. For the former the likelihood ratio test is performed and the significance Z is calculated. For the latter Z is set a-priori by the desired confidence level - typically 90 %, thus $P_{\sigma_\chi} = 1 - 0.9 = 0.1$ - and the corresponding cross section σ_χ has to be determined. Thus, the calculation of an exclusion limit follows the following three steps:

1. Calculate Z for the desired confidence level
2. Find maximum likelihood $\mathcal{L}(\hat{\sigma_\chi}, \hat{\boldsymbol{\theta}})$ with all parameters (signal + nuisance) left free
3. Find maximum likelihood $\mathcal{L}(\sigma_\chi, \hat{\hat{\boldsymbol{\theta}}})$ with fixed cross section σ_χ and free nuisance parameters $\boldsymbol{\theta}$ such that the profile likelihood ratio test yields a p-value of 0.1, thus solving equations 10.13 and 10.14

10.2.3. Technical Remark on Maximum Likelihood Fits

In practice the likelihood function $\mathcal{L}$ is not maximized, but $-\ln\mathcal{L}$ is minimized instead. The logarithm is used to avoid too large numbers with the additional advantage that the ratio simplifies to a simple subtraction, as shown in equation 10.14. Since the logarithm is a continuously increasing function, the sign of $\mathcal{L}$ is not altered by this operation thus:

$\max(\mathcal{L}) = \max(\ln \mathcal{L})$. Taking the negative logarithm turns the maximization into a minimization and allows to use a standard function minimizer. For this work MINUIT [159] is used, as embedded in the ROOT data analysis framework [160]. Via the MINOS-routine, MINUIT also provides the functionality to determine $\mathcal{L}(\sigma_\chi, \hat{\hat{\boldsymbol{\theta}}})$ based on $\mathcal{L}(\hat{\sigma_\chi}, \hat{\boldsymbol{\theta}})$, which was additionally verified for the given application by comparing the MINOS calculation to a numeric iterative solution of equation 10.14.

10.3. Results

As already mentioned, for all likelihood-based results in this work only e^-/γ-backgrounds are considered for the reasons outlined in section 10.1. Free nuisance parameters in the fit are:

L_0^{ref} which accounts for the calibration of the reference detector used to determine the quenching factors.

$LY_{O,Ca}^{\infty}$ which denote the light output for recoils off oxygen and calcium for very high energies.

QF_W being the quenching factor of tungsten (not energy-dependent).

ϵ^d describing crystal-individual quenching effects, defined separately for each detector d.

All parameters above are not determined directly from the dark matter data, but through dedicated, external measurements. To account for the uncertainties of the respective parameters additional terms are added for to the likelihood function. Each term is given by a Gaussian function with its mean at the nominal parameter value, its sigma given by the uncertainty and evaluated at the current parameter value. Thus, the additional terms get smaller the more the parameter value differs from the nominal value. This may be understood as a penalty which has to be paid by the maximum likelihood fit when choosing a parameter different to its nominal value. In the following the parameters mentioned above and their impact will be briefly mentioned.

L_0^{ref} The quenching factors (QFs) used throughout this work are based on measurements of the light yield of scatterings off tungsten, calcium and oxygen, as reported in [148]. As a reminder, the QF is defined as the light yield of a particle X divided by the light yield of a γ-ray depositing the same amount of energy. Hence, to calculate the QF from the measured light yields in [148], the mean of the e^-/γ-band for the detector used in [148] has to be taken into account, including its uncertainty. The mean is, to very good approximation, constant and given by the value $L_0^{\text{ref}} = 1.07 \pm 0.03$. More detailed information on the parameter L_0^{ref} may be found in references [148, 147] and chapter 7.

$LY^{\infty}_{O,Ca}$ and QF_W The QF of tungsten (QF_W) is independent of energy and may be varied by the maximum likelihood fit. For oxygen and calcium, instead, an energy dependence is measured which is parametrized by the light yield at *infinite* energy $LY^{\infty}_{O,Ca}$ and an exponential function describing the light yield decrease towards lower energies (with amplitude $f_{O,Ca}$ and decay length $\lambda_{O,Ca}$, see subsection 7.4.1). The energy-dependence of the QFs for oxygen and calcium are fixed in the maximum likelihood fit, whereas $LY^{\infty}_{O,Ca}$ is a free fit parameter. Hence, all three nuclear recoil bands may be shifted up and down individually in the light yield coordinate, but no change of the *curvature* (accounting for the energy dependence) is allowed for the oxygen and calcium band.

The reason not to include $f_{O,Ca}$ and $\lambda_{O,Ca}$ as free fit parameters is that those parameters are hardly constrained by the dark matter data, in particular since the energy-dependence in the acceptance region is almost negligible. In addition, no realistic uncertainty estimates for the individual parameters are available, as the errors quoted for the individual parameters in reference [148] include statistical uncertainties only. These errors are negligible compared to the systematic error, which dominantly arises from the uncertainty of the phenomenological model used to describe the energy-dependence of the quenching factors. In reference [147] studies on the model-dependence were performed providing an estimate for the systematic uncertainty for the quenching factor averaged over the acceptance region (from threshold up to 40 keV). This uncertainty is included in the likelihood by putting an error on the average quenching factors (being a function of $LY^{\infty}_{O,Ca}$,$f_{O,Ca}$ and $\lambda_{O,Ca}$). In summary, this strategy includes the uncertainty on the absolute value of the QFs of oxygen and calcium, thereby neglecting a potential uncertainty on the energy-dependence of the corresponding QFs. However, it should be pointed out that already uncertainties in the absolute values for the quenching factors hardly affect the final result, which renders uncertainties in the energy-dependence absolutely negligible.

ϵ_d The parameter ϵ_d describes crystal-dependent quenching effects, which affect all three nuclear recoil bands of the same detector in the same manner.

In summary, with the nuisance parameters above the likelihood fit explores the following possible uncertainties in the position of the quenched bands in the light yield - energy plane. The parameter L_0^{ref} affects all nuclear recoil bands in all detectors in the same manner, the parameters $LY^{\infty}_{O,Ca}$ and QF_W allow an up or down shift in light yield individually for the respective nuclear recoil band, but common for all detectors. Finally, the parameters ϵ_d affect all nuclear recoil bands in the same way, but individually for each detector.

The resulting exclusion limits are depicted in figure 10.2 together with the limits obtained using the Yellin optimum interval method (see caption and legend). As one can see, the gain of likelihood methods is particularly evident for the detector Lise with roughly one order of magnitude improvement over the whole dark matter particle mass range. For TUM40 the profit is not as large as for Lise, which can be understood as a consequence of the much lower e^-/γ-leakage in TUM40 compared to Lise. Additionally, the exclusion limit obtained by combining data from Lise and TUM40 is drawn in solid black.

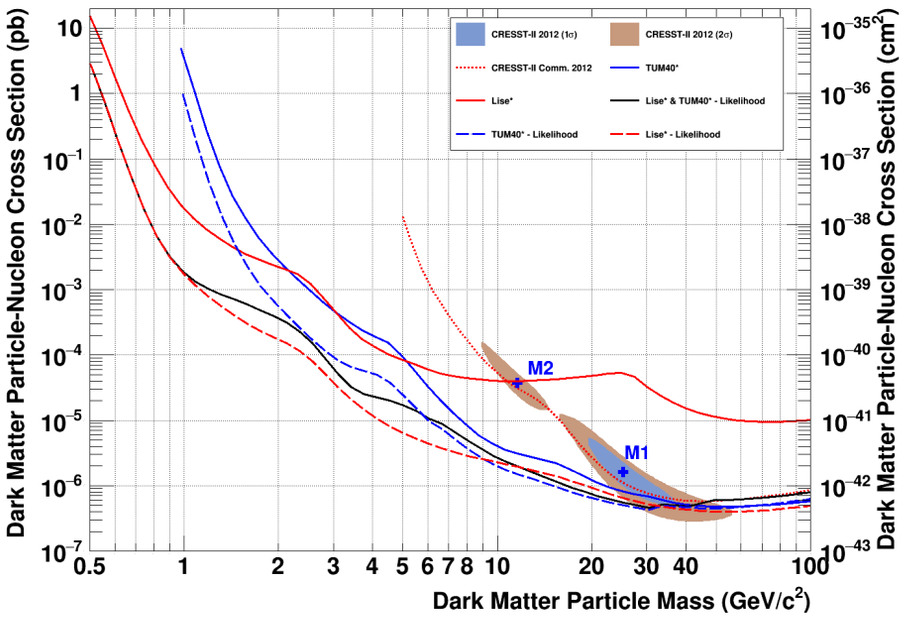

Figure 10.2.: Exclusion limits obtained using the maximum likelihood analysis for Lise (dashed red), TUM40 (dashed blue) and a combination of both detectors (dashed black) in comparison to limits obtained with the Yellin optimum interval method and previous CRESST-II results.

At around 30 GeV/c^2 a kink in the likelihood limit is present for TUM40 and for higher masses the limit stays weaker than naively expected. This behavior is consistent with the comparison of the Yellin limit with the statistical fluctuation expected for only e^-/γ-backgrounds (see figure 9.2). Thus, also the likelihood analysis points to a few events ($\mathcal{O}(\ll 5)$) in the nuclear recoil bands which are in mild tension with the expectation from pure e^-/γ-leakage. The most viable explanation is the existence of at least one neutron interaction for the event observed at 17 keV. As no neutron background estimate is included, events in the nuclear recoil bands beyond the expected e^-/γ-band inevitably lead to a positive signal contribution in the maximum likelihood estimate. However, it should firstly be pointed out that a potential neutron background is negligible for low recoil energies and, thus, for low-mass dark matter particles - which are the main focus of this work - the exclusion limit would not improve including a neutron background estimate. Secondly, an underestimation of the background is conservative for setting exclusion limits. The incompatibility becomes visible in figure 10.3 showing the light yield spectrum of all events in the acceptance region of TUM40 (energies below 1 keV are not included for clarity). A small excess $\mathcal{O}$(1-2 events) is observed for a light yield compatible with nuclear recoils. For this figure the signal contribution was estimated for a dark matter particle mass of 60 GeV/c^2.

The better performance of the likelihood formalism compared to Yellin methods arises from precisely estimating the e^-/γ-leakage into the acceptance region. Figure 10.4 shows the combined energy spectrum (TUM40 and Lise) together with the expected e^-/γ-background and a potential signal contribution of 11.6 GeV/c^2, which corresponds to the mass

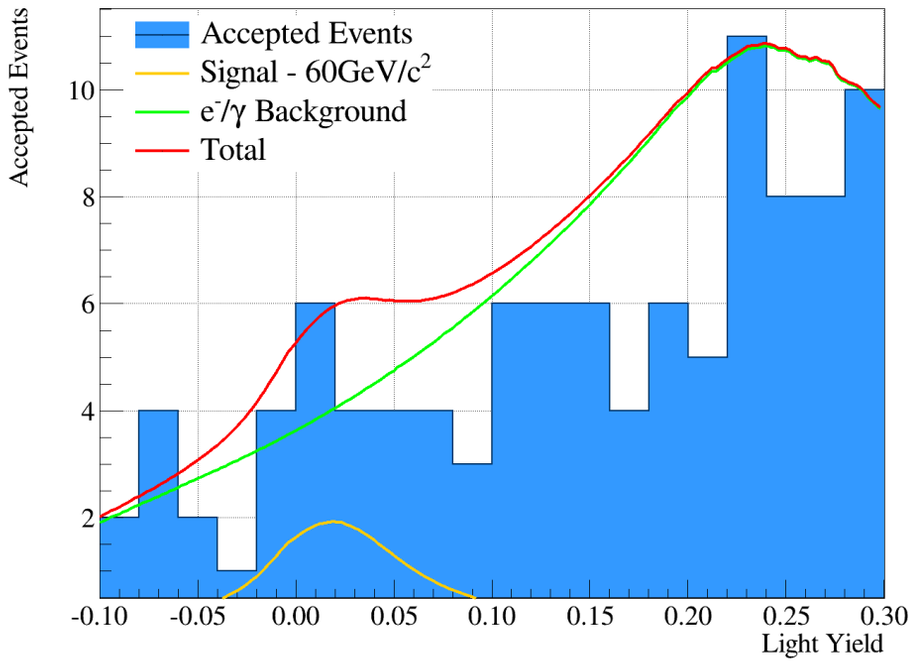

Figure 10.3.: Light yield spectrum of events in the acceptance region of TUM40 with energies between 1 keV and 30 keV. The green line corresponds to the expected leakage from the e^-/γ-band. The signal estimate for a 60 GeV/c^2 dark matter particle is depicted in yellow, the sum of both in red.

of the M2 maximum of the phase 1 analysis. The cross section is given by the best-fit value $\mathcal{L}(\hat{\sigma_\chi}, \hat{\boldsymbol{\theta}})$ which is determined to be $1.2 \cdot 10^{-6}$ pb and yields an 90 % upper limit of $2.0 \cdot 10^{-6}$ pb for this mass. Thus, the M2-solution of phase 1 having a cross section of $3.7 \cdot 10^{-5}$ pb is ruled-out by more than one order of magnitude.

Very good agreement is found between the energy spectrum observed (blue) and the estimated leakage (green solid line)[1]. Both detectors leave their fingerprint in the combined spectrum, the most prominent features are (from high to low energy): 1: The 11 keV double-peak dominantly observed in TUM40. 2: The ^{55}Fe-induced double peak around 6 keV seen in Lise. 3: the 2.6 keV line present mainly in TUM40, but to a smaller extent also in Lise. 4: The rise starting at 1 keV down to the threshold of TUM40 (0.6 keV).

As the e^-/γ-leakage almost perfectly explains the spectrum seen in the acceptance region, hardly any room for a potential signal is left, which becomes obvious comparing the background spectrum with the yellow line depicting the signal estimate for the given example of 11.6 GeV/c^2. Thus, the total spectrum (red line = signal + e^-/γ-background) is dominated by the e^-/γ-leakage. However, one should not forget that this signal estimate is not derived from the depicted combined energy spectrum, but takes into account each detector individually and also uses the light yield information.

The step in the signal estimate at 0.6 keV arises from the threshold of TUM40: for lower

[1] Satisfying compatibility is also found in absolute terms: the expected number of e^-/γ-events leaking into the acceptance regions of TUM40 and Lise is 6044 and 6090 events are observed.

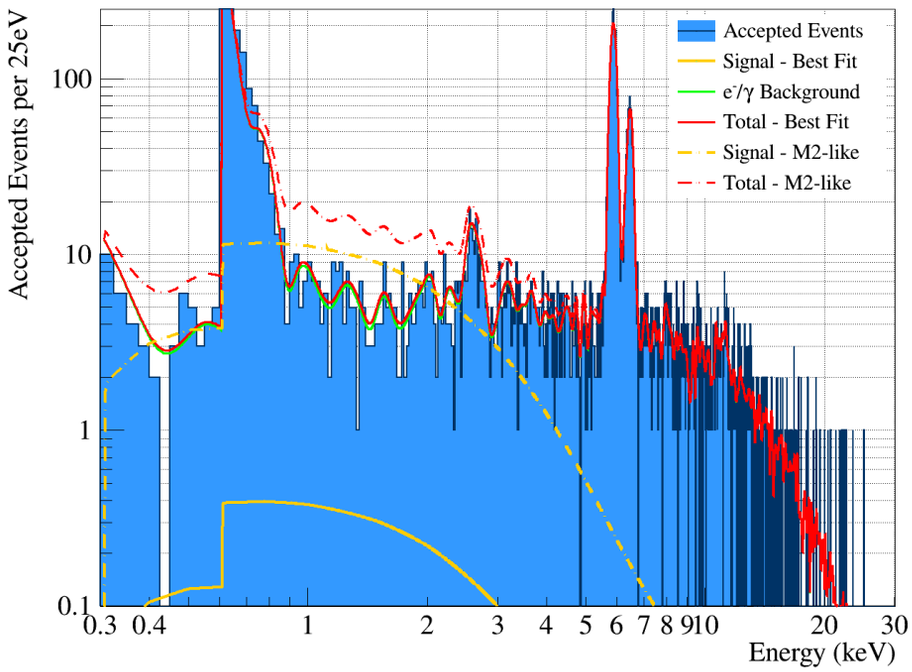

Figure 10.4.: Energy spectrum of all accepted events of TUM40 and Lise in the maximum likelihood analysis. The solid lines depict the expectation of the leakage from the e^-/γ-band into the acceptance region and the best fit value for a WIMP of 11.6 GeV/c^2 (maximum M2 of phase 1 analysis, see chapter 4). A M2-like dark matter particle would yield a signal expectation as drawn in dashed yellow resulting in a total expectation depicted in dashed red.

energies only Lise contributes. The dashed dotted lines show the signal expectation (yellow) and the resulting total spectrum (red) for a M2-like dark matter signal ($m_\chi = 11.6\,\mathrm{GeV/c^2}$,$\sigma_\chi = 3.7 \cdot 10^{-5}$ pb) which is clearly incompatible with the energy spectrum observed in Lise and TUM40.

In conclusion, it was proven in this chapter that the likelihood framework can successfully be applied on CRESST-II data, not only for a positive analysis as done in phase 1, but also to calculate powerful exclusion limits. As the likelihood analysis in this work is a further development of the phase 1 analysis, it cancels out uncertainties on the influence of the analysis method when comparing phase 2 exclusion limits to the phase 1 dark matter interpretation. It was already mentioned that the lower-mass maximum M2 is ruled-out by more than one order of magnitude, but also the M1 solution is in clear tension, being excluded by roughly a factor of three. Further improvements, in particular for higher dark matter particle masses, are within reach by applying likelihood methods on phase 2 data. However, this requires to include more detectors, also those with higher thresholds, which is beyond the scope of the low-threshold analysis presented in this work.

11. Conclusions and Outlook

In the framework of this thesis, CRESST-II data are analyzed which were taken during phase 2 extending from July 2013 to August 2015. Thereby, the complete process from raw data analysis to the final result on spin-independent, elastic scattering of dark matter particles with the $CaWO_4$-target is outlined. The main focus, however, is set on the new developments implemented in the analysis allowing to make use of data down to the trigger threshold. Thereby, this work concentrates on two detectors, named TUM40 and Lise.

TUM40 is chosen for its superior overall performance, out of the eighteen detectors operated in phase 2, regarding energy resolution, trigger threshold and background level. First results, using non-blind data of TUM40 taken in 2013, were already published in [75]. At the time of publication a new exclusion limit on the cross section for dark matter particles scattering off nuclei was set for dark matter particles lighter than 3 GeV/c^2. Since then additional refinements concerning the analysis were developed which are applied to the complete blind dark matter data set of phase 2 in this thesis.

Based on the success of the result obtained with TUM40, the hardware trigger thresholds of several detectors were lowered within this thesis. The lowest threshold was obtained for the detector Lise; results were published very recently [74]. This work describes the corresponding low-threshold analyses of TUM40 and Lise in full detail.

The first two chapters lay out the basics concerning dark matter and its detection. Afterwards, chapter three and four give an introduction to the CRESST experiment and the summarize the findings of the previous phase 1, where an excess of events above the expected background level was observed. Interpreting this excess as a potential dark matter signal yields reasonable properties for the dark matter particle, with two combinations of mass and scattering cross section with similar statistical significance. These two maxima are named M1, with a mass of 25 GeV/c^2 and M2 with a mass of 12 GeV/c^2. A major goal of phase 2 was to clarify the origin of this excess which required a substantial reduction of background level. Measures taken are outlined, with a particular focus on new upgraded detector designs.

The starting point of the analysis is the processing of the raw data discussed in chapter five. The central tool is the so-called standard event fit which is used to extract the amplitude for a recorded pulse and, thus, the deposited energy in the respective detector. As this fit is particularly challenging for the small pulses analyzed in this work, the implemented improvements are a vital component for the success of this low-threshold analysis. The excellent energy resolution of the detectors allow a detailed study of, in particular, the low energy spectrum. To conclude chapter five, measurements of the hardware trigger thresholds are presented, which obviously are essential in the framework of a low-threshold analysis.

For cryogenic detectors a thorough cleaning of the raw data is mandatory. As a general guideline, one aims to discard all events from the data set where a correct reconstruction

is not guaranteed. Chapter six discusses the selection criteria applied to the data. Thereby, a new strategy was pursued compared to previous analyses which were setting an analysis threshold well above the hardware trigger threshold and aimed at selection criteria with an efficiency independent of the deposited energy. For this analysis an energy dependence is explicitly accepted which requires a precisely measured efficiency curve as a function of energy. A new method to determine this efficiency curve using simulated pulses is presented in chapter six.

Chapter seven marks the switch in the analysis chain from the processing and the selection of the (raw) data to the investigation of the data concerning a potential dark matter signal. The first step thereof, as discussed in chapter seven, is to model the position of the different event classes in the light yield-energy plane, in particular concerning the discrimination between e^-/γ-events (dominant background) and nuclear recoils (potential dark matter signal). Including the measured dependence of light quenching for nuclear recoils off oxygen and calcium on the deposited energy [147, 148] marks another novelty of this work.

No excess in the raw data above the known backgrounds is evident for phase 2 data. Thus, so-called Yellin methods are used to derive exclusion limits on the cross section of elastic, spin-independent dark matter particle - nucleus scattering. Basically, Yellin methods exploit the difference in the observed energy spectrum to the energy spectrum expected for dark matter particles interacting in the target. Chapter eight introduces the Yellin methods and their implementation in the low-threshold analysis of CRESST-II data. As Yellin methods only exploit the energy spectrum, but do not make use of the light information a so-called acceptance region in the light yield-energy plane is defined where a potential dark matter signal would be expected. Chapter eight discusses the events seen in the acceptance regions of TUM40 and Lise and the anticipated characteristics of a potential dark matter signal seen therein.

Yellin methods are derived to obtain the main result of this work, which are presented in chapter nine. The limit obtained with Lise currently takes the lead in the field of direct dark matter detection for dark matter particles lighter than 1.7 GeV/c^2. For the first time it is possible to explore the sub-GeV/c^2regime, down to a mass of 0.5 GeV/c^2. It was already pointed out, that an excess has been seen in the previous phase 1; clarifying its origin is a primary aim of phase 2. With the analysis of this work, of in particular TUM40 data, the lower-mass solution M2 can clearly be ruled out and substantial tension is put on M1. A complete exclusion of M1 is within reach using data from phase 2. Since the exposure is a limiting factor in that dark matter particle mass regime, a combination of data from multiple detector modules is mandatory. This, however, is beyond the scope of this thesis being dedicated to a low-threshold analysis and, thus, will be targeted in a future publication.

The presentation of the main result in chapter nine is accompanied by several studies on potential sources of uncertainties, finding only negligible impact for all of them. This outcome once again proves that the analysis in general and the Yellin methods in particular provide robust and convincing exclusion limits. However, since they do not take into account backgrounds, the result might be too conservative. An alternative approach, to extract upper limits from the data, is the maximum likelihood method. Chapter ten introduces the profile likelihood framework, which is for the first time used to set exclusion

limits from CRESST-II data.

As the excess observed in phase 1 was also derived using a comparable likelihood approach, the analysis of this work provides the possibility to directly compare results from the two phases, eliminating potential influence from different analysis frameworks. In particular for Lise a considerable improvement in sensitivity is found for the likelihood method with respect to the Yellin result. Compared to TUM40, Lise exhibits a substantially higher leakage from the e^-/γ-band into the nuclear recoil bands. Since the likelihood method precisely takes the e^-/γ-leakage into account, a higher gain when switching from Yellin to likelihood is expected for Lise than for TUM40. However, also for the latter a better sensitivity is reached over almost the entire dark matter particle mass regime.

For the near future, further progress is expected using profile likelihoods methods. With the present analysis a major step was made to arrive at a complete background model, in particular concerning the dominant e^-/γ-background and its distribution in the light yield - energy plane. With further refinements, a complete and high-precision model of the data seems achievable which will allow to propagate the model of the e^-/γ-band into the likelihood function, thus further reducing uncertainties.

This low-threshold analysis proves that CRESST-II detectors are perfectly suited to measure energy deposits well below 1 keV. Combined with the light elements oxygen and calcium in the $CaWO_4$-target material, CRESST has outstanding sensitivity for the direct detection of light dark matter particles ($\mathcal{O}(\ll 1\,\mathrm{GeV/c^2})$). This consideration yields promising prospects to further explore the low-mass regime, also backed by the growing theoretical interest in light dark matter particles arising from a variety of new dark matter models.

Therefore, the CRESST collaboration decided to consequently optimize their detectors for the detection of very small energy depositions originating from light dark matter particles [112]. CRESST-III is foreseen to start in early 2016 featuring detectors with $CaWO_4$-crystals scaled down to 25 g. It is expected that reducing the size of the crystal will not only provide an energy threshold smaller than 100 eV, but also increase light output and, thus, enhance discrimination power. Beyond that, a substantial improvement in background level is required, which mainly arises from radioactive contaminations inside the $CaWO_4$-crystals. However, the improvements concerning the radiopurity of $CaWO_4$-crystals already achieved by the crystal growth at TU München yields confidence that this challenge can be met in the next years.

A. Appendix

A.1. Further Information on Raw Data Analysis

A.1.1. Values for Quality Cuts

	TUM40	Michael	Lise	Enrico
Amplitude (V)	[0 , 7.0]	[-3.8 , 3.8]	[0 , 2.4]	[-0.11 , 0.11]
Energy (eV)	>606	-	>307	-
Trigger Delay (ms)	>245.76	-	>245.76	-
Delta Voltage-RMS (V)	[-8.0 , 0.5]	[-8.0 , 0.5]	[-7.4 , -1.3]	[-2.6 , 0.10]
Right-Left Baseline (V)	[-0.20 , 0.22]	[-0.15 , 0.20]	[-0.020 , 0.030]	[-0.023 , 0.020]
Peak Position (ms)	-	-	[70.2 , 209.6]	-
Shift (ms)	-	-	[-20 , 180]	-
Peak Position - Onset (ms)	see figure 6.6a	-	[-100 , 5.2]	-

Table A.1.: Cut values for the quality cuts discussed in section 6.5.

Table A.1 lists the values chosen for the quality cuts (see section 6.5) which are applied on the data for the detector modules TUM40/Michael and Lise/Enrico. All cuts are designed on the respective training set and then applied blindly on the dark matter data set (see section 5.1).

A.1.2. Low-Threshold Detectors

In this work the detectors Lise and TUM40 are analyzed. Lise is the detector with the lowest trigger threshold of all detectors operated in CRESST-II phase 2. TUM40 exhibits the best overall performance concerning e^-/γ-background level (due to the crystal being grown at the TU München), trigger threshold (0.4 keV, see section 5.7) and the veto for α-induced events (fully-scintillating stick design). Although a low energy threshold was only a secondary interest during the design of phase 2, five out of 18 detectors feature an energy threshold lower than (or equal to) 500 eV. All those detectors are listed in table A.2. For CRESST-III, with detectors dedicatedly optimized for low trigger threshold, an increased homogeneity in detector performance is expected.

Detector Module	Threshold (eV)	Crystal	Design
Lise	307	commercial	conventional
Daisy	~ 340	commercial	conventional
TUM40	405	grown at TUM	stick-design
VK34	~ 440	commercial	conventional
VK32	~ 500	commercial	conventional

Table A.2.: All detectors operated in CRESST-II phase 2 featuring a threshold setting of $\lesssim 0.5$ keV.

A.2. Expected Signature of Phase 1 Excess

As was mentioned several times throughout this thesis, one main goal of phase 2 was to clarify the origin of the excess in phase 1. Both statistical methods used to derive exclusion limits from the data - Yellin methods in chapters 8 and 9 and a likelihood method in chapter 10 - clearly exclude the lower mass solution M2 and put tension on the higher mass solution M1, in particular using TUM40 data. Simulations are carried out to visualize, how an M1, or M2-like WIMP would manifest itself in the light yield - energy data of TUM40. For these simulations random events are drawn from the expected two-dimensional spectra corresponding to an M1/M2-like WIMP. The outcomes are depicted in figure A.1, showing the measured data (TUM40, dark matter data set) in black and simulated WIMP events in red circles. The bands correspond to the e^-/γ-band in blue and the nuclear recoil bands for oxygen and tungsten in red and green, respectively.

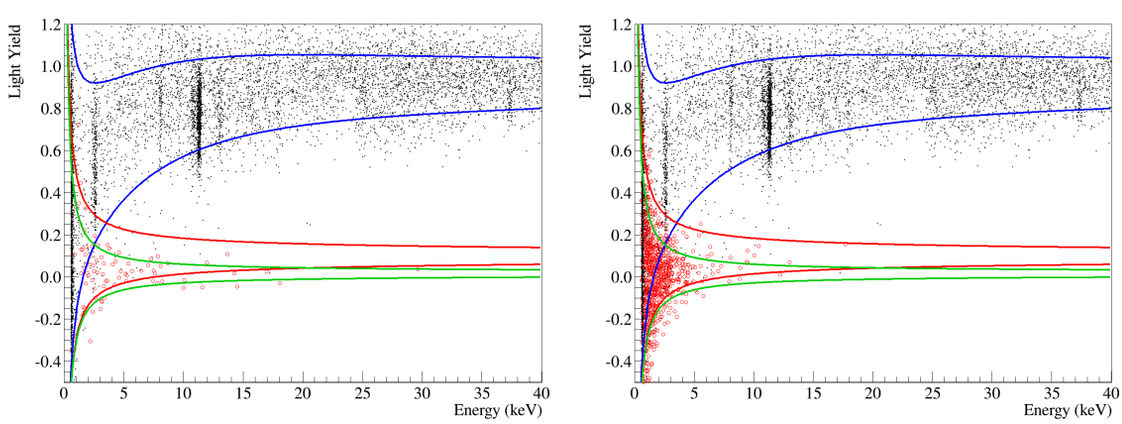

(a) M1: 25.3GeV/c^2- $1.6 \cdot 10^{-6}$pb (b) M2: 11.6GeV/c^2- $3.7 \cdot 10^{-5}$pb

Figure A.1.: Data acquired with TUM40 in the dark matter data set (black) together with simulations for an M1/M2-like dark matter particle (red circles). The bands correspond to scatterings off tungsten (green), off oxygen (red) and to e^-/γ-events (blue).

Figures A.1a and A.1b clearly show typical features of the expected dark matter recoil spectrum. In both cases tungsten is the dominant scattering partner due to the anticipated quadratic scaling of the cross section with the atomic mass number (A^2). For the heavier M1-like WIMP the energy transfer in the scattering is larger, thus the spectrum extends to higher energies. From these simulations it becomes clear, that an M2-like dark matter particle is absolutely incompatible with the measured data, while for M1 the disagreement is much weaker. This optical impression perfectly agrees with the exclusion limits calculated in this work (see chapters 9 and 10).

A.3. Comparison to Published Results

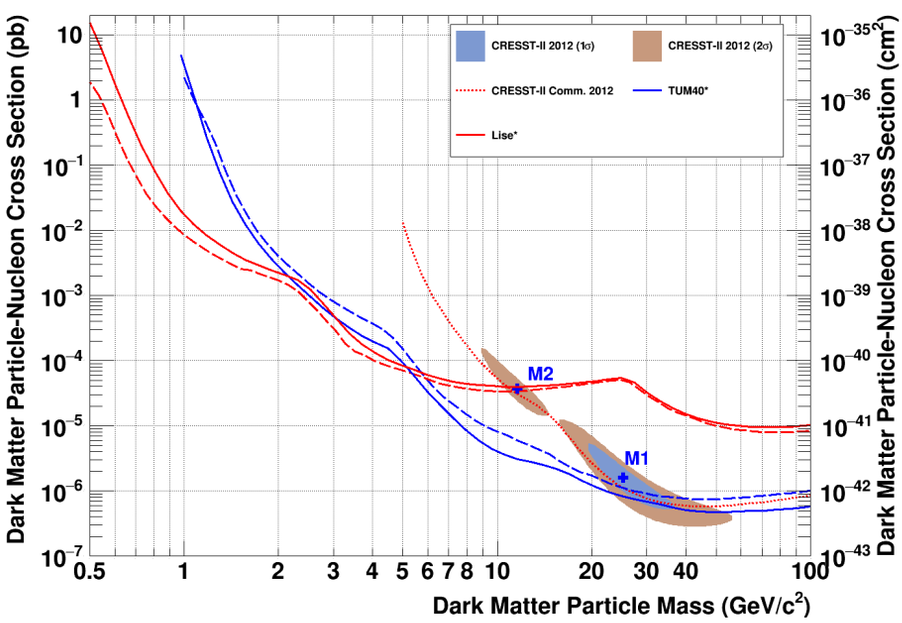

Figure A.2.: Comparison of results of this work (solid red and blue) to published results (dashed red and blue) together with previous CRESST-II results (see legend).

Figure A.2 shows a comparison of the results obtained in this work (solid lines, blue for TUM40 and red for Lise) using Yellin methods (see chapter 9) to the published results (dashed lines) for TUM40 [75] and Lise [74], which also rely on the Yellin optimum interval method. The mild differences observed for TUM40 mainly arise from the different exposures. While the published limit was obtained using non-blind training set data - corresponding to an exposure before cuts of 29 kgd - the result presented here is derived from the blind data set with roughly the triple exposure (98 kgd).

For Lise the same data set is used for this work and for the publication in [74]. Hardly any difference is seen at *high* dark matter particle masses. The small discrepancy observed in the low-mass regime arises from a slightly different setting of the data selection criteria, which were in both cases chosen a-priori on training set data, thus sticking to the concept of a blind analysis. However, achieving agreement on the level of the statistical fluctuation

(see figure 9.2) for different sets of cuts, independently designed by different people, further strengthens the validity of the result obtained.

A.4. Comparison to Collider Limits

The principle of dark matter searches at colliders was already sketched in section 2.1, figure A.3 shows the results of this work together with results from other direct dark matter searches and with selected limits obtained at the LHC-experiments ATLAS and CMS.

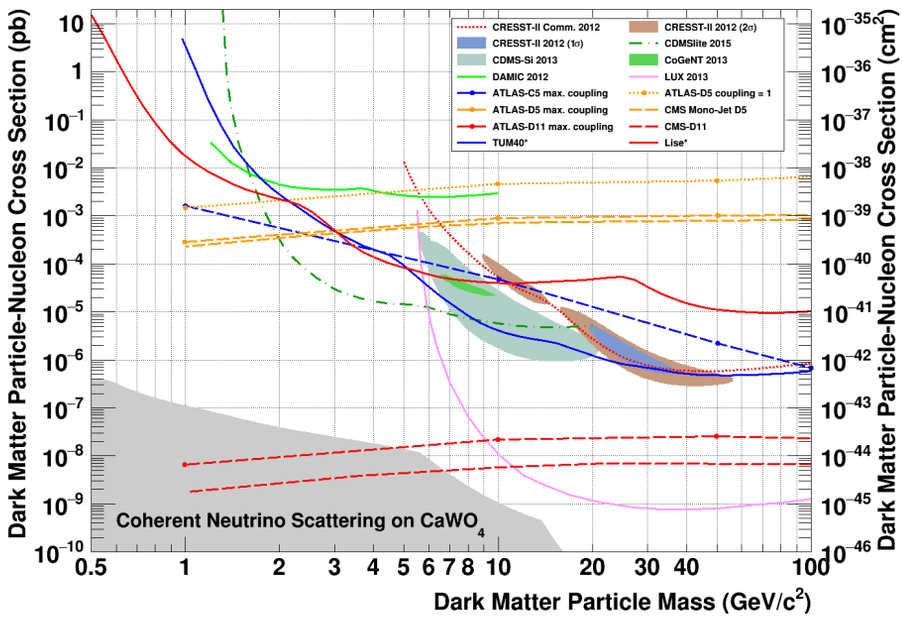

Figure A.3.: Exclusion limits obtained in this work (*), together with results from other direct dark matter searches (see legend) and limits obtained for collider searches (dashed lines) assuming different effective field theory operators. Collider limits are taken from [40].

All exclusion curves from ATLAS and CMS are depicted in dashed lines, limits from ATLAS are additionally marked with a dot. Different colors correspond to different assumptions on the coupling between dark matter and Standard Model particles in the framework of effective field theory (details may be found in [39]). Basically, the operators D11 and C5 (orange and blue lines) describe scalar couplings to gluons ($gg \rightarrow \chi\bar{\chi}$), D11 a Dirac fermion dark matter particle and C5 a scalar dark matter particle. D5 instead, accounts for a vector coupling to quarks of a Dirac fermion dark matter particle. For the operator D5 ATLAS published two exclusion curves, once for the maximal possible coupling to yield a pertubative interaction (dashed) and once for a coupling of one (small dashes). For details on the collider results, including a study on the validity of effective field theory, the reader is referred to [40].

Obviously, figure A.3 shows that the comparison between direct dark matter detection and collider searches strongly depends on the coupling assumed. The general trend, is

that direct searches are more sensitive in the higher mass range of a few ten GeV/c^2, while colliders probe the low-mass regime of parameter space. However, with the low-threshold analyses of, in particular CRESST-II and CDMSlite, the direct searches made a big step forward towards sensitivity for low-mass dark matter particles being competitive (for most assumed couplings) down to ~ 1 GeV/c^2. In the next years further improvements over the whole dark matter particle mass regime are expected, for direct searches (low-threshold detectors and experiments with higher target mass) as well as for LHC experiments (higher center of mass energy, than for the results shown here and more statistics). In summary, collider and direct detection for dark matter are complementary and finding a consistent result with both approaches may one day be a break-through in the understanding of dark matter.

A.5. Projections for CRESST-III Phase 1

Motivated from the success of the low-threshold analyses of CRESST-II phase 2 data (this work, [74, 75]) the CRESST collaboration developed new, upgraded detector modules [112]. These new modules are based on the stick-design, as used for TUM40, however the crystal is sized-down from ~ 250 g to ~ 25 g. This size-down will mainly improve the performance of the phonon channel with anticipated thresholds of ≤ 100 eV. Furthermore, for geometric reasons less scintillation light is expected to be trapped in the crystal or lost in the housing, therefore improving the light signal. In addition to that, further benefits for the light signal are expected, because a smaller crystal allows the use of a smaller light detector, which in general improves its baseline resolution.

In figure A.4 projections for CRESST-III phase 1 are depicted; the red band corresponds to an exposure before cuts of 25 kgd, the blue band to 100 kgd (both with 1 σ confidence level). These projections are based on the performance of TUM40 and the following assumptions:

* Baseline resolution for the phonon detector of $\sigma = 20$ eV corresponding to a threshold of 100 eV (see sections 5.7 and 7.1)
* Baseline resolution for the light detector improved by a factor of two (smaller size)
* Amount of light detected in the light detector improved by a factor of three (geometry)
- Background level of TUM40 for energies above 1 keV and a constant extrapolation for the background level below 1 keV
- Constant cut efficiency of 56 % (asymptotic value of TUM40)

The items listed with a star (*) are chosen in accordance to [112], the last two points deserve a more detailed discussion. The rise observed for TUM40 for energies below 1 keV is not included in the projections, because the investigations performed in subsection 6.10.2 and reference [145] rather point to a non-particle origin for this rise which is connected to

the TES carrier. For CRESST-III the TES will be directly evaporated on the target crystal avoiding the use of a carrier. Therefore, the background level is assumed to be constant for energies below 1 keV down to the new threshold energy of 100 eV.

In section 6.9 it was shown that the energy-dependence of the cuts is to a large extent caused by discrimination of carrier events becoming more challenging for smaller energies (= smaller pulse heights). Since no TES carriers will be used, the projections assume a constant cut efficiency of 56 %, which corresponds to the asymptotic value determined for TUM40 (see figure 6.11a). However, it should be emphasized that in the low-mass regime the achievable sensitivity is dominated by background rather than by exposure, which renders some uncertainty in the cut efficiency a minor effect only. This argument becomes obvious comparing the projections in figure A.4. Although the exposure differs by a factor of four, hardly any difference is observed in the low-mass regime, while for a dark matter particles with masses of $\gtrsim 10\,\mathrm{GeV}/c^2$ exposure is the decisive factor and, thus, the projected exclusion limit scales linearly with exposure.

Following the above assumptions 10,000 data sets for each exposure are created and for each data set a limit is calculated using the Yellin optimum interval method. The use of the Yellin optimum interval method also explains the 1 σ-confidence bands narrowing for higher dark matter particle masses. For these masses the sensitivity is to a large extent given by recoil energies of $\mathcal{O}(10\,\mathrm{keV})$ and more, where the discrimination power is high enough to prevent any leakage from the e^-/γ-band to the acceptance region. Thus, the Yellin optimum interval will include a few leakage events only (or zero) and extend from the leakage events with the highest energies to the end of the acceptance region at 40 keV (see section 8.3). The size of the optimum interval (= the integral over the expected dark matter recoil spectrum), however, then is dominated by the background-free energy range, which is similar for all data sets. Fluctuations in this case solely arise from the position in energy of the last few leakage events from the e^-/γ-band into the acceptance region.

A similar effect is observed for very light dark matter particles, corresponding to very small recoil energies. The maximum recoil energy of a dark matter particle with a mass of $0.3\,\mathrm{GeV}/c^2$ scattering off oxygen is 75 eV, thus an upward baseline fluctuation (expected baseline resolution: 20 eV) of roughly 1 σ is needed to trigger such an event (see discussion in subsection 8.2.2). However, the expected dark matter recoil spectrum then is very steep and quickly drops to practically zero expectation for energies slightly above threshold, as can be seen in figure A.5 depicting the expected recoil spectrum for a dark matter particle with a mass of $0.3\,\mathrm{GeV}/c^2$ and an exposure of 100 kgd (corresponding to the blue band).

For all simulated data sets where (by chance) no events are observed in the energy range of the steep rise (of high expectation) very similar exclusion limits will be obtained. This effect becomes clear, considering tat the size of the optimum interval is given by the integral over the expected recoil spectrum. Thus, if no event is observed in the steep rise the optimum interval will always be found from threshold energy to the first event and also the size of the interval and, thus, the resulting exclusion limit will be very similar. If, on the other side an event is present in the steep rise, the resulting exclusion limit will be significantly weaker.

Following the argument above, the fluctuation of the exclusion limit in case of very few background events in the relevant energy regime does not follow a Gaussian distribution

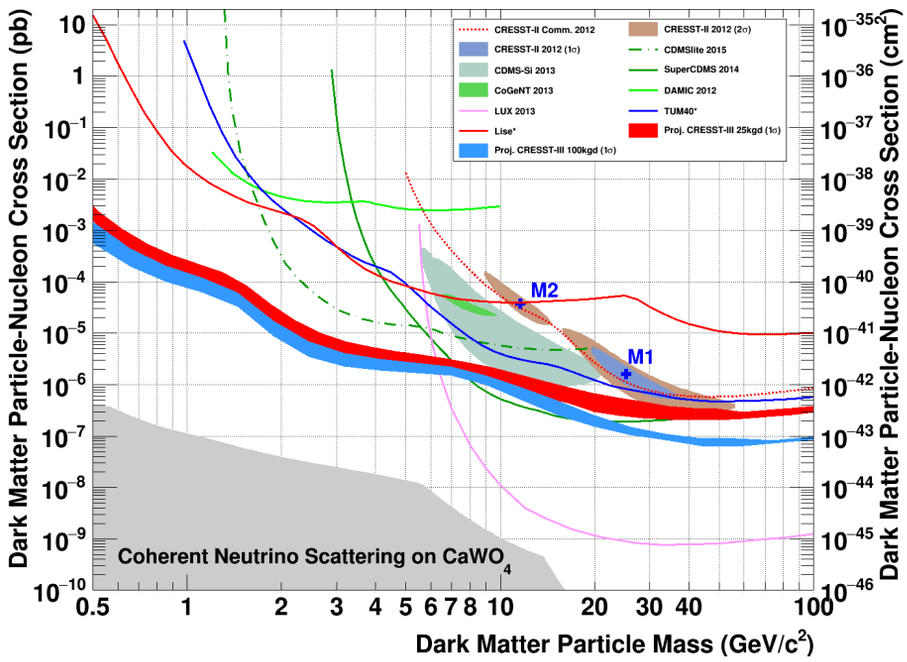

Figure A.4.: Projections for CRESST-III phase 1 for an exposure of 25 kgd (red band) and 100 kgd (blue band) (1σ C.L.). Additionally drawn are results from this work (*), previous CRESST-II results and results from other direct dark matter searches (see legend and caption of figure 2.7). The assumptions made for the projections are given in the text.

any more, but qualitatively approaches a Poisson distribution. This can also be seen by comparing the 25 kgd band (red) to the 100 kgd band (blue), with the red band becoming considerably slimmer than the blue band. Thus, for very low dark matter particles masses interpreting the width of the band as a confidence level is strictly not valid any more. However, it still represents the most probable outcome of the experiment.

The projections convincingly show the potential of CRESST detectors being optimized for low thresholds and, hence, towards sensitivity for light dark matter particles. Achieving a threshold of 100 eV will allow to probe dark matter particle masses as low as 0.3 GeV/c^2. Up to a few GeV/c^2, improvements of two orders of magnitude compared to CRESST-II are within reach for CRESST-III phase 1. For higher masses exposure starts to be more and more relevant. However, comparing the blue band and the limit for TUM40 (blue line), both corresponding to an exposure of 100 kgd before cuts, shows the benefit of the increased discrimination power and, thus, lower background leakage from the e^-/γ-band into the acceptance region. It should be pointed out that these projections solely include e^-/γ-backgrounds. However, as the CRESST-III modules feature a fully-active detector design (see subsection 4.3.2 and [139]) no α-induced background is expected, leaving only neutrons as a potential additional background source. Combining the data of TUM40 and Lise analyzed in this work for the full data sets which corresponds to a total exposure of 289 kgd and, thus is almost a factor of three higher than the exposure goal for CRESST-III phase 1, only one clear neutron candidate event in TUM40 could be identified. However,

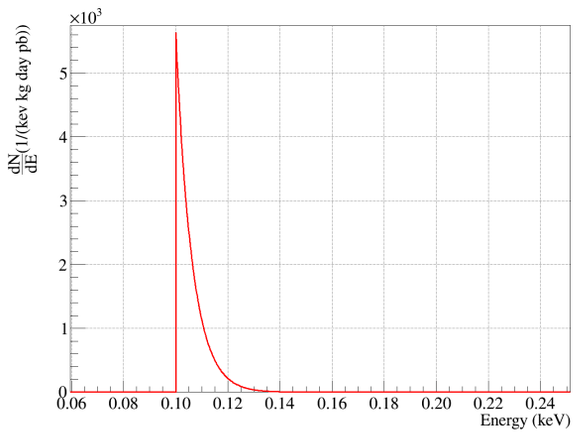

Figure A.5.: Recoil spectrum for a dark matter particle with a mass of 0.3 GeV/c^2, as expected in the acceptance region of CRESST-III phase 1 detectors. The integral over dN/dE yields the total number of 33 expected events for the assumed exposure of 100 kgd.

neutrons appearing at low energies might easily hide in the leakage from the e^-/γ-events, in particular for Lise. With enhanced discrimination power of CRESST-III detectors this might not necessarily be the case any more leading to an enhanced influence of a potential low-energy neutron background. On the other hand, in CRESST-III the detectors will be packed much closer enhancing the probability to tag neutrons via multiple detectors triggering in coincidence.

Bibliography

[1] Ernst Öpik. "Selective absorption of light in space, and the dynamics of the Universe". In: *Bull. de la Soc. Astr. de Russie* 21 (1915), pp. 150–158.

[2] J. C. Kapteyn. "First Attempt at a Theory of the Arrangement and Motion of the Sidereal System". en. In: *The Astrophysical Journal* 55 (May 1922), p. 302. ISSN: 0004-637X, 1538-4357. DOI: 10.1086/142670.

[3] J. H. Jeans. "The motions of stars in a Kapteyn universe". In: *Monthly Notices of the Royal Astronomical Society* 82 (Jan. 1922), pp. 122–132. ISSN: 0035-8711. DOI: 10.1093/mnras/82.3.122.

[4] J. H. Oort. "Observational evidence confirming Lindblad's hypothesis of a rotation of the galactic system". en. In: *Bulletin of the Astronomical Institutes of the Netherlands* 3 (Apr. 1927), p. 275. ISSN: 0365-8910.

[5] J. H. Oort. "The force exerted by the stellar system in the direction perpendicular to the galactic plane and some related problems". In: *Bulletin of the Astronomical Institutes of the Netherlands* 6 (Aug. 1932), p. 249. ISSN: 0365-8910.

[6] Jaan Einasto. "Dark Matter". en. In: *Brazilian Journal of Physics* 43.5-6 (June 2013), pp. 369–374. ISSN: 0103-9733, 1678-4448. DOI: 10.1007/s13538-013-0147-9.

[7] F. Zwicky. "Die Rotverschiebung von extragalaktischen Nebeln". en. In: *Helvetica Physica Acta* 6 (1933), pp. 110–127. ISSN: 0018-0238.

[8] Vera C. Rubin and W. Kent Ford Jr. "Rotation of the Andromeda Nebula from a Spectroscopic Survey of Emission Regions". en. In: *The Astrophysical Journal* 159 (Feb. 1970), p. 379. ISSN: 0004-637X, 1538-4357. DOI: 10.1086/150317.

[9] Planck Collaboration et al. "Planck 2013 results. XVI. Cosmological parameters". In: *Astronomy & Astrophysics* 571 (Nov. 2014). Ed. by Jan Tauber, A16. ISSN: 0004-6361, 1432-0746. DOI: 10.1051/0004-6361/201321591.

[10] Edwin Hubble. "A relation between distance and radial velocity among extra-galactic nebulae". en. In: *Proceedings of the National Academy of Sciences* 15.3 (Mar. 1929), pp. 168–173. ISSN: 0027-8424, 1091-6490. DOI: 10.1073/pnas.15.3.168.

[11] G. Lemaître. "Un Univers homogène de masse constante et de rayon croissant rendant compte de la vitesse radiale des nébuleuses extra-galactiques". In: *Annales de la Société Scientifique de Bruxelles* 47 (1927), pp. 49–59.

[12] Raphael Bousso. "The Cosmological Constant Problem, Dark Energy, and the Landscape of String Theory". In: *arXiv: 1203.0307* (Mar. 2012).

[13] S. Perlmutter et al. "Discovery of a supernova explosion at half the age of the universe". In: *Nature* 391 (Jan. 1998), p. 51. ISSN: 0028-0836. DOI: 10.1038/34124.

[14] Adam G. Riess et al. "Observational Evidence from Supernovae for an Accelerating Universe and a Cosmological Constant". en. In: *The Astronomical Journal* 116.3 (1998), p. 1009. ISSN: 1538-3881. DOI: 10.1086/300499.

[15] D. J. Fixsen. "The Temperature of the Cosmic Microwave Background". en. In: *The Astrophysical Journal* 707.2 (2009), p. 916. ISSN: 0004-637X. DOI: 10.1088/0004-637X/707/2/916.

[16] A. A. Penzias and R. W. Wilson. "A Measurement of Excess Antenna Temperature at 4080 Mc/s." en. In: *The Astrophysical Journal* 142 (July 1965), p. 419. ISSN: 0004-637X, 1538-4357. DOI: 10.1086/148307.

[17] R. H. Dicke et al. "Cosmic Black-Body Radiation." en. In: *The Astrophysical Journal* 142 (July 1965), p. 414. ISSN: 0004-637X, 1538-4357. DOI: 10.1086/148306.

[18] R. K. Sachs and A. M. Wolfe. "Perturbations of a Cosmological Model and Angular Variations of the Microwave Background". en. In: *The Astrophysical Journal* 147 (Jan. 1967), p. 73. ISSN: 0004-637X, 1538-4357. DOI: 10.1086/148982.

[19] K. A. Olive and Particle Data Group. "Review of Particle Physics". en. In: *Chinese Physics C* 38.9 (2014), p. 090001. ISSN: 1674-1137. DOI: 10.1088/1674-1137/38/9/090001.

[20] Douglas Clowe et al. "A Direct Empirical Proof of the Existence of Dark Matter". en. In: *The Astrophysical Journal Letters* 648.2 (2006), p. L109. ISSN: 1538-4357. DOI: 10.1086/508162.

[21] *Chandra - Photo Album - 1E 0657-56 - 21 Aug 06*. URL: http://chandra.harvard.edu/photo/2006/1e0657/index.html (visited on 01/28/2016).

[22] M. Milgrom. "A modification of the Newtonian dynamics - Implications for galaxies". en. In: *The Astrophysical Journal* 270 (July 1983), p. 371. ISSN: 0004-637X, 1538-4357. DOI: 10.1086/161131.

[23] *Galaxy rotation curve*. en. Page Version ID: 701684941. Jan. 2016. URL: https://en.wikipedia.org/w/index.php?title=Galaxy_rotation_curve&oldid=701684941 (visited on 01/28/2016).

[24] Edvige Corbelli and Paolo Salucci. "The extended rotation curve and the dark matter halo of M33". en. In: *Monthly Notices of the Royal Astronomical Society* 311.2 (Jan. 2000), pp. 441–447. ISSN: 0035-8711, 1365-2966. DOI: 10.1046/j.1365-8711.2000.03075.x.

[25] Fabio Iocco, Miguel Pato, and Gianfranco Bertone. "Evidence for dark matter in the inner Milky Way". en. In: *Nature Physics* 11.3 (Mar. 2015), pp. 245–248. ISSN: 1745-2473. DOI: 10.1038/nphys3237.

[26] P. Tisserand et al. "Limits on the Macho content of the Galactic Halo from the EROS-2 Survey of the Magellanic Clouds". In: *Astronomy & Astrophysics* 469.2 (2007), p. 23. DOI: 10.1051/0004-6361:20066017.

[27] C. A. Baker et al. "Improved Experimental Limit on the Electric Dipole Moment of the Neutron". In: *Physical Review Letters* 97.13 (Sept. 2006), p. 131801. DOI: 10.1103/PhysRevLett.97.131801.

[28] R. D. Peccei and Helen R. Quinn. "CP Conservation in the Presence of Pseudoparticles". In: *Physical Review Letters* 38.25 (June 1977), pp. 1440–1443. DOI: 10.1103/PhysRevLett.38.1440.

[29] Yoichiro Nambu. "Quasi-Particles and Gauge Invariance in the Theory of Superconductivity". In: *Physical Review* 117.3 (Feb. 1960), pp. 648–663. DOI: 10.1103/PhysRev.117.648.

[30] Jihn E. Kim and Gianpaolo Carosi. "Axions and the strong CP problem". In: *Reviews of Modern Physics* 82.1 (Mar. 2010), pp. 557–601. DOI: 10.1103/RevModPhys.82.557.

[31] E. Arik et al. "Probing eV-scale axions with CAST". en. In: *Journal of Cosmology and Astroparticle Physics* 2009.02 (2009), p. 008. ISSN: 1475-7516. DOI: 10.1088/1475-7516/2009/02/008.

[32] S. J. Asztalos et al. "SQUID-Based Microwave Cavity Search for Dark-Matter Axions". In: *Physical Review Letters* 104.4 (Jan. 2010), p. 041301. DOI: 10.1103/PhysRevLett.104.041301.

[33] Mark W. Goodman and Edward Witten. "Detectability of certain dark-matter candidates". In: *Physical Review D* 31.12 (June 1985), pp. 3059–3063. DOI: 10.1103/PhysRevD.31.3059.

[34] G. Jungman, M. Kamionkowski, and K. Griest. "Supersymmetric Dark Matter". In: *Physics Reports* 267.5-6 (Mar. 1996), pp. 195–373. ISSN: 03701573. DOI: 10.1016/0370-1573(95)00058-5.

[35] Hsin-Chia Cheng, Jonathan L. Feng, and Konstantin T. Matchev. "Kaluza-Klein Dark Matter". In: *Physical Review Letters* 89.21 (Oct. 2002), p. 211301. DOI: 10.1103/PhysRevLett.89.211301.

[36] Kalliopi Petraki and Raymond R. Volkas. "Review of asymmetric dark matter". In: *International Journal of Modern Physics A* 28.19 (July 2013), p. 1330028. ISSN: 0217-751X. DOI: 10.1142/S0217751X13300287.

[37] Kathryn M. Zurek. "Asymmetric Dark Matter: Theories, signatures, and constraints". In: *Physics Reports*. Asymmetric Dark Matter: Theories, signatures, and constraints 537.3 (Apr. 2014), pp. 91–121. ISSN: 0370-1573. DOI: 10.1016/j.physrep.2013.12.001.

[38] Laurent Canetti, Marco Drewes, and Mikhail Shaposhnikov. "Matter and antimatter in the universe". en. In: *New Journal of Physics* 14.9 (2012), p. 095012. ISSN: 1367-2630. DOI: 10.1088/1367-2630/14/9/095012.

[39] Jessica Goodman et al. "Constraints on dark matter from colliders". In: *Physical Review D* 82.11 (Dec. 2010), p. 116010. DOI: 10.1103/PhysRevD.82.116010.

[40] G. Aad et al. "Search for new phenomena in final states with an energetic jet and large missing transverse momentum in pp collisions at $\sqrt{s} = 8TeV$ with the ATLAS detector". en. In: *The European Physical Journal C* 75.7 (July 2015), pp. 1–43. ISSN: 1434-6044, 1434-6052. DOI: 10.1140/epjc/s10052-015-3517-3.

[41] Daniel Abercrombie et al. "Dark Matter Benchmark Models for Early LHC Run-2 Searches: Report of the ATLAS/CMS Dark Matter Forum". In: *arXiv:1507.00966* (July 2015). FERMILAB-PUB-15-282-CD.

[42] V. Khachatryan et al. "Search for dark matter, extra dimensions, and unparticles in monojet events in proton–proton collisions at $\sqrt{s} = 8TeV$". en. In: *The European Physical Journal C* 75.5 (May 2015), pp. 1–25. ISSN: 1434-6044, 1434-6052. DOI: 10.1140/epjc/s10052-015-3451-4.

[43] CMS Collaboration. "Search for dark matter with jets and missing transverse energy at 13 TeV". In: *CMS-PAS-EXO-15-003* (2015).

[44] Torsten Bringmann et al. "Fermi LAT Search for Internal Bremsstrahlung Signatures from Dark Matter Annihilation". In: *Journal of Cosmology and Astroparticle Physics* 2012.07 (July 2012), pp. 054–054. ISSN: 1475-7516. DOI: 10.1088/1475-7516/2012/07/054.

[45] IceCube Collaboration et al. "Search for Dark Matter Annihilations in the Sun with the 79-String IceCube Detector". In: *Physical Review Letters* 110.13 (Mar. 2013), p. 131302. DOI: 10.1103/PhysRevLett.110.131302.

[46] IceCube Collaboration et al. "Improved limits on dark matter annihilation in the Sun with the 79-string IceCube detector and implications for supersymmetry". In: *submitted to JCAP* (Jan. 2016). arXiv:1601.00653.

[47] Super-Kamiokande Collaboration et al. "Search for Neutrinos from Annihilation of Captured Low-Mass Dark Matter Particles in the Sun by Super-Kamiokande". In: *Physical Review Letters* 114.14 (Apr. 2015), p. 141301. DOI: 10.1103/PhysRevLett.114.141301.

[48] F. Donato, N. Fornengo, and S. Scopel. "Effects of galactic dark halo rotation on WIMP direct detection". en. In: *Astroparticle Physics* 9.3 (Oct. 1998), pp. 247–260. ISSN: 09276505. DOI: 10.1016/S0927-6505(98)00025-5.

[49] Gianfranco Bertone, Dan Hooper, and Joseph Silk. "Particle Dark Matter: Evidence, Candidates and Constraints". In: *Physics Reports* 405.5-6 (Jan. 2005), pp. 279–390. ISSN: 03701573. DOI: 10.1016/j.physrep.2004.08.031.

[50] Julio F. Navarro, Carlos S. Frenk, and Simon D. M. White. "The Structure of Cold Dark Matter Halos". en. In: *The Astrophysical Journal* 462 (May 1996), p. 563. ISSN: 0004-637X, 1538-4357. DOI: 10.1086/177173.

[51] Andrzej K. Drukier, Katherine Freese, and David N. Spergel. "Detecting cold dark-matter candidates". In: *Physical Review D* 33.12 (June 1986), pp. 3495–3508. DOI: 10.1103/PhysRevD.33.3495.

[52] Philipp Grothaus, Malcolm Fairbairn, and Jocelyn Monroe. "Directional Dark Matter Detection Beyond the Neutrino Bound". In: *Physical Review D* 90.5 (Sept. 2014). ISSN: 1550-7998, 1550-2368. DOI: 10.1103/PhysRevD.90.055018.

[53] A. Gütlein et al. "Impact of Coherent Neutrino Nucleus Scattering on Direct Dark Matter Searches based on $CaWO_4$ Crystals". In: *Astroparticle Physics* 69 (Sept. 2015), pp. 44–49. ISSN: 09276505. DOI: 10.1016/j.astropartphys.2015.03.010.

[54] F. Ruppin et al. "Complementarity of dark matter detectors in light of the neutrino background". In: *Physical Review D* 90.8 (Oct. 2014), p. 083510. DOI: 10.1103/PhysRevD.90.083510.

[55] Martin C. Smith et al. "The RAVE survey: constraining the local Galactic escape speed". en. In: *Monthly Notices of the Royal Astronomical Society* 379.2 (Aug. 2007), pp. 755–772. ISSN: 0035-8711, 1365-2966. DOI: 10.1111/j.1365-2966.2007.11964.x.

[56] J. D. Lewin and P. F. Smith. "Review of mathematics, numerical factors, and corrections for dark matter experiments based on elastic nuclear recoil". In: *Astroparticle Physics* 6.1 (Dec. 1996), pp. 87–112. ISSN: 0927-6505. DOI: 10.1016/S0927-6505(96)00047-3.

[57] Marc Kamionkowski and Savvas M. Koushiappas. "Galactic substructure and direct detection of dark matter". In: *Physical Review D* 77.10 (May 2008), p. 103509. DOI: 10.1103/PhysRevD.77.103509.

[58] Marc Kamionkowski, Savvas M. Koushiappas, and Michael Kuhlen. "Galactic substructure and dark-matter annihilation in the Milky Way halo". In: *Physical Review D* 81.4 (Feb. 2010), p. 043532. DOI: 10.1103/PhysRevD.81.043532.

[59] K. Choi, C. Rott, and Y. Itow. "Impact of the dark matter velocity distribution on capture rates in the Sun". en. In: *Journal of Cosmology and Astroparticle Physics* 2014.05 (May 2014), p. 049. ISSN: 1475-7516. DOI: 10.1088/1475-7516/2014/05/049.

[60] Susmita Kundu and Pijushpani Bhattacharjee. "Neutrinos from WIMP annihilation in the Sun : Implications of a self-consistent model of the Milky Way's dark matter halo". In: *Physical Review D* 85.12 (June 2012). ISSN: 1550-7998, 1550-2368. DOI: 10.1103/PhysRevD.85.123533.

[61] Mark Vogelsberger et al. "Phase-space structure in the local dark matter distribution and its signature in direct detection experiments". en. In: *Monthly Notices of the Royal Astronomical Society* 395.2 (May 2009), pp. 797–811. ISSN: 0035-8711, 1365-2966. DOI: 10.1111/j.1365-2966.2009.14630.x.

[62] Miguel Pato and Fabio Iocco. "The dark matter profile of the Milky Way: a non-parametric reconstruction". In: *The Astrophysical Journal* 803.1 (Apr. 2015), p. L3. ISSN: 2041-8213. DOI: 10.1088/2041-8205/803/1/L3.

[63] Chung-Lin Shan. "Reconstructing the WIMP velocity distribution from direct dark matter detection data with a nonnegligible threshold energy". In: *International Journal of Modern Physics D* 24.11 (July 2015), p. 1550090. ISSN: 0218-2718. DOI: 10.1142/S021827181550090X.

[64] Manuel Drees and Chung-Lin Shan. "Reconstructing the Velocity Distribution of WIMPs from Direct Dark Matter Detection Data". In: *Journal of Cosmology and Astroparticle Physics* 2007.06 (June 2007), pp. 011–011. ISSN: 1475-7516. DOI: 10.1088/1475-7516/2007/06/011.

[65] Richard H. Helm. "Inelastic and Elastic Scattering of 187-Mev Electrons from Selected Even-Even Nuclei". In: *Physical Review* 104.5 (Dec. 1956), pp. 1466–1475. DOI: 10.1103/PhysRev.104.1466.

[66] Jonathan Engel. "Nuclear form factors for the scattering of weakly interacting massive particles". In: *Physics Letters B* 264.1 (July 1991), pp. 114–119. ISSN: 0370-2693. DOI: 10.1016/0370-2693(91)90712-Y.

[67] Jonathan Engel. "Nuclear form factors for the scattering of neutralinos". In: *Nuclear Physics B - Proceedings Supplements* 28.1 (July 1992), pp. 310–313. ISSN: 0920-5632. DOI: 10.1016/0920-5632(92)90190-4.

[68] L. Vietze et al. "Nuclear structure aspects of spin-independent WIMP scattering off xenon". In: *Physical Review D* 91.4 (Feb. 2015), p. 043520. DOI: 10.1103/PhysRevD.91.043520.

[69] A. Liam Fitzpatrick et al. "The effective field theory of dark matter direct detection". en. In: *Journal of Cosmology and Astroparticle Physics* 2013.02 (2013), p. 004. ISSN: 1475-7516. DOI: 10.1088/1475-7516/2013/02/004.

[70] Gintaras Dūda, Ann Kemper, and Paolo Gondolo. "Model-independent form factors for spin-independent neutralino–nucleon scattering from elastic electron scattering data". en. In: *Journal of Cosmology and Astroparticle Physics* 2007.04 (2007), p. 012. ISSN: 1475-7516. DOI: 10.1088/1475-7516/2007/04/012.

[71] Jens Schmaler. *The CRESST Dark Matter Search - New Analysis Methods and Recent Results*. Englisch. München: Dr. Hut, 2010. ISBN: 978-3-86853-750-5.

[72] G. Angloher et al. "Results from 730 kg days of the CRESST-II Dark Matter search". en. In: *The European Physical Journal C* 72.4 (Apr. 2012), pp. 1–22. ISSN: 1434-6044, 1434-6052. DOI: 10.1140/epjc/s10052-012-1971-8.

[73] G Angloher et al. "Limits on WIMP dark matter using sapphire cryogenic detectors". In: *Astroparticle Physics* 18.1 (Aug. 2002), pp. 43–55. ISSN: 0927-6505. DOI: 10.1016/S0927-6505(02)00111-1.

[74] G. Angloher et al. "Results on light dark matter particles with a low-threshold CRESST-II detector". en. In: *The European Physical Journal C* 76.1 (Jan. 2016), pp. 1–8. ISSN: 1434-6044, 1434-6052. DOI: 10.1140/epjc/s10052-016-3877-3.

[75] G. Angloher et al. "Results on low mass WIMPs using an upgraded CRESST-II detector". en. In: *The European Physical Journal C* 74.12 (Dec. 2014), pp. 1–6. ISSN: 1434-6044, 1434-6052. DOI: 10.1140/epjc/s10052-014-3184-9.

[76] Andrew Brown et al. "Extending the CRESST-II commissioning run limits to lower masses". In: *Physical Review D* 85.2 (Jan. 2012), p. 021301. DOI: 10.1103/PhysRevD.85.021301.

[77] CDEX Collaboration et al. "Limits on light weakly interacting massive particles from the CDEX-1 experiment with a p-type point-contact germanium detector at the China Jinping Underground Laboratory". In: *Physical Review D* 90.9 (Nov. 2014), p. 091701. DOI: 10.1103/PhysRevD.90.091701.

[78] SuperCDMS Collaboration et al. "New Results from the Search for Low-Mass Weakly Interacting Massive Particles with the CDMS Low Ionization Threshold Experiment". In: *Physical Review Letters* 116.7 (Feb. 2016), p. 071301. DOI: 10.1103/PhysRevLett.116.071301.

[79] SuperCDMS Collaboration et al. "Search for Low-Mass Weakly Interacting Massive Particles with SuperCDMS". In: *Physical Review Letters* 112.24 (June 2014), p. 241302. DOI: 10.1103/PhysRevLett.112.241302.

[80] EDELWEISS Collaboration et al. "Search for low-mass WIMPs with EDELWEISS-II heat-and-ionization detectors". In: *Physical Review D* 86.5 (Sept. 2012), p. 051701. DOI: 10.1103/PhysRevD.86.051701.

[81] J. Barreto et al. "Direct search for low mass dark matter particles with CCDs". In: *Physics Letters B* 711.3–4 (May 2012), pp. 264–269. ISSN: 0370-2693. DOI: 10.1016/j.physletb.2012.04.006.

[82] P. Agnes et al. "First results from the DarkSide-50 dark matter experiment at Laboratori Nazionali del Gran Sasso". In: *Physics Letters B* 743 (Apr. 2015), pp. 456–466. ISSN: 0370-2693. DOI: 10.1016/j.physletb.2015.03.012.

[83] LUX Collaboration et al. "First Results from the LUX Dark Matter Experiment at the Sanford Underground Research Facility". In: *Physical Review Letters* 112.9 (Mar. 2014), p. 091303. DOI: 10.1103/PhysRevLett.112.091303.

[84] PandaX Collaboration et al. "Low-mass dark matter search results from full exposure of the PandaX-I experiment". In: *Physical Review D* 92.5 (Sept. 2015), p. 052004. DOI: 10.1103/PhysRevD.92.052004.

[85] E. Aprile et al. "Dark Matter Results from 225 Live Days of XENON100 Data". In: *Physical Review Letters* 109.18 (Nov. 2012), p. 181301. DOI: 10.1103/PhysRevLett.109.181301.

[86] R. Agnese et al. "Silicon Detector Dark Matter Results from the Final Exposure of CDMS II". In: *Physical Review Letters* 111.25 (Dec. 2013), p. 251301. DOI: 10.1103/PhysRevLett.111.251301.

[87] C. E. Aalseth et al. "CoGeNT: A Search for Low-Mass Dark Matter using p-type Point Contact Germanium Detectors". In: *Physical Review D* 88.1 (July 2013). ISSN: 1550-7998, 1550-2368. DOI: 10.1103/PhysRevD.88.012002.

[88] David Malling and Carlos Faham. *Large Underground Xenon experiment*. en. URL: https://en.wikipedia.org/wiki/File:LUXEvent.pdf (visited on 02/13/2016).

[89] The XENON collaboration et al. "Physics reach of the XENON1T dark matter experiment". In: *submitted to JCAP* (Dec. 2015). arXiv: 1512.07501.

[90] The LZ Collaboration et al. "LUX-ZEPLIN (LZ) Conceptual Design Report". In: *arXiv: 1509.02910* (Sept. 2015).

[91] P.-A. Amaudruz et al. "DEAP-3600 Dark Matter Search". In: *arXiv:1410.7673*. ICHEP 2014. Oct. 2014.

[92] J. Benziger et al. "A Scintillator Purification System for the Borexino Solar Neutrino Detector". In: *Nuclear Instruments and Methods in Physics Research Section A: Accelerators, Spectrometers, Detectors and Associated Equipment* 587.2-3 (Mar. 2008), pp. 277–291. ISSN: 01689002. DOI: 10.1016/j.nima.2007.12.043.

[93] K. Abe et al. "XMASS detector". In: *Nuclear Instruments and Methods in Physics Research Section A: Accelerators, Spectrometers, Detectors and Associated Equipment* 716 (July 2013), pp. 78–85. ISSN: 01689002. DOI: 10.1016/j.nima.2013.03.059.

[94] Andrew Hime. "The MiniCLEAN Dark Matter Experiment". In: *arXiv:1110.1005*. DPF-2011. Oct. 2011.

[95] Ke-Jun Kang et al. "Introduction of the CDEX experiment". In: *Frontiers of Physics* 8.4 (Aug. 2013). arXiv: 1303.0601, pp. 412–437. ISSN: 2095-0462, 2095-0470. DOI: 10.1007/s11467-013-0349-1.

[96] TEXONO Collaboration. "Limits on spin-independent couplings of WIMP dark matter with a p-type point-contact germanium detector". In: *Physical Review Letters* 110.26 (June 2013). ISSN: 0031-9007, 1079-7114. DOI: 10.1103/PhysRevLett.110.261301.

[97] A. Juillard. "Status of the EDELWEISS-II Experiment". en. In: *Journal of Low Temperature Physics* 151.3-4 (Jan. 2008), pp. 806–811. ISSN: 0022-2291, 1573-7357. DOI: 10.1007/s10909-008-9742-5.

[98] P. S. Barbeau, J. I. Collar, and O. Tench. "Large-mass ultralow noise germanium detectors: performance and applications in neutrino and astroparticle physics". en. In: *Journal of Cosmology and Astroparticle Physics* 2007.09 (Sept. 2007), p. 009. ISSN: 1475-7516. DOI: 10.1088/1475-7516/2007/09/009.

[99] R. Agnese et al. "Demonstration of surface electron rejection with interleaved germanium detectors for dark matter searches". In: *Applied Physics Letters* 103.16 (Oct. 2013), p. 164105. ISSN: 0003-6951, 1077-3118. DOI: 10.1063/1.4826093.

[100] R. Agnese et al. "CDMSlite: A Search for Low-Mass WIMPs using Voltage-Assisted Calorimetric Ionization Detection in the SuperCDMS Experiment". In: *Physical Review Letters* 112.4 (Jan. 2014). ISSN: 0031-9007, 1079-7114. DOI: 10.1103/PhysRevLett.112.041302.

[101] R. Bernabei et al. "Final model independent result of DAMA/LIBRA–phase1". en. In: *The European Physical Journal C* 73.12 (Nov. 2013), pp. 1–11. ISSN: 1434-6044, 1434-6052. DOI: 10.1140/epjc/s10052-013-2648-7.

[102] Christopher Savage et al. "Compatibility of DAMA/LIBRA dark matter detection with other searches". In: *Journal of Cosmology and Astroparticle Physics* 2009.04 (Apr. 2009), p. 010. ISSN: 1475-7516. DOI: 10.1088/1475-7516/2009/04/010.

[103] R. Bernabei et al. "DAMA/LIBRA results and perspectives". In: *arXiv:1301.6243*. 15th Bled Workshop "What Comes Beyond Standard Models". Jan. 2013.

[104] J. Cherwinka et al. "A Search for the Dark Matter Annual Modulation in South Pole Ice". In: *Astroparticle Physics* 35.11 (June 2012), pp. 749–754. ISSN: 09276505. DOI: 10.1016/j.astropartphys.2012.03.003.

[105] DM-Ice Collaboration et al. "First data from DM-Ice17". In: *Physical Review D* 90.9 (Nov. 2014). ISSN: 1550-7998, 1550-2368. DOI: 10.1103/PhysRevD.90.092005.

[106] G. Angloher et al. "A CsI low temperature detector for dark matter search". In: *in preparation* (2016).

[107] PICO Collaboration et al. "Dark Matter Search Results from the PICO-2L C_3F_8 Bubble Chamber". In: *Physical Review Letters* 114.23 (June 2015), p. 231302. DOI: 10.1103/PhysRevLett.114.231302.

[108] F. Aubin et al. "Discrimination of nuclear recoils from alpha particles with superheated liquids". In: *New Journal of Physics* 10.10 (Oct. 2008), p. 103017. ISSN: 1367-2630. DOI: 10.1088/1367-2630/10/10/103017.

[109] Alvaro Chavarria et al. "DAMIC at SNOLAB". In: *arXiv:1407.0347*. TAUP2013. June 2014.

[110] The DAMIC Collaboration et al. "DAMIC: a novel dark matter experiment". In: *arXiv: 1310.6688*. ICRC2013. Oct. 2013.

[111] G. Angloher et al. "Commissioning Run of the CRESST-II Dark Matter Search". In: *Astroparticle Physics* 31.4 (May 2009), pp. 270–276. ISSN: 09276505. DOI: 10.1016/j.astropartphys.2009.02.007.

[112] CRESST Collaboration et al. "Probing low WIMP masses with the next generation of CRESST detector". In: *arXiv: 1503.08065* (Mar. 2015).

[113] G. Bellini et al. "Cosmic-muon flux and annual modulation in Borexino at 3800 m water-equivalent depth". en. In: *Journal of Cosmology and Astroparticle Physics* 2012.05 (2012), p. 015. ISSN: 1475-7516. DOI: 10.1088/1475-7516/2012/05/015.

[114] Michael Kiefer. "Improving the Light Channel of the CRESST-II-Dark Matter Detectors". PhD Thesis. München: Technische Universität München, 2012.

[115] *Dilution refrigerator*. en. Page Version ID: 648993131. Feb. 2015. URL: http://en.wikipedia.org/w/index.php?title=Dilution_refrigerator&oldid=648993131 (visited on 05/28/2015).

[116] Frank Pobell. *Matter and Methods at Low Temperatures*. Englisch. 3rd, rev. and exp. ed. 2007. Berlin: Springer, 2007. ISBN: 978-3-540-46356-6.

[117] Stefano Cecchini and Maurizio Spurio. "Atmospheric muons: experimental aspects". In: *arXiv:1208.1171*. MNR 2012. Aug. 2012.

[118] M. Kimmerle. "Data Analysis in the Direct Dark Matter Search Experiment CRESST and Calculation of the corresponding Limit on the Cross Section of Dark Matter". PhD Thesis. Tübingen: Eberhard Karls Universität Tübingen, 2010. URL: https://publikationen.uni-tuebingen.de/xmlui/handle/10900/49525.

[119] Dariusz Malczewski, Jan Kisiel, and Jerzy Dorda. "Gamma background measurements in the Gran Sasso National Laboratory". In: *Journal of Radioanalytical and Nuclear Chemistry* 295.1 (2013), pp. 749–754. ISSN: 0236-5731. DOI: 10.1007/s10967-012-1990-9.

[120] Stephan Scholl. *private communication*. May 2013.

[121] V. B. Mikhailik and H. Kraus. "Cryogenic scintillators in searches for extremely rare events". en. In: *Journal of Physics D: Applied Physics* 39.6 (2006), p. 1181. ISSN: 0022-3727. DOI: 10.1088/0022-3727/39/6/026.

[122] F. Pröbst et al. "Model for cryogenic particle detectors with superconducting phase transition thermometers". en. In: *Journal of Low Temperature Physics* 100.1-2 (July 1995), pp. 69–104. ISSN: 0022-2291, 1573-7357. DOI: 10.1007/BF00753837.

[123] A. Senyshyn et al. "Lattice dynamics and thermal properties of $CaWO_4$". In: *Physical Review B* 70.21 (Dec. 2004), p. 214306. DOI: 10.1103/PhysRevB.70.214306.

[124] M. Kiefer et al. "Composite $CaWO_4$ Detectors for the CRESST-II Experiment". In: *AIP Conference Proceedings*. Vol. 1185. AIP Publishing, Dec. 2009, pp. 651–654. DOI: 10.1063/1.3292426.

[125] Florian Reindl. "Analysis of CRESST Dark Matter Search Data". Diploma Thesis. Munich: Technische Universität München, 2011. URL: https://www.mpp.mpg.de/english/graduate/publicationsGraduate/pubsearch/simple/index.php?action=search&language=&mpi=MPP-2011-175.

[126] CRESST Collaboration et al. "In-Situ Performance Characterization of CRESST Detector Modules". In: *submitted for publication* (Mar. 2015). arXiv: 1503.07806.

[127] A. Münster et al. "Radiopurity of CaWO4 crystals for direct dark matter search with CRESST and EURECA". en. In: *Journal of Cosmology and Astroparticle Physics* 2014.05 (May 2014). arXiv: 1403.5114, p. 018. ISSN: 1475-7516. DOI: 10.1088/1475-7516/2014/05/018.

[128] R. Strauss et al. "Beta/gamma and alpha backgrounds in CRESST-II Phase 2". In: *Journal of Cosmology and Astroparticle Physics* 2015.06 (June 2015), p. 030. ISSN: 1475-7516. DOI: 10.1088/1475-7516/2015/06/030.

[129] F. G. Kondev. "Nuclear Data Sheets for A = 206". In: *Nuclear Data Sheets* 109.6 (June 2008), pp. 1527–1654. ISSN: 0090-3752. DOI: 10.1016/j.nds.2008.05.002.

[130] James F. Ziegler, M. D. Ziegler, and J. P. Biersack. "SRIM – The stopping and range of ions in matter (2010)". In: *Nuclear Instruments and Methods in Physics Research Section B: Beam Interactions with Materials and Atoms*. 19th International Conference on Ion Beam Analysis 268.11–12 (June 2010), pp. 1818–1823. ISSN: 0168-583X. DOI: 10.1016/j.nimb.2010.02.091.

[131] M. Kuźniak, M. G. Boulay, and T. Pollmann. "Surface roughness interpretation of 730 kg days CRESST-II results". In: *Astroparticle Physics* 36.1 (Aug. 2012), pp. 77–82. ISSN: 09276505. DOI: 10.1016/j.astropartphys.2012.05.005.

[132] Stephan Scholl. *Effect of the Surface Roughness on the Low-Energy Background Induced By Nuclear Recoils*. Talk. München, May 2012.

[133] Andreas Erb and Jean-Côme Lanfranchi. "Growth of high-purity scintillating $CaWO_4$ single crystals for the low-temperature direct dark matter search experiments CRESST-II and EURECA". en. In: *CrystEngComm* 15.12 (Feb. 2013), pp. 2301–2304. ISSN: 1466-8033. DOI: 10.1039/C2CE26554K.

[134] Karoline Schäffner. "Study of Backgrounds in the CRESST Dark Matter Search". PhD Thesis. München: Technische Universität München, 2014.

[135] Franz Pröbst and Jens Schmaler. *private communication*. Nov. 2011.

[136] A. Tantot et al. "Sound and light from fractures in scintillators". In: *Physical Review Letters* 111.15 (Oct. 2013). ISSN: 0031-9007, 1079-7114. DOI: 10.1103/PhysRevLett.111.154301.

[137] Anja Tanzke. *Detector Mounting for Run 33*. Sept. 2013.

[138] F. Reindl et al. "Status Update on the CRESST Dark Matter Search". In: *Astroparticle, Particle, Space Physics and Detectors for Physics Applications*. Vol. 8. Astroparticle, Particle, Space Physics, Radiation Interaction, Detectors and Medical Physics Applications. 14th ICATPP Conference (2013). WORLD SCIENTIFIC, Apr. 2014, pp. 290–296. ISBN: 978-981-4603-15-7. URL: http://www.worldscientific.com/doi/abs/10.1142/9789814603164_0045 (visited on 07/11/2015).

[139] R. Strauss et al. "A detector module with highly efficient surface-alpha event rejection operated in CRESST-II Phase 2". In: *The European Physical Journal C* 75.8 (July 2015), pp. 1–8. ISSN: 1434-6044, 1434-6052. DOI: 10.1140/epjc/s10052-015-3572-9.

[140] Rafael Florian Lang. "Search for Dark Matter with the CRESST Experiment". PhD thesis. München: Technische Universität München, 2008.

[141] Franz Pröbst. *private communication*. Sept. 2015.

[142] M. B. Chadwick et al. "ENDF/B-VII.1 Nuclear Data for Science and Technology: Cross Sections, Covariances, Fission Product Yields and Decay Data". In: *Nuclear Data Sheets*. Special Issue on ENDF/B-VII.1 Library 112.12 (Dec. 2011), pp. 2887–2996. ISSN: 0090-3752. DOI: 10.1016/j.nds.2011.11.002.

[143] *ENDF: Evaluated Nuclear Data File*. URL: https://www-nds.iaea.org/exfor/endf.htm (visited on 09/10/2015).

[144] Paul Dierckx. *Curve and Surface Fitting with Splines*. Englisch. Revised. Oxford University Press, 1994. ISBN: 978-0-19-853440-2.

[145] Andreas Zöller. "Artificial Neural Network Based Pulse Shape Analysis for Cryogenic Detectors Operated in CRESSST-II". in preparation. PhD Thesis. Munich: Technische Universität München.

[146] R. F. Lang et al. "Scintillator Non-Proportionality and Gamma Quenching in $CaWO_4$". In: *arXiv:0910.4414* (Oct. 2009).

[147] R. Strauss. "Energy-Dependent Quenching Factor Measurements of $CaWO_4$ Crystals at mK Temperatures and Detector Prototypes for Direct Dark Matter Search with CRESST". PhD thesis. Technische Universität München, 2013. URL: http://mediatum.ub.tum.de/?id=1166886 (visited on 10/26/2015).

[148] R. Strauss et al. "Energy-dependent light quenching in $CaWO_4$ crystals at mK temperatures". en. In: *The European Physical Journal C* 74.7 (July 2014), pp. 1–6. ISSN: 1434-6044, 1434-6052. DOI: 10.1140/epjc/s10052-014-2957-5.

[149] S. Yellin. "Finding an upper limit in the presence of an unknown background". In: *Physical Review D* 66.3 (Aug. 2002), p. 032005. DOI: 10.1103/PhysRevD.66.032005.

[150] S. Yellin. "Extending the optimum interval method". In: *arXiv:0709.2701* (Sept. 2007).

[151] *Optimum Interval Software*. Feb. 2011. URL: http://cdms.stanford.edu/Upperlimit/ (visited on 11/26/2015).

[152] O. Tange. "GNU Parallel - The Command-Line Power Tool". In: *;login: The USENIX Magazine* 36.01 (2011), pp. 42–47.

[153] *Likelihood function*. en. Page Version ID: 694316544. Dec. 2015. URL: https://en.wikipedia.org/w/index.php?title=Likelihood_function&oldid=694316544 (visited on 12/24/2015).

[154] R. Strauss et al. "Exploring Low-Mass Dark Matter with CRESST". en. In: *Journal of Low Temperature Physics* (Jan. 2016). LTD16, pp. 1–7. ISSN: 0022-2291, 1573-7357. DOI: 10.1007/s10909-016-1492-1.

[155] Roger Barlow. "Extended maximum likelihood". In: *Nuclear Instruments and Methods in Physics Research Section A: Accelerators, Spectrometers, Detectors and Associated Equipment* 297.3 (Dec. 1990), pp. 496–506. ISSN: 0168-9002. DOI: 10.1016/0168-9002(90)91334-8.

[156] E. Aprile et al. "Likelihood approach to the first dark matter results from XENON100". In: *Physical Review D* 84.5 (Sept. 2011), p. 052003. DOI: 10.1103/PhysRevD.84.052003.

[157] Glen Cowan et al. "Asymptotic formulae for likelihood-based tests of new physics". In: *The European Physical Journal C* 71.2 (Feb. 2011), pp. 1–19. ISSN: 1434-6044, 1434-6052. DOI: 10.1140/epjc/s10052-011-1554-0.

[158] S. S. Wilks. "The Large-Sample Distribution of the Likelihood Ratio for Testing Composite Hypotheses". EN. In: *The Annals of Mathematical Statistics* 9.1 (Mar. 1938), pp. 60–62. ISSN: 0003-4851, 2168-8990. DOI: 10.1214/aoms/1177732360.

[159] F. James and M. Roos. "Minuit - a system for function minimization and analysis of the parameter errors and correlations". In: *Computer Physics Communications* 10.6 (Dec. 1975), pp. 343–367. ISSN: 0010-4655. DOI: 10.1016/0010-4655(75)90039-9.

[160] Rene Brun and Fons Rademakers. "ROOT - An Object Oriented Data Analysis Framework". In: *Nucl. Inst. & Meth. in Phys. Res. A* 389 (1997), pp. 81–86.

Acknowledgments

Writing a Ph.D. thesis is never the sole achievement of the author, but requires the assistance of many people. This is even more true for a data analysis thesis, as no data would have ever been acquired without a joint effort of the whole CRESST collaboration. I would like to thank all people involved, in particular for all the days spent underground to get and keep the experiment running.

First of all I would like to thank my supervisors Prof. Stefan Schönert (TU München) and Dr. Franz Pröbst (Max-Planck-Institut für Physik) for giving me the opportunity to write this thesis and for the constant support throughout the last years. Equal thanks go to my second referee, Dr. Hubert Kroha (Max-Planck-Institut für Physik) and to Prof. Gilles Gerbier (Queen's University) agreeing to become the external referee on short notice.

Without Franz Pröbst this thesis would have been utterly impossible. His sheer infinite knowledge about every detail of the experiment and data analysis combined with his constant support, even late in the evening, are of invaluable help. Thank you for all the trust you put in me and the freedom to follow my own ideas and interests, which is absolutely exceptional.

I am deeply grateful to my office mate Dr. Federica Petricca. Your quick and thorough proof-reading was only the last little bit of support for this thesis. No matter how stressed you are, I can always count on your advice and assistance, which I truly appreciate. It is very reassuring and fulfilling knowing you on my side pushing in a common direction. Moving into your office was one of my best decisions in the last years, not at least because of the many funny conversations. Mille grazie per tutto!

I would also like to use this opportunity to thank my predecessor Dr. Jens Schmaler, who introduced me during my time as Diploma student to CRESST in general and to data analysis in particular. Thank you for giving me a perfect start into the world of "hands-on" physics beyond university lectures.

I do not know how many *temporary permits* Carlo Bucci issued for me in the last years. Thank you for your constant support which goes far beyond bureaucracy.

I also want to highlight Dr. Raimund Strauss. Your commitment and enthusiasm for the experiment is just intoxicating. Many thanks for the constant interest in my work, your support and of course for the pleasant times, especially at Gran Sasso and in Amsterdam.

Many thanks go to a true CRESST veteran, Dr. Wolfgang Seidel. Although in charge of quite different aspects of the experiment, Wolfgang is always interested in particular if approached with tricky problems demanding unconventional solutions.

I would like to thank Only-In-Coimbra-Prof. Antonio Bento for opening a different perspective on various aspects of physics and life. We are very unhappy having to share you with Portugese students for half a year.

I am deeply indebted to Dr. Karoline Schäffner, my colleague and friend. Karo, I do not even know where to start. You definitely have a much larger contribution to this thesis than you think. Your constant encouragement and belief in me were of invaluable help, in particular during the last year. Thank you for all the pleasant times at, below and on top of Gran Sasso. You are a brilliant physicist, full of energy and never giving up, which I truly admire. I also do not know where to end, so I just say THANK YOU!!!

The working atmosphere in the MPI CRESST group is remarkably enjoyable, Dieter Hauff untiringly working on new detectors, Anja Tanzke my fellow sufferer since the beginning of my Diploma thesis, Dr. Godehard Angloher accepting me, although I am just a return physicist. Not to forget the all new group members and the ones who left during the last years

Special thanks goes to Marc Wüstrich, not only for proof-reading part of this thesis, but for always being up for an exchange of information when I sneak into the group office for a coffee and keep him from work.

I am also thankful to my friend and former-and-again-colleague Dr. Michael Kiefer. Michael, I would like to thank you in particular for the one or other liquid evening in the last months providing a very welcome distraction!

Throughout the whole time, I enjoyed the collaboration the TU München, Dr. Jean-Côme Lanfranchi and Prof. Lothar Oberauer, both always being encouraging and cooperative. I would like to thank, Andrea Münster whose analysis skills we *unfortunately* lost to crystal-growing and Prof. Stefan Schönert in particular for his valuable contribution to the last publication. Special thanks goes to Dr. Walter Potzel for sharing his immense experience and helping me to improve many of my publications and talks and: Toi Toi Toi. Equally, I would like to thank all the other members of TU München, I will not even try to list all of them here, since this is bound to fail.

Special gratitude I want to express to Andreas Zöller, my comrade in numerous fights (yes, fights IS the right word) against software issues and discussion partner for many analysis topics. Thank you Andi for your restless commitment to CRESST, not only being the Run33 shift king, but also for your close collaboration especially in the last year.

I would like to thank my Vienna colleague Dr. Achim Gütlein, for his constant interest in analysis topics, his valuable comments for numerous talks and publications and in particular for recalculating the neutrino floor on short notice.

Ich danke meiner Familie, die mich immer auf meinem Weg unterstützt haben und gerade in der letzten Zeit viel auf mich verzichten musste. Ihr habt die richtige Balance gefunden zwischen “Stress dich nicht so!” und “Wann wirst jetzt endlich fertig?”.

Johanna, du solltest nicht in der Danksagung meiner Doktorarbeit stehen, sondern in der meines Lebens. Wie glücklich es mich macht, dass du deines mit mir teilst!